Università degli Studi di Palermo

AREA RICERCA E TRASFERIMENTO TECNOLOGICO
SETTORE DOTTORATI E CONTRATTI PER LA RICERCA
U. O. DOTTORATI DI RICERCA

Dottorato di Ricerca in Scienze Fisiche e Chimiche
Dipartimento di Fisica e Chimica – Emilio Segrè
Settore Scientifico Disciplinare CHIM/02

COMPUTATIONAL STUDIES OF MODIFIED H-BETA ZEOLITES FOR HYDROCARBON CATALYTIC CONVERSION

IL DOTTORE
LAURA GUECI

IL COORDINATORE
PROF. MARCO CANNAS

IL TUTOR
PROF. FRANCESCO FERRANTE

Il CO-TUTOR
PROF. DARIO DUCA

CICLO XXXVI
ANNO CONSEGUIMENTO TITOLO 2024

Contents

Preface

This thesis collects the research conducted over the three years of my doctoral studies in the field of computational catalysis. I investigated platinum-modified Beta zeolite for its application as a heterogeneous catalyst in reactions of significance within the industrial sector of fuels, particularly structural conversion processes of hydrocarbons.

Initially, I constructed a model of the catalyst, considering its two types of active sites, acidic and metallic, treated independently. I employed various computational approaches and attempted to discern which would be most suitable. In this I faced challenges, particularly in the case of acidic functionality, in line with the current literature debate. Once I achieved a satisfactory description, I proceeded to investigate the interactions between the two functionalities, approaching this aspect experimentally as well. Indeed, I spent three months at the "Industrial Chemistry and Reaction Engineering" group of Åbo Akademi University (FIN), where I prepared and characterized bifunctional catalytic materials, analyzing how the presence of metal affected acidic properties. Then, I endeavored to integrate these two perspectives, with potentially interesting results. Finally, I addressed an atomistic-level study of a model reaction mechanism, focusing on the isomerization of a small alkene. This served as an initial exploration into structural conversion processes.

The organization of the dissertation follows the outlined chronological order. After a general introduction and a more in-depth focus on the aim of the research, the thesis is divided into four main chapters, each one presenting its own final thoughts. Lastly, the overall conclusions are drawn, together with future perspectives. In the appendix, the two articles that I authored on the topic are provided, published in indexed journals in the course of these three years.

It has been a long and at times challenging journey, albeit undeniably rewarding, yet it feels like it passed in the blink of an eye. I am grateful for every moment. I hope I have made the most of them...

I would like to express my heartfelt appreciation to my tutors, Prof. Francesco Ferrante and Prof. Dario Duca, for their guidance and assistance, spanning not only the duration of this project but several years now.
I would also like to acknowledge Prof. Dmitry Yu. Murzin of the Åbo Akademi University, who generously hosted me and participated in a productive collaboration that deepened my understanding.
Special gratitude goes to my family, whose support has been a constant of my life and to my colleagues and friends, that offered useful insights into the study and played a significant role in my personal development. Thank you, in alphabetical order, Ph.D. Marco Bertini, Chiara Ferlito, Ludovico Guercio, Iryna Kovinchuk, Ph.D. Lorenzo Lisuzzo, Ph.D. Mark E. Martínez-Klimov, Chiara Nania.

Enjoy reading,
Laura

Introduction

1.1 Transportation fuels

The global demand for energy to fuel transportation is exceptionally high, reaching approximately 11 billion liters per day, encompassing gasoline, diesel, heavy fuel oil, and jet fuel collectively. At present, the vast majority of global transportation relies on combustion engines, predominantly consuming liquid petroleum fuels [1].

Gasoline is a refined petroleum product comprising a mixture of over 500 hydrocarbons with 5 to 12 carbon atoms, along with additives and blending agents. It serves as the primary fuel for spark-ignition engines in cars and motorcycles, where a spark plug ignites the fuel-air mixture in the cylinder engine [2]. The composition of gasoline varies significantly, influenced by factors such as the crude oils used, available refinery processes, overall product demand, and product specifications. Further, hydrocarbon blends may contain contaminants like sulfur, nitrogen, oxygen, and specific metals [3]. Consequently, the typical composition of gasoline hydrocarbons (in volume %) includes 4-8% alkanes, 2-5% alkenes, 25-40% *iso*-alkanes, 3-7% cycloalkanes, 1-4% cycloalkenes, and 20-50% total aromatics, of which 0.5-2.5% is represented by benzene. The four major constituent groups of gasoline are therefore olefins, aromatics, paraffins, and naphthenes.

The fundamental characteristics of gasoline include density, vapor pressure, distillation range, octane number and chemical composition. In the context of motor gasoline, its appeal depends on having optimal volatility, resistance to knocking (linked to octane rating), efficient fuel economy, minimal deposition on engine components, and achieving complete combustion with low pollutant emissions. The octane number, or octane rating, quantifies the resistance of gasoline to abnormal combustion phenomena such as pre-detonation, commonly referred to as knocking. This measurement is relative to a blend of 2,2,4-trimethylpentane and *n*-heptane. Higher octane numbers are preferable in internal combustion

engines [4]. Current environmental standards have prompted governments and industries to advocate for gasoline production with minimal content of environmentally or health-harmful compounds, such as lead, aromatics, and oxygenated compounds. However, the reduction in these detrimental compounds adversely affects the octane number of the gasoline pool [5].

Diesel fuel finds widespread use in diesel engines, prevalently employed in trucks, buses, and some automobiles. Differing from spark ignition engines, diesel engines operate on the principle of compression ignition, where the fuel-air mixture ignites due to the heat generated by compressing the air in the engine cylinders. Diesel fuel is a denser and less refined product compared to gasoline, characterized by a hydrocarbon chain in the range of 15-18 carbon atoms with fewer volatile compounds [6]. Similar to diesel, jet fuels are liquid transportation fuels specifically designed for use in aircraft. Commercial jet fuel constitutes a complex mixture of various compounds, including *n*-paraffins, *iso*-paraffins, olefins, naphthenic, and aromatic compounds, distributed in the ranges of 0-7.5 wt%, 38-81 wt%, 0.3-6.6 wt%, 4.9-15.1 wt%, and 2.6-14.4 wt%, respectively [7]. The hydrocarbon chain length in jet fuels typically falls between 9 and 14 carbon atoms.

For complex hydrocarbon mixtures like diesel, jet fuels, and lubricants, the pivotal characteristics revolve around their cold flow properties, typically indicated by the cloud point, cold filter plugging point, or the pour point of the fuel. Importantly, all these are interconnected and depend on the composition of the fuel. The specifications for cold flow properties in diesel fuel differ based on the geographical region of use; for instance, the pour point can range from +3 °C in tropical regions to -35 °C in cold regions [8]. If *n*-paraffins exhibit a higher melting point compared to other hydrocarbons with equivalent molecular weights, conversely, *iso*-paraffins display superior cold flow properties having at the same time a lesser impact on other fuel properties. For this reason, the hydroisomerization process of *n*-paraffins has garnered increased attention in recent years, as outlined in the subsequent section.

All the energy sources discussed so far for transportation derive from fossil fuels. Concerns have been raised about the potential depletion of petroleum-based fuel resources and the environmental issues arising from the release of greenhouse gases and other pollutants into the atmosphere. These factors make it crucial to earnestly explore alternative fuels. While these substitutes aim to replace petroleum fuels, some still incorporate a small amount of petroleum in their composition. Key alternative fuels include alcohol, liquefied petroleum gas, compressed natural gas, hydrogen, and electricity for gasoline-type vehicle oper-

ation. For diesel engines, Fischer-Tropsch liquids derived from natural gas and ethanol from biomass may gain prominence, alongside the use of vegetable oil and dimethyl ether [4, 9]. However, despite the ongoing efforts towards alternative fuels and propulsion systems, projections for the year 2050 indicate that petroleum fuels will continue to play a substantial role in global transportation [1].

1.2 Hydroconversion reactions of hydrocarbons

Hydroconversion has played a pivotal role in the petroleum industry for decades, being a well-explored and established technology that has been extensively used in crude oil refining. The term hydroconversion generally refers to two distinct but interconnected processes, *i.e.*, hydrocracking and hydroisomerization, carried out in the presence of hydrogen for different oil fractions. In hydrocracking, the feedstock is catalytically converted to lower carbon numbers, while in hydroisomerization normal hydrocarbons are transformed into branched ones having the same number of carbon atoms in the chain.

Among the first to exploit the possibilities offered by the hydrocracking process, Mobil commercialized selective catalytic cracking of long-chain hydrocarbons in the lube dewaxing process, using a ZSM-5 catalyst with strong acidity and a uniform pore size [10]. Following this, extensive research has been devolved, either in partnership with oil companies or within an academic context, to achieve a deeper understanding of the process [5, 11, 12, 13, 14]. Even in the current scenario, where the focus is on renewable sources, hydrocracking is always a hot topic. For example it has been reported within the conversion of algae oil to aviation fuel-range hydrocarbons [15]. Selective hydroisomerization is mainly desired for the improvement of the octane number, when the interest is in the gasoline pool (C5–C6), and for dewaxing of long-chain hydrocarbons aimed at improving their cetane number and cold flow properties [16]. Notably, even when producing green diesel by vegetable oil hydrodeoxygenation, the so formed *n*-paraffins have to be isomerized in order to comply with the commercial diesel fuel specifications [17, 18].

Both hydrocracking and hydroisomerization are catalyzed by bifunctional catalysts, that combine two catalytic functions in the same material, *i.e.* in this case, the acidic function of a support and the hydrogen affinity properties found in many noble metals. In fact, the metal is responsible of the hydrogenation/dehydrogenation steps, while acidity is required for isomerization [16, 19, 20]. Hence the balance between the two functionalities, together with their grade of intimacy,

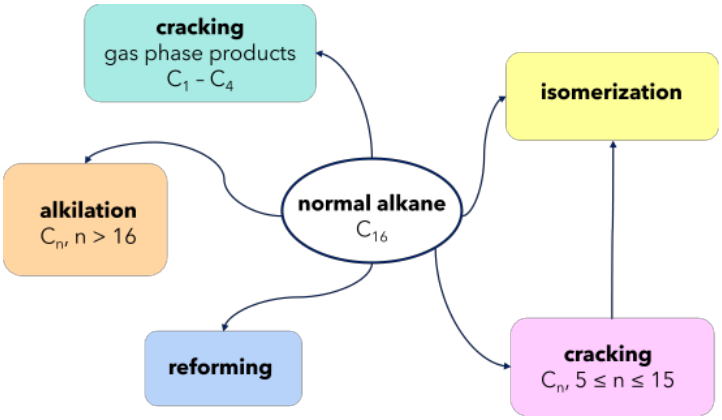

Figure 1.1: A selection of possible processes and products connected to hydrocracking, taking hexadecane as a model hydrocarbon.

are fundamental factors orienting activity and selectivity of the catalyst towards one or the other hydroconversion process [21].

Selective isomerization of gasoline range alkanes is easier to realize than for long-chain hydrocarbons, because the latter are more prone to rapid and diverse cracking during hydroisomerization. As an example, an overview of all the possible products originating from hexadecane hydrocracking is given in Figure 1.1. Still, also long-chain hydrocarbons (C≥15) are of primary interest, since they make up to 80 wt% of material known as wax and, as already mentioned, extensive research has been carried out to obtain, from a waxy feedstock, value-added products with improved fuel quality [22]. Therefore catalyst development become a crucial area of investigation, aimed at optimizing the relation between substrate molecules and suitable materials specifically tailored to maximize the isomer yield.

Table 1.1 summarizes the great variety of catalyst that has been proposed during the years. More information can be found in several reviews on the topic, that have been published in the last decade [16, 23, 24]. As metallic component, most catalysts contain platinum or palladium, but also Ni-Pt and Ni-Mo have been recently employed in hydroisomerization of long-chain alkanes. For the acidic supports Beta-zeolites, SAPO-11, and ZSM-5 are well established; besides, composite materials containing mesoporous MCM-41, MCM-48, and SBA-15 were explored [25], together with the more recent inclusion of hierarchical zeolites [26, 27].

As regards operating conditions, hydroisomerisation of long chain paraffins has been typically performed in continuous reactors in the 220-300 °C range of temperature, under 20-45 bar of pressure. The continuous operation facilitates a high hydrogen to liquid feed ratio giving relatively high conversions and selectivity

Table 1.1: Different catalysts employed for the hydroconversion of alkanes in the $C_{18}-C_6$ range, together with the optimum reaction condition and conversion levels reported, in percentage yield or selectivity.

Feed	Conditions	Catalyst	Conversion	Ref
C_{15}-C_{18} alkanes	310 °C, 30 bar, LHSV=1 hr^{-1}, H_2/oil=800	Ni-Mo-SAPO-11	S=58-65	[28]
n-hexadecane	220 °C, 30 bar	0.7 wt% Pt-H-Beta/Al_2O_3	80	[21]
n-hexadecane	290 °C, 75 bar, WHSV=1.3 hr^{-1}	Pt-Al-Beta (80)	35.5	[20]
n-hexadecane	280 °C, 60 bar	Pt-SAPO-11-S	80	[29]
n-hexadecane	280, 290 and 300 °C, 55 bar	Pt/Al-SBA-15	S=43	[30]
n-hexadecane	8 points in the 280-370 °C range, 20 bar, WHSV=3.7 hr^{-1}	Pd-SAPO-41	89	[31]
n-dodecane	300 °C	Pt-ZSM-22-BUN	49	[32]
n-decane	270-280 °C, 20 bar, WHSV=2.5 hr^{-1}	Ni/Pd-ZSM-22	S=74	[33]
n-hexane	205-358 °C, 17 bar, H_2=180 mL/min, feed=0.24 mL/min	Pt-H-Beta-25/Bentonite	S=80	[34]
n-hexane	250 °C, 0.066 bar in C_6H_{14}	Ni/Pt-HZSM-5	90	[35]

towards isomerisation products opposite to the batch operation [10]. Similarly, also the hydrocracking process has been very scarcely investigated batch-wise [36], while a continuous reactor was employed, for example, by Kaka Khel *et al.* [37]. They prepared several catalysts based on H-Beta zeolites, varying the silicon-aluminium ratio and the metal used (Pt, Ni, Ru), to then study the hexadecane hydrocracking at *ca.* 230 °C and a H_2 pressure of 40 bar.

1.2.1 Hydroisomerization reaction: the mechanism

The scheme of bifunctional *n*-alkane hydroisomerization was established more than 60 years ago [38]. Later on, a comprehensive review was given by Weitkamp [19] and many applicative papers were based on this mechanism [16, 20, 21, 39]. Hydroisomerization occurs as shown in Figure 1.2. The reactant (in blue) is first dehydrogenated on a metallic site forming an alkene, or more precisely a mixture of *n*-alkenes, *n*-C_iH_{2i}. These desorb from the metallic sites and diffuse to Brønsted acidic sites (the portion represented inside the rectangle in the Figure) where they are protonated to the secondary alkylcarbenium ions, *n*-$C_iH^+_{2i+1}$. Carbenium ions are reactive intermediates which can undergo a number of conversions, such as skeletal rearrangements and carbon-carbon bond rupture, through β-scission. The latter consists of a radical reaction that takes places two carbons away from the charged carbon: breaking that bond an olefin and a free radical with two fewer carbon atoms are produced. In the case of β-scission of *n*-$C_iH^+_{2i+1}$ a primary carbenium ion would be formed, which is energetically unfavorable. The *n*-alkylcarbenium ions hence undergo skeletal rearrangements exclusively, whereby monobranched alkylcarbenium ions, *iso*-$C_iH^+_{2i+1}$, are formed. If there is an efficient mechanism of desorption from the acidic sites, monobranched alkenes, *iso*-C_iH_{2i}, are released and diffuse to metallic sites where they are hydrogenated

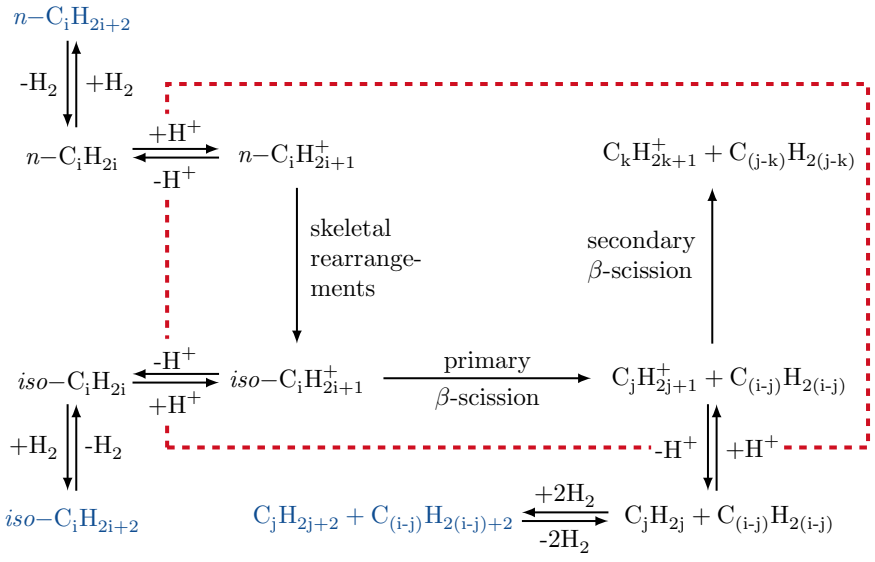

Figure 1.2: The reaction mechanism of isomerization and hydrocracking of an *n*-alkane on a bifunctional catalyst. The reactants and the main products are depicted in blue. The steps enclosed by the red rectangle occur on Brønsted acidic sites, while the other steps take place on the metallic sites. Adapted from [19].

to monobranched alkanes, *iso*-olefins, *iso*-C$_i$H$_{2i+2}$. These are the primary products observed at low conversions [19].

Summing up, 7 successive steps are required, namely 3 chemical and 4 physical steps. In the order, dehydrogenation on the metallic site of the *n*-alkane into *n*-alkene, isomerization over the acidic site into a *iso*-alkene molecule, hydrogenation of this *iso*-alkene, diffusion of *n*-alkane molecule from the gas phase to the metallic site, diffusion of the *n*-alkene from the metallic to the acidic site, diffusion of *iso*-alkene from the acidic to the metallic site, and finally diffusion of the *iso*-alkane from the metallic site to the gas phase.

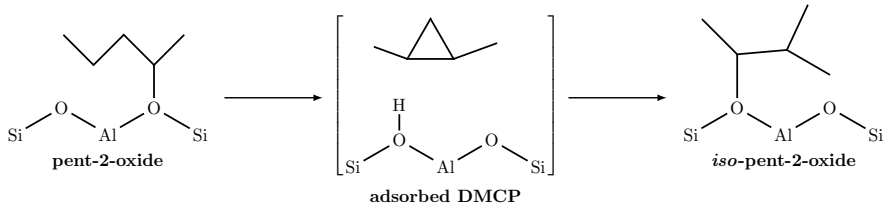

Figure 1.3: Skeletal isomerization scheme of pent-2-oxide into *iso*-pent-2-oxide. Either the formation of an adsorbed dimethyl-cyclopropane (DMCP) could be involved as an intermediate species or not.

If a sufficient number of dispersed metallic species are present so that equilibrium in the (de)hydrogenation step is allowed, then the skeletal isomerization is the rate-determining step. Support for this mechanism is provided by the fact that the rate of *n*-pentene isomerization on a metal-free catalyst is essentially equal to that of the above overall reaction [40, 41].

A remarkable advantage in using a bifunctional catalyst for this hydrocarbon hydroisomerization is that the concentration of alkenes within the zeolite micropores remains low, thus minimizing consecutive cracking or oligomerization. The latter reactions lead to coke formation and hence deactivate the catalysts. However, as the conversion increases, consecutive reactions can occur at the acidic sites, specifically a second and a third branching rearrangement forming dibranched *iso*-$C_iH_{2i+1}^+$ and tribranched alkylcarbenium ions. These tribranched cations are not desorbed, they rather undergo β-scission into an alkylcarbenium ion $C_jH_{2j+1}^+$ and an alkene $C_{(i-j)}H_{2(i-j)}$, where j is an integer lower than i [19].

Going deeper in detail into the skeletal isomerization step of the process, the most likely mechanism, according to literature [40, 42] involves at first the interaction of a secondary alkylcarbenium ion with a zeolitic oxygen atom (alkoxy species). Subsequently, a proton backdonation to the framework occurs, leading to the closure of the hydrocarbon into a three-membered protonated ring. Then, the ring is reopened by protonation and a different bond is broken, leading to a secondary alkoxide. The isomerization is finally completed when a hydrogen atom is donated from the hydrocarbon intermediate to the zeolite, restoring the Brønsted acidic site, and the *iso*-olefin is obtained.

As depicted in Figure 1.3, the critical point lies in the formation of the cyclopropane-like species interacting with the zeolite, specifically dimethyl-cyclopropane (DMCP) if referring to *n*-pentene as isomerization substrate.
Weitkamp *et al.* [19] found that the traditional methyl or hydride transfer mechanism could not explain the product distribution in the study of C6-C15 *n*-alkane isomerization catalyzed by the Pt/CaY molecular sieve. Therefore, the involvement of some protonated cyclopropene-like species (PCP) was used to explain isomerization in zeolite catalysts [40, 43]. However, the hypothesis is based on indirect experimental evidence and, to the best of the present knowledge, substituted cyclopropane species have never been isolated. This is the reason why the nature of these species has been debated for long time [44]. The possibility of DMCP as intermediate is often disregarded [43] and static *ab initio* calculations dealing with zeolites suggest instead a PCP as a transition state [45, 46]. Demuth *et al.* [40], on the other hand, were the firsts, nearly 20 years ago, to propose a mechanism via cyclopropane intermediates for the isomerization of 2-pentene

using a periodic model. In support of this, recent *ab initio* molecular dynamics showed that, at a certain temperature, tertiary carbenium ions exist in significant concentrations [47, 48]. A possible scenario could be a transfer of a hydrogen atom within the ring of the cyclopropane, in an edge-protonated transition state, thus avoiding the formation on the physisorbed intermediate. Otherwise, the existence of an ephemeral intermediate could be effectively feasible, being however difficult to prove experimentally.

1.3 Zeolites

1.3.1 Origins and applications

Zeolites are among the most abundant minerals on Earth. They are crystalline aluminosilicates with a three-dimensional structure characterized by channels and cavities of molecular size.

Of mainly volcanic origin, they can be found in crystallized forms in igneous and metamorphic rocks or, in grains of smaller diameters, accumulated in sedimentary rocks [49]. For example, ocean bottom sediments are moderately rich in zeolites, but these deposits are so far rather inaccessible. Luckily, zeolites may also constitute important components of tufs or clay, that is relatively simple mining, creating perfect conditions for their wider use. The zeolites occurring in nature that possess practical significance principally are clinoptilolite, mordenite and chabazite. They can find application, for example, in agriculture, as carriers of compounds or in the treatment of soil and fish ponds and as a feed additive [49, 50]. However, natural zeolites can hardly be employed in industrial processes, mainly because of the fact that their properties strictly depend on their crystal structure. First of all, the channel diameters are too small (in the case of clinoptilolite, for instance it is 0.30–4 nm [51]), not allowing for the adsorption of larger gas molecules and organic compounds. Moreover, a time-related and "green" concern is that zeolite deposits are non-renewable sources. Thus, even if natural zeolites were discovered in the 18th century, industrial applications did not began before the 1950s, when procedures were developed to obtain synthetic zeolites of commercial interest [52].

The first attempt to synthesize zeolites in laboratory conditions was to imitate hydrothermal processes, using elevated temperature or pressure and natural raw materials and/or synthetic silicates as initial substrates. They showed that, by heating the aluminosilicate raw materials in the presence of alkaline solutions within a few hours or days, depending on the case conditions, the final desired product could be obtained. However, since appropriate equipment, clean sub-

strates and energy are required, the price of the product may be much higher than that of natural zeolite. Therefore, current trends in the synthesis of zeolites are focused both on finding cheaper and greener substrates and on reducing the cost of the reaction itself.

Today, in addition to hydrothermal synthesis several methods are known, such as: molten salt method, fusion method, alkali activation, microwave-assisted synthesis, synthesis by dialysis [49]. In general, the synthetic approaches can be divided into two main assembles on the basis of secondary porous formation, namely, bottom-up and top-down approaches [53]. The bottom-up is a one-step approach, that results in a sequential rotational intergrowth of zeolite frameworks, in which the secondary porous is created during templates' stage [54]. Conversely, in the "top-down" approach, the secondary porous is created at the post-synthesis stage [55], through demetallation, delamination, and recrystallization processes [56].

A huge effort has been devoted to zeolite syntesis because numerous studies confirmed the superiority of synthetic zeolites compared to natural ones. To name a few, they showed much higher adsorption capacity for heavy metal ions than the natural zeolites [57] and, as already stressed out, the significantly larger pore size of synthetic zeolites happens to constitute another sensible advantage. In fact, this not only extends the range of application to reaction involving larger compounds, but lowers the risk of pore blockage and catalyst deactivation that zeolites with smaller pore size, as natural ones, may suffer.

In nature, zeolites can contain aluminium, hydrogen, alkaline or alkaline earth metals and water molecules. Due to the continuous development of synthetic strategies, it is possible to obtain modified zeolites, for example, the Al content can be adjusted, or noble/transition metals can be inserted, embedded in the structure [37] or supported on the zeolite surface [58]. Thus, the possibility of tuning the properties is probably the major advantage of synthetic zeolites. It should be however pointed out that synthetic zeolites does not come without disadvantages [49]. The most trying problem regards their form of finely grained crystalline and highly dispersive powder (single crystals have sizes up to a few microns), which certainly limits their use. Shaping procedures such as extrusion are often necessary for an industrial scale application [34, 59]. Moreover, due to the diverse origin of substrates and different methods of synthesis, the products have various chemical and physical properties, so that ongoing research is required to intimately understand all aspects of the interrelation. Many subjects still remain hot topics that need to be tackled to fully exploit the enormous zeolite potentialities.

The distinctive properties of zeolites, including porosity, shape-selectivity, acidic sites, and reversible dehydration, render them highly versatile. In addition to what already reported, they find usage as absorbents and molecular sieves, in water softening, and in heterogeneous catalysis [60, 61]. Major areas of catalytic application encompass biomass conversion, direct valorization of natural gas, methanol-to-olefins processes, hydroisomerization/hydrocracking reactions in oil refining and the catalytic reduction of nitrogen oxides. However, this list is not exhaustive, given the broad scope of zeolite catalysis, making a comprehensive exploration of all relevant reactions impractical. Therefore, given the focus of the present investigation, a deliberate decision has been made to delve in greater detail solely into the state-of-the-art description of hydrocarbon conversion processes. For a broader overview of other reactions, please refer to the comprehensive reviews available in the literature, each dedicated to specific aspects of zeolite catalysis [62, 63, 64, 65, 66].
It is here noteworthy to acknowledge the role of quantum chemical methods in zeolite catalysis. Modern computational methodologies, encompassing semi-empirical methods, *ab initio* methods, and density functional theory (DFT), have significantly contributed to elucidating the molecular nature of active sites in zeolite catalysts and studying reaction mechanisms from an atomistic perspective [67, 68, 69, 70, 71, 72].

1.3.2 Structure

The fundamental units of zeolites are the TO_4 tetrahedra (with T = Si or Al), joined by the vertices via the oxygen atoms. The ways in which these tetrahedra connect determines a great variety of structures. To date, the International Zeolite Association (IZA) has approved 260 distinct structures, identified by a framework type code: a three-capital-letter code uniquely assigned to each distinct zeolite [51]. As special rules, type codes beginning with a "-" indicate an interrupted framework, whereas codes beginning with a "*" are indicative of an experimentally observed zeolite that possesses intergrowth or structural disorders, such as β-zeolite, *BEA.

Describing the structure of a zeolite framework has always been a challenging task. Toward this end, many structural descriptors have been devised during the past decades. In the following an overview of the most notable is given, focusing in particular on β-zeolite, since it is the one studied in this thesis.

Zeolite structures contain rings, cavities and channels. A ring is usually referred to as a cycle of T and O atoms that is not the sum of any number of shorter cycles. A ring composed of n T and n O atoms is called an n-ring.

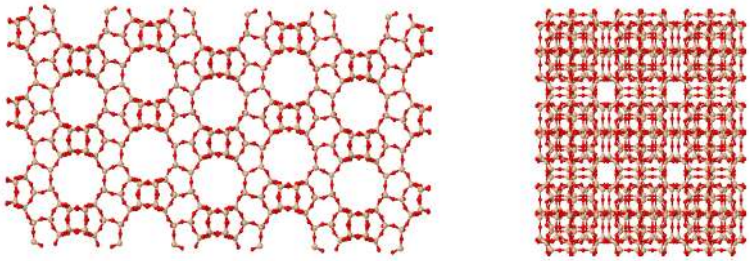

Figure 1.4: Two perspectives of Beta zeolite.

According to the definition reported by Li *et al.* [73], a cage is a polyhedral pore whose faces are all too narrow to be penetrated by guest species larger than a water molecule, whereas a cavity is the pore with at least one face large enough to be penetrated. In practice, a cage has no face larger than 6-ring, whereas a cavity has at least one. Finally, the channel in a zeolite framework is a pore infinitely extended in one dimension, large enough for guest species to diffuse along its length. Channels may intersect to form two- or three-dimensional channel systems. In BEA structure, silicon and oxygen atoms are linked together forming 3D twelve-membered rings (diameter of 6-7 Å along the [010] and [100] axes, 5-6 Å along [001]), together with 6, 5 and 4-membered rings (see Figures 1.4 and 1.6).

Each T atom in a zeolite framework corresponds to a coordination sequence and a vertex symbol. The first consists of a sequence of integers, where the n^{th} integer represents the number of T atoms involved in the n^{th} neighboring shell surrounding the original T atom. The vertex symbol indicates the size of the smallest ring associated with each of the six angles of a T atom. Zeolite frameworks with different coordination sequences or vertex symbols are topologically different; see Table 1.2 for data relative to BEA. As mentioned in passing, the T letter is used either for Si or Al, since a silicon to aluminum isomoprhous substitution in the zeolite framework could take place, leading to the formation of a Brønsted acidic site, after compensating the extra negative charge with a hydrogen atom. Hence the wide application that involves zeolites as acid catalysts. A new descriptor was proposed by Sastre and Corma in 2009 [74] that can be used to locate catalytically active Brønsted sites in a zeolite framework, the ring index. It describes the rings present in a zeolite structure, and it is applicable for both T and O atoms. The ring index of an atom is defined as the list showing the sizes and numbers of rings that pass through that atom. To give an example, in zeolite BEA, the ring index of the T1 atom is $4{\cdot}5{\cdot}4{\cdot}12_3{\cdot}5{\cdot}5$, indicating that it is involved in two 4-rings, three 5-rings, and three 12-ring.

Table 1.2: Coordination sequences (left) and vertex symbols (right) for each topologically distinct tetrahedral site of the BEA framework, see reference [51].

Coordination sequences and vertex symbols:											
T1	4	10	19	32	51	77	105	133	167	207	$4{\cdot}5{\cdot}4{\cdot}12_3{\cdot}5{\cdot}5$
T2	4	10	19	32	51	77	102	133	170	208	$4{\cdot}5{\cdot}4{\cdot}12_6{\cdot}5{\cdot}5$
T3	4	10	21	32	49	76	109	137	170	207	$4{\cdot}6{\cdot}4{\cdot}12_3{\cdot}5{\cdot}5$
T4	4	10	21	32	49	74	105	139	173	204	$4{\cdot}6{\cdot}4{\cdot}12_6{\cdot}5{\cdot}5$
T5	4	11	18	29	48	80	107	133	160	203	$4{\cdot}5_2{\cdot}5{\cdot}5{\cdot}5{\cdot}6$
T6	4	11	18	29	48	77	106	134	160	204	$4{\cdot}5_2{\cdot}5{\cdot}5{\cdot}5{\cdot}6$
T7	4	12	18	31	51	76	109	133	164	210	$5{\cdot}5{\cdot}5{\cdot}6{\cdot}5_2{\cdot}12_5$
T8	4	12	19	32	48	75	112	134	164	206	$5{\cdot}5{\cdot}5_2{\cdot}12_7{\cdot}6{\cdot}6$
T9	4	12	17	30	54	77	106	134	160	212	$5{\cdot}5{\cdot}5{\cdot}5{\cdot}5_2{\cdot}12_3$

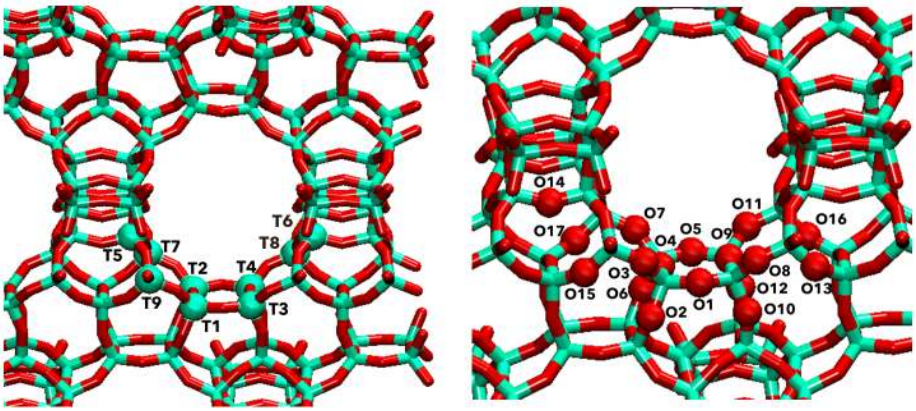

Figure 1.5: On th left, all the 9 topologically distinct T sites that characterize the BEA framework, with their labels (T= Si or Al); on the right, all the uniques oxygen atoms, from O1 to O17.

This corresponds to the vertex symbol of T1 (see Table 1.2). However by applying the same definition to oxygen atoms, all the different local environments can be identified, that directly relate to distinct Brønsted sites. In BEA there are 9 and 17 crystallographically non-equivalent Si and O atoms, respectively, causing the topological possibility of 32 unique Brønsted acidic sites. See Figure 1.5 for a depiction of all these topological T and O sites, with their labels. Another advantage of using ring indices is that the numbers of rings of various sizes and the average ring size in a zeolite framework can be calculated, which cannot be deduced from vertex symbols in general cases.

A zeolite framework can be deconstructed in building units, in a wide variety of possible ways. Some of these lack strict definition thus, in practice, people tend

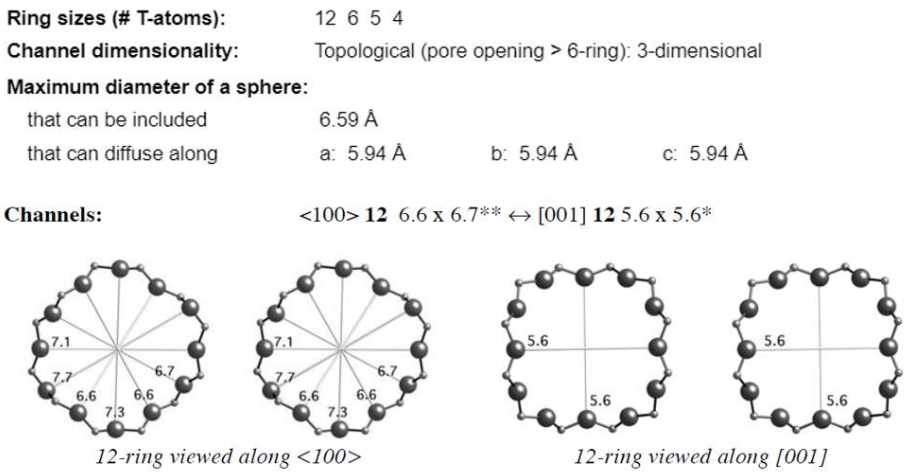

Figure 1.6: Sizes and diameters of rings and channels characterizing the BEA framework, as reported by IZA [51].

to focus on the simplest or the most representative building units that reflect the topological characteristic of the given zeolite framework. Among these, the secondary building unit (SBU) and the composite building unit (CBU) are the most frequently encountered. Figure 1.7 shows building units involved in the BEA framework. This was the state of the art until 2010, when Blatov and co-workers showed that a zeolite framework could be unambiguously decomposed in only one way following the geometric concept of natural tiling [75]. In this approach, the zeolite framework corresponds to a three-dimensional net, and the tiles composing the natural tiling of the zeolite net are the natural building units (NBUs). Blatov and co-workers constructed the natural tilings for nearly two hundred IZA structures and assigned a unique name to every located NBU. Decomposing zeolite frameworks into NBUs has several important advantages over other decomposition methods. First, the choice of NBU is unambiguous, and the decomposition procedure can be done easily by computer programs. Second, NBUs are able to represent all of the cages, cavities and pores of a zeolite framework. Third, the similarities between different zeolite frameworks can be analyzed by comparing their NBUs and natural tilings. Because of all these reasons, IZA has promptly embraced the concept of natural tiling to describe zeolite frameworks in its official database. In this thesis NBU labels of BEA, as reported in Figure 1.8 will be used to identify cavities when necessary.

Figure 1.7: The three composite building units in which the BEA framework can be deconstructed, from the International Zeolite Association [51].

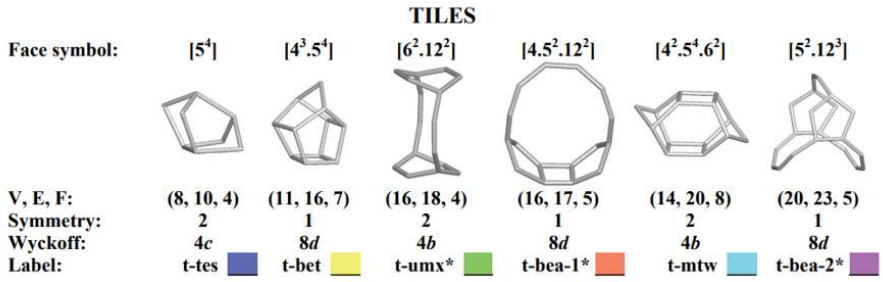

Figure 1.8: The natural building units that characterize the BEA framework [51].

1.3.3 Synthesis and characterization of metal modified zeolites

There are various methods for preparing catalysts based on zeolites modified with transition metals. As a general approach, one can either opt for an *in situ* synthesis or a subsequent modification of the zeolite [76, 77, 78].

In case of the *in situ* approach, metal precursors are introduced into the zeolite synthesis gel so that the coordination and interaction between the metal ions and the zeolite framework occur concurrently with the crystallization process. This method offers advantages in terms of enhanced metal dispersion, homogeneous distribution of metal species and structural stability, making it a valuable strategy for the development of advanced bifunctional catalysts [79]. From the point of view of the metal, in particular, the incorporation during the synthesis can prevent its leaching in subsequent catalytic reactions [80]. However, *in situ* synthesis may present challenges in precisely controlling the loading of metals within the zeolite framework. In fact, tuning the metal accessibility can be more challenging compared to post-synthesis modification methods. In addition, the latters typically pose fewer risks of undesired changes in the zeolite structure, while the incorporation of metals within the crystallization process could potentially alter the pristine framework. This structural modification may negatively impact the intrinsic properties and catalytic behavior of the zeolite. Finally, post-synthesis modification methods are convenient and simple, as numerous commercial zeolites can be purchased and modified, even if they may not be suitable if one is interested in achieving a precise Si/Al ratio that is not readily available [81].

The choice between these approaches depends on the specific requirements of the desired catalyst and the trade-offs deemed acceptable for the given application.

Among the most widely used methods for post-synthesis metal-modification of zeolites there are: ion exchange, impregnation (wet or dry), template-assisted synthesis and deposition-precipitation. Focusing on impregnation, it stands out as a commonly employed preparation method due to its technical simplicity, cost-effectiveness, and minimal waste production. In this process, the zeolite is impregnated with a solution containing metal precursors and subsequently dried. The resultant dry product undergoes further treatment, typically involving calcination and/or reduction, to obtain the desired catalyst [82]. Commonly used metal precursors include inorganic salts such as metal sulfates, carbonates, chlorides, nitrates, or acetates, as well as organic metal complexes like metal acetylacetonates. Water is the preferred solvent for inorganic salts due to the high solubility of many precursors, while organic solvents find application with organometallic precursors [83].

Two distinct methods of solid-solution contact are employed based on solution volume: wet impregnation (or evaporation-impregnation, EIM) and incipient wetness impregnation (IW). Wet impregnation involves an excess of solution; after a designated time, the solid is separated and excess solvent is removed either by drying or evaporation in a rotoevaporator, in this instance, without involving the filtration stage. In incipient wetness impregnation, also known as dry impregnation, the solution volume, at an appropriate concentration is equal or slightly less with respect to the pore volume of zeolite. Once impregnated, the catalyst is directly dried. However, this results in the retention of counterions from the metal precursor salt. To eliminate these substances, additional processing is required. To obtain the final catalysts with zero-valent metal particles, the impregnated and dried powder undergoes thermal treatment in a calcining and/or reducing environment [84].

Several factors impact the effectiveness of the impregnation method in producing catalysts, including temperature and precursor concentration [85]. Temperature affects both precursor solubility and solution viscosity, consequently influencing wetting time. The duration of contact between the zeolite and the metal precursor solution further influences metal loading and dispersion. The maximum loading is however constrained by precursor solubility. Stirring or mixing during impregnation also plays a crucial role in ensuring the uniform distribution of metal. Adequate agitation facilitates homogeneous metal dispersion, preventing the formation of metal aggregates. Understanding and optimizing these factors is crucial for tailoring the properties of metal-modified zeolite catalysts to meet

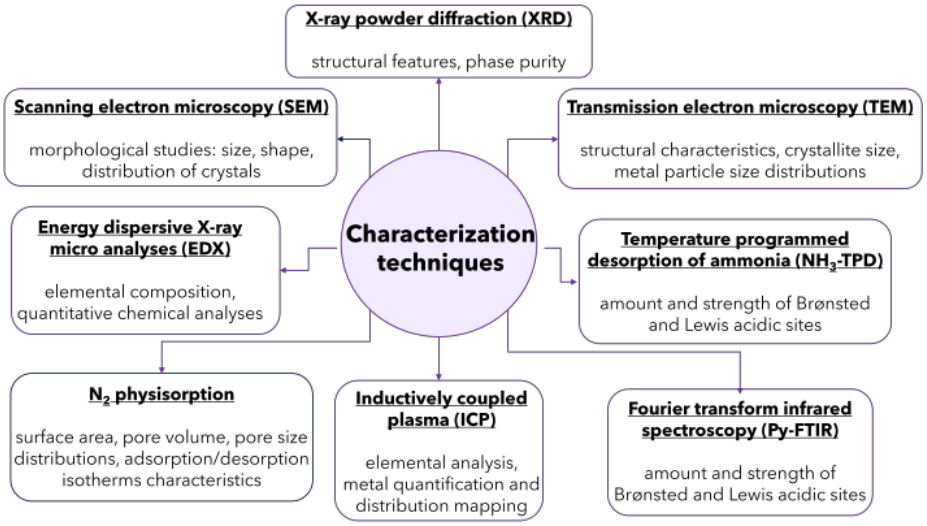

Figure 1.9: A selection of the characterization techniques useful for metal-modified zeolite materials, and the features they enable to investigate.

the desired specifications for a given catalytic application.

Figure 1.9 provides an overview of some among the numerous techniques that could be useful to characterize the prepared metal modified zeolite catalysts. These encompass, to name a few, elemental analysis techniques (EDX, ICP), microscopic approaches aimed at studying the morphological and structural properties of zeolite crystals and metal particles (SEM, TEM), methods such as N_2 physisorption, which analyze pore volume and adsorption/desorption characteristics of these materials. Finally, of special importance, there are techniques that enable to assess the Brønsted and Lewis acidity of the catalysts, through the use of probe molecules. These will be discussed in greater detail subsequently.

1.3.4 Applications as catalysts for hydroconversion

For zeolites to be used as catalysts in the hydroconversion process, among all, large effort was devoted both through theoretical studies and experimental techniques to characterize the number, strength, and location of the potentially active acidic sites, aiming at a formulation of acidity-reactivity relationships [86, 87, 88, 89]. A key role in these applications is played by the presence of metallic components, thus forming a bifunctional catalyst that exploit the hydrogenation/dehydrogenation activity of a noble metal such as platinum or palladium. Hence many experimental studies have been focused to unveil the effects of synthesis variables on the metal location and particle dispersion, which in turn affect activity and selectivity of the catalyst [34, 79, 80, 90, 91]. Still, being the advantages of an atomistic approach on tuning catalyst properties well estab-

lished [92, 93, 94, 95, 96, 97, 98, 99, 100], models and theories of computational chemistry have been extensively used to investigate the stabilization of metal atoms and/or small clusters within the zeolite cavities [101, 102, 103, 104]. In the following an overview of the current state of the art is given, concerning the two isolated functions and their interactions.

From an experimental point of view, proton affinity was used as a mean to evaluate Brønsted acidity. Common approaches to measure proton affinity of zeolites include IR and NMR spectroscopy, calorimetry and temperature-programmed desorption (TPD), exploiting the interaction of the acidic sites with basic probe molecules such as ammonia and pyridine [105, 106, 107, 108, 109]. Ammonia IRMS-TPD experiments, for example, have been used in combination with DFT studies to assign the stretching vibration bands of acidic OH groups in the IR spectrum to each Brønsted acidic site, located at crystallographically non-equivalent position in MOR, FAU, CHA and BEA zeolite frameworks [110, 111, 112, 113]. The research group led by Professor Murzin extensively employed the pyridine-FTIR technique, which allows for distinct information to be obtained, concerning either Brønsted and Lewis acidic sites and weak, medium and strong acidity features of a catalyst [34, 114, 115, 116]. The Brønsted acidity of sites belonging to FAU, CHA, IFR, MOR, FER, and TON zeolites was investigated by Trachta *et al.* [117] by the analysis of the adsorption of base molecules with different proton affinities. Even if the authors recognize the difficulties in estimating a site acidity ranking, they recommended a best acidity order based on the use of probes (such as acetonitrile) whose proton affinity is just below the site deprotonation threshold.

The use of the adsorption properties of small molecules to sample the acidity of zeolites Brønsted sites is complicated by many factors, such as accessibility of the involved zeolitic site, the orientation of the probe with respect to the framework, the tendency of the base to accept protons, and the stabilization of the resulting ion pair. As a matter of fact, the above mentioned orientation is driven by a delicate balance between the directional interaction with the acid hydrogen atom and a number of weak interactions with the zeolite walls; just these latters, from the computational point of view, are very difficult to be estimated and, even if a number of correction schemes for dispersion interactions was proposed in the recent years, it is not guaranteed that these corrections allow to reach the accuracy needed for the most reliable description. Accordingly, for an atomistic analysis, it is perhaps a better idea to avoid these complications and resort to acidity rankings based on deprotonation energies, even if this quantity is not accessible by direct measurements [118].

DPEs in various zeolites have been estimated from quantum chemical calculations using either isolated or embedded clusters [119, 120, 121] and periodic models [118, 122], each method bearing its advantages and disadvantages. In particular, values obtained using small cluster models show significant variations with cluster size, reaching convergence only when systems containing more than 20 tetrahedral SiO_4 units are investigated [107]. In case of embedded clusters, for example within a QM-Pot approach, the influence of cluster size is much smaller although, as a downside, issues associated with embedding may arise. In this context, Brändle and Sauer reported that all the calculated DPE values for FAU and MFI are within a range 3 and 6 kJ mol^{-1} wide, respectively, while values for different crystalline structures span within a range of less than 30 kJ mol^{-1} [119, 123]. These findings would indicate that the intrinsic acidic strength of zeolites is hardly influenced by the framework structure. To avoid embedding artifacts, periodic DFT was used by Jones *et al.* [118] in a broad study of deprotonation energies for several zeolites, mapping every unique crystallographic position for the Al-Si substitution. They reported mean DPE values, obtained by averaging over the four distinct proton locations at each Al atom, in the range 1190-1212 kJ mol^{-1} for all crystalline frameworks considered. This investigation suggested that DPEs are insensitive to the Si – O – Al bond angles, but conversely exhibit a dependence on the framework densities [122, 124]. However, the employed method is prone to errors, having to account for the artificial interactions arising among charged cells, created after the deprotonation of a zeolite site, in periodic calculations [125, 126]. More recently, the fact that the sites Brønsted acidity strength is inversely correlated with the framework density was confirmed by Trachta and coworkers [127], which used a series of increasing-size cluster models to estimate the deprotonation energies in FAU, CHA, IFR, MOR, FER, MFI, and TON zeolites. After the results of cluster models have been corrected by applying an electrostatic embedding, from the proposed deprotonation energies reported there a mean value of 1245±9 kJ mol^{-1} can be calculated, which is sensibly higher than the one obtained by Jones *et al.*

In spite of the significant number of studies reported on this topic, the effect of zeolite topology and composition on intrinsic acidity and reactivity is far from being fully understood. Many questions are still open and, especially from an atomistic-scale point of view, more accurate treatments are desirable, being however challenging the attempt to correlate computational results and experimental data, due to the inherent dissimilarity in what can be investigated in the two cases.

As for the metal component characterization, the discussion appears to be equally complex and open for further advances. In fact, a step by step computational approach on platinum clustering inside large pores of aluminosilicates, and BEA in particular, is still missing. Commonly either singly supported platinum atoms or Pt nanoparticles are considered, without giving any clues about their formation yet [102, 103]. For example, in the work by Li *et al.* a cubic nano-particle of Pt_{13} (size about 0.5 nm) located inside the main 12T channel of β-zeolite was used to simulate the noble metal particles. The same choice of a Pt_{13} cluster, corresponding to a so called "magic size number" [99], is found in the investigation performed by Xu *et al.* in case of the KL framework [101]. As a matter of fact, a more systematic procedure was implemented by Hou *et al.* [104] that have investigated, by means of periodic DFT calculations, the stabilization of platinum atom and/or clusters inside the cavities of medium size high-silica zeolites (*i.e.* LTA, SOD, CHA, FAU), but have not considered larger pore frameworks such as BEA.

In real catalysts the metal can be located not only inside the cavities but also on the outer surface of the crystals, or even supported on an inorganic binder[1] in composite materials [21, 128, 129]. It is indeed uniformly reported that the small metal particles, obtained through the most frequently used impregnation methods, albeit a few nanometers in diameter, are still too big to fit in the zeolite channels [21, 115].

In addition to zeolite topology, acid strength and metal properties by themselves, the performance of bifunctional catalysts is determined by the ratio of metallic to acidic sites and the distance between the two functional sites, often described as proximity or intimacy degree [130, 131].

The acidity of zeolites can be adjusted in relation to the silica-to-alumina ratio. As an example, for Beta zeolite specific commercial ratios are available, with Zeolyst offering catalysts, in the powder form, showing SiO_2/Al_2O_3 molar ratio of 25, 38 and 300 [132]. However, employing suitable synthesis methods allows for the creation of materials with the desired ratio. Acidity can be mitigated by introducing basic elements into the structure, such as Ba, Mg, Fe, or by coating zeolite with alumina [16]. Regarding metal loading, it is essential to consider the drawback of using noble metals, that is their high cost. Therefore, recent efforts have focused on hydroisomerization using cost-effective transition metals

[1]For industrial application, zeolites are often pelletized with a binder, typically a natural clay such as bentonite, attapulgite, and kaolin, added in amount of 15-20%. The primary objective of this procedure is to achieve the necessary mechanical strength to resist attrition losses and ensure chemical stability for prolonged use. While binders themselves may not possess catalytic activity, the interactions between binders and zeolites can influence catalytic performance [114].

like Ni, but the results have proven to be not sufficiently promising to cause a shift [28, 35]. Consequently, the majority of studies on hydroisomerization of alkanes currently utilizes Pt-supported catalysts with very low loadings. According to the literature, an effective balance is generally achieved with 0.4-0.6% Pt [22, 133].

The n_{Pt}/n_A ratio, defined as the ratio of the total number of exposed Pt atoms (on the surface of Pt particles) to the total number of Brønsted acidic sites, has been usually used to characterize the balance between the hydrogenation-dehydrogenation function and acidic function [25]. The first reported attempt of quantification was made in *n*-heptane and *n*-decane hydroisomerization on a series of Pt-USHY catalysts differing by their Pt content (from 0.07 to 1.5 wt%) [134]. There, in particular, the ratio between the concentrations of accessible Pt and acidic sites on which the enthalpy of NH_3 adsorption was greater than 100 kJ mol^{-1} was chosen to quantitatively express this balance. The activity, stability, and selectivity of the catalysts were shown to be definitely governed by the n_{Pt}/n_A ratio, even if the results also suggested the effect of one additional parameter. This was proposed to be the number of acidic sites encountered by the olefinic intermediates during their diffusion between two Pt sites. It is noteworthy to emphasize that this value is expected to be substantially influenced by the level of intimacy between Pt and acidic sites. Nevertheless, there has been no proposed quantification for it. Later on, Bathala *et al.* [21] suggested to use the C_{Pt}/C_{H^+} ratio between the concentrations of accessible Pt and protonic sites, known to be the acidic sites active in the olefinic intermediates rearrangement and cracking. In particular, for C_{H^+} the concentration of Brønsted sites able to retain pyridine at 150 °C was considered. They studied the *n*-hexadecane trasformation over three series of catalysts based on H-BEA and Pt and different ratios of alumina. In the three series, the activity and the selectivity of the catalysts were shown to be dependent on the balance between hydrogenating and acidic functions expressed by their ratio, thus confirming the previous findings. Once again, however, some observations showed that the balance between the two functions is not the only parameter determining the catalytic properties; instead the degree of intimacy of active Pt and protonic sites should be somehow taken into account.

The average number of acid steps (n_{as}) involved in the apparent formation of one product molecule from n-C_{16}, which can be estimated from the product composition, was proposed for expressing the intimacy between hydrogenating and acidic functions. The calculated n_{as} values were used to estimate corrected TOFs, which were shown to be similar for the three series of catalysts. This similarity demonstrated that both the activity and selectivity of the bifunctional

Pt/H-BEA catalysts depend on just the two mentioned parameters.

Vajglova *et al.* [114] obtained various shaped catalysts based on H-Beta-25:bentonite, in the form of extrudates with a controlled deposition of platinum (nominal loading of 2 wt%) in different locations, by altering the sequence of steps for the preparation of these zeolite-binder composites. The resulting n_{Pt}/n_A ratio was extremely different, from 0.07 to 1.12 among the catalysts. Testing them in the *n*-hexane hydroisomerization it was interestingly found that, in agreement with the reasoning above, catalytic activity and isomerization selectivity increased with increasing the metallic to acidic sites ratio also in the case of extruded Pt catalysts.

Overall, it is evident that significant attention has been devoted to the metal-acid balance and its impact on the product distribution, activity, and stability of Pt/zeolite catalysts [133]. According to the summary of the recent studies given by Wang *et al.* [109], an optimal hydroisomerization catalyst is the one in which a close-to-one ratio is maintained. In this scenario the acid-catalyzed reaction (cracking and isomerization) becomes rate-limiting, while the hydrogenation/dehydrogenation steps are in quasi-equilibrium and the number of acidic sites between two metallic sites is sufficiently low. When either metallic or acidic functions dominate, excessive hydrogenolysis on metallic sites or cracking on acidic sites occurs, respectively. Hence, while it remains imperative for the ratio to be sufficiently high, it should not escalate infinitely. Instead, there exists an optimal range of values for the metallic-to-acidic sites ratio that ensures the bifunctional catalysts to feature ideal catalytic performances.

For many years, proximity of metallic and acidic sites has been quantified through the so called intimacy criterion proposed by Weisz [38], often applied as "the closer the better" for optimizing the spatial arrangement of sites [39]. Many studies in the literature have indeed shown that maximal intimacy enhances selectivity to skeletal isomers in the reaction of interest [115, 135, 136]. They consisted in comparative analyses of catalysts where, thanks to the synthetic strategies that allowed tuning the proximity, the metallic functionality was located either only in the zeolite (nanoscale intimacy), in the binder (microscale intimacy) or both in the zeolite and on the binder, to mimick an in-between degree of intimacy. For example, Vajglova *et al.* [34] showed that for Pt/H-Beta-25 catalysts the highest conversion of *n*-hexane and selectivity to C_6 isomers was obtained with extrudates prepared via *in situ* synthesis, with platinum located on the zeolite. An increasing degree of intimacy of hydrogenation/dehydrogenation and acidic sites in bifunctional Pt/BEA and Pt/USY also positively affected the activity and selectivity in *n*-hexadecane transformation [136].

Recent reports reopened the debate about the ideal proximity between both functions for optimal performances, in terms of selectivity but also resistance to deactivation [116, 137]. In the work of Gutierrez-Acebo *et al.* [128], focusing on platinum as the metallic function and EU-1 zeolite as the acidic one for the ethylcyclohexane hydroconversion, no influence of the distance between both functions on catalytic performance was observed up to a micrometer scale. Instead, in the hydroisomerization of n-heptane using catalysts consisting of zeolite ZSM-22, mordenite, and γ-alumina binder, the nanoscale intimacy between active sites was even unfavorable for selectivity, leading to undesired cracking reactions [130]. Oenema *et al.* [138] also observed beneficial effects in n-heptane hydroisomerization when Pt nanoparticles were placed on the binder of zeolite/binder composite as opposed to Pt located inside zeolite crystals.

Numerous factors come into play underlying a certain grade of intimacy and its impact on the catalytic performances, such as the dimensions of zeolite channels and metal particles, and the length of hydrocarbon chains, their differences contributing to the reported divergent results over the years. If limitations in substrate diffusion arise due to the interplay among these factors, effect on the activity and selectivity of the reaction that often tend to favor cracking over isomerization can be reasonably elucidated. Consequently, the conventional belief that a closer proximity is preferable is no longer accepted. On the contrary, the new paradigm emphasizes the importance of examining the effects of site proximity on a case-by-case basis.

A computational approach enables the modeling of nanoscale proximity, with distances on the order of a few angstroms between the acidic site and the metallic center, whether it is a single atom or a small cluster. To simulate a less intimate scenario, resembling the experimental setup where the metal is located in the binder, the model could consider only the acidic functionality of the zeolite, while the reaction steps involving the metal may be modeled on a supported cluster. Therefore, these types of investigations are certainly likely to contribute advancing the comprehension of this subject.

Scope and organization

Intensive research is currently devoted to renewable and sustainable transportation fuels, obtained from waste materials, as suitable alternatives for their fossil based counterparts. The rheological properties of green diesels and jet fuels can be enhanced to meet the requirements for their industrial exploitation by means of hydroconversion processes, like isomerization and cracking of paraffines, which occurs over bifunctional catalysts.

The present dissertation is framed within this context, aimed at investigating a metal modified β-zeolite as a catalytic material for such fundamental reactions of hydrocarbons, that require both an acidic substrate and a hydrogenation/dehydrogenation function. Here the models and theories of quantum chemistry, in particular those based on density functional theory, are employed as a main tool to unveil the atomistic features of the catalytic material of interest. Experimental insights, arising from the close collaboration with the "Industrial Chemistry and Reaction Engineering" group of Åbo Akademi University (FIN), provide an additional perspective in addressing this wide and complex research topic. Although zeolites are well established as bifunctional catalysts, in fact, many questions are still open and unresolved issues are associated with the characterization of either the two functionalities and their interaction.

The thesis is divided into four main chapters, which incidentally follow the chronological order of the activities carried out during my PhD course. The first chapter concerns the study of intrinsic Brønsted acidity, for the β-zeolite framework, in terms of site deprotonation energies computed according to different computational approaches. Advantages and disadvantages coming along each method being discussed, the acidity order among 30 topologically distinct sites is assessed, through a newly proposed procedure that avoids the necessity of empirical corrections and the occurrence of embedding artifacts, to date likely involved in the other commonly used approaches.

The second chapter is devoted to the characterization of zeolite-embedded platinum atoms and small clusters, aimed at identifying their preferential location

and the corresponding energetics, together with unraveling the kinetics associated with the Pt migration between cages. The investigation employs an one-by-one atom addition approach, driven by an unbiased algorithm, and outlines the cluster growth process up to a Pt_3 seed.

Mutual interactions between acidic sites and platinum centers are discussed in the third chapter, that collects on this regard the experimental work on bifunctional catalysts synthesis and characterization performed during my three-months research in Finland and a preparatory atomistic analysis about the effects of a single Pt atom on the site acidity.

Finally, the last part of the dissertation addresses, in a small and contained way, a possible catalytic application of the mimicked zeolite-based catalyst. The 2-pentene molecule is taken as a model compound for the study of olefins isomerization mechanism, focusing on the steps which involve the acidic functionalities.

In the appendix section supplementary data and images which did not found place in the main text without interfering too much with the reading experience are reported. Additionally, one of the appendices is dedicated to the two papers that where published during the course of my PhD, on which the first and second chapter are based.

Acidic sites

Since Brønsted acidity is a crucial aspect for the applications of zeolitic materials in heterogeneous catalysis, great effort was devolved to characterize the number, strength and location of the potentially active acidic sites. Quantum chemical calculations can turn out essential in estimating the intrinsic acidity by computing deprotonation energy (DPE) values, although each method comes with its own difficulties.

In this chapter, the study is reported regarding the intrinsic acidity of 30 topologically distinct Brønsted sites in the β-zeolite framework, that was investigated by calculating DPEs through three different approaches, all within the DFT paradigm. In particular they are: i) an ONIOM embedding scheme, ii) periodic calculations according to the SIESTA formalism and iii) a novel cluster method specifically designed to avoid the disadvantages related to the other two approaches.

3.1 Models and Methods

3.1.1 ONIOM approach

The β-zeolite periodic framework, shaped using the crystallographic information file from the IZA website [51], was utilized to select a segment comprising approximately 800 atoms that featured two intersections between the main twelve-membered ring channels (12T). Terminal hydrogen atoms were added to this fragment, to satisfy the valences of the dangling oxygen atoms, resulting in a model consisting of 864 atoms. This was chosen as the real system for subsequent ONIOM calculations (refer to Figure 3.1). Six distinct model systems, denoted as m1-m6, were chosen, ranging in size from 39 to 102 atoms. Models m1 to m4 were employed to examine multiple topological silicon sites, while the smaller m5 and m6 were designed to investigate specific T sites, namely T9 and T1, respectively, which were not adequately embedded in the other models. Special attention was

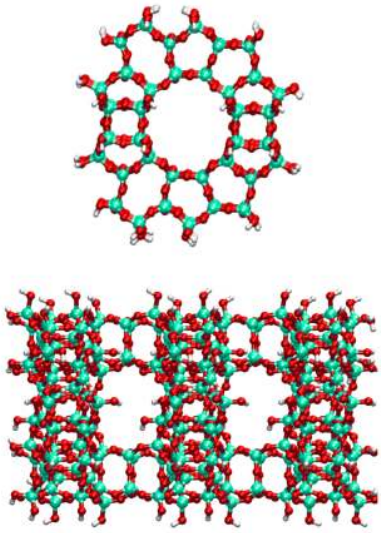

Figure 3.1: The selected real system for the ONIOM approach that comprises 864 atoms is illustrated from two perspectives (O=red, Si=green, H=white).

given to ensuring that the portion containing the silicon atoms of interest was centered within the model system, placing them at an appropriate distance in all directions from the boundary with the low level. Figure 3.2 illustrates the six model systems embedded in the real system, with a close-up view displaying all labels for the examined acidic sites.

Geometry optimizations were conducted for three scenarios: i) the silicalite systems as the starting point, ii) anionic structures with one Si atom replaced by Al, and iii) neutral structures with aluminum and a hydrogen atom. In the latter, the hydrogen was positioned so that it interacted, in turn, with three of the four oxygen atoms of the AlO_4 tetrahedral unit. The different acidic sites are labeled as TnOm, where T represents the tetrahedral center corresponding to the silicon atom substituted by aluminum, and n and m are pairs of numbers indicating the specific topological site, as reported in Figure 3.2.

Excluding T5O14 and T6O14 sites, where the added hydrogen would not be accessible, 40 cases were obtained from the 32 topologically distinct acidic sites in the β-zeolite. Some aluminum-hydrogen configurations were considered twice in different model systems for internal consistency checks. Site-topological label assignments were made by comparison with labels shown in the crystallographic information file of the BEA framework, using the VESTA program [139].

The Gaussian16 software [140] was utilized, employing the B3LYP hybrid exchange-correlation functional corrected by the third-order Grimme empirical treatment of dispersion interactions (B3LYP-D3, [141]). A cc-pVDZ basis set

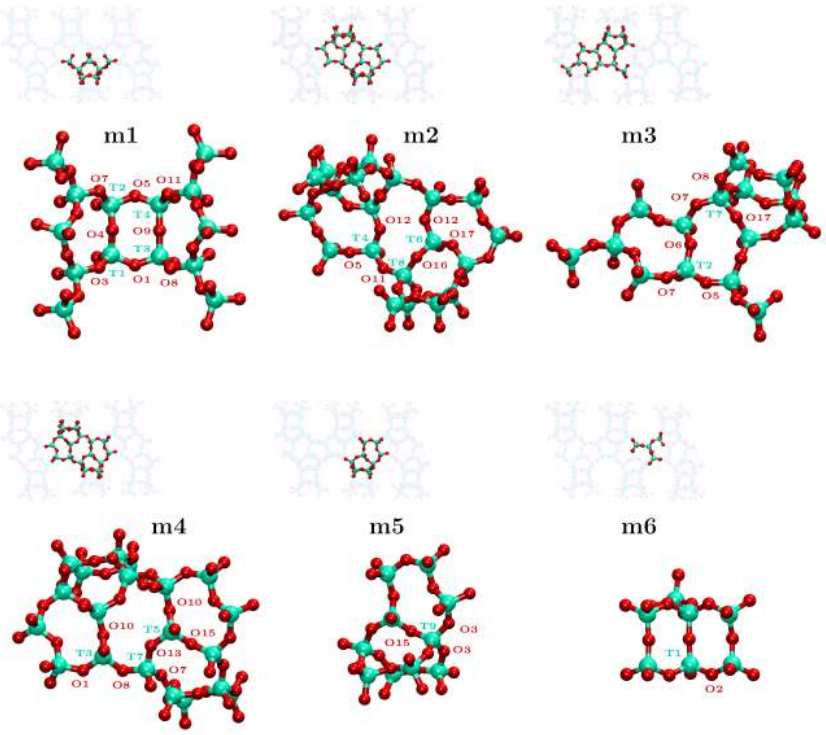

Figure 3.2: The ONIOM model systems, denoted as m1-m6, are displayed both embedded in the real system and isolated, having selected a convenient orientation. The topological labels for the examined tetrahedral and oxygen sites are provided for each model system.

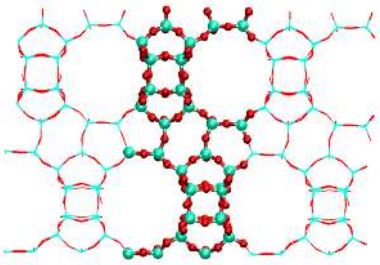

Figure 3.3: A depiction of the BEA unit cell consisting of 192 atoms, represented in a ball-and-stick model, is illustrated within the periodic framework shown in wireframe. The view is along the ac plane, and the cell parameters are as follows: a = b = 12.631 Å, c = 26.186 Å, $\alpha = \beta = \gamma = 90°$.

was applied to all atoms. For the ONIOM application, the Universal Force Field served as the chosen low-level theory. A singlet multiplicity state was considered for both high and low level. Examination of the calculated harmonic vibrational normal modes provided confirmation that the investigated structures correspond to minima on the potential energy surface of their respective systems.

3.1.2 Periodic DFT calculations

The structural model employed for periodic DFT calculations is the BEA unit cell (a = b = 12.631 Å, c = 26.186 Å, $\alpha = \beta = \gamma = 90°$) provided by IZA [51] and depicted in Figure 3.3. It is reported in the atlas as a mixture of α and β BEA polymorphs, most properly labeled as *BEA. It has to be noted that, for the sake of brevity, the asterisk is omitted in this thesis. Periodic geometry optimizations were performed for the 30 structures originated by replacing, one at a time, all the topologically distinct silicon atoms with aluminum and adding one H atom on the corresponding not equivalent oxygen centers.

All periodic calculations were executed using the SIESTA approach as implemented homonym code [142]. The PBE exchange-correlation functional was selected, along with double-ζ quality numerical basis sets generated using an energy shift of 0.005 Ry. Norm-conserving pseudopotentials from the PseudoDojo project [143] (labeled as *nc-sr-04_pbe_standard*) were utilized. The psml format is supported by the dedicated SIESTA-PSML-R1 version of the code [144]. Sampling was performed with a mesh cutoff value of 450 Ry and a 2×2×2 Monkhorst-Pack grid, which was subsequently refined to 4×4×4 after the initial relaxation of the system geometry.

3.1.3 Cluster approach

Starting from optimized structures obtained through periodic DFT calculations, a zeolite unit cell reshaping procedure was undertaken to generate clusters. These were then adjusted for the valences of terminal oxygen and silicon atoms. The reshape procedure aimed to place the acid hydrogen atom roughly in the center of the newly formed fragment, replicating the neighborhood of the hydrogen atom that resulted from the specific arrangement in the periodic calculation after geometry optimization. As a result, the obtained clusters were homogeneous, both with each other and individually with their starting optimized structures. In detail, to construct a reshaped cell, the position of the aluminum atom was fixed at the center of a newly defined cell with the same constants (a, b, and c) as the original BEA repetition unit. Atoms within this new cell retained their coordinates, while those outside of it were translated back inside using the a, b, c vectors. The choice of Al as the center of the new cell is justified by its proximity to the acid hydrogen atom, and its absence in the anionic structures. Figure 3.4 illustrates the system at the start and end of this procedure, taking the T1O1 site as an example. This process was applied to 30 neutral species and their 9 corresponding anions. After reshaping, the system retained undersaturated Si and O nuclei at the cell boundaries. An automatic saturation procedure was then applied to prepare the structure for a cluster calculation. For every undersaturated nucleus in the cell: 1) if it is a Si atom, up to three neighboring oxygen atoms could be missing: in this case, the correct number of hydrogen atoms was placed in a suitable tetrahedral arrangement around Si, considering the position and orientation of the existing Si−O bonds. Whenever a Si−H moiety was less than two Si−O bonds apart from the acidic site, it was substituted by Si−OH; 2) if it is an O atom, only a single neighboring Si could be missing, and consequently, a single hydrogen was added at a 109.5° Si−O−H angle. It is noteworthy that the 109.5° value was chosen to address concerns about the average Si−O−Si value of 136° typical of zeolites, which could result too wide for a proper Si−O−H angle and lead to energetic artifacts depending on the number of its occurrence. All terminating −OH groups were oriented in the same spatial direction, avoiding the direction of the next Si in the zeolite framework to prevent two saturating hydrogens from being too close each another, which is a possibility since two different oxygen atoms may be bonded to the same silicon atom. Wherever this is not the case and the saturated hydroxyl group is close to the Al region, the orientation was adjusted in order to match the one occurring in the zeolite structure.

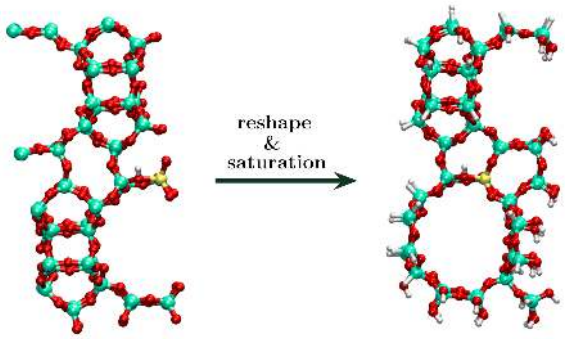

Figure 3.4: The T1O1 acidic site within the BEA unit cell is depicted on the left, while the corresponding fragment chosen to describe the same site in the cluster approach is shown on the right. In both representations, oxygen is in red, silicon in green, aluminum in yellow, and hydrogen in white.

The final geometry was checked to ensure that no border H-atom was less than 4.5 Å from the acid hydrogen site, a distance considered negligible for dispersion interactions between real and fictitious hydrogen atoms.

For the cluster approach, the same exchange-correlation functional and basis set used for the model systems in the ONIOM calculations were employed. It is important to emphasize the intimate relationship between the SIESTA and cluster approaches, with the latter serving as an automatic, non-empirical correction of the former for the evaluation of deprotonation energies.

3.2 Results and Discussion

In Table 3.1, DPE values for the 30 investigated topologically distinct acidic sites of BEA are reported using three different computational approaches (ONIOM, SIESTA, cluster), each as a separate set. The deprotonation energy was calculated as the difference between the Self-Consistent Field (SCF) energy of the aluminated β-zeolite anionic form and the SCF energy of the corresponding neutral form. Extrapolated energies were used in the case of the ONIOM approach. The use of ONIOM allows the definition of systems small enough to make the calculation of vibrational frequencies, and hence thermochemical properties, feasible. By comparing the calculated DPE values based on the ONIOM energy with those based on the ONIOM enthalpy, it was estimated that the thermal contributions to the deprotonation energy (leading to a decrease of the DPE) span between 27 and 36 kJ mol^{-1}, depending on the nature of the zeolite site. This range is in agreement with the average value of 29 kJ mol^{-1} estimated in the literature [127] for the contribution due to the difference of vibrational zero-point

energies in various zeolites. This contribution can be considered constant for the purpose of comparing the results obtained with the three approaches described here.

The three sets of energy values obtained with the different methods were normalized in the 0–100 interval using the following expression

$$\mathrm{DPE}^{\mathrm{M}}_{\mathrm{n},i} = 100 \cdot \frac{\mathrm{DPE}^{\mathrm{M}}_{i} - \mathrm{DPE}^{\mathrm{M}}_{\mathrm{min}}}{\mathrm{DPE}^{\mathrm{M}}_{\mathrm{max}} - \mathrm{DPE}^{\mathrm{M}}_{\mathrm{min}}} \tag{3.1}$$

where the normalized deprotonation energy of the i-th site according to method M, $\mathrm{DPE}^{\mathrm{M}}_{\mathrm{n},i}$, is defined with respect to the raw $\mathrm{DPE}^{\mathrm{M}}_{i}$ and the minimum and maximum DPE values found within the corresponding set. All the data were then collected in the histogram of Figure 3.5, which is divided into three equally spaced bands to qualitatively indicate low, medium and high site acidity, being clear that the x-axis is sorted in ascending order based on the numbering of silicon (and then oxygen) labels only.

Table 3.1: DPE values[a] calculated whith the the ONIOM (O), SIESTA (S) and cluster (C) approaches.

site	O	S	C	site	O	S	C
T1O1	1344.9 (m1)[b]	1019.8	1220.9	**T4O12**	1355.2 (m2)	1049.3	1237.9
T1O2	1367.4 (m6)	1042.7	1233.3	**T5O10**	1275.3 (m4)	1034.7	1210.2
T1O3	1351.9 (m1)	1025.7	1223.8	**T5O13**	1352.3 (m4)	1022.8	1189.7
T1O4	1354.0 (m1)	1007.9	1197.6	**T5O15**	1336.6 (m4)	1026.4	1192.2
T2O4	1357.0 (m1)	1008.9	1209.0	**T6O12**	1324.0 (m2)	1037.6	1230.3
T2O5	1370.3 (m1) — 1304.0 (m3)	1025.6	1219.5	**T6O16**	1336.3 (m2)	1036.2	1227.4
T2O6	1339.0 (m3)	1014.2	1210.9	**T6O17**	1330.6 (m2)	1021.9	1213.2
T2O7	1368.7 (m1) — 1330.8 (m3)	1013.2	1202.1	**T7O7**	1328.6 (m3) — 1313.6 (m4)	1011.6	1181.8
T3O1	1364.8 (m1) — 1339.1 (m4)	1019.1	1205.9	**T7O8**	1306.1 (m3) — 1313.4 (m4)	1020.1	1195.3
T3O8	1346.8 (m1) — 1218.8 (m4)	1016.6	1211.5	**T7O13**	1319.3 (m4)	1020.2	1189.1
T3O9	1371.0 (m1)	1025.6	1219.0	**T7O17**	1287.6 (m3)	1024.2	1204.4
T3O10	1336.5 (m4)	1031.4	1217.4	**T8O11**	1326.6 (m2)	1027.4	1178.8
T4O5	1370.8 (m1) — 1355.0 (m2)	1015.2	1195.4	**T8O16**	1340.9 (m2)	1043.1	1192.5
T4O9	1382.3 (m1)	1031.4	1216.5	**T9O3**	1331.8 (m5) — 1318.1 (m5)	1028.0	1194.7
T4O11	1371.9 (m1) — 1288.8 (m2)	1020.3	1202.4	**T9O15**	1316.6 (m5) — 1345.8 (m5)	1015.8	1194.9

[a] Expressed in kJ mol^{-1}.
[b] The employed model system is indicated in parentheses.

A tentative explanation for the observed behavior in the ONIOM histogram is provided below. Figure 3.2 indicates that in β-zeolite, the T8 and T9 sites feature only two non-equivalent oxygen atoms (O11 and O16 for the former, O3 and O15 for the latter). The two T9O3 and the two T9O15 sites are well defined in the same m5 model. Additionally, as revealed by the presence of double ONIOM bars in the histograms shown in Figure 3.5, some cases were examined twice (duplicate sites) using different model systems. This duplication allows for insights into the suitability of the model system choice and the application of the ONIOM method itself to this zeolitic system. Among the 8 duplicate sites, there are some cases where the ONIOM results fall into different acidity groups, depending on the chosen model system. The most notable ones are T2O5 and T4O11, and to

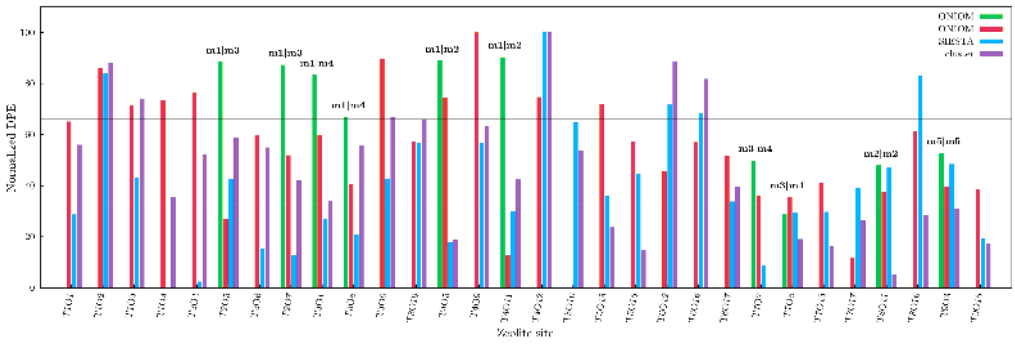

Figure 3.5: Sub-histograms of normalized DPE values calculated using ONIOM, SIESTA, and cluster approaches for the topologically distinct acidic sites of BEA. When four bars are present on a site sub-histogram, the first two refer to ONIOM results obtained from two different model systems (indicated by the labels above) or even from different sites of the same model system. A missing bar in a sub-histogram indicates a zero value for the corresponding case. Horizontal lines equally divide the histogram into three acidity zones.

a lesser extent, T2O7. For example, T4O11 is predicted to have very low acidity according to the m1 model, while it is among the most acidic sites according to the m2 model. Conversely, consistent results are obtained for T4O5 and T7O7 sites, which belong to the same acidity zone, while small differences are reported for T3O1, T3O8, and T7O8. Notably, in all three duplicate sites exhibiting more significant differences, the model system m1 is involved and consistently gives the highest value, suggesting a potential bias of this model system. For the T4O5 site, on the other hand, m1 and m2 are in excellent agreement.

The observed phenomenon may find an explanation in the fundamental nature of a model, which by definition cannot capture all facets of reality. It is conceivable that the same ideal topological site in the periodic zeolite can be described differently by two distinct model systems. Specifically, the neighborhood of the rings to which the site belongs may differ, as this neighborhood necessarily represents a subset of what defines the topology of the same model site.

It is essential to emphasize that special attention was given to ensuring that the acidic hydrogen was surrounded by atoms treated at the DFT level within the ONIOM approach and that it was positioned at least 3 bonds away from the low-level region. However, in almost all the model systems, the silicon atom replaced by the aluminum atom featured only three of the four Si atoms belonging to the tetrahedrons around it in the high level of calculation. This limitation could affect the relaxation of the structure during geometry optimization, potentially influencing the deprotonation energies. Attempts were made to address this issue by including the missing silicon and some other oxygen atoms in the model

systems. This however proved to be unviable due to the intrinsic characteristics of the β-zeolite structure. The addition of atoms into the model system often made ONIOM layer definition impossible due to, for example, showing one atom in the real system bonded to more than one atom of the model system. Even the shaping of smaller 5T systems centered at the topological silicon of interest was not always possible due to similar problems in the ONIOM partitioning. Li *et al.*, in fact, got around the problem by removing some oxygen atoms from the high level, creating model systems that were not homogeneous with each other and that might cause significant artifacts considering their small size. Taking into account these challenges, the ONIOM approach does not seem to be a satisfactory means to adequately investigate the acidity of the 9 topologically distinct sites of β-zeolite. To overcome the issues of duplicate sites and incomplete silicon tetrahedra around the topological site, it is suggested to eliminate the choice of model systems upfront and carry out periodic calculations followed by a refining treatment using a cluster approach.

Actually, a drawback still exists in using periodic DFT when dealing with charged unit cells, namely in geometry optimizations of zeolite anionic structures: the interaction between charges of all the images leads, in fact, to energy artifacts that must be taken into account and compensated. This is an open problem yet, as highlighted by the work of Iglesia *et al.* [118]. One of the best proposed procedures to address this issue contemplates an *a posteriori* correction, following the Freysoldt-Neugebauer-Van de Walle (FNV) scheme [125], which applies to the energies, while the respective geometries remain unchanged. Therefore, one can reasonably trust on the optimized geometries found for anions and, as proposed in this thesis, use them as a starting point for a cluster DFT approach.

In the proposed cluster approach, each acidic site within the unit cell, subject to periodic boundary conditions in periodic calculations, is now described by a finite fragment of the zeolite framework. For this reason, changes to the starting structures are necessary to reproduce in the new system the chemical local environment that characterizes each site, hence the reshape procedure detailed in the Models and Methods section. This approach offers several advantages: (i) it avoids issues arising in the choice of a model system, (ii) even if the geometry optimization is not performed again, it is based on reliable geometries, properly adapted by placing the acid hydrogen atom homogeneously in all the sites, (iii) without suffering from charges interaction artifacts, it supplies DPE values more accurate than those obtained by any periodic DFT analysis and (iv) it offers the possibility to choose exchange-correlation functionals and basis sets more appropriate, with respect to those commonly available in softwares for periodic

calculations, to discriminate the intrinsic acidity of the zeolitic sites.

Referring to the DPE values obtained with the proposed cluster approach, an acidity strength order of the investigated 30 topologically distinct acidic sites of BEA can be extrapolated. Among them, 11 belong to the middle portion of the range, 11 cases feature the highest intrinsic Brønsted acidity, and the remaining 8 sites are less acidic, especially T4O12, T1O2, and T6O12. A structural analysis of the 30 sites in terms of hydrogen bond parameters involving the acid hydrogen atom was performed to gain insight into the cause of the acidity trend. Structures with strong hydrogen bonds, namely those showing H-bond, O···H, distance ranging from 1.5 to 3.0 Å and O−H···O angle in-between 150° and 180° are depicted in Figure 3.6, ordered by descending acidity.

The presence of hydrogen bonds was detected in almost all the sites belonging to the low and medium-low acidity groups and only occasionally in the other groups (high and medium-high acidity). When hydrogen bond formation occurred in the latter cases, the site was less acidic than the one that did not show H-bond formation, such as the case of T8O16 and T8O11. A correlation may be therefore drawn between hydrogen bond formation and the occurrence of low acidity in the corresponding site. In particular, H-bonds were formed when proton donor and acceptor oxygen atoms belonged to the same (5- or 6-membered) ring. At the bottom of the low acidity range, sites T4O12, T6O12, and T6O16 showed two hydrogen bonds with the correct orientation. This correlation supports the findings of Katada *et al.* [113] about the factors affecting the vibrational frequency of the O−H stretching, taken as an index of site acidity.

At this point, it is noteworthy to compare the most and least acidic sites according to the three computational approaches employed. The site demonstrating the highest intrinsic acidity is T8O11 according to the cluster approach, closely followed by T7O7. These two sites exhibit an acid hydrogen that protrudes into the main channel, a desirable characteristic when β-zeolite is utilized as an acidic catalyst. Conversely, ONIOM and SIESTA methods indicate T5O10 and T1O4, respectively, as the most acidic sites. In this regard, the ONIOM approach sensibly fails when compared to the cluster method. Both the optimized ONIOM and SIESTA structures display hydrogen bonds in the corresponding most acidic site (see Figure 3.6), potentially explaining their classification within the medium acidity group when treated by the cluster approach. An excellent agreement between SIESTA and the cluster approach is observed for the least acidic site, as both methods predict T4O12 to hold this role, where the proton is engaged in two strong hydrogen bonds. Conversely, ONIOM designates the nearby T4O9 site as the least acidic, yet T4O12 is consistently placed within the low acidity

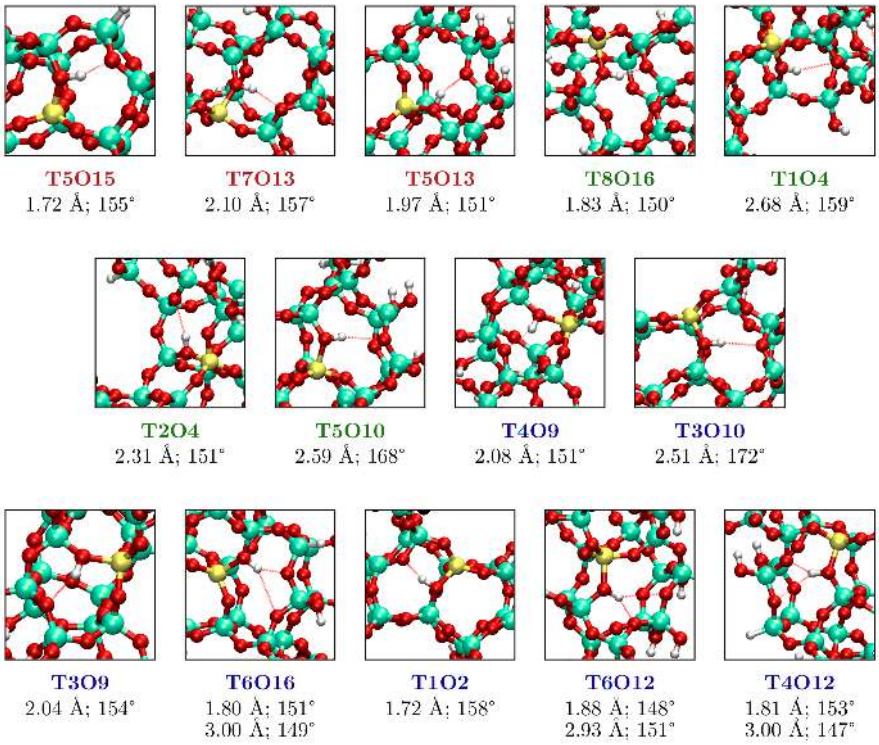

Figure 3.6: Structural details of the most significant hydrogen bonds detected in the topological configurations investigated, according to the cluster method. The respective images are accompanied by values indicating the O···H distances and the O−H···O angles. Each site is color-coded to denote its acidity group: red for high acidity, green for medium acidity, and blue for low acidity.

region. Deprotonation energies range from 1382 to 1275 kJ mol^{-1} in the case of ONIOM, while they fall between 1049–1008 kJ mol^{-1} for periodic calculations and 1238–1179 kJ mol^{-1} employing the cluster approach. It is important to note that only the acidity interval resulting from the cluster approach aligns with the range proposed for zeolites by Jones *et al.* [118] and Trachta *et al.* [117], while the one guessed by ONIOM is overestimated. This discrepancy may be attributed to a destabilization of the anionic form caused by the fact that its negative charge cannot be properly delocalized on the small model systems. Considering the average Brønsted acidity of all the Al−O sites, as evaluated by the cluster method, a value of 1207 kJ mol^{-1} is obtained, with a root mean square deviation of 15 kJ mol^{-1}.

A notable disparity between the data of Jones *et al.* on β-zeolite and those obtained in this thesis becomes evident when comparing periodic and cluster outcomes. According to Jones *et al.*, the DPE values for BEA, based on their periodic calculations, range from 1561 to 1583 kJ mol^{-1} (excluding the Al5O14 and Al6O14 sites), and their ensemble-averaged $\langle$DPE$\rangle$ only decreases to around 1200 kJ mol^{-1} after applying an empirical shift determined through comparison with previous results based on embedded or cluster models. Conversely, the periodic SIESTA results reported here, with an average DPE of 1025 kJ mol^{-1} (RMSD of 6 kJ mol^{-1}), are significantly lower than the cluster values. Jones *et al.* [118] demonstrated that their overestimated data were not solely due to issues related to the charged cell problem, as the FNV correction [125] increased the divergence from the seemingly accepted value of 1200 kJ mol^{-1}. The FNV correction, intended to destabilize charged species, should not have a significantly pronounced effect for singly negatively charged systems and large employed cells [145]. In the work of Trachta *et al.* [117], raw periodic data are not provided, but they approach the mean value of 1245 kJ mol^{-1} after correction. Still, in one of the latest studies on zeolite acidity, specifically on the same β-zeolite investigated here, Vorontsov and Smirniotis [146] reported uncorrected data, suggesting DPE values in the narrow range of 1592–1603 kJ mol^{-1}. Given that all the authors mentioned above used plane waves as a basis set for their periodic calculations, it could be hypothesized that the divergence between the here reported and their data should be attributed to the difference in the computational approaches used. Specifically, considering the same DFT exchange-correlation functional, it seems that a plane-wave-type description of the zeolite electron density produces results that substantially differ from those obtained using a SIESTA-based approach with strictly localized numerical basis sets.

To facilitate a comparison between the present results and those in the literature, and to report Brønsted acidities that depend solely on the position of the Al/Si-substituted T site, a Boltzmann average of the DPE values corresponding to different oxygen sites attached to the same T site was considered. Barrierless processes were assumed for the proton shifts between the oxygen centers above.

The energies used for the determination of Boltzmann populations are those obtained through the SIESTA approach for the optimized geometries (the relative energy values should be reliable, as they are those of neutral systems), while the DPE values employed in the average are those obtained with the cluster method (see Table 3.1). Observing Table 3.2, it is evident that the $\langle$DPE$\rangle$ values span a narrower segment (45 kJ mol^{-1}) compared to the raw values, showing a mean value of 1212.8 kJ mol^{-1}. Furthermore, this acidity interval can be divided into three subranges, with an energy interval of approximately 10 kJ mol^{-1} in between; specifically, the high acidity sites T7, T8, and 79 are in the 1195–1200 kJ mol^{-1} range, the medium acidity T1, T2, T3, and T5 sites fall within 1209–1219 kJ mol^{-1}, and the two low acidity sites T4 and T6 are in the 1229–1238 kJ mol^{-1} range. If DPE differences within each interval are neglected, the following acidity ranking of the β-zeolite T sites can be finally written:

$$\mathrm{T8} \approx \mathrm{T7} \approx \mathrm{T9} > \mathrm{T5} \approx \mathrm{T1} \approx \mathrm{T3} \approx \mathrm{T2} > \mathrm{T6} \approx \mathrm{T4} \tag{3.2}$$

This $\langle$DPE$\rangle$ order is obviously affected by the stability of the protonated form, which in turn depends on the occurring of hydrogen bond interactions. If only the most acidic site of each TnOm set is considered for the ranking, this one would become

$$\mathrm{T8} \approx \mathrm{T7} > \mathrm{T5} > \mathrm{T4} \approx \mathrm{T9} \approx \mathrm{T1} > \mathrm{T2} \approx \mathrm{T3} > \mathrm{T6} \tag{3.3}$$

with all the DPEs falling within the 1179–1213 kJ mol^{-1} range. By comparing the two rankings above, the most striking difference is the position of T4, which is not surprising since the most acidic T4 site (T4O5) is also the least stable, and the very low acid T4O12 site is the only one having an appreciable Boltzmann population at room temperature. Moreover, it is essential to emphasize that the Boltzmann-averaged DPE ranking (3.2) could differ if other computational approaches were employed. This discrepancy arises not only from the approximations inherent in the modelistic choices but also from the intrinsic accuracy of energy differences calculated by (periodic) density functional theory, which could be far from the chemical accuracy (4 kJ mol^{-1}) needed to obtain trustworthy Boltzmann populations. In particular, within the investigated cases, the position of T1 is believed to suffer from the largest uncertainty. T1 (and, to a lesser

extent, T7) is the only site whose acidity is heavily affected by the Boltzmann averaging procedure (see Table 3.2); the two sites T1O2 and T1O4 are essentially isoenergetic, but their DPEs differ by approximately 35 kJ mol^{-1} according to the cluster approach (and also according to the SIESTA one, see Table 3.1).
If the error on their energy difference was ± 4 kJ mol^{-1} (but almost surely it is much larger than this), the error on the $\langle$DPE$\rangle$ would be ± 12 kJ mol^{-1}, meaning that T1 would be placed either higher or lower on the acidity scale.

Finally, the discrepancy between the position of T8 in the acidity order calculated by the here proposed cluster approach (identifying T8 as the most acidic site) and the one reported by Vorontsov and Smirniotis [146] (assigning T8 as the least acidic) needs discussion. In fact, the difference between the raw, periodic, DPE values of T8 and the most acidic site (T2) according to Vorontsov and Smirniotis is only approximately 8 kJ mol^{-1}, and could be affected by accuracy flaws. The T8 site is indeed in the least acidic range if the SIESTA values are considered, but it becomes the one with the lowest DPE after the application of the cluster approach correction.

Table 3.2: DPE values according to the Boltzmann average over the different oxygen sites next to a common tetrahedral site.

T site	**O sites**	$\langle$DPE$\rangle$[b]
1	O1 (23.0, 0.000)[a]; O2 (0.1, 0.487); O3 (17.1, 0.001); O4 (0.0, 0.512)	1215.0
2	O4 (16.7, 0.001); O5 (0.0, 0.982); O6 (11.4, 0.010); O7 (12.4, 0.007)	1219.3
3	O1 (12.3, 0.006); O8 (14.9, 0.002); O9 (5.8, 0.087); O10 (0.0, 0.905)	1217.5
4	O5 (34.1, 0.000); O9 (17.9, 0.001); O11 (29.0, 0.000); O12 (0.0, 0.999)	1237.9
5	O10 (0.0, 0.958); O13 (11.9, 0.008); O15 (8.3, 0.034)	1209.4
6	O12 (0.0, 0.632); O16 (1.3, 0.367); O17 (15.7, 0.001)	1229.2
7	O7 (12.6, 0.004); O8 (4.0, 0.140); O13 (4.0, 0.143); O17 (0.0, 0.712)	1199.6
8	O11 (14.8, 0.003); O16 (0.0, 0.997)	1192.5
9	O3 (0.0, 0.993); O15 (12.1, 0.007)	1194.7

[a] (e,p) numbers in parenthesis are the energy excess (relative to the most stable case in the considered T site) and population at room temperature, respectively.

[b] Relative energy values and $\langle$DPE$\rangle$ are expressed in kJ mol^{-1}.

3.3 Conclusions

The Brønsted acidity of β-zeolite has been characterized in terms of the deprotonation energy (DPE) values of 30 topologically distinct acidic sites. DPEs were computed through three different approaches within the DFT framework, namely: (i) an ONIOM embedding scheme, (ii) periodic calculations according to the SIESTA formalism and (iii) a novel cluster method specifically designed to

avoid the disadvantages related to the other two approaches. By the cluster approach a range of nearly 60 kJ mol^{-1} was found which, divided into three equally spaced portions, gives 11, 11 and 8 sites setting high, medium and low Brønsted acidity, respectively. The formation of hydrogen bonds, actually detected in all the three groups of sites, was identified as a significant factor, if only to determine, within the same T site, to which oxygen atom the proton is preferentially bonded hence site Boltzmann populations. As a matter of fact, if Boltzmann averaged DPE values are calculated, even considering that the limited accuracy of the computational methods could heavily influence the position of some sites in the acidity scale, it can be concluded that three acidity groups invariably exist, which are separated by about 10 kJ mol^{-1} one from the other. This insight on the acidity of β-zeolite as well as the relative topology can provide fundamental information for the use of this material in catalysis, orienting the active sites optimization through the occurring relationship between the aluminum placement and the activity/selectivity of the catalyst.

A general disagreement is found between the results obtained by the employed approaches, ONIOM, SIESTA and cluster, both in the absolute and relative DPE values. If the cluster method is taken as the most appropriate, this disagreement is to be attributed to the difficulty in the definition of a generally reliable model system, in the case of ONIOM, and to the intrinsic problems of periodic formalisms related to charged cells, in the SIESTA case. Regarding the latter, it seems that the use of localized atomic orbitals, which defines the SIESTA formalism, leads to underestimate the site deprotonation energies in β-zeolite, oppositely to what happens in calculations based on plane waves, delocalized by definition. The suggested cluster approach, consisting in the evaluation of DPE by means of non-periodic single point DFT calculations starting from reshaped zeolite cell whose geometry was optimized by the SIESTA method, is therefore proposed as a suitable tool to correct in an algorithmic way the DPE values resulting from periodic calculations. This because it avoids the necessity of empirical corrections and constitutes a homogeneous computational model. Indeed, it would allow to treat essentially in the same modelistic way the zeolite acidic sites, possible modifiers of the acidity strength (like, *e.g.* defects or embedded metal particles) and the reactions in which zeolite catalytic activity is eventually involved. In the investigation of processes occurring inside the zeolite cavities, for example, the reacting molecule would conveniently result located at the center of the system, just like the zeolite proton itself.

Metallic sites

The preferred location and the corresponding energetics of zeolite-embedded single metal atoms and small metal particles are hot topics within active site optimization and catalyst tuning, even as part of bifunctional materials design.

Periodic density functional theory was used to provide atomistic-level insights on this account, by employing a one-by-one atom addition approach driven by an unbiased algorithm. Migration of a platinum atom between different zeolite cages was also addressed, searching for the related transition state.

The investigation was focused on a pristine BEA structure, being this the necessary starting point for every wider study aiming at the characterization of the growth energetics of metal particles in zeolite models, which include, *e.g.*, aluminum substitution in different ratios or the presence of various kinds of defects.

4.1 Models and Methods

The structural model utilized for periodic DFT calculations is the same already presented in section 3.1. Following the geometry optimization of the silicate structure, a comprehensive mapping of the embedding sites was executed using a systematic approach, as detailed below, to identify the preferred positions for single platinum atoms. Given the diverse topological sites in β-zeolite, an unbiased approach was crucial to determine the initial coordinates for the platinum atoms systematically. Only with this approach, after optimizing the geometry of the embedded platinum fragments, it is conceivable to generate minima suitable for characterizing the potential energy surface arising from different starting configurations. The procedure involved creating a 3D grid of points with predefined thickness to map the BEA unit cell, resulting in 10 points along the crystallographic a and b axes (ranging from 0.00 to 12.43 Å) and 20 points along c (ranging from 0.00 to 26.21 Å). Each of the 2000 grid points represented a potential set of xyz coordinates for an embedded platinum atom. Cases where the added Pt

atom was too close to silicon and/or oxygen atoms in the zeolite framework were excluded based on van der Waals radii, specifically using a minimum Pt–O (or Pt–Si) distance threshold of 1.8 Å. To discard weak platinum-zeolite interaction geometries, another constraint was introduced, specifying that the distance between Pt and the nearest framework center should not exceed 3.0 Å. This led to the selection of 683 cases out of thousands. Single-point calculations were performed on these, and relative energies were used to sort the structures in order of stability. Noticeably, many of them showed almost identical energies, corresponding to similar structures. A relative energy threshold (first sieve) identified the most promising 14 cases out of the 683. These underwent an additional geometry optimization (second sieve), collapsing some structures to the same minimum and resulting in 8 Pt-zeolite structures. Following this, another energetic filter (third sieve), ruled by visual inspection, selected new geometries for adding a second platinum atom. The procedure was repeated for each of these selected geometries to find the best arrangements for two platinum atoms inside the zeolite cages. This process was then repeated, once again, for the Pt_3@BEA case.

For systems with two or three Pt atoms, minimum and maximum Pt–X (X=Si, O, Pt) distances were also set. In particular, coordinates of the new atom were accepted if the distance relative to the already adsorbed Pt center(s) fell within the range of 2.4–2.8 Å, the thresholds with silicon and oxygen remaining the same as before. The grid step was adjusted to locate a greater number of geometries near the already adsorbed Pt center(s). The flowchart of this procedure, aimed at including the largest number of significant structures, is illustrated in Figure 4.1. Information related to the different steps of the algorithm for the three Pt_n systems is reported in Table 4.1. It is essential to note that the criteria adopted for the sieves were designed to reduce the number of structures to investigate, isolating the most significant cases. Due to the topological heterogeneity of the analyzed systems, the energetic threshold values were varied, being lower when the number of structures to be selected was greater. In any case, during the analysis, structures were included, irrespective of their relative energetic stability, if after thorough visual inspection, they showed heuristic potential to evolve into structures of likely interest when the number of included platinum atoms changed.

The cluster growth was evaluated calculating the ΔE for the following processes:

$$2\,\mathrm{Pt@BEA} \longrightarrow \mathrm{Pt_2@BEA} + \mathrm{BEA} \tag{4.1}$$

$$3\,\mathrm{Pt@BEA} \longrightarrow \mathrm{Pt_3@BEA} + 2\,\mathrm{BEA} \tag{4.2}$$

$$\mathrm{Pt_2@BEA} + \mathrm{Pt@BEA} \longrightarrow \mathrm{Pt_3@BEA} + \mathrm{BEA} \tag{4.3}$$

where the reactants are the same zeolite fragments in which either two or three

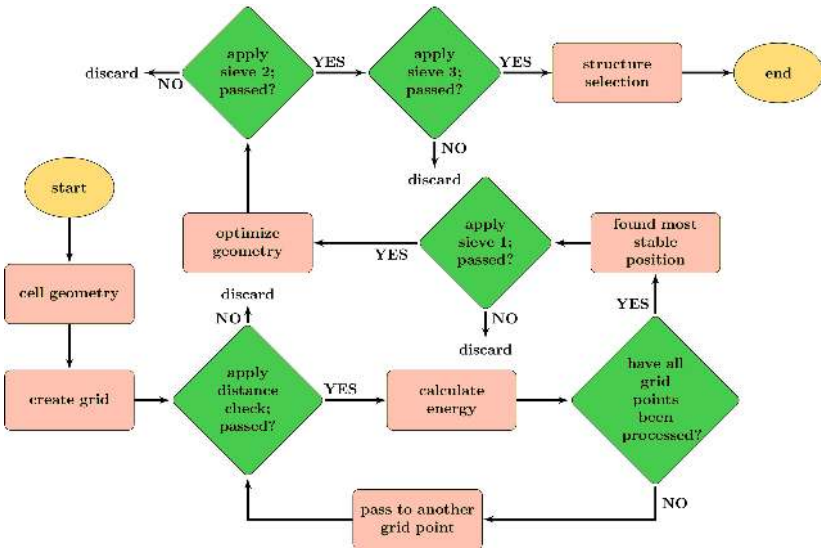

Figure 4.1: Flowchart depicting the algorithm used to identify the optimal position for a single platinum atom and to investigate cluster formation. The process initiates with the optimized silicate framework as the starting geometry; chosen geometries are subsequently employed as input for the addition of the second and third platinum atoms.

Table 4.1: Numbers of structures following the application of the three sieves characterizing the systems with one, two and three platinum atoms.

	Starting structures	**Structures after**		
		1st sieve[a]	**2nd sieve**[a]	**3rd sieve**[a,b]
Pt$_1$@BEA	683	14	8	4
Pt$_2$@BEA	10, 19, 61, 58	40	3, 4, 3, 2	5
Pt$_3$@BEA	17, 18, 17, 17, 29	20	2, 3, 2, 4, 3	–

[a] For details on the procedure summarized by the term "sieve" see text and Figure 4.1.

[b] The third sieve selects the m most stable structures with n Pt atoms and allow one to pick out m sets of new starting structures containing $n+1$ Pt atoms. For example, after having applied the third sieve to the Pt$_1$@BEA case, four geometries are left, which can be labeled a, b, c, d; a second Pt atom is added to each of these, so that 148 new structures are formed for the Pt$_2$@BEA system, *i.e.* 10 structures originating from a, 19 structures from b, 61 from c and 58 from d.

platinum atoms, or a single atom with a diatomic cluster, were adsorbed but not interact each other. The products instead represent a zeolite in which a platinum cluster is formed. A negative value of the concurrent energy differences indicates a preference for the formation of a product cluster inside the zeolite.

To examine the distortions of zeolite cavities induced by the embedding of platinum atoms, a reference point R, with coordinates matching those of the first embedded platinum atom, was selected. The nuclear distribution around this point was explored, considering all O−R and Si−R distances, corresponding to the O−Pt and Si−Pt distances in the Pt-zeolite system. These were then sorted in increasing order and by setting an exploration radius around R and excluding nuclei beyond this radius, the analysis focused on the vicinity of R. To avoid artifacts from periodic boundary conditions, a radius of 6.2 Å was chosen based on the cell parameters of the model. For each oxygen and silicon center within the exploration radius of individual pairs of pristine and platinum-embedded structures, two displacements were computed. The first is the absolute displacement of nucleus A, $\Delta_a^A \equiv |\mathbf{R}\mathrm{p}^A - \mathbf{R}\mathrm{e}^A|$, reflecting the platinum presence, where $\mathbf{R}\mathrm{p}^A$ represents the coordinates of A in the pristine zeolite, and $\mathbf{R}\mathrm{e}^A$ corresponds to those in the embedded zeolite. The second, conversely, is the radial displacement of A with respect to the central point R, $\Delta_r^A \equiv |\mathbf{R}\mathrm{e}^A - \mathbf{R}| - |\mathbf{R}\mathrm{p}^A - \mathbf{R}|$.

All calculations were performed within the framework of density functional theory (DFT) using the SIESTA approach, implemented in the code bearing the same name [142]. The chosen exchange-correlation functional was the PBE in its spin-polarized form [147], and a double-ζ quality numerical basis set was employed. Reciprocal space sampling was achieved using a 2×2×2 Monkhorst-Pack grid, and a mesh cutoff of 450 Ry. Preliminary calculations in specific cases indicated that a larger Monkhorst-Pack grid had a negligible effect on the energy of the studied systems.

The search for transition states associated with Pt atom migration utilized the Empathes code [148], which implements the Nudged Elastic Band method (NEB) and interfaces with the SIESTA program. Each NEB calculation involved 8 images generated by the image-dependent pair potential approach, connected by dynamic springs. The optimization of the elastic band employed the FIRE algorithm, with a convergence threshold of $(5 \times 10^{-3}\ \mathrm{E}_h/\text{Å})$ on the norm of NEB total forces.

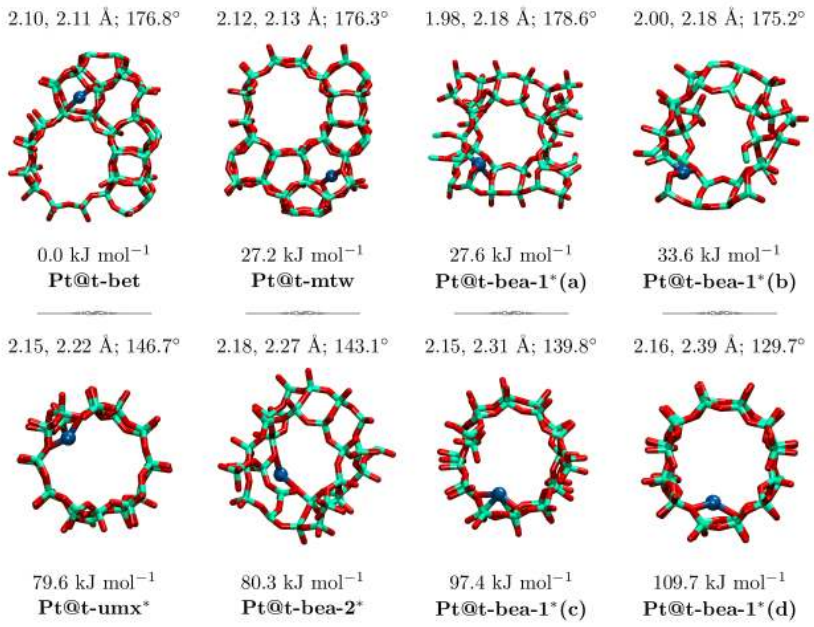

Figure 4.2: Detailed perspectives of the eight optimized geometries for Pt@BEA are shown, with oxygen (O) in red, silicon (Si) in green, and platinum (Pt) in blue. The relevant Pt−O distances and O−Pt−O angles are indicated above each structure. Additionally, the relative energy values, calculated with respect to the most stable species, are provided below. The tiling arrangement labels, following IZA [51], are included to specify the cavity where the platinum atom is situated.

4.2 Results and Discussion

4.2.1 Single Pt atom embedded in BEA cages

Figure 4.2 illustrates the 8 distinct structures that were identified for the adsorption of a single platinum atom within the BEA framework. In these configurations, the metal atom resides within a unique zeolite cavity. The energy differences among these structures can be attributed to the presence of different local topologies. Notably, despite performing spin-polarized calculations, the results consistently indicate a singlet multiplicity state for all investigated systems. This aligns with observations of spin state lowering occurring in supported systems when a platinum atom interacts with the zeolite framework compared to unsupported ones [104]. Figure 4.2 provides a local view of the eight optimized geometries. To enhance the visualization of rings and cavities, only a portion of the zeolite framework near the Pt atom is shown, obtained by repeating the unit cell in space when needed. Following the tiling arrangement accepted by IZA [51], the optimized structures can be grouped into five sets:

- t-bet cavity, in which the Pt atom interacts with 5-membered rings (5T);
- t-mtw cavity, with the Pt atom located in-between two 6-membered rings;
- t-bea-1* cavity, where the Pt atom protrudes towards the main channel and interacts with 5T or 4T rings;
- t-umx* cavity, in which the Pt atom interacts with a 6T ring in a main channel;
- t-bea-2* cavity, where the Pt atom located in the main channel is near but not inside the t-bet cavity.

Among the investigated Pt@BEA systems, four cases fall under the t-bea-1* cavity category. To differentiate them, additional letters "a-d" are assigned. For all cases, the structures, along with significant structural parameters, are presented in Figure 4.2. They include bond distances between platinum and the two nearest oxygen atoms, as well as the corresponding O–Pt–O bond angle. Additionally, relative energies are indicated, calculated as the difference between the energy of the specific structure and that of the most stable one, which serves as a reference for establishing an order of stability. Structures containing the t-bet smallest cavities resulted preferred, followed by those showing 6T ring pore. Systems in which platinum is located within the main channel are up to 80-110 kJ mol^{-1} higher in energy with respect to the most stable Pt@t-bet species.

Upon detailed analysis, it becomes evident that the observed trend is not solely dependent on channel sizes but rather on local interactions involving different zeolite surface fragments and metal atoms. In the most stable configurations, platinum forms strong bonds with a pair of oxygen atoms (2.09-2.12 Å) and, notably, exhibits an almost straight O–Pt–O bond angle. Regardless of cavity size, optimized structures tend to be more stable when the O–Pt–O angle approaches 180°. This observation is exemplified by the energetics of Pt@t-bea-1*(a) and Pt@t-bea-1*(b) species, featuring O–Pt–O angles of 178.6 and 175.2°, respectively. In these cases, the platinum atom in the main channel is stabilized by an energy close to that observed when allocated in a smaller cavity. Conversely, the four t-bea-1* fragments hosting the platinum atom in the same cavity display varying energies, with stronger interactions consistently occurring when the O–Pt–O bond angle approaches linearity. It is worth noting that in the case of Pt@t-bea-1*(a) and Pt@t-bea-1*(b) species, the formation of this specific bond angle is driven by the displacement of an oxygen atom from the silicon to which it was originally bonded. This displacement results in a visible alteration

of the framework regularity, a phenomenon that will be discussed in more detail later on.

4.2.2 Pt migration

In the scenario where a metal atom approaches the smaller cages of a zeolite from its main channels, the migration of platinum from the latter to the Pt@t-bet cavity was modeled. Additionally, the shift of the metal between the two smaller cavities was examined. For the first process, the Pt@t-bea-1*(b) species was chosen as the initial arrangement, representing a system with a platinum atom in the main channel. The Pt atom shift occurred in two steps, with an intermediate state that proved to be 20.5 kJ mol^{-1} more stable than the corresponding starting system and 13.1 kJ mol^{-1} higher in energy compared to the final one (refer to Figure 4.3). The energy barriers from the reactant to the intermediate and from the intermediate to the Pt@t-bet product were 102.6 and 127.6 kJ mol^{-1}, respectively.

In the second process, the platinum atom migrated in a single step (an high energy ephemeral intermediate is actually in the path), crossing the wall that separates the two cavities, with an associated energy barrier of 203.4 kJ mol^{-1}. Notably, along the minimum energy path identified by the NEB calculation (Figure 4.4), the platinum atom underwent rotation by pivoting on an oxygen bridging the two cavities. Consequently, a breakage in the zeolite structure was observed, with the O – Si bond distances returning to their usual values in the product. The occurrence of structures featuring the breaking of the zeolite framework warrants further discussion. This phenomenon has been previously explored in the literature for zeolites with 6-membered rings [104], where such a situation represented the most stable configuration for an embedded platinum atom. In the present case, it is interesting to observe also geometries in which the breaking occurs in the proximity of a 5T ring. However, these structures exhibit energies significantly higher than those of the most stable structures found using the systematic search algorithm employed in this thesis (see Figure 4.1).

4.2.3 Pt_2 and Pt_3 clusters inside BEA framework

Starting from the four most stable geometries with one adsorbed platinum atom, 12 cases of Pt_2@BEA systems have been identified (see Table 4.1), and five were selected after applying the third sieve. All systems, whose optimized geometries are reported in Figure 4.5, are in a singlet multiplicity state. In the most stable one, the second platinum atom i) is placed at about 2.5 Å from the first, ii) slightly protrudes into the main zeolite channel, and iii) attracts one oxygen

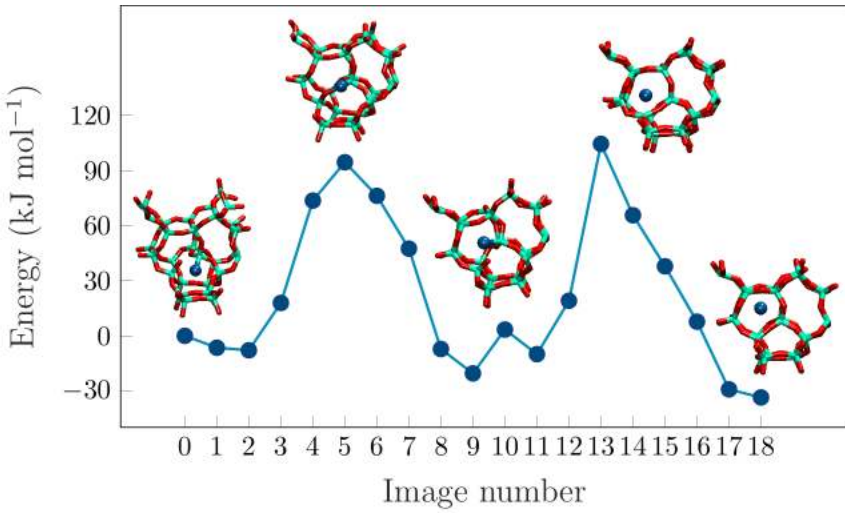

Figure 4.3: The minimum energy path for the migration of a platinum atom from the main channel of BEA to a cavity defined by a six-membered ring, found according to CI-NEB algorithm. The geometries of minima and TSs in the path are shown.

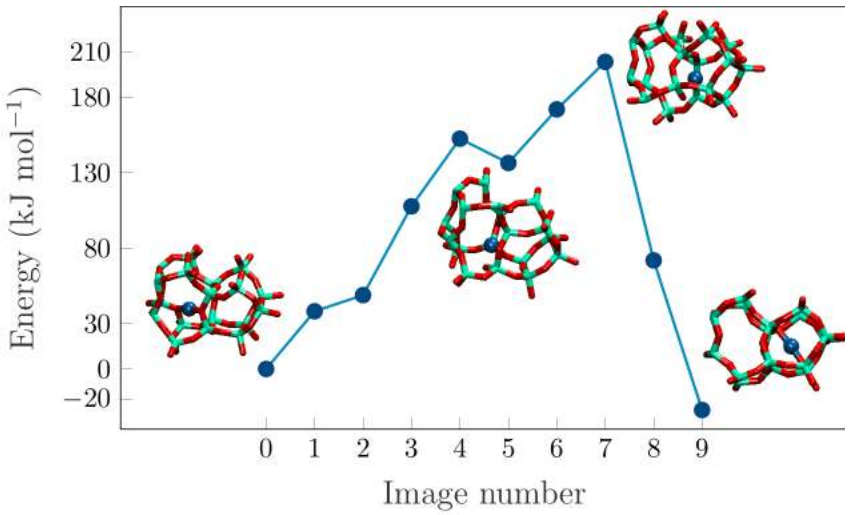

Figure 4.4: The minimum energy path for the migration of a platinum atom from a six-membered to a five-membered cavity, found according to CI-NEB algorithm. The geometries of minima and TSs in the path are shown.

atom, forming an almost straight bond angle. Two similar cases follow, where, once again, the first platinum atom is located in the t-mtw cavity, and the second, positioned in the main t-bea-1* channel, attracts one oxygen atom towards itself to form an almost linear bond angle. In a *ca.* 50 kJ mol^{-1} less stable arrangement, the first Pt atom is located in the smaller t-bet cavity, while the second, at 2.87 Å from the first, protrudes into the main channel and causes the rupture of the zeolite framework with the formation of a 176.7° O–Pt–O bond angle. Notably, two of these platinum-oxygen interactions, which seemingly rule the energetics of Pt@BEA adducts, are present. Since the analysis performed on the framework (see Section "Cavity distortions") showed minor distortions, the lower stability of this system can be interpreted in terms of the Pt–Pt distance. In fact, the interaction between the two metal atoms is rather weak, with the bond distance sensibly higher than the optimal value of 2.34 Å, obtained for the isolated Pt_2 dimer in the triplet state, at the same calculation level of theory. Finally, two platinum atoms at 2.78 Å from each other are located in the t-bea-1* channel and share an oxygen atom to form bond angles that strongly deviate from linearity (151.5° and 169.8°), presumably leading for this reason to the less stable among the considered Pt_2@BEA systems, with its relative energy being 61.9 kJ mol^{-1}.

The tendency of platinum to cluster was evaluated for the various cases, and a clustering behavior was found that allows further justification of the particular stability of the Pt_2@t-mtw structures, where the platinum atoms are more intimately bonded. Thus, the Pt–Pt distance plays a significant role in understanding the energetics of Pt_2@BEA systems, together with the O–Pt–O interactions and framework distortions.

An analogous analysis was performed for the addition of the third platinum atom. According to the proposed systematic approach, 14 Pt_3@BEA structures were identified and grouped into 5 sets originating from the Pt_2@BEA system (see Table 4.1). In the following, however, only minima within 30 kJ mol^{-1} of relative energy are taken into account for each cavity group, for a total of 8 cases. The optimized structures, all in the singlet multiplicity state, along with significant structural parameters of the three metal atoms, are reported in Figure 4.6. In the most stable configuration, two platinum atoms are situated inside the t-mtw cavity, while the third Pt protrudes into the main channel, forming an isosceles triangle with Pt–Pt bond distances of 2.56, 2.57, and 2.72 Å. Only one platinum atom, the second added to the zeolite structure, exhibits the typical O–Pt–O interaction. In a structure nearly 35 kJ mol^{-1} less stable, the Pt_3 cluster takes the shape of a reversed isosceles triangle, with a single Pt inside the t-mtw cavity and the other two in the main channel. The second platinum

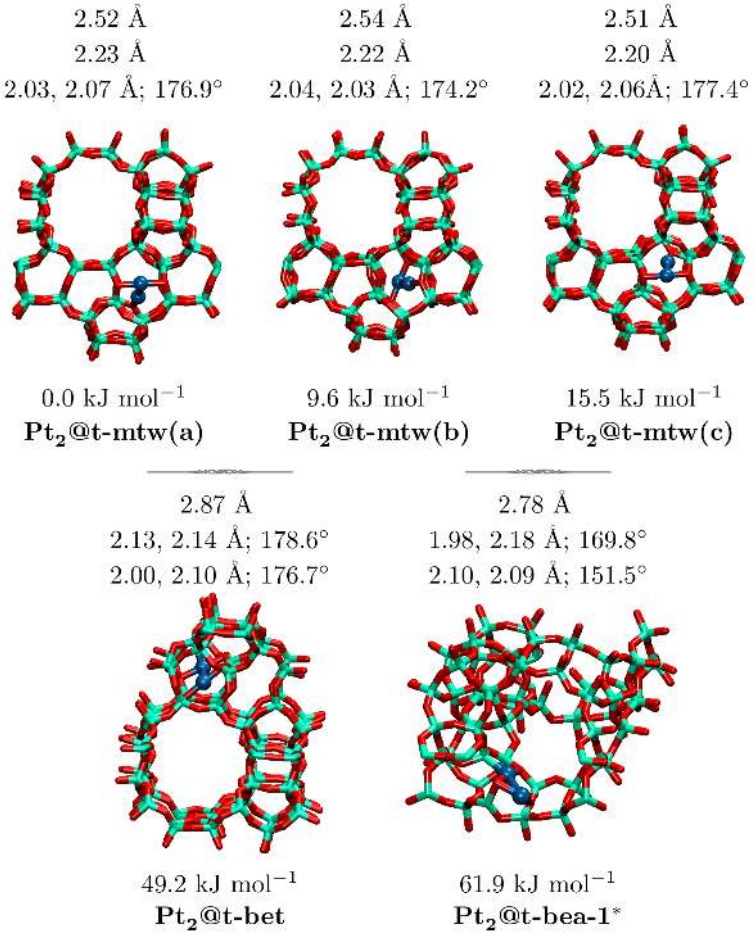

Figure 4.5: Local views of the five Pt_2@BEA optimized geometries (O=red, Si=green, Pt=blue). Above each structure Pt−Pt bond distance is reported, together with relevant Pt−O distances and O−Pt−O angles for the first and the second embedded Pt atom. Below there are the relative energy values, calculated with respect to the most stable species, along with the label used to identify the systems, underlying the cavity in which the first platinum atom is located.

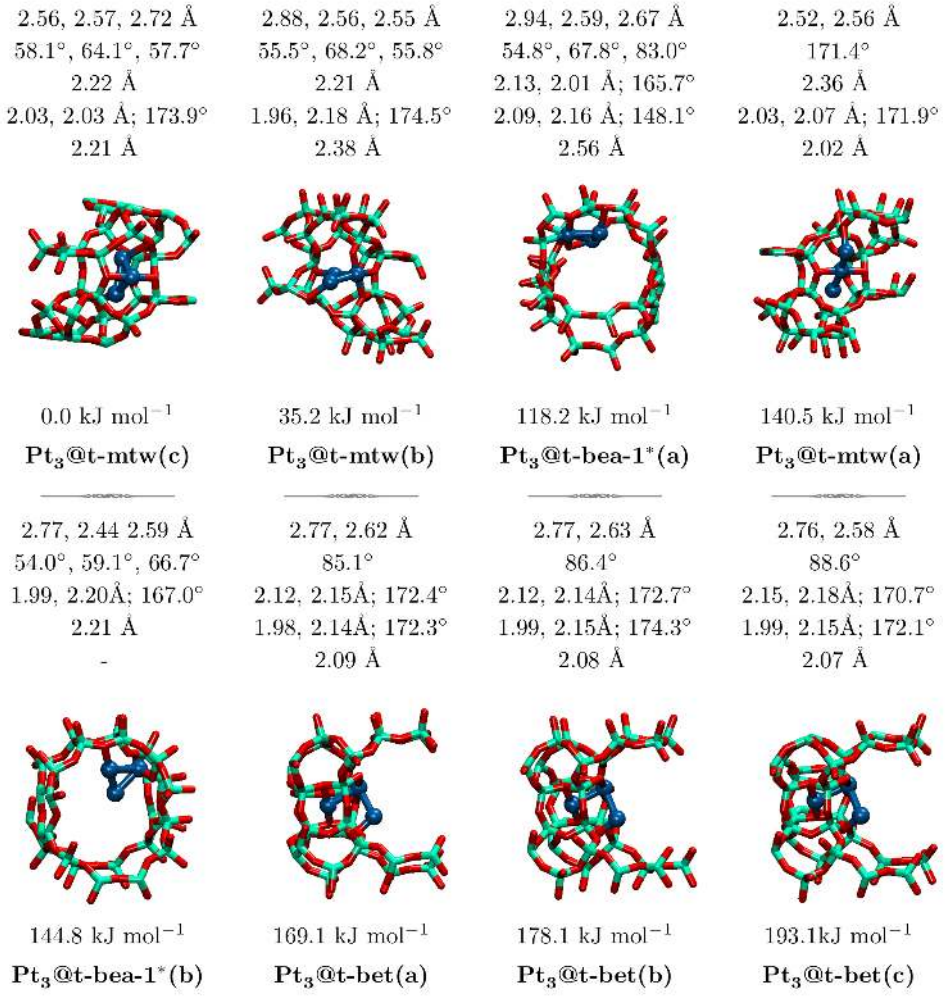

Figure 4.6: Local views of the eight Pt_3@BEA optimized geometries. O=red, Si=green, Pt=blue. Above each structure Pt−Pt distances and angles are reported, together with relevant Pt−O distances and O−Pt−O angles for the first, second and third embedded Pt atom. The relative energy values, calculated with respect to the most stable species, are shown below each structure, together with the tiling label identifying the cavity where the first platinum is located.

atom evenly interacts with three oxygen atoms, causing a rupture in the zeolitic framework regularity due to the formation of a linear O–Pt–O configuration, as discussed in the next section. With the third structure, Pt_3@t-bea-1*(a), the relative energy rises to 118.2 kJ mol^{-1}, and the cluster assumes the shape of a scalene triangle at the intersection between the two main 12T channels of BEA. Two platinum atoms share one oxygen within the favorable O–Pt–O interacting mode, leading to framework distortions similar to what happens to the Pt_2@t-bea-1* system. The fourth system, characterized by a relative energy of 140.5 kJ mol^{-1}, features an almost linear arrangement of the three platinum atoms (angle 171.4°) with distances of 2.52 and 2.56 Å. Only the second Pt atom interacts with two oxygens in the linear O–Pt–O fragment, with the framework only slightly perturbed. At almost equal energy (144.8 kJ mol^{-1}), a new structure similar to the other Pt_3@t-bea-1* follows, in which, however, the scalene triangle formed by the Pt_3 cluster at the intersection between the channels has fewer interactions with the zeolite walls, especially for the third platinum atom, that finds the closest oxygen 3.66 Å apart. Moreover, only the first Pt shows the preferential interaction with two oxygens and due to this a t-bet cavity is broken, as for the same site with one and two platinum atoms.

The last three systems, belonging to the t-bet group, feature a Pt_3 cluster in a bent shape with angles of 85.1°, 86.4°, and 88.6°, going towards the least stable case with a relative energy of 193.1 kJ mol^{-1}. In these systems, irrespective of the involved energy, two platinum atoms interact with two oxygen atoms, causing the connected cavity to break. The third platinum atom just has a single oxygen atom nearby.

Overall, there is a significant energy difference among the 8 selected systems, where the first two differ by 35.2 kJ mol^{-1}, while the least stable structure is nearly 190 kJ mol^{-1} higher in energy than the Pt_3@t-mtw(c) reference. These findings can be rationalized in terms of the embedded cluster geometry compared to that of the *in-vacuo* Pt_3 structure, investigated at the same computational level. The latter appears to be an equilateral triangle in the singlet multiplicity state, with Pt–Pt bond distances of 2.48 Å. It can be therefore argued that the system is more stable as the embedded Pt_3 cluster approaches this ideal configuration. The second factor determining the stability of the studied systems is the possibility of interactions with the zeolite walls. In these terms, the energetic order found between the two Pt_3@t-bea-1* cases can be interpreted. Interestingly, Pt_3@t-mtw(a), where a linear arrangement occurs, has an energy in between the two Pt_3@t-bea-1* systems. It evidently represents a peculiar zeolitic fragment suitable to accommodate the three platinum atoms without significant framework

distortions, characterized by Pt−Pt bond distances similar to those of both the more stable Pt_3@BEA system and the *in-vacuo* triangular platinum cluster.

4.2.4 Cavity distortions

Figures 4.7 to 4.9 illustrate distortion analysis graphs focused on oxygen atoms for all Pt_n@BEA systems, following the approach outlined in the "Models and Methods" section. In these graphs, the abscissa values represent the distance between the reference point R and the oxygen atoms in the pristine BEA cell, while the ordinate displays the modules of both absolute (Δ_a^O) and radial (Δ_r^O) displacements from that distance.

The corresponding graphs that refer to the silicon atoms are reported in the appendix A section (Figures A.1, A.2, A.3). It is important to note that, for Pt@BEA structures, only cases corresponding to cavities with equivalent systems having two and three platinum atoms were considered; the t-bea-1*(b) species of Figure 4.2 was, for example, not considered.

The graph for the t-bet system in Figure 4.7 shows minimal distortions. The two most intense peaks consist of displacements of approximately 0.3 and 0.2 Å, while the positions of silicon atoms in the framework remain nearly unchanged (see Figure A.1). These findings help interpret the particular stability of the t-bet cage structure, where the O−Pt−O interaction occurs naturally in a framework that is already suitable, both in terms of volume and zeolite framework topology, to effectively host one platinum atom. Rising in relative energy, the graph of the t-mtw system shows, among all, 5 oxygen peaks between 2.10 and 2.80 Å, mostly of the radial kind, whose absolute displacements range from 0.4 to 0.8 Å. They correspond to five of the t-mtw cavity oxygen atoms closer to the reference point R. Therefore, these oxygen centers undergo sensible modifications when Pt is inserted, while once again the Si atoms mostly maintain their positions, since the oxygen atom rotates around the Si−O−Si axis. The last graph of Figure 4.7 shows several oxygen peaks with magnitude greater than 0.5 Å: at 1.45 Å, 2.40 Å, 2.46 Å and then again at 3.79 Å. Also two silicon atoms have undergone displacements of *ca.* 0.4 Å. The corresponding distortions showed different Δ characters, as proved by the peaks at 2.18 and 2.32 Å in Figure A.1. Analyzing the structure in more detail, it can be observed that the latter are indeed coupled with the first two oxygen signals discussed above, jointly corresponding to a situation in which the framework is broken. In fact, the silicon atoms move away from each other, each bringing an oxygen atom with itself. As a consequence, there is a Si−O distance of 2.66 Å (whereas in the pristine zeolite framework it is 1.66 Å).

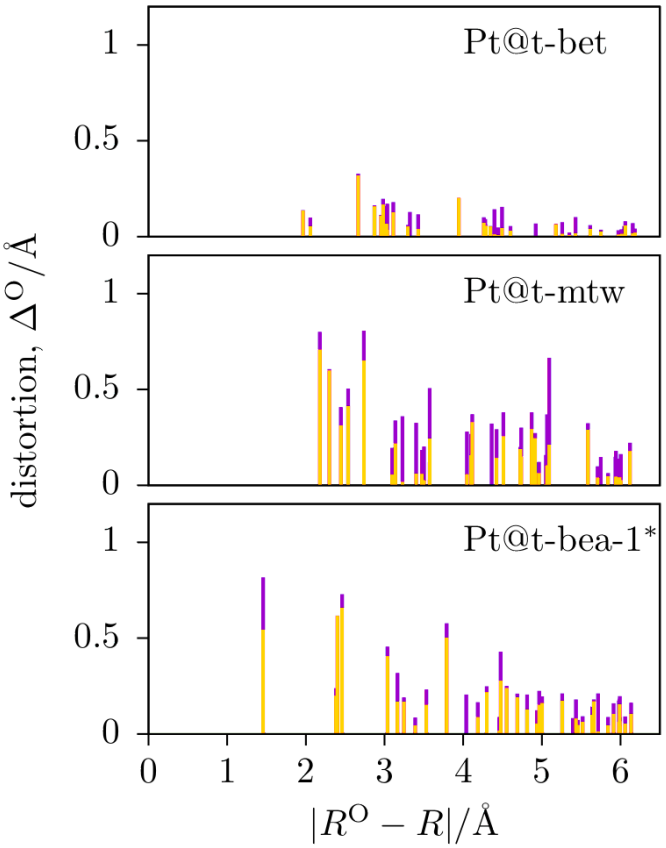

Figure 4.7: Absolute (Δ_a^{O}, purple) and radial (Δ_r^{O}, yellow) displacements of the framework oxygen atoms in Pt@BEA systems with respect to the pristine zeolite structure, within an exploration radius of 6.2 Å around the coordinates of the reference point R. Panels of the different cavities in which the platinum atom is located are reported in increasing relative energy, from top to bottom.

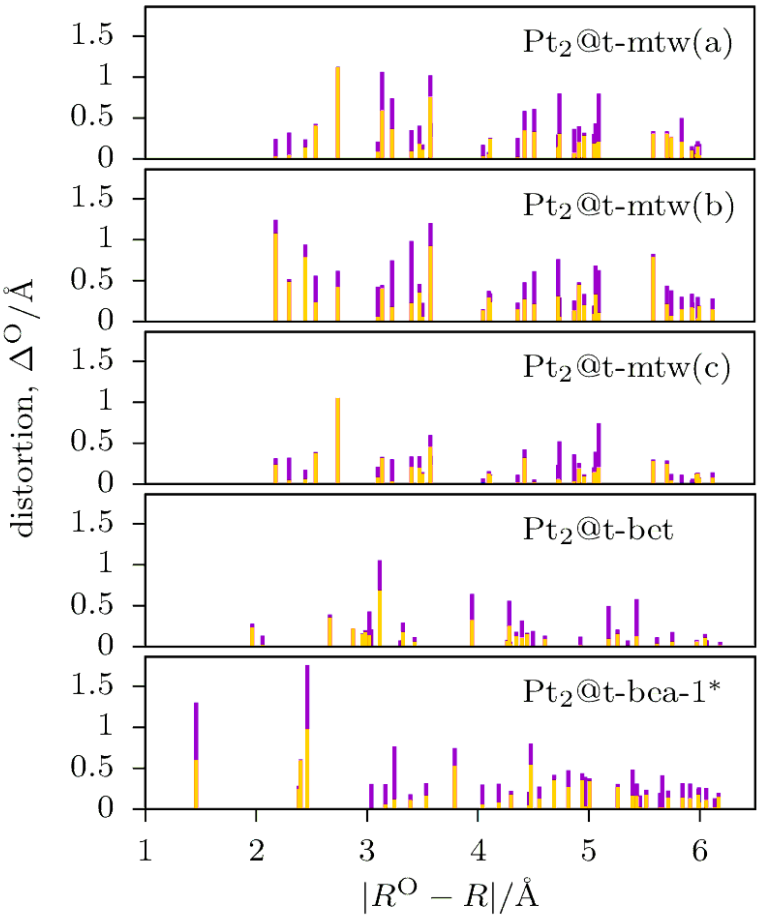

Figure 4.8: Absolute (Δ_a^{O}, purple) and radial (Δ_r^{O}, yellow) displacements of the framework oxygen atoms in Pt_2@BEA systems with respect to the pristine zeolite structure, within an exploration radius of 6.2 Å around the coordinates of the reference point R. Panels of the different cavities in which the platinum dimer is located are reported in increasing relative energy, from top to bottom.

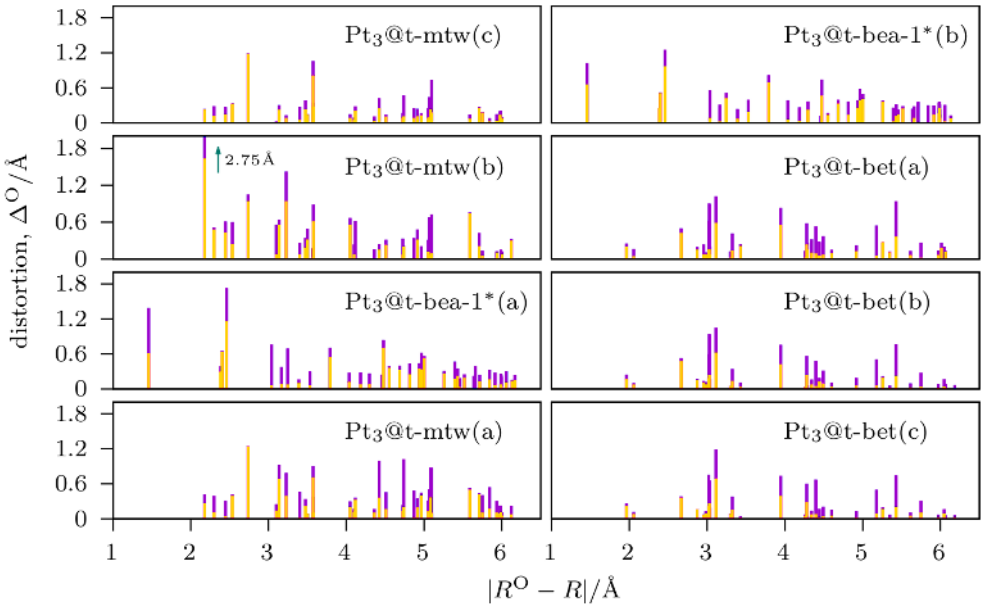

Figure 4.9: Absolute (Δ_a^{O}, purple) and radial (Δ_r^{O}, yellow) displacements of the framework oxygen atoms in Pt_3@BEA systems with respect to the pristine zeolite structure, within an exploration radius of 6.2 Å around the coordinates of the reference point R. Panels of the different cavities in which the platinum cluster is located are reported in increasing relative energy, from top to bottom, left to right. The arrow in the Pt_3@t-mtw(b) panel indicates an off-scale point at $\Delta_a^{\mathrm{O}} = 2.75$ Å.

Moving to systems with two zeolite-embedded platinum atoms, Figure 4.8 shows the Δ_a^O and Δ_r^O characteristics of the two platinum atoms systems. The first three panels, corresponding to the most stable t-mtw structures, display several prominent peaks up to 1.1 Å of absolute displacement and closely spaced peaks in the range between 2.17 and 3.57 Å. This finding lets to infer that for the Pt_2@BEA systems, the zeolite distortions are not predominant in destabilizing the supported structures with respect to the original BEA units. The box associated to the Pt_2@t-bet species shows minimal distortions compared to the others, despite the presence of a peak for oxygen at *ca.* 3.10 Å, with a distortion value close to 1.0 Å, and two peaks for silicon at distances of 2.76 and 3.95 Å, both displaying a distortion value equal to 0.4 Å (see Figure A.2), that were negligible in the graph of the Pt@t-bet system. They correspond to a break of the zeolite framework in which the Si atom, showing larger radial displacements, moves away, jointly with the oxygen atom, from the other silicon so that the latter is found at a distance of 2.83 Å (against 1.66 Å of the original structure). The driving force behind this break can be attributed to the oxygen attraction exerted by the platinum atom, leading to an almost linear arrangement. Lastly, for the less stable Pt_2@t-bea-1* structure the same Si and O peaks observed in the cavity with a single embedded platinum atom are present. However they are subjected both to subtle variations in magnitude and to the already outlined framework modifications. It is interesting to point out that the first oxygen peak, located at 1.45 Å and showing a distortion value equal to 1.3 Å, is now associated with one O – Pt – O interaction mode between the oxygen and both the two metal atoms, as discussed in the previous section. Furthermore, this peak and the one centered at 2.46 Å exhibit average radial displacements, but they reach the maximum values of the absolute displacement among all the systems.

Figure 4.9 reports the distortion behaviors taking place in the different BEA cavities related to systems with three platinum atoms embedded in the zeolite framework. The most stable Pt_3@t-mtw(c) case unveils the two highest peaks (1.18 and 1.06 Å) at 2.73 and 3.57 Å from the center taken as reference, thus being very similar to the behavior of the corresponding site with two platinum atoms, in fact only the second peak became slightly more intense. The next panel shows the same peaks in the range 2.17–3.57 Å that were already observed for the Pt_2@t-mtw structures, with little changes in the signal behaviors. The one at 3.22 Å couples with the silicon peak at 2.94 Å of 1.08 Å of absolute displacement (which conversely was negligible in the Si graph of the supported Pt_2 structure) in a break of the zeolitic framework where the two atom move apart to a final Si-O distance of 3.30 Å. An off-scale oxygen peak is also observed,

corresponding to an O atom that moved, significantly, in order to bond with two other silicon atoms different to those present in the initial couple. Its position is now actually occupied by the added third platinum atom. The behavior of t-bea-1*(a) has not undergone substantial changes passing from the system involving two to that involving three embedded platinum atoms, neither for oxygen nor for silicon displacement. The same result observing the subsequent panel and the, there represented, Pt_2@t-mtw(a) system. The Pt_3@t-bea-1*(b) species presents a framework break produced by the first Pt atom already added to the zeolite. However, the graph shows less intense peaks with respect to both its parent structure having two platinum atoms. Pt_3@t-bea-1*(a) is less stable than the related (b) one, due to fewer interactions occurring between the cluster and the zeolite walls. The values reported in the panels regarding the Pt_3@t-bet geometry group are very similar to each other. If compared to the equivalent structures characterized by the presence of two platinum atoms, the O and Si peaks related to the rupture of the framework are once again systematically observed, being those of silicon at slightly higher intensity (0.50-0.60 Å against the previous values of 0.40 Å, see Figures 4.9 and A.3). Furthermore, other peaks of oxygen atoms reaching values of about 1.0 Å are also present, with a characteristic prevalence of an angular component of the displacement, as can be deduced by the large difference between Δ_a^{O} and Δ_r^{O}.

4.2.5 Energetics of the clustering process

The tendency for clustering was assessed within all the considered cavities by calculating the ΔE values based on processes (4.1)-(4.3). The results are collected in Table 4.2. Additionally, Figure 4.10 depicts the relative energies for sets of systems characterized by the presence of embedded Pt cluster having a different number (1-3) of atoms inside the cavities. The negative values in the first column, indicate that Pt_2 clusters are favored over two isolated Pt atoms, regardless the kind of cavity. However, the greatest tendency towards growth occurs in the cases where the t-mtw cavity is involved. While being the second in order of stability concerning the location of a single platinum atom, this cavity is actually energetically the preferred over the others for the Pt_2@BEA systems. The structures involved in the different systems readily explain these findings. In fact, as previously highlighted, the t-bet cavity is already suitable for hosting one platinum atom, while the t-mtw cavity undergoes distortions of the framework. In the latter, however, two metal atoms exhibit a smaller bond distance hence higher cluster-like features.

The values reported in the second column shows that Pt_3@BEA systems are

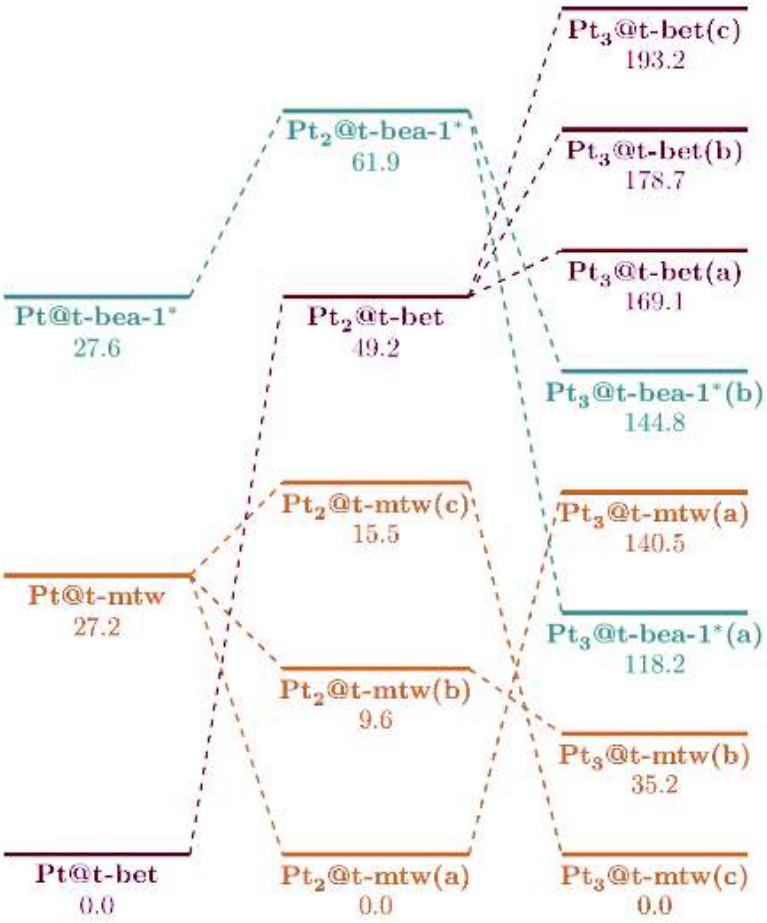

Figure 4.10: Energetics of and relations between the Pt_n@BEA systems considered for evaluating the clustering tendency. Vertically, cases with 1, 2 and 3 platinum atoms inside the different cavities are reported (left to right). The relative energy within the group is given below the cavity label. Horizontally, cases with the metal atoms in a certain cavity (t-bet, t-mtw and t-bea-1*, represented by different colors) are connected to their parent Pt_{n-1} system by dashed lines.

Table 4.2: ΔE values related to the processes represented by equations (4.1)-(4.3), calculated for every BEA cavity investigated.

Structure	**Process ΔE (kJ mol^{-1})**		
	step 1	**step 2**	**step 3**
t-bet(a)	-16.2	+8.6	+24.8
t-bet(b)	-16.2	+18.1	+34.3
t-bet(c)	-16.2	+32.6	+48.8
t-bea-1*(a)	-70.8	-143.3	-72.5
t-bea-1*(b)	-70.8	-116.7	-45.9
t-mtw(a)	-119.8	-101.7	+18.1
t-mtw(b)	-110.3	-207.0	-96.7
t-mtw(c)	-104.3	-242.2	-137.9

favored over three isolated atoms, except for the t-bet sites. Growth in this cavity is indeed thermodynamically unfavorable. This is not surprising given that in this case a comparison is performed between the worst condition for clustering within the Pt_3 group (see Figure 4.10) with the best energetic condition that is possible to find for a single Pt embedded in the zeolite. From the structural point of view, the t-bet cavity is too small to accommodate the three platinum atoms; in fact already the second Pt added in this cavity protrudes towards the main channel, so that the cluster is characterized by little interactions with the zeolite walls. In the case of the other two types of cavities, on the other hand, the presence of a Pt_3 particle is strongly favored, with ΔE values ranging from about 115 to 240 kJ mol^{-1}.

The third column presents the energy difference between an embedded Pt_3 cluster in a given cavity and that associated to both one metal dimer and one metal atom placed in two distinct cavities of the same type. Notably, the positive value of +18.1 kJ mol^{-1} characterizing the t-mtw(a) cavity, see Table 4.2, stands out, as an example, from this kind of data adjustment, which leads to an internal comparison of the three possible structures in the t-mtw group. If the preferred system for two platinum atoms is the first, the addition of a further Pt atom leads to a not particularly stable situation, due to the lack of significant interactions between the metal triangle-shaped cluster and the zeolite framework. Thus the growth process to Pt_3 most likely follows the c-type structure formation.

4.3 Conclusions

An approach within the DFT framework was employed to identify the preferential location of platinum atoms inside a β-zeolite model and to study the growth of a minimal cluster. Pt atoms migration through cages was also addressed, by means of a transition state search following the NEB approach.

A comparative structural analysis involving different cavities and platinum atom numbers showed that the optimal geometry involving a single platinum atom takes place when the formation of a O−Pt−O unit in an almost linear arrangement occurs. This seems to be the driving force that mainly determine the local structure properties of the metal-functionalized BEA and may cause breaking of the zeolite structure even when only one platinum atom is included in a cage. Energetic preference for clustering was observed against the occurring of multiple distinct interactions between zeolite sites and metal centers, leading to slightly different cluster geometries. With respect to this, the Pt−Pt distance is actually a sensible factor in orienting the energetics of the Pt_2@BEA species while the cluster geometry become very significant in the case of the Pt_3@BEA species, where the closer the shape of the cluster is to that of an equilateral triangle, the more stable the corresponding fragment results.

Platinum migration characterized by the crossing of the wall of different cavities may occur with relatively low energy barriers, although occasionally, due to the local topology, the same process could be hindered by prohibitive energy values.

Given the intended use of these studied systems as catalysts, a minimum size is desirable, concurrently ensuring that the resulting cluster is available to interact with substrates in the main zeolite channel. This is believed to be the case for the here investigated Pt_3@BEA species, suggesting that further advances in addressing the cluster growth process may not be imperative. Nonetheless, delving into specific larger clusters with a "magic size number", such as Pt_{10} and Pt_{13}, can be of particular interest due to their proven significance in modeling catalysis.

Pt-modified H-Beta zeolite

Based on evidence related to activity, stability, and selectivity, it has been asserted that the performance of catalysts containing Pt and a three-dimensional large-pore zeolite like BEA predominantly depends on just two key parameters. They are the ratio of metallic to acidic sites and the proximity of both sites to each other, hence the key lies in the synergy between the two functionalities.

The investigation presented in this chapter addresses the topic of metal-acid interactions both from an experimental and atomistic perspective. The acidity features of platinum-modified zeolite catalysts, prepared via different impregnation methods, were measured through FTIR of adsorbed pyridine and compared to those of the pristine materials. The effect of a single Pt atom on the intrinsic Brønsted acidity of BEA was evaluated, in terms of DPE variations for selected cases and, *vice versa*, energy assessments have been carried out regarding the influence of the acidic sites on platinum stability.

5.1 Pt deposition on acidic zeolite

5.1.1 Impregnation and reduction

Zeolite NH_4-Beta-38 (CP814C*) and H-Beta-300 (CP811C-300) were purchased from Zeolyst International in a powder form and calcined in a muffle oven with a step calcination method, through the procedure detailed in the following. The temperature was increased from room temperature to 450 °C with a ramping rate of 2 °C/min, held for 300 min and decreased in 100 min again to room temperature (see Figure 5.1 a). Notably, this was just a precaution in case of H-Beta-300, while it was necessary for the Beta-38 sample, to remove the $-NH_4$ group and substitute it with a proton, being the protonic form the acidic substrate of interest for the metal modified catalyst preparation.

Two approaches were used for platinum deposition, namely Evaporation Impregnation (EIM) and Incipient Wetness (IW). Since each method was applied

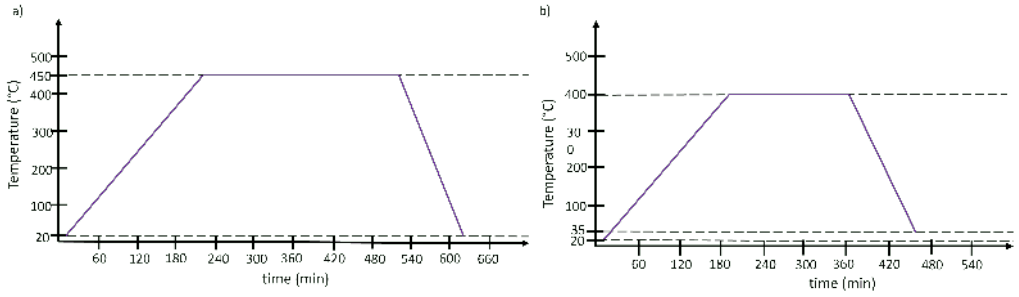

Figure 5.1: Visual depiction of the step calcination procedure carried out for a) proton and ammonium form of commercial zeolite powders and b) Pt-containing catalysts.

to both commercial zeolites with different silica to alumina ratio, four modified catalysts were obtained, referred to as Pt-H-Beta-38-EIM, Pt-H-Beta-38-IW, Pt-H-Beta-300-EIM and Pt-H-Beta-300-IW.

Evaporation Impregnation method Nearly 2 g of Beta Zeolite (38 or 300) and 0.04 g of $Pt(NH_3)_4(NO_3)_2$ (Alfa Aesar) as a platinum precursor were weighted, to obtain a Pt loading of 1 wt%. The powders were transferred into a round-bottomed flask of 50 mL of capacity, with distilled water. A rotoevaporator was used (Buchi R-114) in which the solution was rotated for 24 h at 60 °C to trigger the impregnation; subsequently water was evaporated at the same temperature under vacuum. The catalyst was scratched from the flask walls, then subjected to drying and finally to calcination steps, at 110 °C overnight following the program reported in Figure 5.1 b. The most significant phases of the procedure are illustrated in Figure 5.2.

Incipient Wetness method The pore impregnation volume of H-Beta-38 and H-Beta-300 zeolites was preliminarily measured, dropping Elga water from a burette until the samples were uniformly wet. From the value, equal to 1.48 mL for both the zeolite frameworks, the amount of platinum precursor to be used in order to prepare 2 g of catalyst with a Pt nominal loading of 1 wt% was calculated. Hence, the setup shown in Figure 5.3 was assembled, the burette being filled with 5 mL of a solution 0.073 M in $Pt(NH_3)_4(NO_3)_2$. This was added dropwise into the crucible containing the zeolite powder, mixing with a spatula until the proper texture was reached (see Figure 5.3 b). The so prepared Pt-H-Beta-38-IW and Pt-H-Beta-300-IW materials were then subjected to drying and calcination steps, as already described for the Evaporation Impregnation method.

Reduction The 4 Pt-modified catalysts (Pt-H-Beta-38-EIM, Pt-H-Beta-38-IW, Pt-H-Beta-300-EIM, Pt-H-Beta-300-IW) were reduced in a glass reactor, to obtain metallic platinum particles-zeolite systems which are required for the

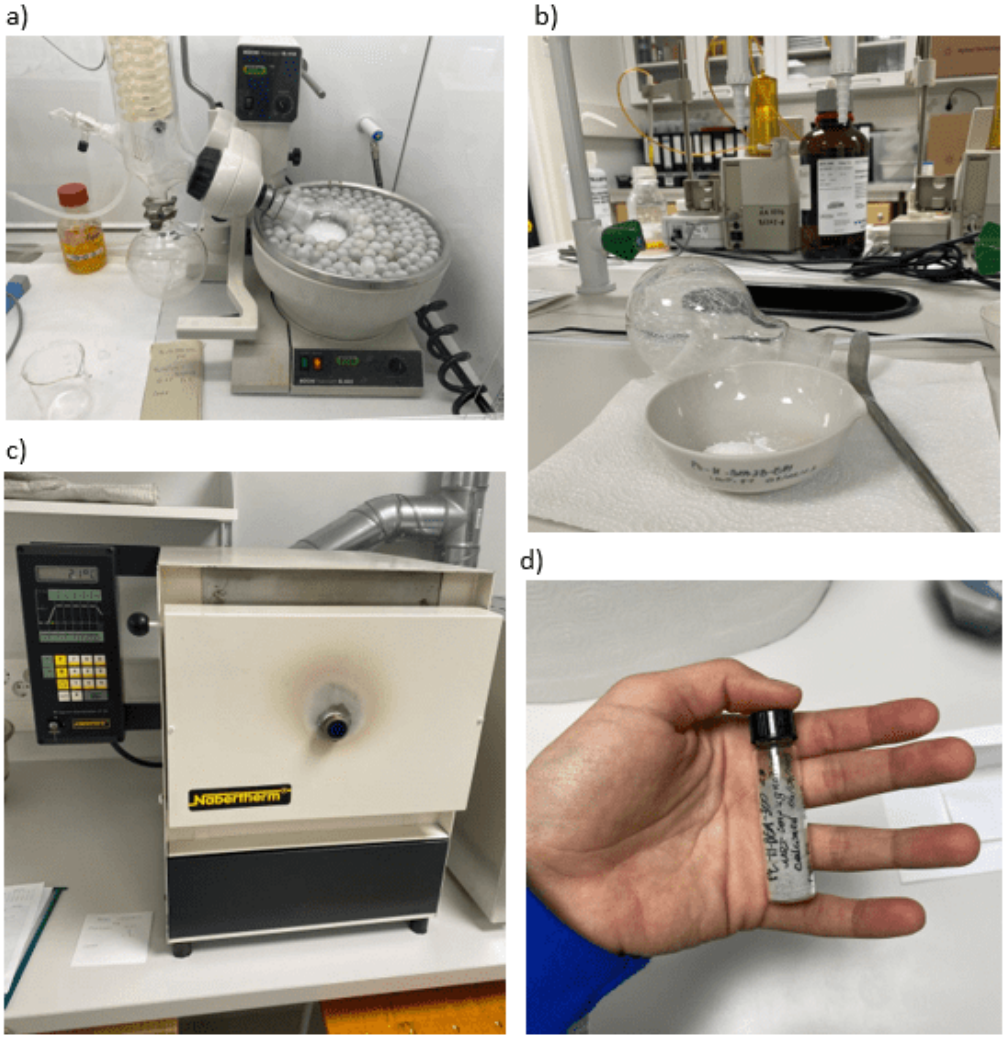

Figure 5.2: The most significant phases of the EIM method: a) the zeolite-platinum solution is rotated and solvent evaporated in a rotoevaporator, b) the white powder, scratched from the flask walls, is transferred into a crucible, c) after drying, calcination is performed in a muffle oven, d) the Pt-modified catalyst, in the form of a greyish powder, is stored in a vial.

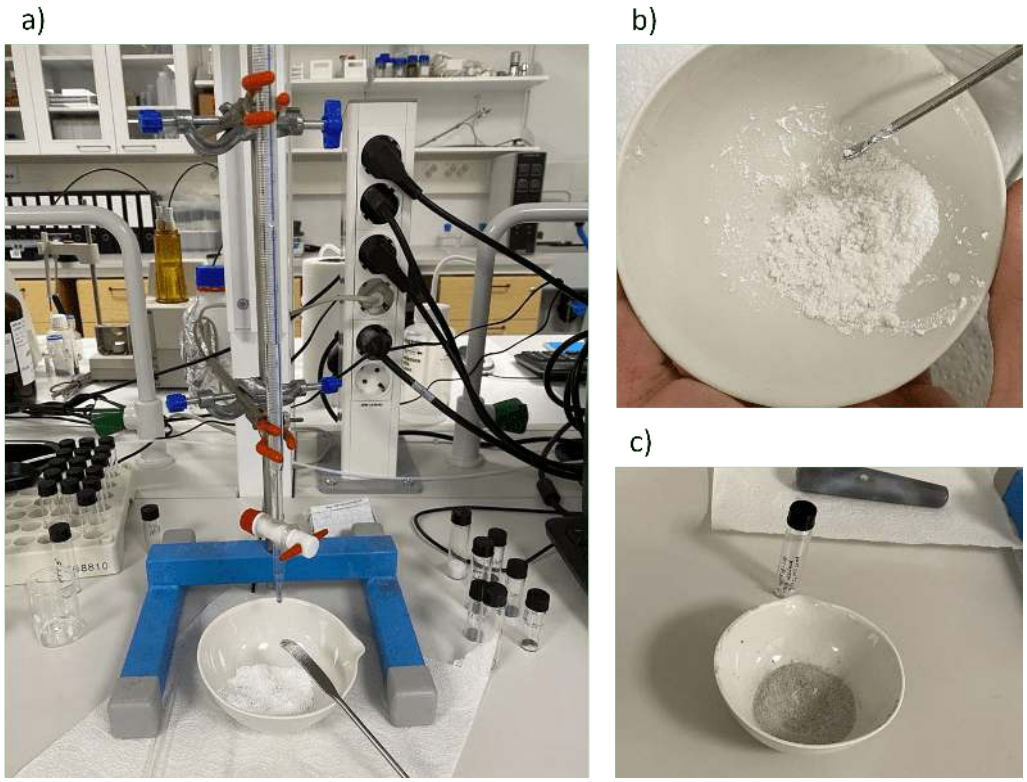

Figure 5.3: The most significant phases of the IW method: a) the burette is filled with the platinum precursor solution, that is dropped into the crucible containing the H-zeolite (38 or 300), b) the white powder has reached the desired texture, being uniformly wet, c) after drying and calcination, the Pt-modified catalyst, in the form of a greyish powder, is ready to be stored in a vial.

use of these materials in hydroconversion catalytic tests. For all samples, half of the available amount, *i.e.* nearly 1 g, was reduced. A continuous hydrogen flow of 40 mL/min was used for 120 min at a temperature of 400 °C, reached with a heating rate of 10 °C/min. Prior and after the reduction procedure, the system was flushed with argon (50 mL/min, 5 min), to remove air and hydrogen, respectively.

5.1.2 Characterization

Scanning Electron Microscopy (SEM) and Energy-Dispersive X-ray Microanalysis (EDX)

Morphological studies were performed on all the prepared catalytic materials by scanning electron microscopy (Zeiss Leo Gemini 1530). Elemental analysis of microporous materials was done by energy-dispersive X-ray microanalysis using the same instrument. SEM images were obtained by depositing the samples on a thin carbon tape and using an accelerating voltage of 2.7 kV with a working distance of *ca.* 4–5 mm. Determination of zeolite crystallites size was done from the SEM images using the ImageJ program [149]. For each sample, 80-100 measurements were collected.

Transmission Electron Microscopy (TEM)

Metal particle sizes of the platinum modified catalysts were measured by transmission electron microscopy (JEM-1400Plus, JEOL, Japan). The samples were suspended in ethanol and blowed on a carbon tape with a pipette; after solvent evaporated, the solid circles were injected in the instrument, see Figure 5.4. H-Beta-38 and H-Beta-300 were also analyzed for comparison. Determination of Pt particle size was done from the TEM images using the ImageJ program [149]. For each sample, more than 100 measurements were collected.

Fourier Transform Infrared Spectroscopy (FTIR)

Quantification of the Brønsted and Lewis acidic sites (BAS and LAS) of the H-Beta-300, Pt-H-Beta-300-EIM and Pt-H-Beta-300-IW samples was done by Fourier transform infrared spectroscopy (ATI Mattson FTIR Infinity Series) of adsorbed pyridine (Sigma-Aldrich), as a probe molecule.

The samples were pressed into thin pellets (20-30 mg) and placed in the measurement cell; they were outgassed under vacuum (0.08 mbar) at 350 °C for 2 h as a pretreatment to remove humidity and impurities prior to recording two background spectra at 100 °C. These were mediated, to be later automatically

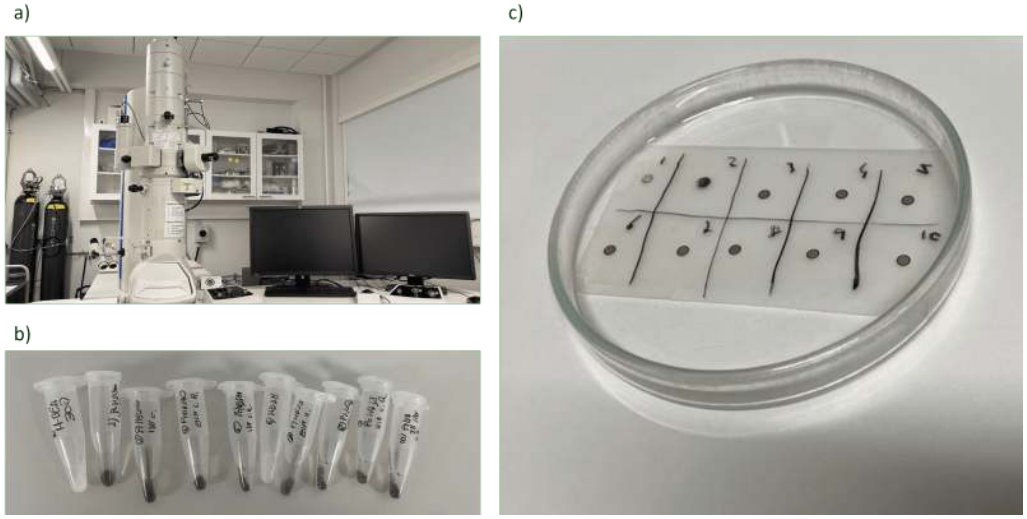

Figure 5.4: A visual depiction of the TEM characterization: a) the instrument employed (JEM-1400Plus, JEOL, Japan) and the samples, suspended in ethanol and ready to be injected, b) and c) respectively.

subtracted from the sample spectra. A pyridine atmosphere was created and pumped into the cell, after closing the vacuum valve and opening the outlet, producing a pyridine flow that, for 30 min and at 100 °C passes trough the sample, being adsorbed, and goes outward to a fume hood. After the instrument settings were restored to that of the background measurements, the heating program was set, making use of a macro for about 7 hours. The temperature was steadily increased to 250, 350 and 450 °C and six spectra were recorded after each heating step, always at 100 °C. Attention was payed that the sensor was cool for the scan, by providing liquid nitrogen during the descending part of the three temperature ramps.

Pyridine desorbing from the sample at 250, 350, and 450 °C allowed to determine the weak, medium, and strong acidic sites, respectively. Areas were manually integrated from the peaks, using the instrument software. The Lewis acidity was determined from the adsorption band at 1450 cm^{-1} and the Brønsted acidity from that centered at 1550 cm^{-1}. Using molar extinction coefficients reported in the literature [150], the amount of acidic sites, in micromoles per gram of catalyst were obtained.

5.1.3 Results and Discussion

The shape, size and distribution of the Beta zeolite crystals were observed and measured in the characterized catalytic materials for the Pt-modified and pristine Beta zeolite catalysts, through SEM analysis. Figure 5.5 shows the overall images, taken at 10x of magnification. The characteristic features, namely a

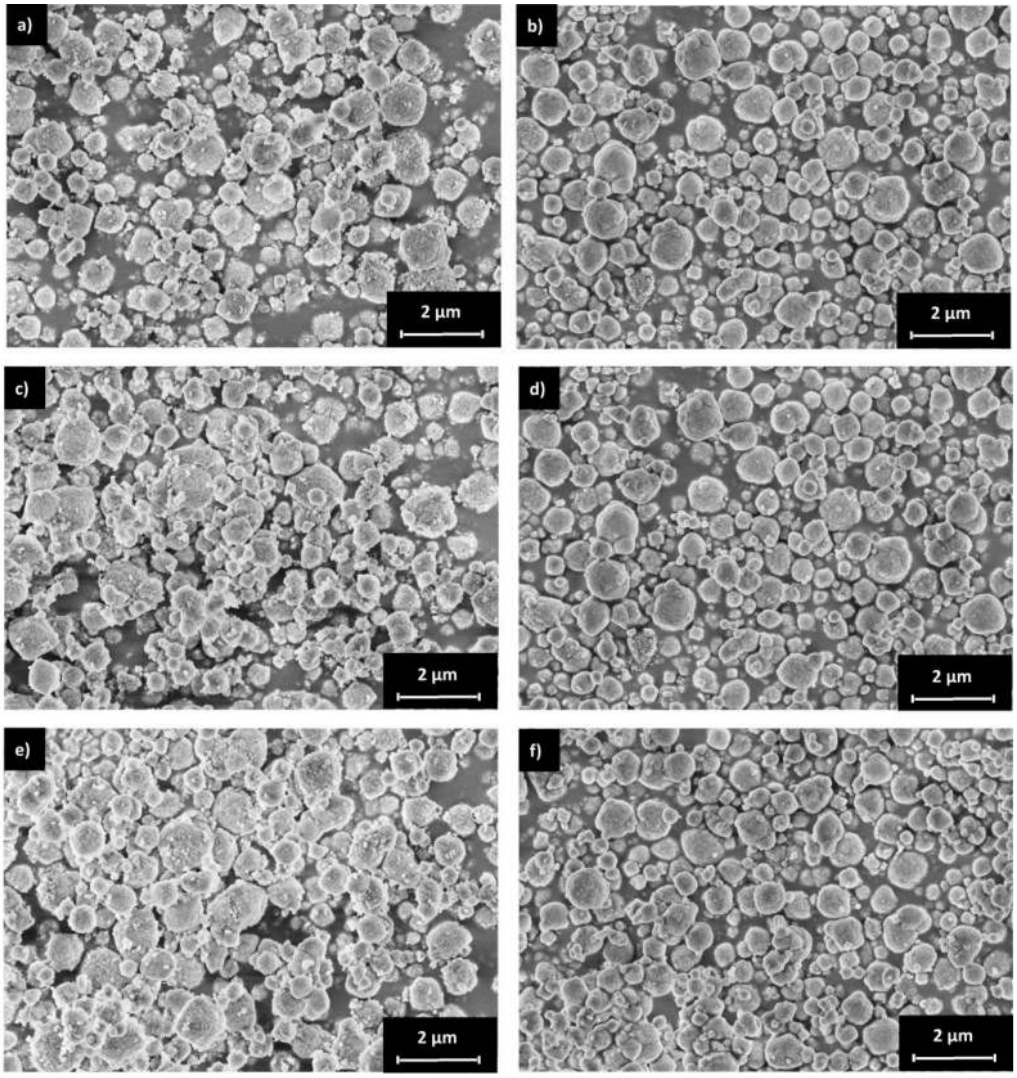

Figure 5.5: SEM micrographs at 10x of magnification for a) H-Beta-38, b) H-Beta-300, c) Pt-H-Beta-38-EIM, d) Pt-H-Beta-300-EIM, e) Pt-H-Beta-38-IW, f) Pt-H-Beta-300-IW. All samples are calcined and the Pt modified ones, with nominal loading of 1 wt%, are also reduced.

spherical shape, of Beta zeolite crystallites can be observed in all samples. This allowed to infer that neither the two modification methods employed for platinum impregnation (EIM and IW) altered the morphology of the pristine zeolite framework, both in the case of H-Beta-38 and H-Beta-300. The same considerations apply for the post-synthesis reduction procedure the Pt-modified materials were subjected to in order to be used for the reactions of interest, that is, no morphological differences were observed neither among the reduced and the corresponding calcined only samples, nor with respect to the pristine H-Beta frameworks.

Images at 25x and 50x of magnification are reported in Figure 5.6 and Figure 5.7, respectively, with Beta-38 based catalysts, named as a), c) and e) on the left and Beta-300 ones on the right. These micropragphs at higher magnification were used to estimate particle size distribution, two places being analyzed for each sample. Considering the diameter of 80-100 particles on average, the dimension range was found to span approximately from 100 to 1200 nm for both the H-Beta-38 and H-Beta-300 based materials, being in good agreement with literature [37, 115, 151, 152]. More in detail, three well resolved distributions were observed within the particle size range in all samples, with non-significant deviations in the mean values (within the associate errors), going from the pristine zeolites to the metal modified catalysts. Thus, both platinum impregnation methods and the reduction process did not significantly affected neither the shape nor the distribution of zeolite particles, as auspicated. The EDX analysis showed peaks of C (from the carbon tape), Si, O, Al and Pt only, the latter of course in case of the platinum-modified materials. No other elements were detected, indicating an high purity of the prepared samples. It was not possible to confirm the nominal platinum loading of 1 wt%, due to the instrument detection limit and the measure error that came along the Pt peak (see appendix A); however the application of the EDX technique provided the qualitative information that platinum impregnation was successful for all the methods and zeolite frameworks employed.

The TEM analysis allowed a more in-depth investigation of the Pt nanoparticles incorporation and dispersion. From the high scale bar images of Figure 5.8 (reference unit being 500-1000 nm) the presence of rather large metal clusters can be observed. In all samples, darker spot of nearly 70 nm in diameter are located as being possibly anchored on the surface of the greyish zeolite crystallites, or even isolated, like it is more evident in the case of panel d). By observing images of Figure 5.9, that feature a lower scale bar, polydispersion of the samples can be inferred. In fact, in addition to approximately micrometric size of particles, Pt aggregates of few nanometers are also found, see specially

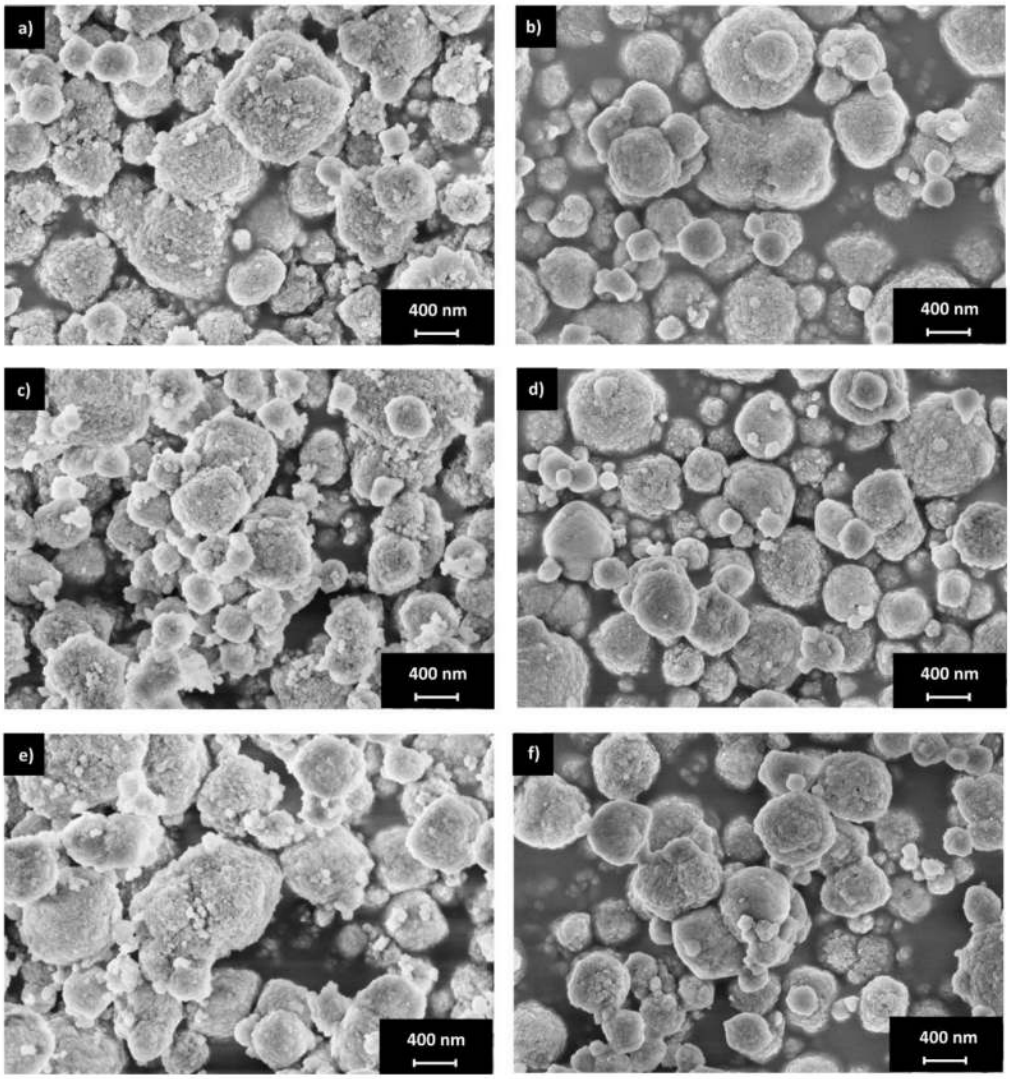

Figure 5.6: SEM micrographs at 25x of magnification for a) H-Beta-38, b) H-Beta-300, c) Pt-H-Beta-38-EIM, d) Pt-H-Beta-300-EIM, e) Pt-H-Beta-38-IW, f) Pt-H-Beta-300-IW. All samples are calcined and the Pt modified ones, with nominal loading of 1 wt%, are also reduced.

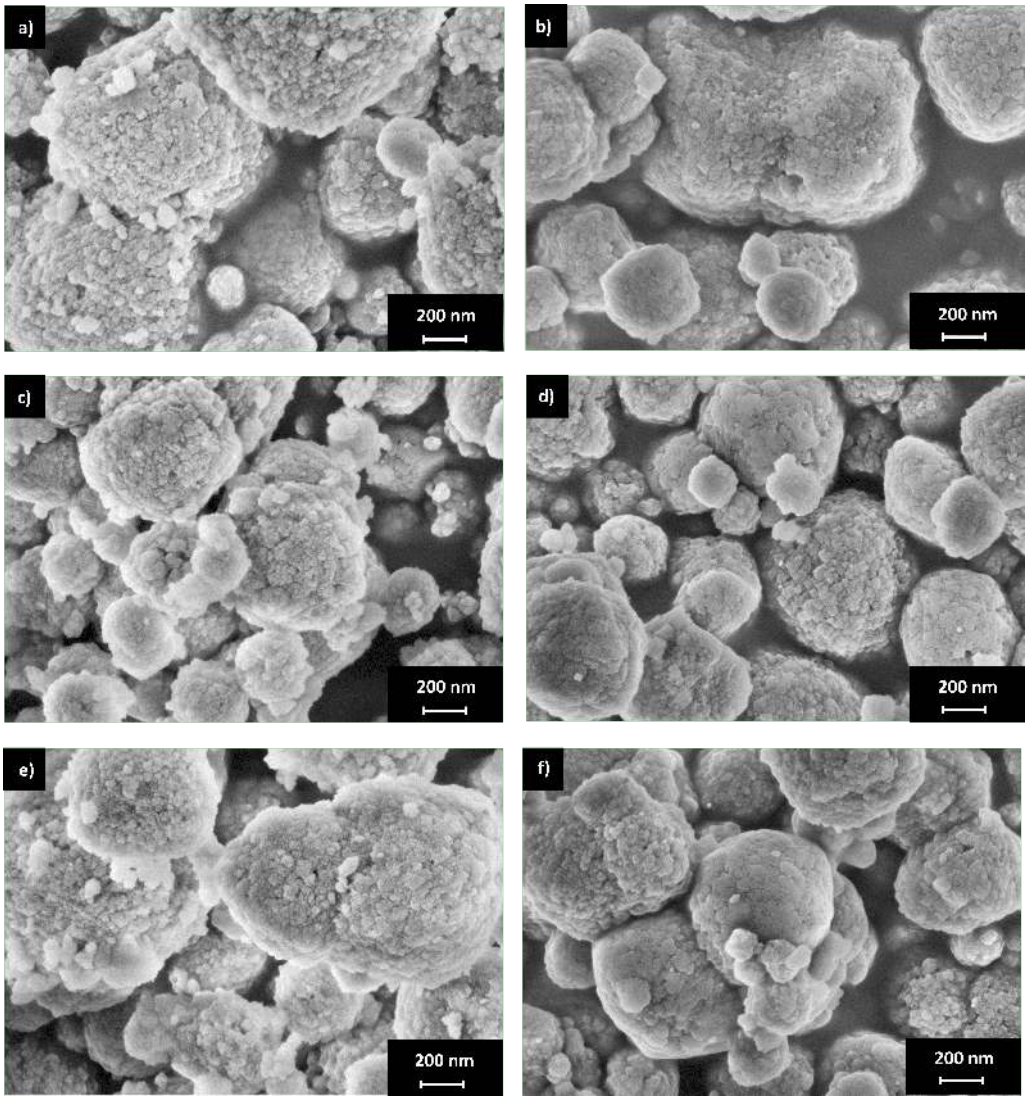

Figure 5.7: SEM micrographs at 50x of magnification for a) H-Beta-38, b) H-Beta-300, c) Pt-H-Beta-38-EIM, d) Pt-H-Beta-300-EIM, e) Pt-H-Beta-38-IW, f) Pt-H-Beta-300-IW. All samples are calcined and the Pt modified ones, with nominal loading of 1 wt%, are also reduced.

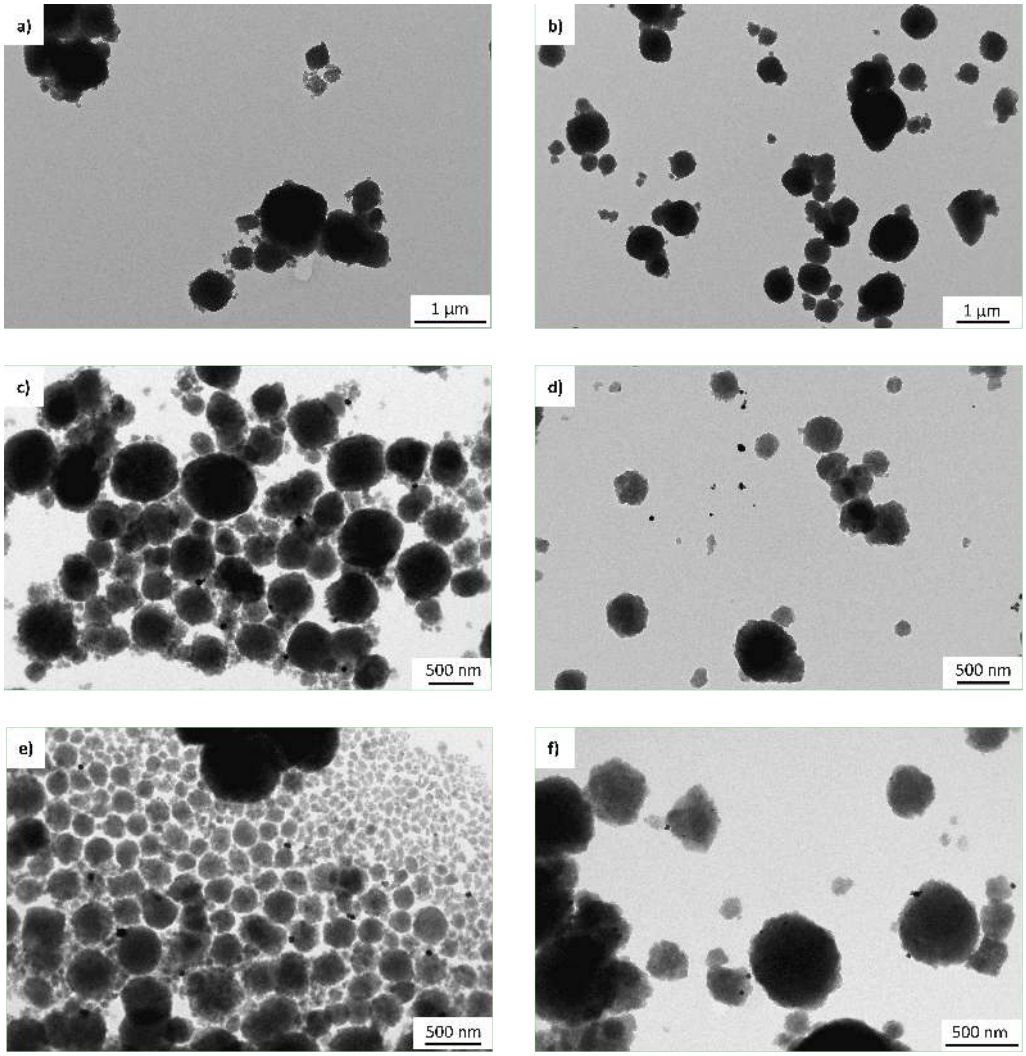

Figure 5.8: High scale bar TEM images of a)H-Beta-38, b)H-Beta-300, c)Pt-H-Beta-38-EIM, d)Pt-H-Beta-300-EIM, e)Pt-H-Beta38-IW, f)Pt-H-Beta-300-IW. Pt-modified samples are in the reduced form.

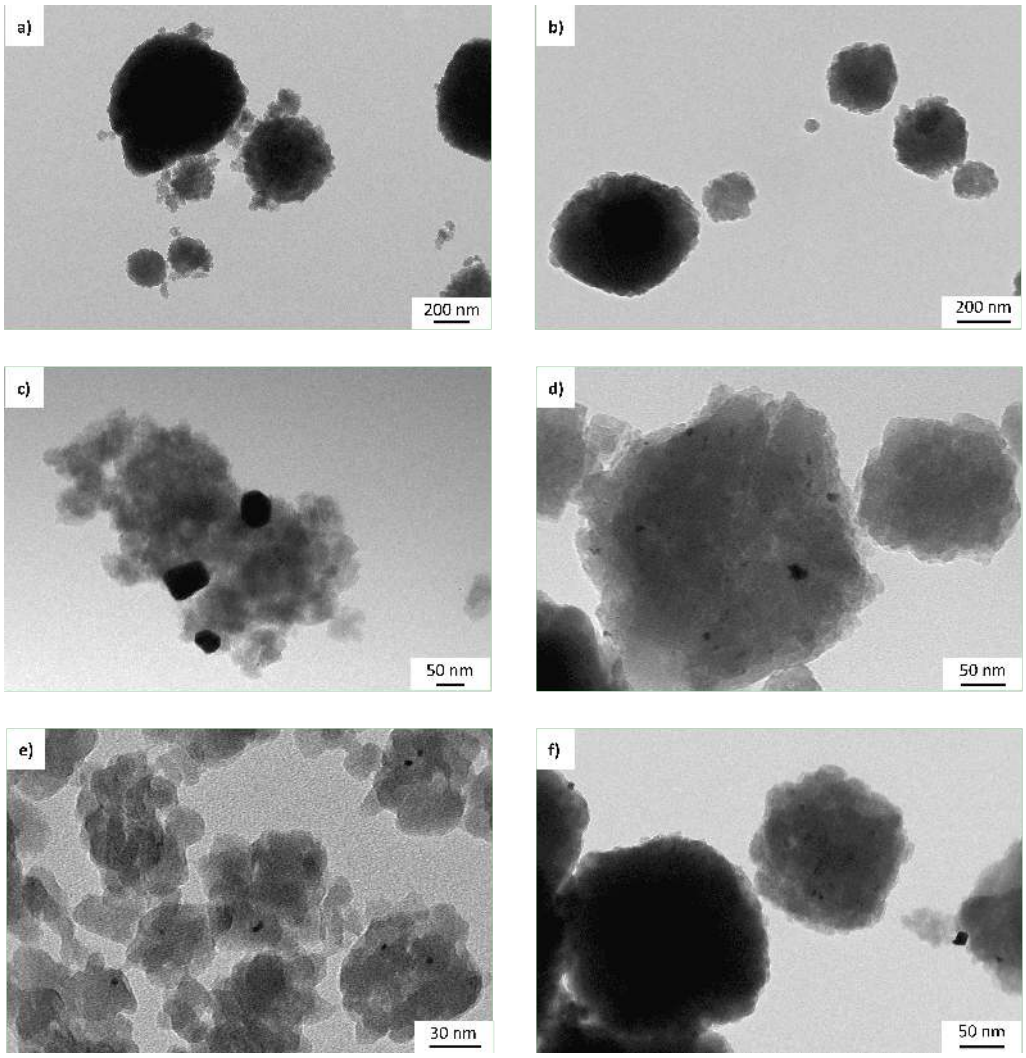

Figure 5.9: Low scale bar TEM images of a)H-Beta-38, b)H-Beta-300, c)Pt-H-Beta-38-EIM, d)Pt-H-Beta-300-EIM, e)Pt-H-Beta38-IW, f)Pt-H-Beta-300-IW. Pt-modified samples are in the reduced form.

panels d), e) and f). For a more quantitative discussion, histograms of particle size distribution were generated, after collecting 100 and more entries for each sample (see appendix A, Figure A.4), and average particle dimensions were calculated. Regarding the latters, they were found to be in-between 16 and 18 nm for all the samples. Therefore, no differences were detected depending on the method employed for platinum impregnation, nor did the silica to alumina ratio of the two investigated zeolite frameworks influences particle size. Related to this, although not attributed to acidity, a direct correlation has been reported by Kaka Khel *et al.* [37] between the dimensions of the zeolite crystals and metal particles size, when modified catalysts were prepared via the EIM method, using H_2PtCl_6 as a platinum precursor and H-Beta-25 or H-Beta-300 as zeolite substrate. While H-Beta-25 crystallites are sensibly smaller (60-140 nm), the dimensions of H-Beta-38 and H-Beta-300 appear to be quite similar (see above), so that the emerging homogeneity in platinum particle size can be considered as an unsurprising result in this context. Notably, an average particle size of 14.8 nm was indicated for the 2wt% Pt-H-Beta-300 material, in excellent agreement with the here findings. On the other hand, nearly 4 nm on average was the diameter reported by Martínez-Klimov *et al.* [115] for platinum particles on a Beta-300 modified material, prepared with the evaporation-impregnation method, showing also a 20-25% dispersion. If the synthesized materials were to be used in catalytic tests, smaller particle sizes and monodispersion would have been desirable. However, a further comment is required concerning platinum aggregates location, given the particle dimensions: being the maximum diameter of a sphere that could be included in the BEA main channel about 7 Å, even the smallest particles here detected, of *ca.* 3 nm in diameter, results unable to fit. They are instead more likely anchored on the surface of zeolite crystallites, as standardly observed in literature [136, 153, 154, 155]. Therefore the bifunctional behavior of these materials has to be intended in a quite macroscopic way, with the platinum centers that feature a close proximity to acidic sites if compared to the case in which metal particles are anchored on a binder, but on an atomistic level they are rather distant from Brønsted sites located on the pore mouth. It is also possible that subatomic particles made of just some atoms are present, even if the TEM images cannot reveal them. It is planned to perform nitrogen physisorption measurements before and after platinum impregnation. In fact, these could turn out significant to detect eventual changes in the pore volume caused by the presence of subatomic particles.

Results of pyridine FTIR measurements, performed to evaluate the acidic sites amount and strength of Pt-modified and pristine H-Beta-300 materials are

Table 5.1: Brønsted, Lewis and total acidity of H-Beta-300 based materials, in the reduced form in case of the metal modified ones.

Catalyst	**Brønsted sites** (μmol/g)			**Lewis sites** (μmol/g)			**Total acidic sites** (μmol/g)		
	W[a]	**M**[a]	**S**[a]	**W**[a]	**M**[a]	**S**[a]	**BAS**[b]	**LAS**[b]	**Total**
H-Beta-300	20	6	12	25	0	0	38	25	63
Pt-H-Beta-300-EIM	11	31	0	72	6	0	42	78	120
Pt-H-Beta-300-IW	14	19	8	36	4	0	41	40	81

[a] Desorption of pyridine at 250, 350 and 450 °C was done to determine the weak (W), medium (M), and strong (S) sites, respectively. Measurements were taken at 100 °C.

[b] Brønsted and Lewis acidic sites are also indicated with the acronyms BAS and LAS, for brevity.

presented in Table 5.1. A decrease in the amount (μmoles per gram of material) of weak and strong Brønsted acidic sites is observed in both the two Pt-containing catalysts, with respect to the non modified H-Beta-300 sample. In the case of the Pt-H-Beta-300-EIM, the strong ones are actually zeroed. Sites of medium acidity (determined from the 350 °C desorption) are conversely increased, for the catalyst prepared through the EIM method to a greater extent than for the IW modified one. Regarding Lewis acidity, the amount of weak sites increases, particularly in the case of the Pt-H-Beta-300-EIM sample, exceeding by nearly three times the value reported for H-Beta-300. Strong Lewis sites are zero for all the catalysts. The last three columns in Table 5.1 show the sum of Brønsted and Lewis acidic sites, independently, together with a total BAS+LAS value. It can be inferred that both overall Brønsted and Lewis acidity increase going from the pristine to the Pt-modified catalysts, just slightly the former while sensibly the latter, in particular in case of the EIM catalyst.

The here observed increasing in Lewis acidity, supported by many other works, might find a conclusive explanation in the interaction of pyridine with platinum crystallites, given that they are known to act as acceptors of electron pairs. This, as an additional factor, would lead to enhance the LAS value with respect of that characterizing the pristine zeolite framework [153]. If a higher concentration of Lewis acidic sites is desired for catalytic application, the evaporation-impregnation method seems to be more appropriate than the incipient wetness technique. However, the greater enhancement in Lewis acidity observed for the EIM modified sample cannot be ascribed to larger platinum particles size, since the TEM analysis showed similar values for both the EIM- and IW- prepared catalysts. It is intended to carry out Inductive Coupled Plasma spectroscopic

Table 5.2: Brønsted, Lewis and total acidity for pristine and platinum-modified H-Beta-25 and H-Beta-300 catalysts.

Catalyst	REF[a]	Brønsted sites (μmol/g)			Lewis sites (μmol/g)			Total acidic sites (μmol/g)		
		W	**M**	**S**	**W**	**M**	**S**	**BAS**	**LAS**	**Total**
H-Beta-25	[153]	269	207	120	162	128	113	596	403	999
H-Beta-25	[114]	53	42	191	287	35	17	10	63	349
H-Beta-25	[115]	67	33	129	26	5	6	229	37	266
Pt-H-Beta-25	[153]	304	178	0	163	33	0	482	196	678
Pt-H-Beta-25	[114]	62	0	28	89	0	0	13	13	103
Pt-H-Beta-25	[115]	44	10	4	12	4	2	58	18	76
H-Beta-300	[115]	7	29	19	4	1	1	55	6	61
Pt-H-Beta-300	[115]	9	2	0	5	3	0	11	8	19

[a] See the corresponding reference for information regarding catalyst preparation and details about temperature used for pyridine desorption and measurements.

measurements, that could prove useful to determine if this evidence is to be interpreted as deriving from a difference in platinum loading between the two samples.

Accounting for the Brønsted acidic site features trend, on the other hand, results to be more complicated. Kubicka *et al.* [153] reported, in case of modified Beta-25 based catalysts, a decrease in the amount of strong sites, while the total BAS value did not change substantially or even increased, that is the case here. They concluded that platinum should affect and modify acid strength through mutual interactions, not considering possible effects arising from the impregnation phase. Vajglova *et al.* [34] also observed the same trend regarding strong sites, which however resulted in a lower overall Brønsted acidity. For Beta-300 catalysts specifically, in the very recent investigation by Martínez-Klimov *et al.* [115], the presence of a binder was also studied. Since the catalysts where the Pt functionality was located into the binder were the more acidic, it was conversely proved, once again, that the presence of platinum in the zeolite lowers its Brønsted acidity. All these data are reported in Table 5.2 for comparison. It can be noted that even the values of pristine H-Beta zeolites sensibly vary among the cases, possibly due to the commercial material itself, different calcination conditions or FTIR settings such as temperature ramps, pyridine adsorption time *etc.*

A computational investigation can be instrumental to elucidate the atomistic-scale interactions between metallic and acidic functionalities that are hypothesized underlying these experimental evidence of acidity variation related to the presence of platinum centers.

5.2 Acidity and metal sites: DFT investigation

5.2.1 Models and Methods

The three most stable geometries with one embedded platinum atom within the zeolite framework, namely those corresponding to the uniques cavities labeled as Pt@t-bet, Pt@t-mtw and Pt@t-bea-1*(a), see Figure 4.2, were selected to model a system with a platinum atom located in close proximity to an acidic site. Starting from these structures, the isomorphous Si-Al substitution followed by the H atom addition was performed, obtaining Brønsted acidic sites as indicated in Figure 5.10. That is, the two oxygen atoms involved in the almost straight $O-Pt-O$ angle were chosen for the H atom to be added and the two Si atoms bonded to those oxygen were, one at a time, replaced with aluminum, resulting theoretically in four distinct acidic sites for each cavity. Also the third closest oxygen atom with respect to the Pt center was taken into account in case of the Pt@t-bea-1*(a) structure, while the T5O14 and T6O14 sites of Pt@t-bet were discarded, for the reason already adducted when treating Brønsted acidity of BEA in absence of the metallic functionality, that is the hydrogen inaccessibility. Out of the 12 configurations that were investigated, 10 represented topologically unique TnOm couples, in fact the T1O4 and T2O4 acidic sites were described in the systems arising both from the Pt@t-bet and Pt@t-bea-1*(a).

It is here to be stated that choosing different criteria for the creation of the metal modified acidic zeolite model was also possible, for example all the oxygen atoms belonging to the same ring or cavity of the Pt atom could have been considered for the H addition. The following has to be intended as a preliminary yet methodologically sound investigation which will be extended in the future to comprise other acidic to metal ratios and/or intimacy degrees, that is in this second case varying the proximity of the platinum atom to the acidic site. It should also be noted that, in order to examine all the 32 acidic sites of BEA, the possibility of implementing the opposite methodological approach, *i.e.* starting from all the SIESTA optimized structures featuring acidic sites and inserting Pt therein, would result highly inconvenient. To proceed systematically the preferred Pt location around an Al-OH moiety should be searched by means of the same algorithm employed in case of a Pt embedded in the silicalite framework (see section 4.1), leading to an extremely time and computational-cost demanding study.

As in the case of independently treated acidic sites, both neutral and anionic forms of the metal-acid configurations were investigated, through periodic geometry optimization calculations according to the SIESTA formalism, followed by

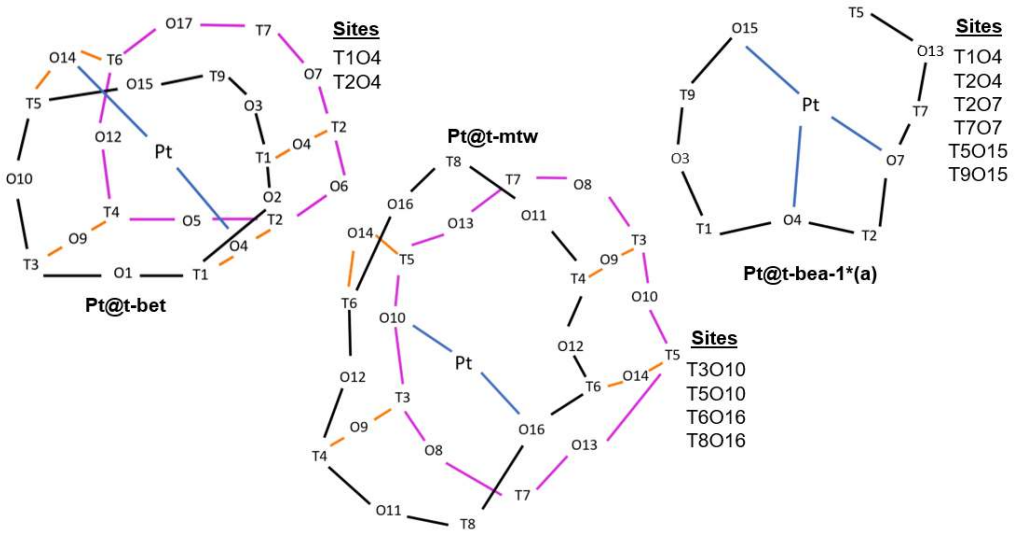

Figure 5.10: The three BEA cavities where a platinum atom is embedded (the most stable situations within 35 kJ mol^{-1}) are schematically depicted, the topological labels for Si/Al and O atoms being indicated. The Brønsted acidic sites considered for each structure are listed alongside, using the TnOm notation. The oxygen atoms involved in the almost linear O−Pt−O arrangement are chosen for the H atom addition, the two Si atoms bonded to those oxygen being, one at a time, replaced with aluminum.

the application of the proposed cluster approach (see sections 3.1 and 4.1 for calculation details). In the second calculation phase, performed with Gaussian, the hybrid B3LYP functional associated with the cc-pVDZ effective core potential was employed for platinum together with the cc-pVDZ basis set for light atoms. Deprotonation energies were calculated as the difference between the SCF energy of the platinum modified aluminated β-zeolite anionic form and the SCF energy of the corresponding neutral form.

For the cluster model definition, the reshape procedure (see section 3.1.3) was centered site by site on the Al atom, so that it resulted homogeneous with the reshape performed on the acidic only systems. Also, the usual criteria for saturation with H atoms were applied; in addition, all Si-H moieties eventually present in the ring or cavity hosting the Pt atom were replaced with an −OH group, both in the anion and the neutral structure.

5.2.2 Results and Discussion

The results of this investigation are collected in Table 5.3, in terms of DPE values for each of the considered cases (DPE$_{Pt-Al-H}$), compared to the deprotonation energy computed for the corresponding acidic sites in absence of the platinum atom (DPE$_{Al-H}$). As can be observed from the third column, the difference

Table 5.3: Deprotonation energy values for the platinum-containing systems, for the corresponding Brønsted acidic sites and the difference between the two sets. All values are expressed in kJ mol^{-1}.

Cavity	Site	$\mathbf{DPE}_{Pt-Al-H}$	$\mathbf{DPE}_{Al-H}$	delta
Pt@t-bet	**T1O4**	1101.4	1197.6	-96
	T2O4	1084.2	1209.0	-125
Pt@t-mtw	**T3O10**	1100.6	1218.2	-118
	T5O10	1175.5	1210.2	-35
	T6O16	1095.8	1227.4	-132
	T8O16	1097.9	1192.5	-95
Pt@t-bea-1*(a)	**T1O4**	1145.8	1197.6	-52
	T2O4	1147.9	1209.0	-61
	T2O7	1116.9	1202.1	-85
	T5O15	1235.0	1192.2	+43
	T7O7	1099.0	1181.8	-83
	T9O15	1241.6	1194.9	+47

(delta) between this two sets of data spans in the negative range from −35 to −125 kJ mol^{-1}, meaning that the metal effect goes in the direction of increasing the site Brønsted acidity, except for two cases (T5O15 and T9O15), whereby a positive value was recorded.

A structural analysis of interatomic distances and angles was performed for all the cases, considering both the anions and the neutral forms, to shed light on the above findings. This demonstrated that when the platinum atom is naturally accommodated in the cavity without significant distortions or novel interactions that were not present in the silicalitic structure, an enhancement in the site acidity of the site is consistently observed, in comparison to when Pt is absent. This phenomenon is particularly marked in the six cases depicted in Figure 5.11, which can be collectively categorized as featuring a DPE decrease of approximately 100 kJ mol^{-1}. In these systems, the environment around the acidic hydrogen atom undergoes changes due to the presence of platinum. For instance, in the Pt@t-bet−T1O4 and Pt@t-bet−T2O4 structures, the H atom is oriented towards Pt and protrudes less into the main channel compared to the same sites when the metal is absent. Conversely, in cases c), d) and e) the typical hydrogen bond of the site is disrupted because the platinum atom is inserted along the O−H···O axis. However, the most crucial aspect appears to be that platinum consistently form its preferred linear O−Pt−O interactions, effectively fitting into the cavities. In the neutral form corresponding to f) inset, for example, the cavity breakage, typical of the Pt@t-bea-1*(a) structure is observed, which was not present in the pure T2O7 case, precisely to facilitate a better placement of the embedded

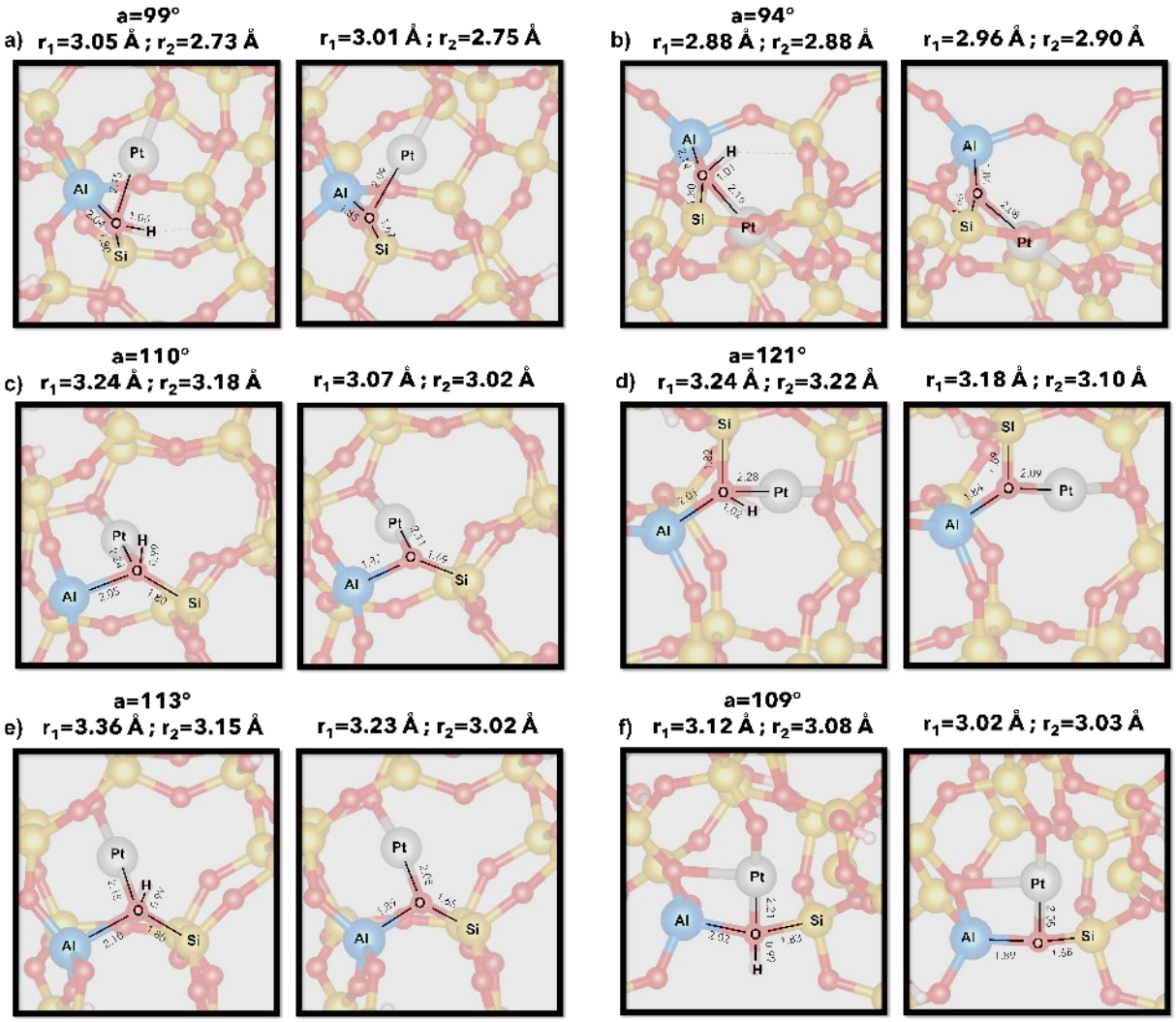

Figure 5.11: In trasparency, a ball-and-stick representation is provided for the neutral (left) and anionic forms (right) of systems featuring both an acidic site and a platinum center: a) Pt@t-bet−T1O4, b) Pt@t-bet−T2O4, c) Pt@t-mtw−T3O10, d) Pt@t-mtw−T6O16, e) Pt@t-mtw−T8O16 and f) Pt@t-bea-1*(a)−T2O7. In the foreground, values of the significant bond distances are reported, expressed in Å, together with the relative atomic labels. Above each structure there are also the Al−Pt and Si−Pt distances (r_1 and r_2, respectively), being the involved silicon atom the one bonded to the acidic oxygen, and the Al−O−H angle (a).

platinum atom. This seems to be the predominant factor that is common to all the structures. Concerning geometrical parameters, an overall uniformity is observed in the most significant interatomic distances, showed in Figure 5.11. For the neutral forms, the Pt−O distances vary in the 2.14-2.24 Å range, while the Al−O and Si−O bond distances of the zeolite are found to span between 2.02-2.10 Å, and 1.80-1.83 Å, respectively. The distances between framework silicon and aluminum atom and the embedded Pt, reported above each structure, generally settle around 3 Å. The O−H distance is 0.99 Å when no hydrogen bond formation is involved, whereas it elongates in the presence of such interactions. All the aforementioned bond distances are usually shorter in the anions.

The remaining cases of Table 5.3 elude categorization, exhibiting unique characteristics that necessitate individual examination. Their respective structures are presented and discussed sequentially below. In accordance with the previous definition, the Al−O−H angle is indicated with the letter "a", while r_1 and r_2, are the Al−Pt and Si−Pt distances, respectively.

Pt@t-mtw−T5O10

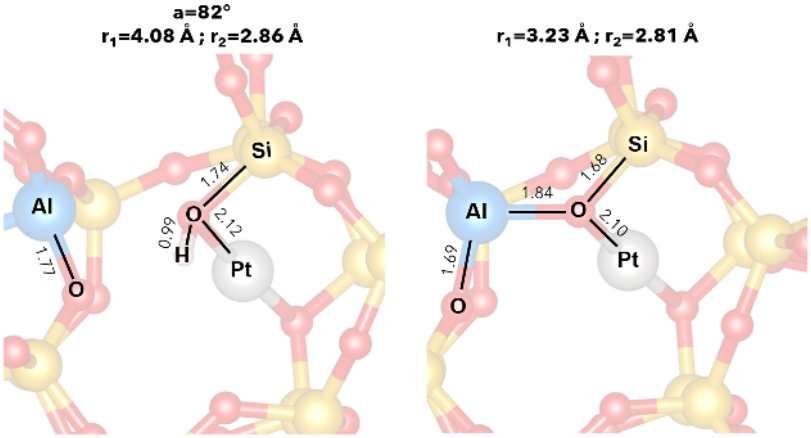

While the anionic form aligns with the standard characteristics found for the other cases already discussed, the geometrical features of the neutral form are notably unique. The platinum atom, situated within the t-mtw cavity, forms an angle of 177.4° in O−Pt−O, even slightly closer to linearity (preferred situation) than the 176.3° value observed in case of the pristine cavity, see Figure 4.2. However, achieving this configuration necessitated a significant distortion in the zeolite structure, unprecedented in its nature. The platinum atom, in adapting to the non-solely silicalitic framework caused the breaking of the Al−O_a bond, increasing their separation to 2.67 Å, whereas the bond length in the absence of Pt at the T5O10 acidic site was 1.96 Å. This could be considered as a different species as compared to those showing a wholly linked and unbroken aluminum

substituted zeolite. The Al−Pt distance indeed reaches the value of 4.08 Å, exceeding by one unity the usual one. The geometry of the acid hydrogen atom also undergoes alterations. It loses the hydrogen bond characteristic of the site, with the O···H distance of 2.59 Å and O−H···O angle equal to 169° (see Figure 3.6), now measuring 2.83 Å and 124°, respectively. As a consequence of these structural anomalies, the Pt@t-mtw−T5O10 is associated with a less pronounced increase in acidity, delta=−35 kJ mol^{-1}, compared to the cases collected in Figure 5.11.

Pt@t-bea-1*(a)−T1O4 and Pt@t-bea-1*(a)−T2O4

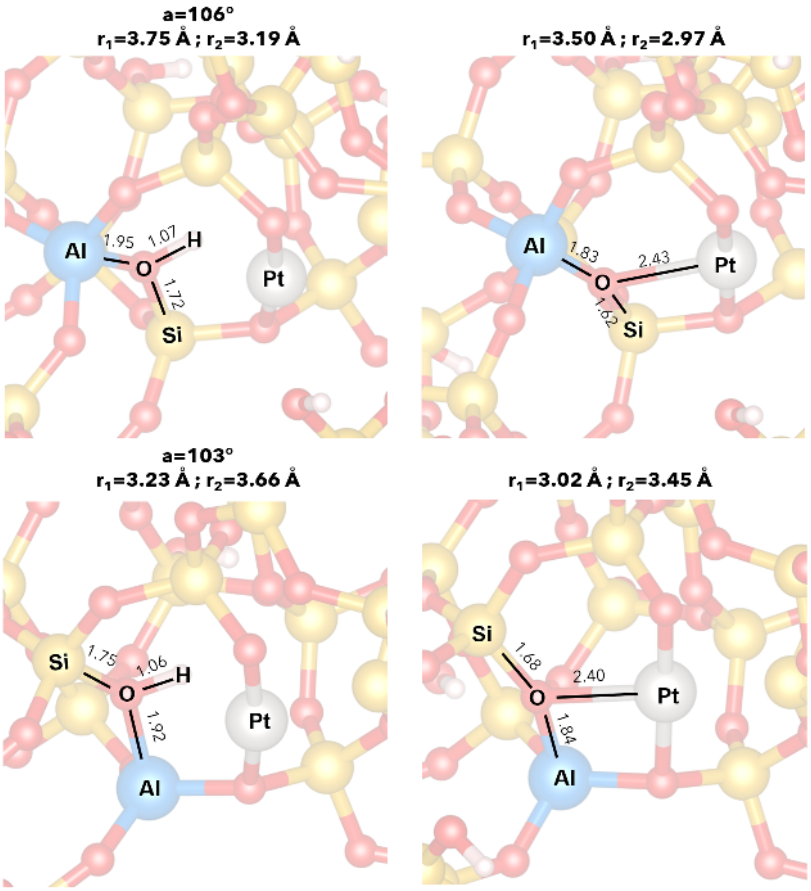

These two cases distinguish themselves from the others, and therefore, the non-alignment of their delta values is not surprising. The difference resides in the acidic oxygen atom, to which the hydrogen is bonded, that is not one of the two involved in the nearly linear O−Pt−O angle. Instead, it is a third oxygen atom, which was found at an interacting distance with the platinum atom in the Pt@t-bea-1*(a) structure and was consequently investigated, as already stated in the Models and Methods section. The delta values for these two structures were determined to be −52 and −61 kJ mol^{-1}, respectively, indicating a less

pronounced increase in acidity compared to the reference value of -100 mol^{-1}. Upon closer examination, these two structures reveal an acid hydrogen atom more directly oriented towards the platinum center and positioned closer to it. The O–H bond distance is slightly elongated compared to the typical value of 0.99 Å, and the H–Pt interatomic distance is significantly shorter, ranging from 1.91 to 1.93 Å, as opposed to the average of 2.50 Å for the other structures analyzed. The anionic forms do not exhibit significant distortions, with Al–O and Si–O distances essentially identical to those reported in Figure 5.11. Only the O–Pt distance is larger, but a comparison cannot be drawn homogeneously, because of the different environment of the involved oxygen atom, here not participating in the O–Pt–O interaction mode. The investigation of these two cases provides additional insights, especially considering that the same T1O4 and T2O4 acidic sites were also examined in the presence of a platinum atom located inside the t-bet cavity. Results revealed that the systems substantially differ, making it challenging to directly correlate changes in acidity to the platinum atom location. Apart from the O–Pt–O arrangement, the presence or not of hydrogen bonds also appears to be a contributing factor in determining differences going from one cavity to the other. Pristine T1O4 and T2O4 sites exhibited strong hydrogen bonds (see Figure 3.6), which persisted in Pt@t-bet structures with only slight changes in the O···H distances and O–H···O angles. Conversely, in the present two cases, these values deviate from the accepted range for a hydrogen bond. Therefore, while a greater proximity between the acid hydrogen and the platinum atom was observed, the less significant increase in acidity cannot be solely attributed to that, emphasizing the challenges in cumulatively interpreting these structures where multiple factors come into play.

Pt@t-bea-1*(a)–T7O7

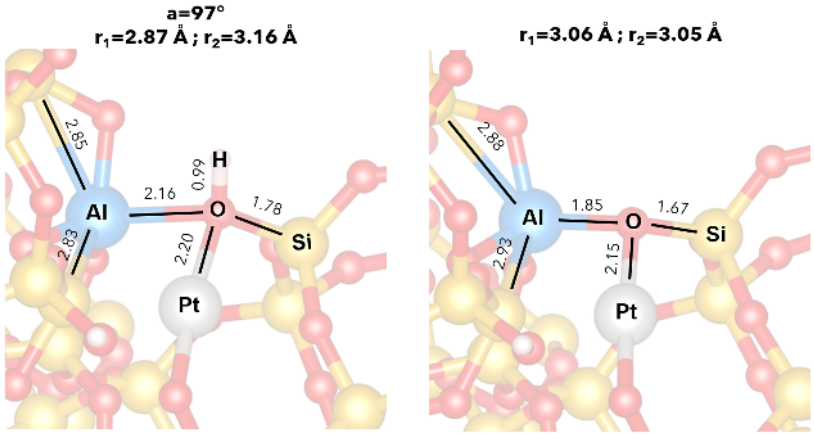

This case exhibits a platinum placement within a t-bea-1*(a) broken cavity that closely resembles what is observed in the pristine Pt@t-bea-1*(a). For instance, the O−Pt−O angle measures 174.2°, as opposed to 178.6°. However, both in the anion and in the neutral species, likely owing to this cavity rupture hence to the presence of platinum, unusually short Al−Si bonds are formed (2.83-2.93 Å instead of the typical 3.00-3.40 Å distances). The acidic hydrogen protruding into the main channel is maintained, with an Al−O_a−H angle of 97.4° instead of 106.3°. All things considered, even this case cannot be grouped with those reported in Figure 5.11 due to the mentioned structural anomalies, despite having a delta of −83 kJ mol^{-1}, which is quite close to that of the group.

Finally, it is pertinent to examine in detail the cases where a positive delta is observed, signifying a decreased acidity of the Al-H site with the introduction of the metallic functionality.

Pt@t-bea-1*(a)−T5O15

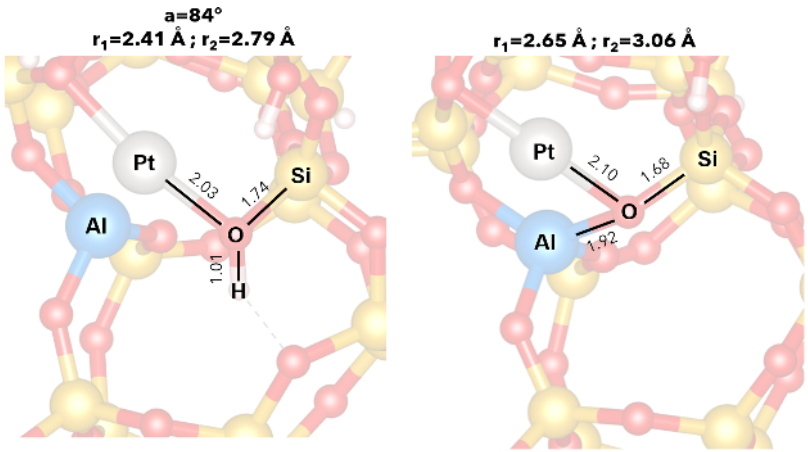

Compared to the same site in absence of the metal atom, the O−Si and O−H distances remain unchanged. However, while a single hydrogen bond was present in the T5O15 site (see Figure 3.6), another oxygen atom from the t-bea-1*(a) cavity is properly oriented for hydrogen bonding, resulting in the formation of two of these interactions. The O···H distances and O−H···O angles measure 1.66 Å, 148°, and 2.83 Å, 146°, respectively. The Al−O bond distance undergoes a substantial change, increasing from 1.93 Å to 3.28 Å and leading to a break in the zeolite structure and a significantly short Al−Pt distance (2.41 Å). This breakage was typical of the purely siliceous cavity with the embedded platinum atom. Notably, as for the anionic form, the opposite situation is realized: an unbroken framework is observed, in line with the anion of the T5O15 site, and the presence of Pt does not induce a break. A deviation from the cases showing a delta of nearly −100 kJ mol^{-1} is found in the Pt−H distance, which measures 2.76

Å, being hence greater than the mean value of 2.56 Å. These factors collectively result either in the destabilization of the anionic form and the stabilization of the neutral one, or just one of the two possibilities, anyhow leading to a consequential increase in the site deprotonation energy.

Pt@t-bea-1*(a)−T9O15

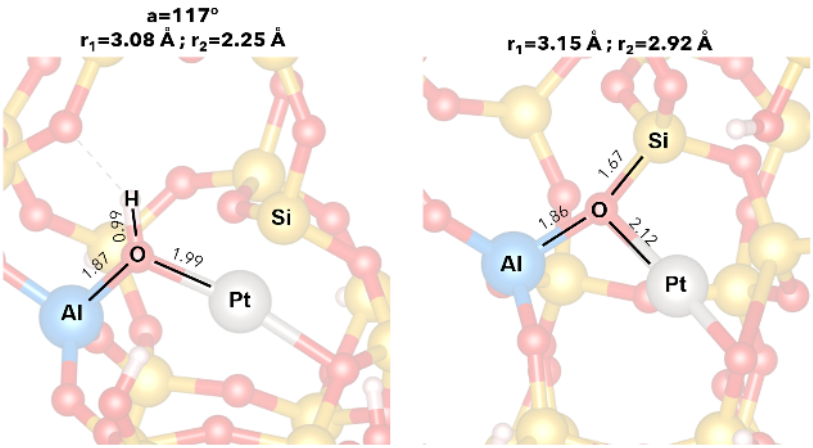

A similar scenario is observed here in comparison to the previous case. In the neutral form, there is a break in the t-bea-1*(a) cavity and the establishment of an H-bond with a O···H distance of 2.91 Å and a O−H···O angle of 151°, which was not detected in the T9O15 acidic site, where the O−H···O angle was found to be 81°. These two factors likely contribute to stabilizing the species, even if an incredibly short Si−Pt distance is observed. On the other hand, the anionic form, while featuring average Al−O, Si−O, and O−Pt bond distances, exhibits a notable distortion of the cavity to achieve the O−Pt−O linear arrangement, differently from both its neutral form and the Pt@t-bea-1*(a) system. All considered, it is not surprising that a positive delta of +47 kJ mol^{-1} is associated with this case.

Overall, a consistent trend in intrinsic acidity variation caused by the presence of an embedded Pt atom, as manifested in terms of differences in deprotonation energies (delta in Table 5.3), was not found among all 12 cases examined. There was also no observed dependence on Pt−H distances or other geometric parameters. With numerous variables at play, including distances and angles involving the acid hydrogen and other atoms, potential H-bond formation, Pt interactions with the hydrogen and oxygen atoms, and cavity breakage, identifying a clear trend or isolating a predominant factor is challenging if not unlikely. What was observed is that in most cases the presence of the metal led to an increase in site acidity, typically on the order of 100 kJ mol^{-1} in the deprotonation energy values. However, in two cases, a decrease (positive delta) was found, causing a

non-rigid shift in the relative rank of acidity among the 12 sites. A more in-depth analysis can be attempted on this matter.

Experimental results, as described in section 5.1.3, report a decrease in the number of strong Brønsted acidic sites, with the total number of sites either remaining unchanged or decreasing. Having the same μmoles per gram of catalysts of acidic sites could imply that strong and weak sites are transformed into medium-strength ones. This would explain the presence of data in both directions in Table 5.3, prompting a closer examination of the hypothesis. According to this interpretation, the strong T5O15 site (see Table 3.1) is expected to decrease in acidity, as it is showed by its delta value of +43 kJ mol^{-1}, conversely, the T7O7, considered one of the weakest Brønsted acidic sites by the cluster approach, should feature a decrease in acidity, yet it undergoes an increase (delta=-83 kJ mol^{-1}). Therefore, it can be argued that experimental evidence cannot be explained in terms of interactions between the two functionalities at the atomic level, neither the overall decrease in acidity triggered by the metal modification nor the alterations in strength, maintaining the same amount of acidic sites. This suggests the presence of additional influencing factors when exploring the impact of platinum centers on zeolite acidity. The assumption is however made under the condition that substantial differences in the two approaches do not hinder a flawless exchange of interpretative insights for the systems under examination.

Energetics of platinum atom embedding

In the preceding sections the primary focus was on investigating the effect related to the presence of a platinum atom on the intrinsic acidity of selected Brønsted sites within the β-zeolite. However, it is also interesting to consider, from the perspective of the metal center, the influence of an Al−H moiety in contrast to a purely siliceous framework. To explore this, in terms of the energetics hence the stability of a Pt atom embedded in a given cavity, δE values have been computed, according the following expression:

$$\delta E = E(Pt@Zeo_{Al-H}) - E(Zeo_{Al-H}) - E(Pt@Zeo_{Si}) + E(Zeo_{Si}) \qquad (5.1)$$

where the first term represents the energy of systems that exhibit both the acidic site and the platinum atom (the 12 studied cases), the second term corresponds to the energy of the zeolite framework in which a certain Si-Al substitution occurred, the third denotes the energy of systems featuring an embedded metal atom (inside a t-bet, t-mtw or t-bea-1* cavity), and the last is just the energy of the pristine unit cell of BEA, common to all cases. The employed energy values are those obtained from periodic SIESTA calculations, as no charged species are involved.

Table 5.4: δE values (kJ mol^{-1}), according to equation 5.1, for all the platinum-containing systems.

Cavity	Site	δE
Pt@t-bet	**T1O4**	+11
	T2O4	+38
Pt@t-mtw	**T3O10**	+58
	T5O10	+18
	T6O16	+40
	T8O16	+62
Pt@t-bea-1*(a)	**T1O4**	+17
	T2O4	-33
	T2O7	+2
	T5O15	-19
	T7O7	+30
	T9O15	-85

The results of these differences are presented in Table 5.4, where a negative value indicates that the situation with both a platinum atom and a specific TnOm site nearby is energetically favored compared to the case where Pt is incorporated into a siliceous β-zeolite structure.

Overall, positive values are observed, ranging from 2 to 62 kJ mol^{-1} in magnitude. Therefore, in almost all cases analyzed, it is energetically favored for the platinum atom to be located within a purely siliceous cavity rather than in proximity to an acidic site. The only exceptions are the Pt@t-bea-1*(a)−T2O4, T5O15, and T9O15 cases.

These findings refer to a situation in which an acid-to-metal ratio of one to one was modeled. It would correspond to a real system where the platinum center could result located either close to an acidic site or, thermodynamically preferred, within a siliceous portion. If more acidic zeolite structures are considered (higher Al/Si ratio), mimicked by performing more than one isomorphic substitution, it is likely that the platinum atom would find itself in any case interacting with Al-H moieties, constrained by spatial proximity. In this second scenario, varied correlations between the presence of metal sites and acidity could potentially exist, differing from what has been examined. Therefore, if there were indeed an effect exerted by platinum on the Brønsted acidity of bulk sites, it should be sought in these more acidic systems.

5.3 Conclusions

The metal-acid interactions in platinum-modified β-zeolite catalysts were explored from both experimental and atomistic perspectives, aiming at shedding light on the complex synergy between these functionalities.

Two methods, Evaporation Impregnation (EIM) and Incipient Wetness (IW), were utilized to prepare modified catalysts from H-Beta-38 and H-Beta-300. Various characterization techniques, including Scanning Electron Microscopy, Energy-Dispersive X-ray Microanalysis, Transmission Electron Microscopy (TEM), and Fourier Transform Infrared Spectroscopy (FTIR), were employed. The analysis revealed that the morphology the pristine zeolite framework remained unaltered by metal modification. TEM micrographs demonstrated the presence of platinum nanoparticles with similar size distributions for samples prepared via both impregnation methods, indicating incorporation predominantly on the surface rather than inside the main channels of BEA. Pyridine FTIR measurements, assessing the acidity features in Pt-modified and pristine H-Beta-300 materials, indicated a decrease in the amount of weak and strong Brønsted acidic sites in Pt-modified catalysts. Conversely, Lewis acidity increased, particularly for the EIM-prepared catalyst, aligning with literature findings attributing acidity variations to mutual interactions with the metallic component.

To investigate these interactions at an atomistic level, the impact of a single embedded platinum atom on the intrinsic acidity of selected Brønsted acidic sites was explored. Energy assessments were carried out to understand the influence of acidic sites on platinum stability. The results showed a general trend of increased acidity in the presence of the platinum atom, with deprotonation energy values typically decreasing by around -100 kJ mol^{-1}. However, two cases exhibited a positive difference, highlighting the challenges in isolating all the involved factors that affect these acidity changes. Regarding the energetics of platinum-embedded systems in aluminated versus siliceous frameworks, it was found to be energetically favored for the platinum atom to be located within a purely siliceous cavity in most cases.

Overall, it is suggested that, at least according to the atomic-level interaction of a single platinum atom with an inner acidic site, the intrinsic Brønsted acidity variation should go in the opposite direction of what is experimentally observed. The underlying reason may be of steric nature, attributable to the dimension of the metal center, which is a nanometric particle rather than a single atom in real systems. Notably, the more acidic sites, T8O11 and T7O7, feature an hydrogen atom that protrudes into the main channel. If the presence of a platinum particle

impede the accessibility of a pore, hindering the adsorption of the probe, the site will remain undisclosed by the FTIR technique, resulting in a decreased amount of acidic sites per gram of catalyst. Furthermore, considering the more likely placement of platinum particles, due to their size compared to zeolite channels, it is also conceivable that the acidic sites affected by modifications are those on the surface of the zeolite crystallites rather than internal sites within the bulk framework. Consequently, it is crucial to take into account the potential presence of silanols and other surface-related defects, which undoubtedly also influence acid-metal interactions.

In conclusion, the investigation provided valuable insights into the intricate relationship between platinum incorporation and zeolite acidity, serving as a methodologically sound preliminary exploration that could open avenues for future studies focused on different intimacy degrees and acid-to-metal ratios.

5.4 Acknowledgments

Part of the research presented in this chapter has been performed within the "Industrial Chemistry and Reaction Engineering" group of the Åbo Akademi University (FIN). I would like to gratefully acknowledge Professor Dmitry Yu. Murzin, all the research personnel, and Ph.D. Mark E. Martínez-Klimov in particular.

Mimicking alkene isomerization

The present chapter reports an atomistic investigation that outlines the energy barriers and the intermediates along the path for the isomerization of *n*-pent-2-ene to *iso*-pent-2-ene (2-methyl-2-butene). This is the second step within a hydroisomerization process and takes place on a Brønsted acidic site of the zeolite, after *n*-pentane was dehydrogenated by the metallic functionality.

Pentene was chosen as a model of small molecules that could form a cyclopropene-like species, whose nature (transition state or intermediate) is debated in literature. This is addressed in the following, albeit not in a conclusive way, on just a single selected Brønsted acidic site, to provide an example of catalytic application of the modeled zeolitic catalyst.

6.1 Models and Methods

The T7O7 Brønsted site was chosen, as representative of the most acidic sites according to the proposed cluster approach, and at the same time accessible to reacting molecules, since it protrudes on the main 12T channel of the zeolite framework.

Periodic calculations within the SIESTA formalism were performed, in case of geometry optimizations of minima (adsorbed reactant, product and intermediates) by using the same calculation parameters already employed for the catalyst modeling phase (see sections 3.1 and 4.1). Interaction energies for adsorbed species were evaluated as the difference between the energy of the whole system and the energies of its constituents, not accounting for the Basis Set Superposition Error (BSSE). In the search for transition states, every NEB calculation used 6 images, generated by the image dependent pair potential approach and connected each other by dynamic springs. The FIRE algorithm was employed to optimize the elastic band, with a convergence threshold of 3×10^{-3} $E_h/Å$ on the norm of NEB total forces. A 1×1×1 Monkhorst-Pack grid was used, that allowed to reduce the calculation time without significant differences with respect to the

2×2×2 grid used for minima.

To determine the nature (minima or transition state) of the structures identified in this investigation, phononic mode calculations were performed using the SIESTA program. Since the zeolite is chemically an oxide, these calculations were carried out without fixing any nucleus of the structure — a strategy commonly applied, for example, in case of metal-organic systems, to reduce computation time — given that the nuclei of the crystalline structure and those of the adsorbed organic species have comparable mass. It was ensured, therefore, that no phononic mode was associated with a negative eigenvalue in the case of a minimum and that precisely one phononic mode with a negative eigenvalue was present in the case of a transition state, disregarding additional negative eigenvalues if they were very close to zero. Finally, for each transition state, the vibration associated with the negative eigenvalue was visualized to confirm that the structure truly represented the transition state relative to the considered step.
The energetics of the reaction will be given in terms of vibrational zero-point corrected energy.

6.2 Results and Discussion

Firstly the adsorption of 2-pentene was investigated, finding that it physically adsorbs on the Brønsted T7O7 site via a π interaction between the acid proton and the C−C double bond. The resulting species, named **1**, features an interaction energy that was computed to be 96.2 kJ mol^{-1}, not considering BSSE correction.

Details on the selected geometrical parameters (bond distances and angles) for both the adduct and the isolated structures are reported in Table 6.2. The labels there used to indicate the carbon atoms (C_1-C_5), the zeolitic acid hydrogen (H_z) and the aluminum-bonded O of interest (O_b) other than the one involved in the acidic portion (O_a) are introduced in Figure 6.1 and will be maintained throughout. Please note that in case of isolated and adsorbed dimethyl-cyclopropane and *iso*-pentene a convenient choice was made for labeling, to keep track of the skeletal isomerization process (see Figure 6.1).

The O_a−H_z bond distance of the zeolite slightly elongates from 0.99 to 1.05 Å in the adduct, and the corresponding O_a−Al−O_b angle increases by 2.1° (from 90.7 to 92.8°), whereas the Al−O_a−Si angle decreases by 8.3°. The greatest structural deviation is found in the Al−O_a−Si angle, changing from 106.3° to 114.0°. The C−C double bond distance is instead almost unchanged, being 1.36 Å in the isolated reactant and 1.38 Å in the adduct.

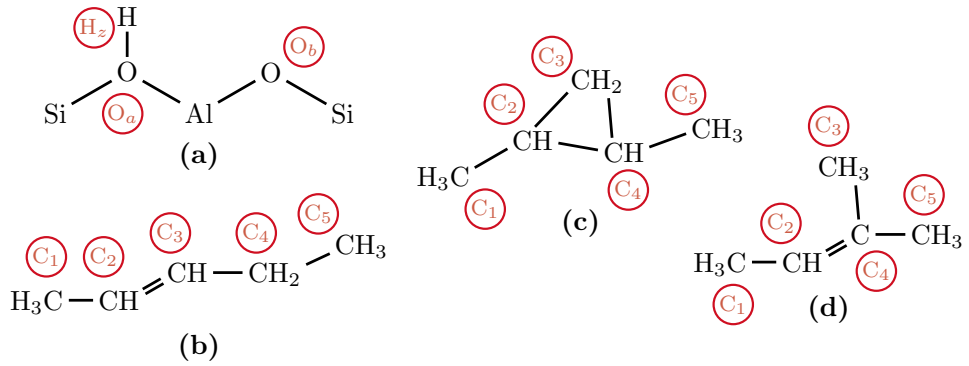

Figure 6.1: The labels used to indicate the zeolitic acid hydrogen (H_z) and the aluminum-bonded O of interest (O_b) other than the one involved in the acidic portion (O_a) are given for the zeolite framework (a). Carbon atom numbers, from C_1 to C_5, of isolated (and adsorbed, not shown) dimethylcyclopropane (c) and *iso*-pentene, (d), are assigned homogeneously with respect to the isolated *n*-pentene species (b), to keep track of the skeletal isomerization process.

The Brønsted proton of the acidic site is essentially equidistant from both the C_2 and C_3 atoms ($C_2 \cdots H_z$ = 1.92 Å; $C_3 \cdots H_z$ = 1.93 Å).

After 2-pentene is adsorbed on the zeolite, it undergoes isomerization according to the proposed reaction path that is depicted in Figure 6.2, involving 5 intermediates (**2a, 2b, 3a, 3b, 4**) and 4 energy barriers associated to transition states. Being one of the potential mechanisms proposed in literature, as outlined in the introduction of this thesis, it can be summarized as follows: 1) protonation of the double bond, leading to the formation of an alkoxy species; 2) proton backdonation to the zeolite framework, inducing the closure of the hydrocarbon into a substituted cyclopropane; 3) ring opening through the breakage of a different bond, resulting in a secondary *iso*-alkoxide ; 4) proton backdonation to the zeolite, restoring the Brønsted acidic site and generating the *iso*-olefin. A detailed description of each passage is given in the following.

In the first step, the acid hydrogen atom, H_z, is transferred to C_3, with an energy barrier equal to 34.5 kJ mol^{-1}, forming the alkoxide intermediate labeled as **2a**, where the hydrocarbon is covalently bonded to the framework O_b atom ($C_2 - O_b$ bond distance equal to 1.56 Å). Notably, this is a standard value for a C–O bond in alkoxides [45].

The optimized structure of the transition state shows the expected changes in the hydrocarbon C–C bond distances, going in the direction of a disappearance of the double bond. The H_z is found to be 1.17 Å apart from the C_3 and the C_2 carbon atom is placed at 2.61 Å from the O_b oxygen. Geometrical features

Table 6.1: Relevant interatomic distances and bond angles for the alkoxide-zeolite systems involved in the 2-pentene isomerization pathway.

	2a	**2b**	**4**
		Distances/Å	
$\mathbf{C_1-C_2}$	1.52	1.52	1.53
$\mathbf{C_2-C_3}$	1.53	1.54	-
$\mathbf{C_3-C_4}$	1.54	1.54	1.55
$\mathbf{C_4-C_5}$	1.54	1.54	1.54
$\mathbf{C_2-C_4}$	-	-	1.54
$\mathbf{C_2-O_b}$	1.56	1.57	1.56
$\mathbf{Al-O_a}$	1.75	1.75	1.75
$\mathbf{Al-O_b}$	1.94	1.95	1.94
$\mathbf{Si-O_a}$	1.62	1.62	1.62
		Angles/°	
$\mathbf{C_2-O_b-Al}$	119.9	123.9	119.5
$\mathbf{O_a-Al-O_b}$	105.7	107.1	105.3
$\mathbf{Al-O_a-Si}$	145.0	143.1	144.9

for the **2a** species, and for all the other alkoxide-like intermediates, are reported in Table 6.1. Incidentally, in the eventuality of a hydrogen (H_z) attack on the C_2 atom instead of C_3, a secondary carbocation would invariably be implicated as a transition state. While this represents a possibility, it does not alter the subsequent course of the reaction since the ramification would reconnect to the same intermediate, as long as the cyclic species is formed.

The **2a** system is nearly 20 kJ mol^{-1} more stable than the reactant, taken as reference for the energetic scale. A barrier-free rearrangement, indicated with the ρ letter inside a blue circle in Figure 6.2 is assumed to transform it to the slightly less stable **2b**, that has the correct orientation to react and afterwards gives the substituted cyclopropane species adsorbed on BEA named **3a**. Geometrical features related to the latter, and to all the other neutral molecule-zeolite systems, are reported in Table 6.2 in comparison with the same distances and angles characterizing the isolated reactant, product, dimethyl-cyclopropane and the T7O7 site. The **2b** $\rightarrow$ **3a** elementary step is further detailed in Figure 6.3, where the associated NEB profile is shown together with a schematic depiction. Contributing to an overall energy barrier of 55.7 kJ mol^{-1}, two transition states and an intermediate species were identified by the NEB algorithm. The first transition state, whose image is reported in Figure 6.2, features a carbocation nature and corresponds to the C_2-O_b bond cleavage, the related interatomic distance becoming equal to 2.88 Å.

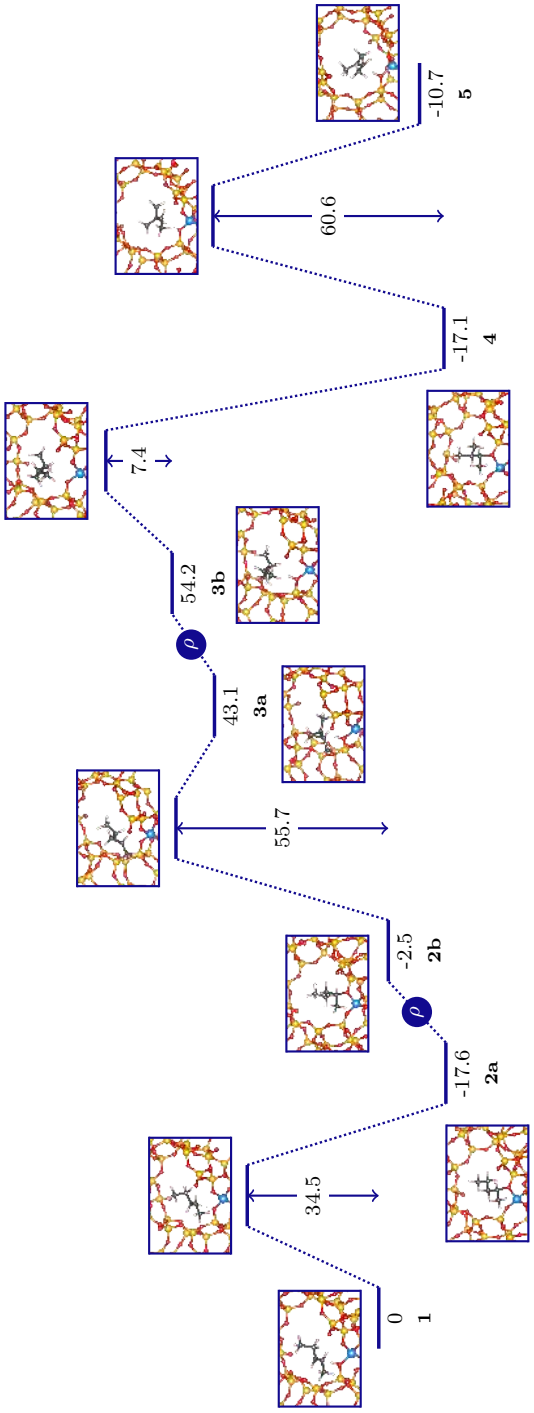

Figure 6.2: Reaction profile of the *n*-pentene isomerization to *iso*-pentene (2-methyl-2-butene), occurring on the T7O7 Brønsted acidic site of BEA. Vibrational zero-point corrected energies of the starting reactants, minima and final products are relative to that of **1**, taken as reference, while the energy barriers are calculated with respect to the energies of the species preceding the corresponding transition states. All values are expressed in kJ mol^{-1}. The ρ letters inside the blue circles indicate barrier-free rearrangements. Si=yellow, O=red, Al=blue, C=grey, H=pink.

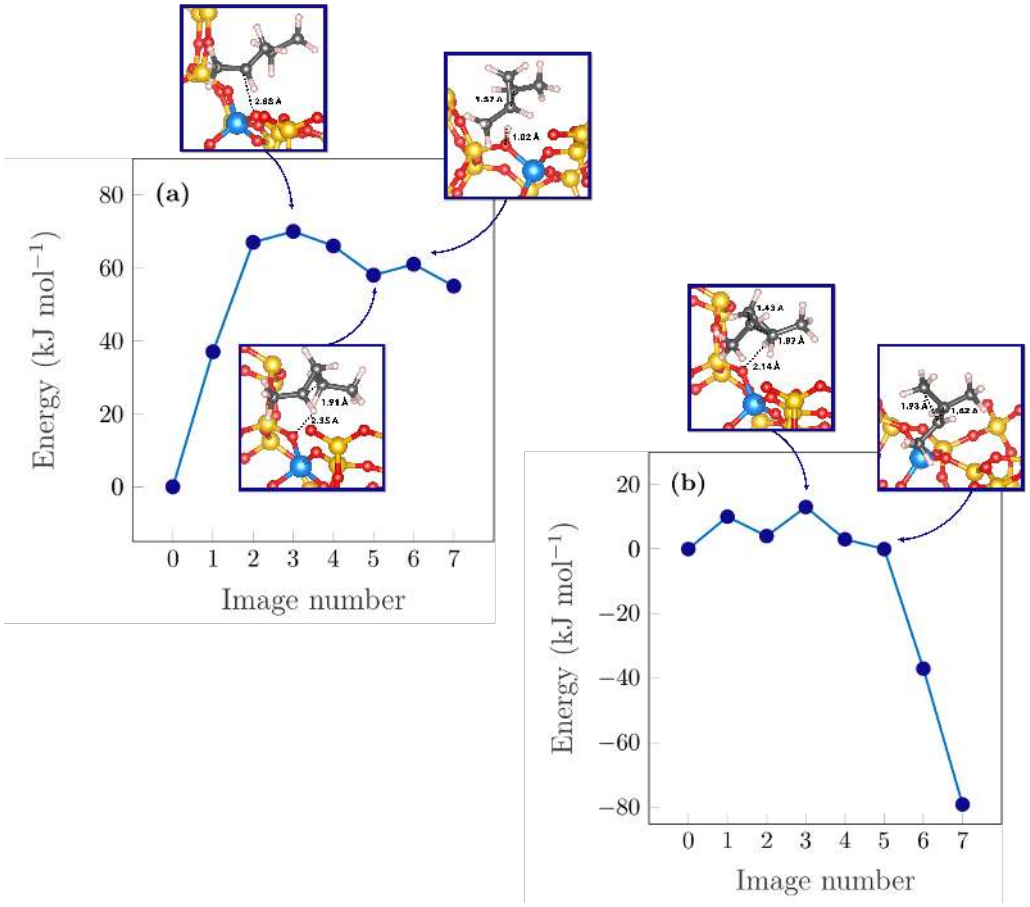

Figure 6.3: CI-NEB profiles for the elementary steps connecting: (a) species **2b** to **3a** and (b) species **3b** to **4**. Insights of the most significant structures with the relevant interatomic distances are given.

Table 6.2: Relevant interatomic distances and bond angles for the neutral molecule-zeolite systems involved in the 2-pentene isomerization pathway and for isolated significant species.

Distances/Å	**1**	**3a**	**3b**	**5**	**T7O7-BEA**	***n*-pentene**	**DMCP**	***iso*-pentene**
$\mathbf{C_1-C_2}$	1.51	1.53	1.52	1.51	–	1.51	1.52	1.51
$\mathbf{C_2-C_3}$	1.38	1.52	1.53	n.b.	–	1.36	1.53	–
$\mathbf{C_3-C_4}$	1.52	1.53	1.54	1.52	–	1.51	1.53	1.52
$\mathbf{C_4-C_5}$	1.54	1.53	1.52	1.52	–	1.54	1.52	1.52
$\mathbf{C_2-C_4}$	-	1.58	1.53	1.38	–	-	1.53	1.37
$\mathbf{O_a-H_z}$	1.05	1.03	0.99	1.05	0.99	–	–	–
$\mathbf{H_z-C_2}$	1.92	2.06	3.70	1.83	–	–	–	–
$\mathbf{H_z-C_3}$	1.93	3.08	2.73	3.31	–	–	–	–
$\mathbf{H_z-C_4}$	2.74	1.89	2.73	2.22	–	–	–	–
$\mathbf{Al-O_a}$	1.90	1.90	1.92	1.91	1.94	–	–	–
$\mathbf{Al-O_b}$	1.75	1.75	1.75	1.72	1.76	–	–	–
$\mathbf{Si-O_a}$	1.70	1.71	1.72	1.71	1.74	–	–	–
Angles/°								
$\mathbf{Al-O_a-H}$	114.0	114.1	113.9	114.2	106.3	–	–	–
$\mathbf{O_a-Al-O_b}$	92.8	94.4	91.8	98.7	90.7	–	–	–
$\mathbf{Al-O_a-Si}$	128.9	128.5	130.4	130.0	137.2	–	–	–

After the proper orientation is reached between one H atom of the C_4 and the zeolitic O_a (distance of 1.91 Å), the hydrogen shift takes place together with the formation of the C_2-C_4 bond, involving a second transition state with a direct energy barrier of 2.5 kJ mol^{-1} (backward 5.8 kJ mol^{-1}). As a result, the adduct between dimethyl-cyclopropane and the zeolite framework, **3a**, is obtained featuring an interaction energy equal to 67.2 kJ mol^{-1}.

This would suggest the adsorbed DMCP to be a rather unstable ephemeral intermediate within the 2-pentene isomerization patwhay. It was indeed characterized as a minima in the potential energy surface, showing a relative energy of +43.1 kJ mol^{-1}. As indicated by the negligible backward barrier, it is likely to undergo hydrogenation, on a –CH group. Therefore, the present findings support the conclusions drawn in the DFT investigation by Demuth *et al.* [40] regarding the isomerization of 2-pentene within H-ZSM-22, while other studies suggest the involvement of protonated cyclopropene-like species as a transition state in the mechanism [19].

Then, after a barrier-free rearrangement connecting **3a** to **3b**, the H_z acidic proton attacks the –CH– moiety of C_4 with an associated energy barrier of 7.4 kJ mol^{-1} (transition state shown in Figure 6.2). The hydrogen atom then follows a non-activated intramolecular shift, to the C_3 carbon atom, and the simultaneous C_2-C_3 bond cleavage leads to the ring opening (see Figure 6.3),

with the formation of the *iso*-pentoxide species, **4**. The NEB profile for this step is reported Figure 6.3, showing also some insights on the geometrical features that characterize the most significant structures involved.

The *iso*-pentoxide is just slightly more stable than the **2a** species and, as it is evident from Table 6.1, exhibits essentially the same structural parameters (such as the C_2-O_b bond distance and zeolite-related distances and angles). The significant distinction lies in the branched versus linear carbon skeletal structure. The isomerization process has reached its final elementary step: by overcoming an energy barrier of 60.6 kJ mol^{-1}, the hydrogen atom bonded to C_4 is backdonated to O_a, restoring the catalytic T7O7 site and resulting in the formation of the adduct between *iso*-pentene and the zeolite. This is found to be 10.7 kJ mol^{-1} more stable in energy than the reactant, with an interaction energy of 92.4 kJ mol^{-1}, without BSSE.

6.3 Conclusions

A DFT analysis was performed to investigate the transformation of *n*-pent-2-ene to *iso*-pent-2-ene occurring on the T7O7 Brønsted acidic site of β-zeolite, as part of a hydroisomerization process. Periodic calculations within the SIESTA formalism were carried out, allowing for detailed descriptions of each step, in terms of optimized geometries of all the involved species, energetics and transition state characteristics.

The proposed mechanism encompasses the following steps: i) protonation of the double bond, leading to the formation of an alkoxy species; ii) proton backdonation to the zeolite framework; iii) ring opening through the breakage of a different bond and iv) proton backdonation to the zeolite, generating the *iso*-olefin and restoring the catalytic site. All associated energy barriers are below 65 kJ mol^{-1}, with the highest ones being those related to the second and fourth steps. Notably, the study suggests the involvement of dimethyl-cyclopropane as a potentially unstable intermediate within the isomerization pathway, contributing to the ongoing debate in the literature regarding the nature of this cyclic species.

The results offer valuable insights into the molecular-level details of zeolitic catalysis in this specific hydroisomerization process. However, further research may be necessary for a comprehensive exploration of catalytic applications and reaction pathways. For example, the mechanism should also be tested on less acidic sites and in the presence of metallic functionality, to assess the effects on the structures of transition states and energy barriers, or even the occurence of other parasitic reactions. To gain a more comprehensive understanding, it would be beneficial to investigate the effects of varying the length of the hydrocarbon chain as well.

Conclusions and Afterwards

A platinum-modified β-zeolite was investigated as a catalytic material for hydroisomerization reactions of hydrocarbons, requiring both an acidic substrate and a hydrogenation/dehydrogenation function. The nature and properties of the active sites were examined independently, laying the groundwork for understanding the effects of their interactions. Quantum chemistry models, particularly those based on density functional theory (DFT), served as the primary tools in this exploration. The study contributed to the ongoing scientific discourse, focusing on the evaluation of zeolite acidity and the stability of molecular-sized platinum clusters within framework cavities. It established robust methodological foundations and proposed innovative computational approaches readily applicable in future investigations.

Furthermore, the research extended into the realm of experimental catalysis through a close collaboration with the Finnish "Industrial Chemistry and Reaction Engineering" group at Åbo Akademi University. Indeed, the role of platinum species in altering material acidity was analyzed by integrating computational and experimental perspectives, thus enhancing the depth of examination and providing a richer understanding.

As a logical progression in catalyst modeling, the performance testing was conducted for a small hydrocarbon, albeit not comprehensively, simulating the mechanism of the conversion from a linear to a branched chain occurring on the acidic functionality. This marked the initial exploration of an area with immense potential for future research endeavors.

In accordance with this workflow, a concluding overview of the findings and potential developments of the present thesis is here provided. It is however recalled that more detailed conclusions, along with specific results, can be found at the end of each chapter composing the dissertation.

Firstly, the intrinsic Brønsted acidity of β-zeolite has been examined by evaluating the deprotonation energy (DPE) values for 30 topologically distinct acidic sites within the DFT framework. Three different approaches were used, referred

to as ONIOM, SIESTA, and cluster. The cluster approach, specifically designed to overcome drawbacks associated with the other two, has been proposed as a suitable algorithmic tool to correct DPE values obtained from periodic calculations. In this method, an appropiately reshaped zeolite cell, whose geometry was optimized via the SIESTA paradigm, serves as input for non-periodic single-point DFT calculations. Forthcoming advances on this regard may focus on enhancing the definition of the reshaped portion, for an even more accurate treatment of each individual acidic site. It is worth to emphasize the transferability of the proposed procedure as a modeling tool. For future investigations, it would enable to treat essentially in the same modelistic way the zeolite acidic sites, possible modifiers of the acidity strength (such as defects or embedded metal particles) and the reactions involving zeolite catalytic activity.

The second part of the study delved into the preferential location and energetics associated with the migration of platinum atoms embedded in the framework of β-zeolite, using an unbiased periodic DFT calculation approach. The primary factors determining the stability of these systems were identified, including the formation of linear O−Pt−O units intimately related to framework breakage, Pt−Pt distance, and cluster geometry. Up to the Pt_3 seed that was studied, an energetic preference for growth was observed. It could prove intriguing, as further advances, to address the exploration of growth energetics, as well as for the pristine zeolite framework already considered, also in the presence of acidic sites.

The third section of this dissertation involved experimental and atomistic exploration of metal-acid interactions in platinum-modified β-zeolite catalysts. Pyridine-FTIR measurements were employed to assess the Brønsted and Lewis acidity of both pristine and modified catalytic materials. From an atomistic viewpoint, the influence of a single embedded platinum atom on the deprotonation energy of selected Brønsted acidic sites was examined. Since the intrinsic acidity variation in the presence of a metal center deviated from the observed experimental trends, it was suggested that the experimental evidence regarding the effects of metal on acidity cannot be solely explained by atomic-level interactions between the two functionalities. Other influencing factors should be considered, possibly associated to the dimensions of the metal particles in relation to zeolite channels and their positioning on the outer surface of zeolite crystals, where the potential presence of silanols and other surface-related defects may also play a role.

Finally, the reaction mechanism for the isomerization of *n*-pent-2-ene to *iso*-pent-2-ene on the T7O7 Brønsted acidic site was characterized in terms of elementary steps. This served as a preliminary exploration of structural conversion

processes, representing a potential catalytic application of the simulated zeolite-based catalyst. It is evident that there is room for several future investigations. For instance, different acidic sites could be examined, varying the carbon chain length, and also considering steps involving metallic sites. Both functionalities simultaneously playing an active role may give rise to other parasitic reactions, such as cracking, which should be taken into consideration for a more comprehensive understanding of these processes.

Additional data and images

Project: 2023-05-17

H-Beta-38 calcined 30x (1)

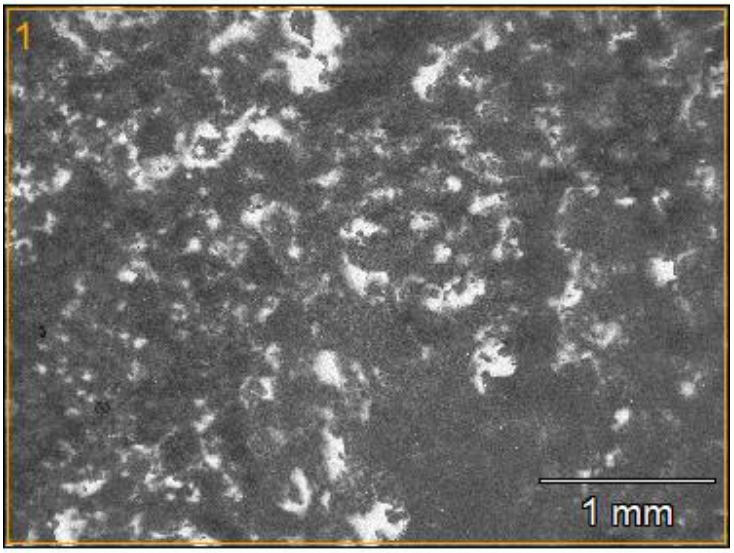

Image Name:	H-Beta-38 calcined 30x (1)
Image Resolution:	1024 by 768
Image Pixel Size:	4.06 µm
Acc. Voltage:	20.0 kV
Magnification:	30

Full scale counts: 15990
Integral Counts: 300739

H-Beta-38 calcined 30x (1)_pt1

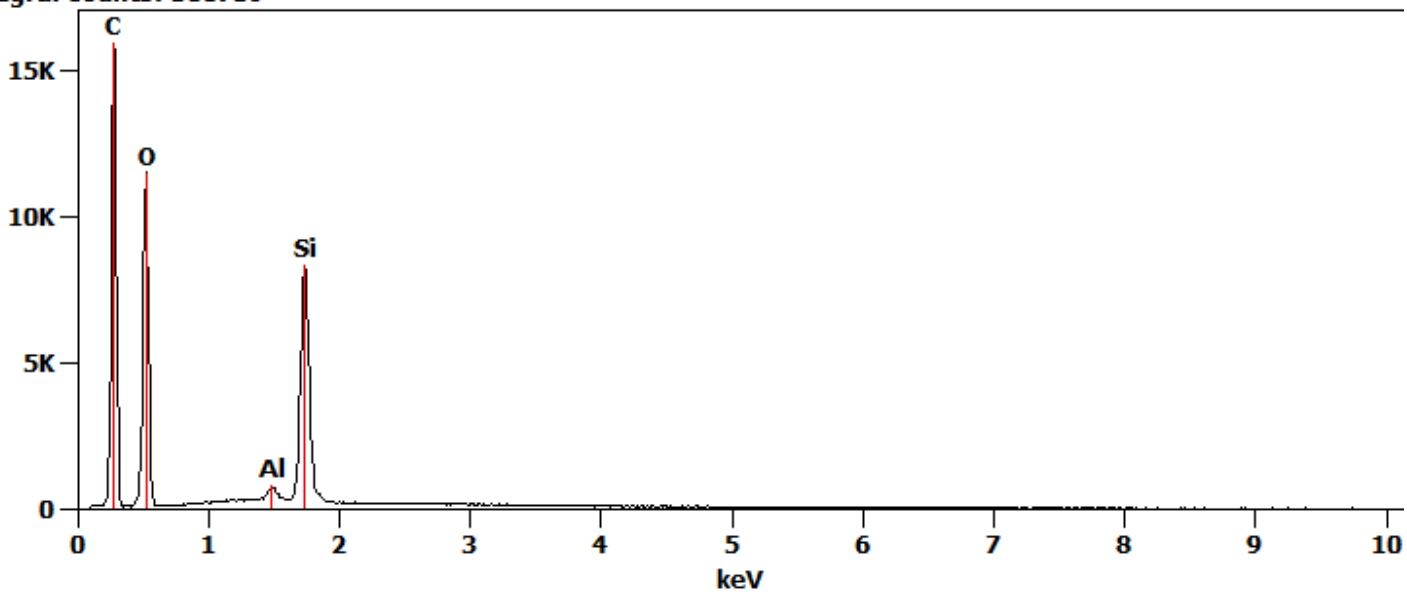

Project: 2023-05-17

Weight %

	O	Al	Si
H-Beta-38 calcined 30x (1)_pt1	52.95S	2.62	44.43

Weight % Error (+/- 1 Sigma)

	O	Al	Si
H-Beta-38 calcined 30x (1)_pt1	±0.33	±0.13	±0.25

Atom %

	O	Al	Si
H-Beta-38 calcined 30x (1)_pt1	66.34	1.95	31.71

Atom % Error (+/- 1 Sigma)

	O	Al	Si
H-Beta-38 calcined 30x (1)_pt1	±0.41	±0.09	±0.18

Formula

	O	Al	Si
H-Beta-38 calcined 30x (1)_pt1		Al2O3	SiO2

Compound %

		Al2O3	SiO2
H-Beta-38 calcined 30x (1)_pt1	0.00	4.96	95.04

Project: 2023-05-17

Pt-H-Beta-38-EIM reduced 30x (1)

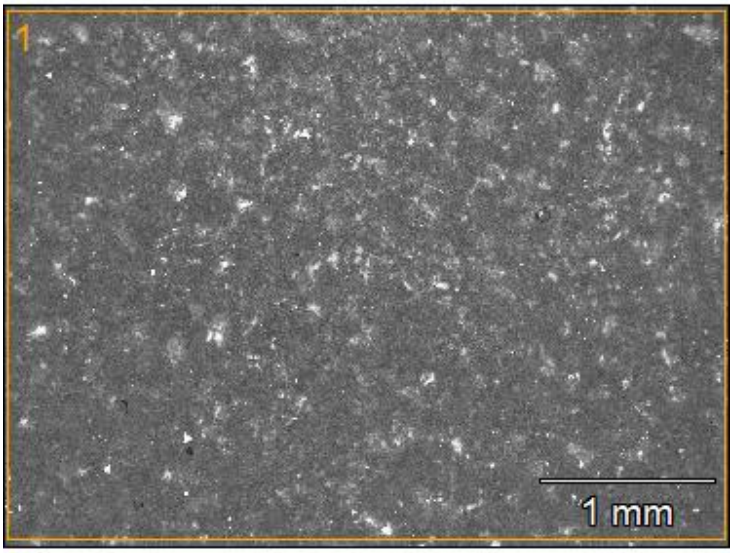

Image Name:	Pt-H-Beta-38-EIM reduced 30x (1)
Image Resolution:	1024 by 768
Image Pixel Size:	4.06 µm
Acc. Voltage:	20.0 kV
Magnification:	30

Full scale counts: 44898
Integral Counts: 580495

Pt-H-Beta-38-EIM reduced 30x (1)_pt1

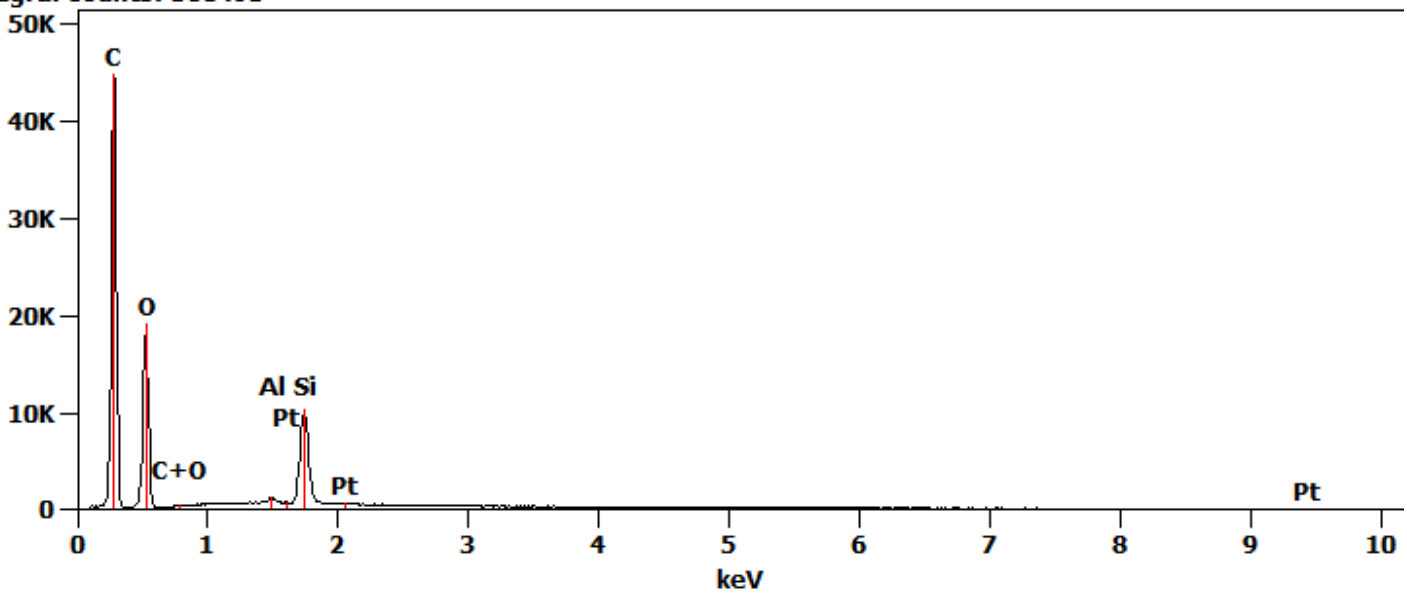

Project: 2023-05-17

Weight %

	O	Al	Si	Pt
Pt-H-Beta-38-EIM reduced 30x (1)_pt1	52.13S	2.76	43.61	1.50

Weight % Error (+/- 1 Sigma)

	O	Al	Si	Pt
Pt-H-Beta-38-EIM reduced 30x (1)_pt1	±0.30	±0.14	±0.25	±0.32

Atom %

	O	Al	Si	Pt
Pt-H-Beta-38-EIM reduced 30x (1)_pt1	66.22	2.08	31.55	0.16

Atom % Error (+/- 1 Sigma)

	O	Al	Si	Pt
Pt-H-Beta-38-EIM reduced 30x (1)_pt1	±0.38	±0.10	±0.18	±0.03

Formula

	O	Al	Si	Pt
Pt-H-Beta-38-EIM reduced 30x (1)_pt1		Al2O3	SiO2	Pt

Compound %

		Al2O3	SiO2	Pt
Pt-H-Beta-38-EIM reduced 30x (1)_pt1	0.00	5.21	93.29	1.50

Project: 2023-05-17

Pt-H-Beta-38-IW reduced 30x (1)

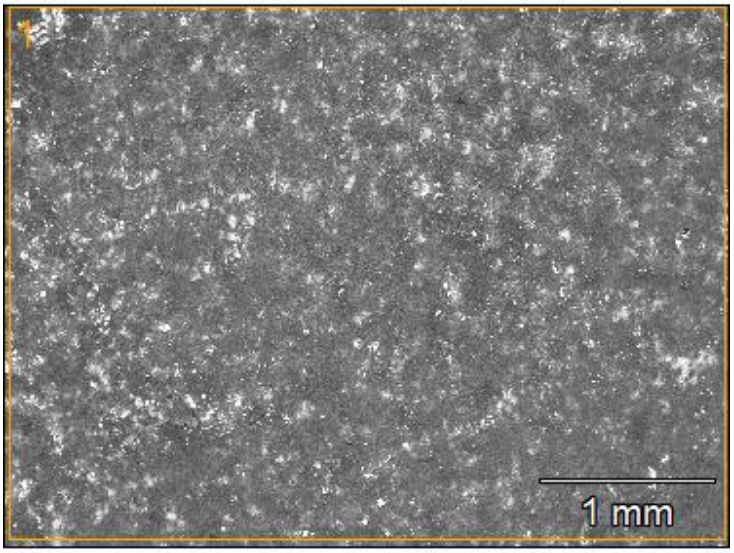

Image Name:	Pt-H-Beta-38-IW reduced 30x (1)
Image Resolution:	1024 by 768
Image Pixel Size:	4.06 µm
Acc. Voltage:	20.0 kV
Magnification:	30

Full scale counts: 12849
Integral Counts: 287464

Pt-H-Beta-38-IW reduced 30x (1)_pt1

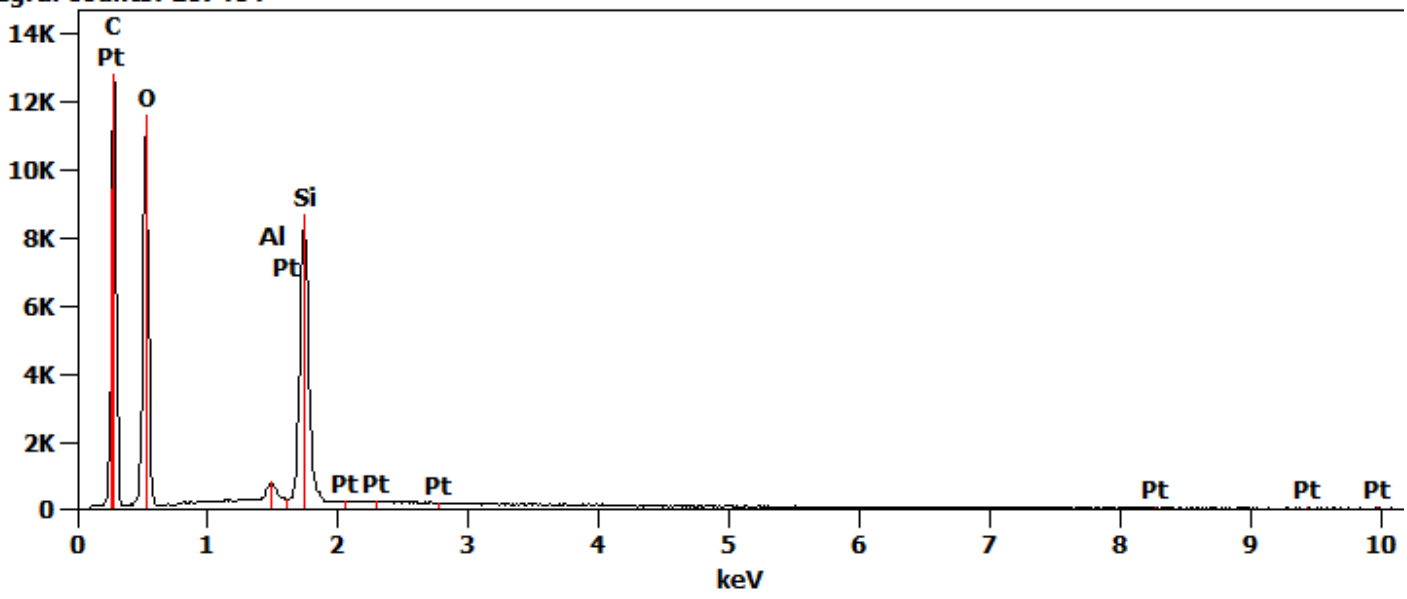

Project: 2023-05-17

Weight %

	O	Al	Si	Pt
Pt-H-Beta-38-IW reduced 30x (1)_pt1	52.42S	2.59	43.99	1.00

Weight % Error (+/- 1 Sigma)

	O	Al	Si	Pt
Pt-H-Beta-38-IW reduced 30x (1)_pt1	±0.32	±0.12	±0.24	±0.26

Atom %

	O	Al	Si	Pt
Pt-H-Beta-38-IW reduced 30x (1)_pt1	66.27	1.94	31.68	0.10

Atom % Error (+/- 1 Sigma)

	O	Al	Si	Pt
Pt-H-Beta-38-IW reduced 30x (1)_pt1	±0.41	±0.09	±0.18	±0.03

Formula

	O	Al	Si	Pt
Pt-H-Beta-38-IW reduced 30x (1)_pt1		Al2O3	SiO2	Pt

Compound %

		Al2O3	SiO2	Pt
Pt-H-Beta-38-IW reduced 30x (1)_pt1	0.00	4.89	94.11	1.00

Project: 2023-05-10

H-Beta-300 calcined 30x (1)

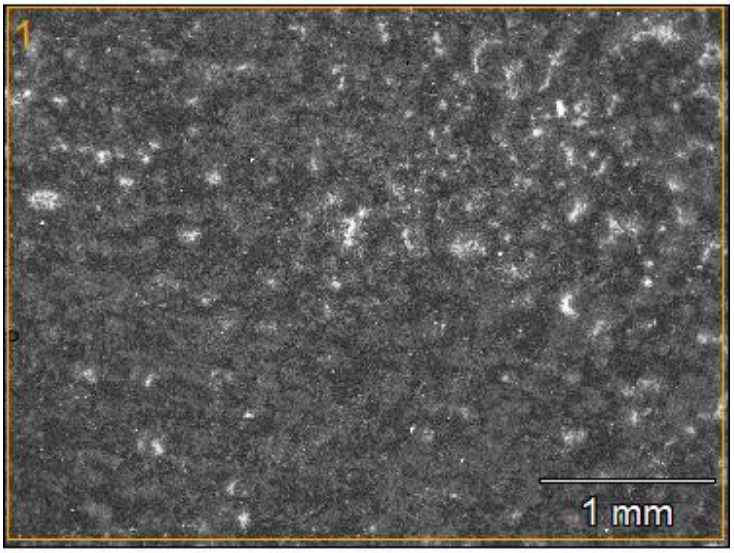

Image Name:	H-Beta-300 calcined 30x (1)
Image Resolution:	1024 by 768
Image Pixel Size:	4.06 µm
Acc. Voltage:	20.0 kV
Magnification:	30

Full scale counts: 27717 **H-Beta-300 calcined 30x (1)_pt1**
Integral Counts: 307824

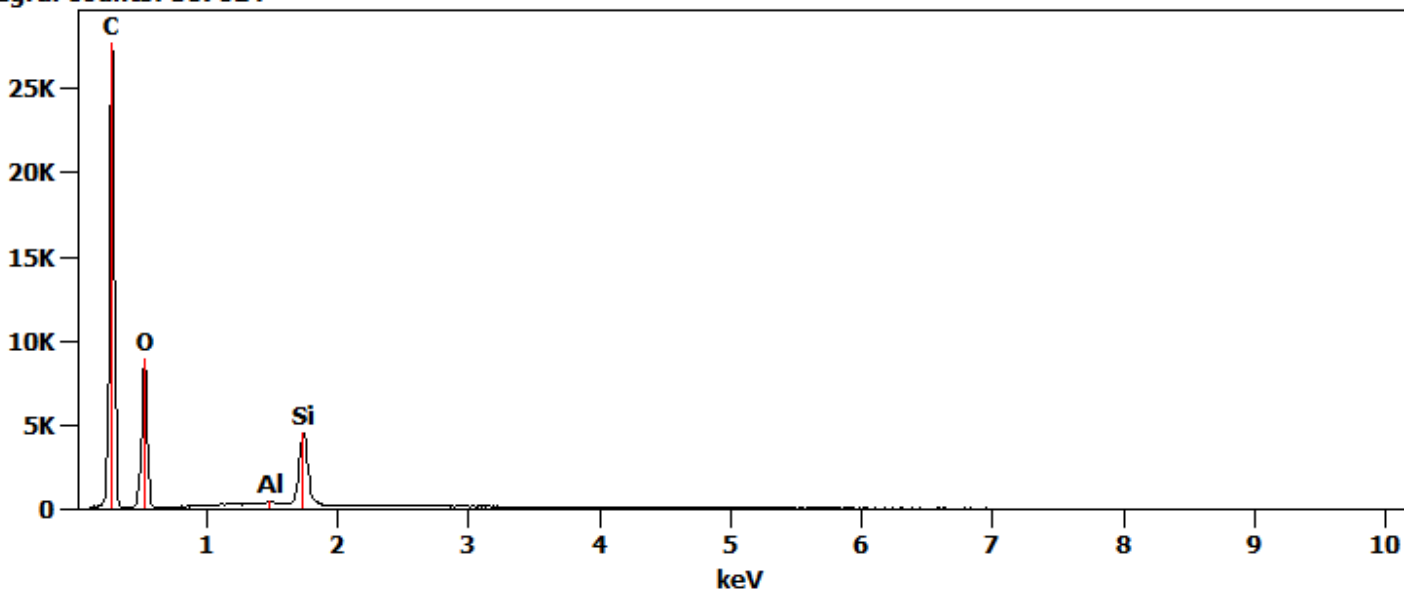

Project: 2023-05-10

Weight %

	O	Al	Si
H-Beta-300 calcined 30x (1)_pt1	53.12S	1.14	45.74

Weight % Error (+/- 1 Sigma)

	O	Al	Si
H-Beta-300 calcined 30x (1)_pt1	±0.36	±0.12	±0.33

Atom %

	O	Al	Si
H-Beta-300 calcined 30x (1)_pt1	66.53	0.85	32.63

Atom % Error (+/- 1 Sigma)

	O	Al	Si
H-Beta-300 calcined 30x (1)_pt1	±0.45	±0.09	±0.24

Formula

	O	Al	Si
H-Beta-300 calcined 30x (1)_pt1		Al2O3	SiO2

Compound %

		Al2O3	SiO2
H-Beta-300 calcined 30x (1)_pt1	0.00	2.15	97.85

Project: 2023-05-10

Pt-H-Beta-300-EIM reduced 30x (1)

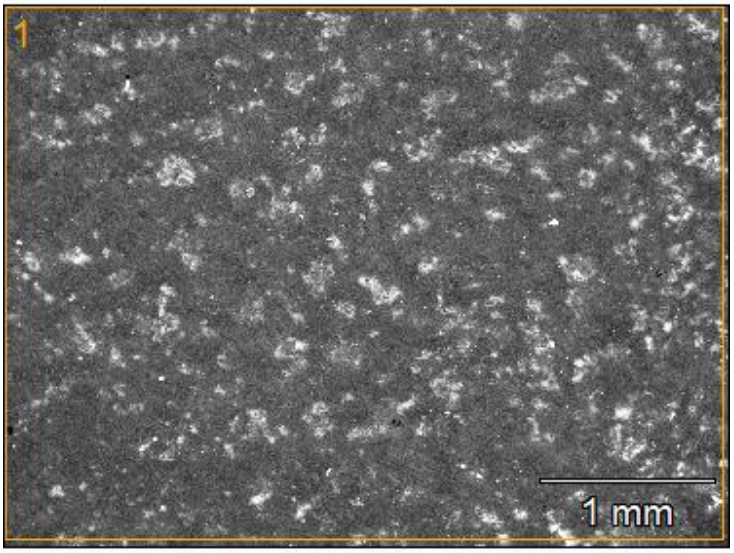

Image Name:	Pt-H-Beta-300-EIM reduced 30x (1)
Image Resolution:	1024 by 768
Image Pixel Size:	4.06 µm
Acc. Voltage:	20.0 kV
Magnification:	30

Full scale counts: 16845
Integral Counts: 291181

Pt-H-Beta-300-EIM reduced 30x (1)_pt1

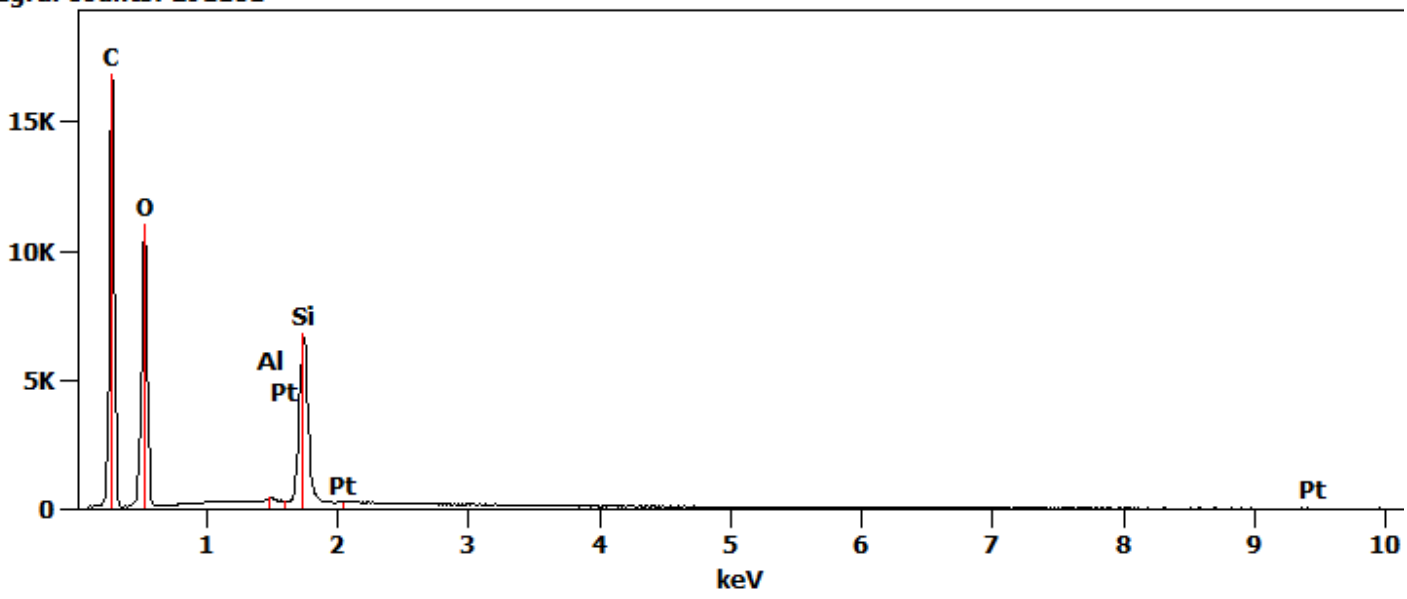

Project: 2023-05-10

Weight %

	O	Al	Si	Pt
Pt-H-Beta-300-EIM reduced 30x (1)_pt1	51.74S	0.98	44.65	2.63

Weight % Error (+/- 1 Sigma)

	O	Al	Si	Pt
Pt-H-Beta-300-EIM reduced 30x (1)_pt1	±0.33	±0.08	±0.26	±1.25

Atom %

	O	Al	Si	Pt
Pt-H-Beta-300-EIM reduced 30x (1)_pt1	66.36	0.75	32.62	0.28

Atom % Error (+/- 1 Sigma)

	O	Al	Si	Pt
Pt-H-Beta-300-EIM reduced 30x (1)_pt1	±0.42	±0.06	±0.19	±0.13

Formula

	O	Al	Si	Pt
Pt-H-Beta-300-EIM reduced 30x (1)_pt1		Al2O3	SiO2	Pt

Compound %

		Al2O3	SiO2	Pt
Pt-H-Beta-300-EIM reduced 30x (1)_pt1	0.00	1.85	95.51	2.63

Project: 2023-05-10

Pt-H-Beta-300-IW reduced 30x (3)

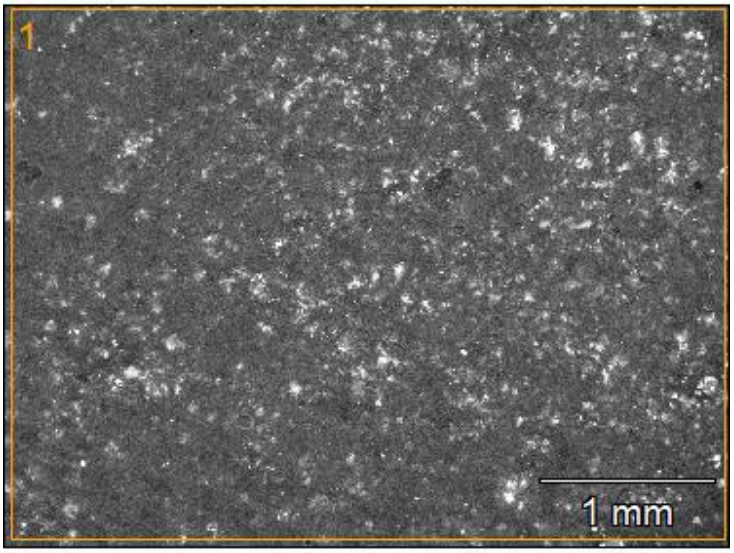

Image Name:	Pt-H-Beta-300-IW reduced 30x (3)
Image Resolution:	1024 by 768
Image Pixel Size:	4.06 µm
Acc. Voltage:	20.0 kV
Magnification:	30

Full scale counts: 15128 **Pt-H-Beta-300-IW reduced 30x (3)_pt1**
Integral Counts: 280187

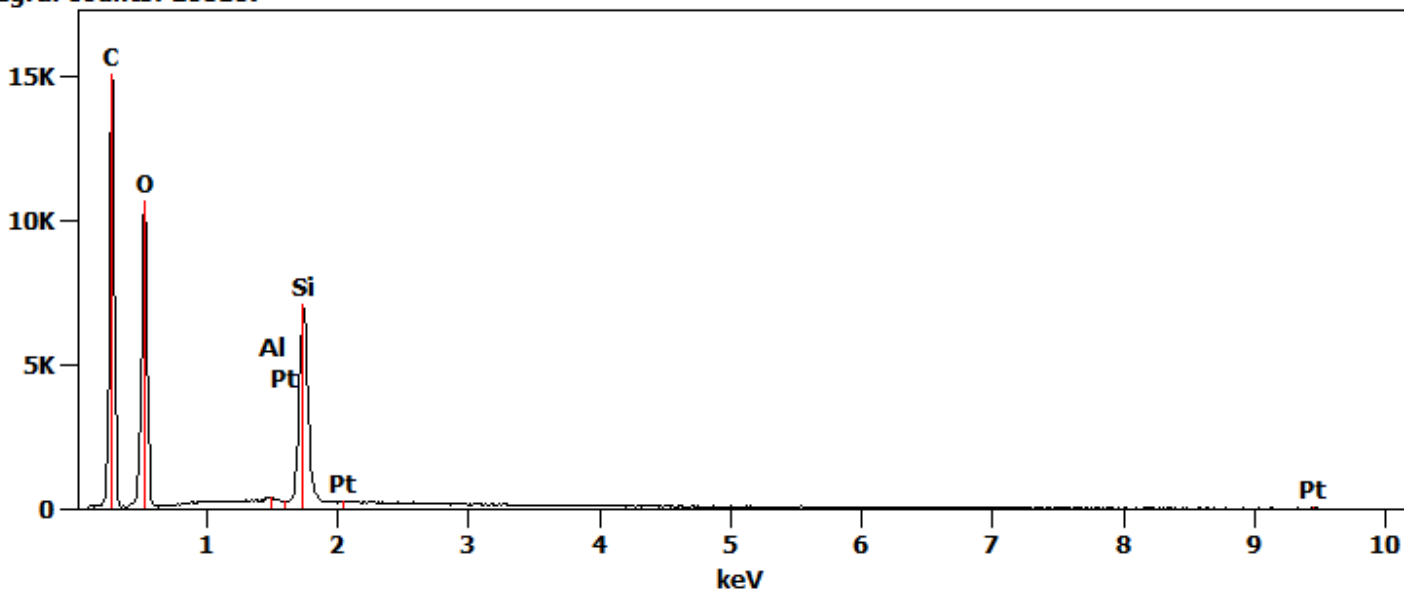

Project: 2023-05-10

Weight %

	O	Al	Si	Pt
Pt-H-Beta-300-IW reduced 30x (3)_pt1	51.57S	0.72	44.70	3.00

Weight % Error (+/- 1 Sigma)

	O	Al	Si	Pt
Pt-H-Beta-300-IW reduced 30x (3)_pt1	±0.33	±0.08	±0.26	±1.21

Atom %

	O	Al	Si	Pt
Pt-H-Beta-300-IW reduced 30x (3)_pt1	66.36	0.55	32.77	0.32

Atom % Error (+/- 1 Sigma)

	O	Al	Si	Pt
Pt-H-Beta-300-IW reduced 30x (3)_pt1	±0.42	±0.06	±0.19	±0.13

Formula

	O	Al	Si	Pt
Pt-H-Beta-300-IW reduced 30x (3)_pt1		Al2O3	SiO2	Pt

Compound %

		Al2O3	SiO2	Pt
Pt-H-Beta-300-IW reduced 30x (3)_pt1	0.00	1.37	95.63	3.00

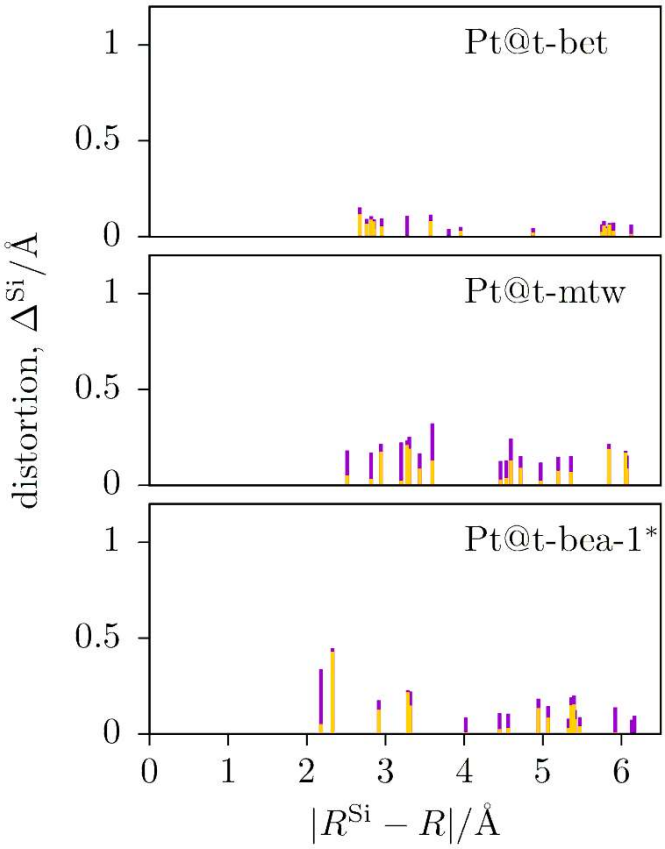

Figure A.1: Absolute (Δ_a^{Si}, purple) and radial (Δ_r^{Si}, yellow) displacements of the framework silicon atoms in Pt@BEA systems with respect to the pristine zeolite structure, within an exploration radius of 6.2 Å around the coordinates of the central point taken as reference. Panels of the different cavities in which the platinum atom is located are reported in increasing relative energy, from top to bottom.

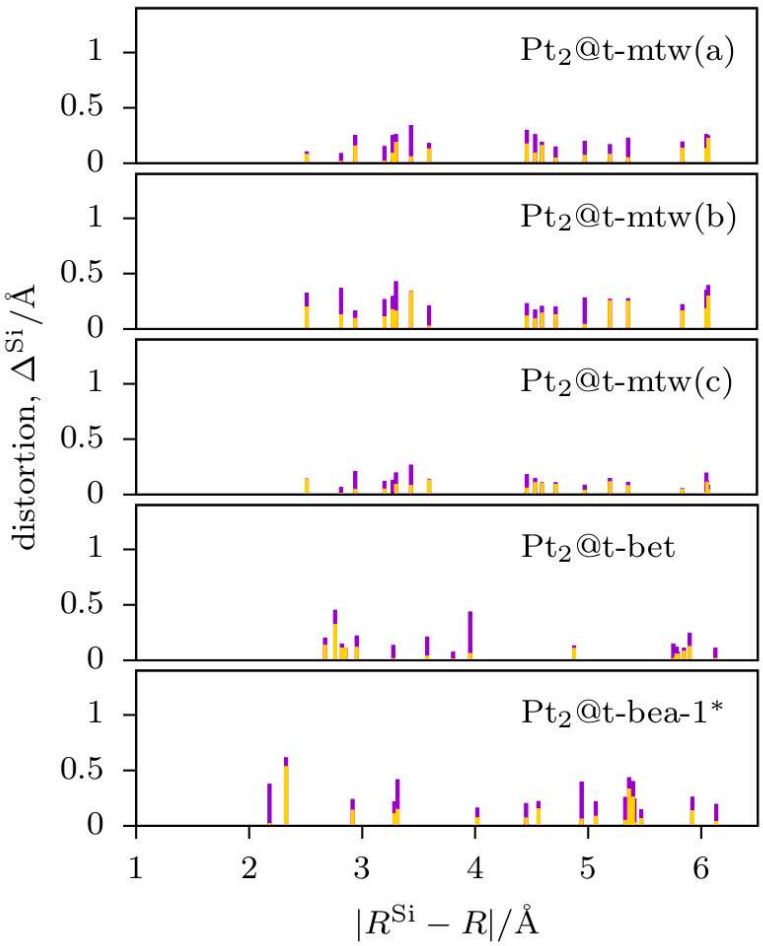

Figure A.2: Absolute (Δ_a^{Si}, purple) and radial (Δ_r^{Si}, yellow) displacements of the framework silicon atoms in Pt_2@BEA systems with respect to the pristine zeolite structure, within an exploration radius of 6.2 Å around the coordinates of the central point taken as reference. Panels of the different cavities in which the platinum dimer is located are reported in increasing relative energy, from top to bottom.

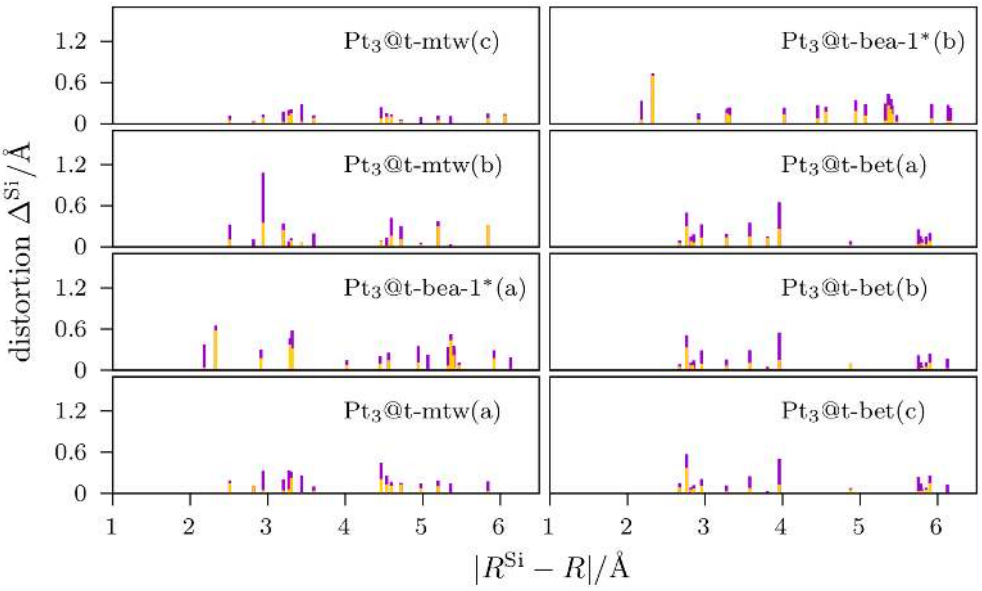

Figure A.3: (Δ_a^{Si}, purple) and radial (Δ_r^{Si}, yellow) displacements of the framework silicon atoms in Pt_3@BEA systems with respect to the pristine zeolite structure, within an exploration radius of 6.2 Å around the coordinates of the central point taken as reference. Panels of the different cavities in which the platinum cluster is located are reported in increasing relative energy, from top to bottom starting from the left.

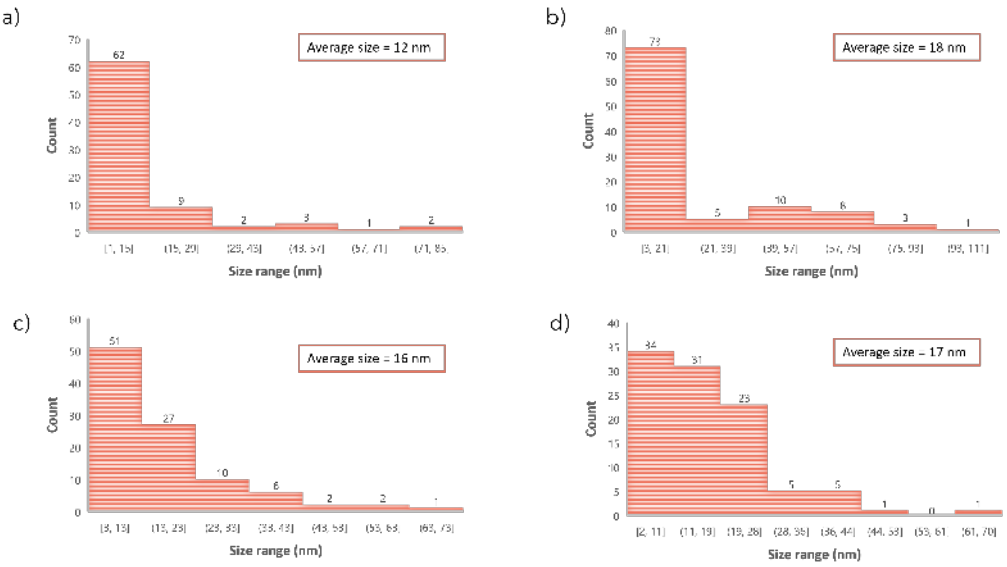

Figure A.4: Histograms of platinum particle size of a) Pt-H-Beta38-EIM, b) Pt-H-Beta-38-IW, c) Pt-H-Beta-300-EIM and d) Pt-H-Beta-300-IW catalysts.

Papers

Computational Materials Science 232 (2024) 112687

Contents lists available at ScienceDirect

Computational Materials Science

journal homepage: www.elsevier.com/locate/commatsci

Full length article

DFT study on zeolites' intrinsic Brønsted acidity: The case of BEA

Laura Gueci, Francesco Ferrante *, Marco Bertini, Chiara Nania, Dario Duca

Dipartimento di Fisica e Chimica "E. Segrè" - Università degli Studi di Palermo, Viale delle Scienze Ed. 17, I-90128 Palermo, Italy

ARTICLE INFO

Keywords:
β-zeolite
DFT
Intrinsic acidity
Topological sites

ABSTRACT

Since Brønsted acidity is a crucial aspect for the applications of zeolitic materials in heterogeneous catalysis, great effort was devolved to characterize the number, strength and location of the potentially active acidic sites. Quantum chemical calculations can turn out essential in estimating the intrinsic acidity by computing deprotonation energy (DPE) values, although each method comes with its own difficulties. In this context, three approaches within density functional theory were employed to study the intrinsic acidity of 30 topologically distinct Brønsted sites in the *β*-zeolite framework. Advantages and disadvantages of the three methods were outlined and the acidity order between the sites was assessed, being the DPE range 59 kJ mol^{-1} wide, with the proposed best approach. By dividing the range into three portions, the sites were classified as having high, medium and low acidity. Hydrogen bonds formation was found to be a contributing factor in determining a low Brønsted acidity.

1. Introduction

Zeolites are crystalline aluminosilicates with a specific microporous structure that find wide application as heterogeneous catalysts, especially in the petrochemical industry [1–6]. From the isomorphous substitution of a silicon atom by an aluminum atom in the pure-silica framework, a negative charge is generated which can be balanced by a proton. This gives rise to the zeolites' pronounced Brønsted acidic properties, responsible for most of their usage and notability [7–9]. The intrinsic strength of a zeolite Brønsted acidic site can be quantified in terms of its deprotonation energy (DPE), that is the energy needed to separate a proton at an infinite distance from the resulting anion. In real systems, however, Brønsted acidity can only be observed if a base is present, so that additional factors become important, such as accessibility of the involved zeolitic site, steric hindrance, the tendency of the base to accept protons, and the stabilization of the resulting ion pair.

According to this distinction, large effort was devoted, both through theoretical studies and experimental techniques, to characterize the number, strength, and location of the potentially active acidic sites, aiming at a formulation of acidity–reactivity relationships in zeolite catalysis [10–13]. As a matter of fact, the synergism between experiment and quantum chemistry calculation is instrumental to unveil the fundamental aspects of catalytic reactions, assisting the design of new catalysts and orienting the optimization of active sites [14–21]. For zeolite-based catalyst specifically, Density Functional Theory (DFT) proved to be essential in the development of materials and processes [22–25]. Common approaches to measure proton affinity of zeolites include IR and NMR spectroscopy, calorimetry and temperature-programmed desorption (TPD), exploiting the interaction of the acidic sites with basic probe molecules such as ammonia and pyridine [26–30]. Ammonia IRMS-TPD experiments, for example, have been successfully used in combination with DFT studies to assign the stretching vibration bands of acidic OH groups in the IR spectrum to each Brønsted acidic site, located at crystallographically non-equivalent position in MOR, FAU, CHA and BEA zeolite frameworks [31–34]. The Brønsted acidity of sites belonging to FAU, CHA, IFR, MOR, FER, and TON zeolites was investigated by Trachta et al. [35] by the analysis of the adsorption of base molecules with different proton affinities. Even if the authors recognize the difficulties in estimating a site acidity ranking, they recommended a best acidity order based on the use of probes (such as acetonitrile) whose proton affinity is just below the site deprotonation threshold. However, it is our opinion that the use of the adsorption properties of small molecules to sample the acidity of zeolites Brønsted sites is complicated by the orientation of the probe with respect to the zeolite framework. As a matter of fact, this orientation is driven by a delicate balance between the directional interaction with the acid hydrogen atom and a number of weak interactions with the zeolite walls; just these latters, from the computational point of view, are very difficult to be estimated and, even if a number of correction schemes for dispersion interactions was proposed in the recent years, it is not guaranteed that these corrections allow to reach the accuracy

* Corresponding author.
E-mail addresses: laura.gueci@unipa.it (L. Gueci), francesco.ferrante@unipa.it (F. Ferrante), marco.bertini@unipa.it (M. Bertini), chiara.nania@unipa.it (C. Nania), dario.duca@unipa.it (D. Duca).

https://doi.org/10.1016/j.commatsci.2023.112687
Received 27 July 2023; Received in revised form 2 November 2023; Accepted 26 November 2023
Available online 30 November 2023

needed for the most reliable description. Accordingly, it is perhaps a better idea to avoid these complications and resort to acidity rankings based on deprotonation energies, even if this quantity is not accessible by direct measurements [36].

DPEs in various zeolites have been estimated from quantum chemical calculations using either isolated or embedded clusters [37–39] and periodic models [36,40], each method bearing its advantages and disadvantages. In particular, values obtained using small cluster models show significant variations with cluster size, reaching convergence only when systems containing more than 20 tetrahedral SiO_4 units are investigated [28]. In case of embedded clusters, for example within a QM-Pot approach, the influence of cluster size is much smaller although, as a downside, issues associated with embedding may arise. In this context, Brändle and Sauer reported that all the calculated DPE values for FAU and MFI are within a range 3 and 6 kJ mol^{-1} wide, respectively, while values for different crystalline structures span within a range of less than 30 kJ mol^{-1} [37,41]. These findings would indicate that the intrinsic acidic strength of zeolites is hardly influenced by the framework structure. To avoid embedding artifacts, periodic DFT was used by Jones et al. [36] in a broad study of deprotonation energies for several zeolites, mapping every unique crystallographic position for the Al-Si substitution. They reported mean DPE values, obtained by averaging over the four distinct proton locations at each Al atom, in the range of 1201 ± 11 kJ mol^{-1} for all crystalline frameworks considered. This investigation suggested that DPEs are insensitive to the Si–O–Al bond angles, but conversely exhibit a dependence on the framework densities [40,42]. However, the employed method is not immune to errors, having to account for the artificial interactions arising among charged cells, created after the deprotonation of a zeolite site, in periodic calculations [43,44]. More recently, the fact that the sites Brønsted acidity strength is inversely correlated with the framework density was confirmed by Trachta and coworkers [45], which used a series of increasing-size cluster models to estimate the deprotonation energies in FAU, CHA, IFR, MOR, FER, MFI, and TON zeolites. After the results of cluster models have been corrected by applying an electrostatic embedding, from the proposed deprotonation energies reported there a mean value of 1245 ± 9 kJ mol^{-1} can be calculated, which is sensibly higher than the one obtained by Jones et al.

In spite of the significant number of studies reported on the topic, the effect of zeolite topology and composition on intrinsic acidity and reactivity is far from being fully understood. Many questions are still open and, especially from an atomistic-scale point of view, more accurate treatments are desirable, being however challenging the attempt to correlate computational results and experimental data, due to the inherent dissimilarity in what can be investigated in the two cases.

This work aims to add a piece of knowledge on the study of zeolite acidity based on quantum chemical descriptors, providing a comparative analysis of DPEs calculated through three different approaches, focusing on β-zeolite's framework (*BEA, if considering a mixture of polymorphs) as a case study.

Belonging to the large pore zeolites, BEA is one of the most notable and extensively used [46–51]. In BEA structure, silicon and oxygen atoms are linked to form 3D twelve-membered rings (diameter of 6-7 Å along the [010] and [100] axes, 5-6 Å along [001]), together with six, five and four-membered rings. This give rise to 9 and 17 crystallographically non-equivalent Si and O atoms, respectively, causing the topological possibility of 32 unique Brønsted acidic sites [52]. The intrinsic strength of all these sites is investigated in the present study by using (i) an ONIOM method, (ii) periodic DFT calculations and (iii) a specially designed cluster approach based on the latter.

2. Models and methods

2.1. ONIOM approach

From the periodic framework of the β-zeolite built by using the crystallographic information file provided by International Zeolite Association (IZA) website [52], a portion of about 800 atoms was selected,

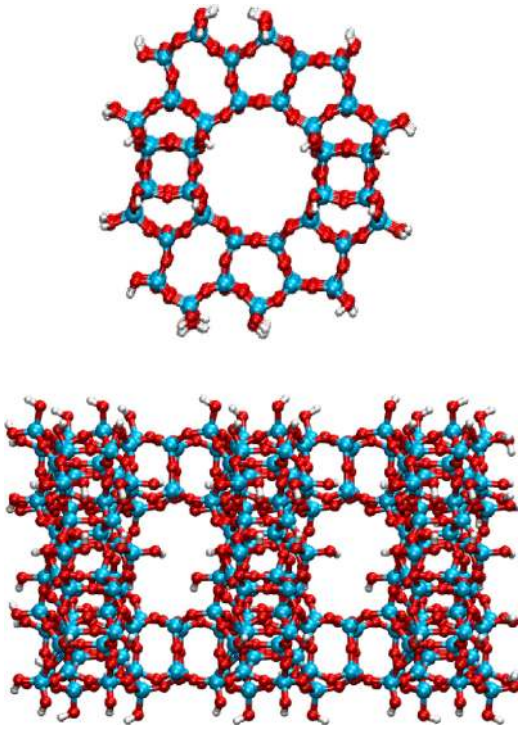

Fig. 1. Two views of the zeolite portion, consisting of 864 atoms, selected as the real system for the ONIOM approach (O=red, Si=cyan, H=white).

featuring two intersections between the main twelve-membered ring channels (12T). To this fragment, terminal hydrogen atoms were added to complete the valences of the dangling oxygen atoms, thus obtaining the model, consisting of 864 atoms, chosen as the real system for the subsequent ONIOM calculations (see Fig. 1). Six model systems, in the following indicated as m1–m6, were selected, ranging in size from 39 to 102 atoms. Model systems from m1 to m4 were used to study more than one topological silicon, while the smallest ones, m5 and m6, were defined to investigate just one specific *T* site, namely T9 and T1, respectively, being these not properly embedded in the other models. In fact, careful attention has been paid so that the portion with the silicon atoms of interest was centered with respect to the model system itself, so to place these at a suitable distance in all directions from the boundary with the low level. Fig. 2 shows the six model systems embedded in the real system and, in a close-up view of the model systems, all the labels of the investigated acidic sites.

Geometry optimizations were performed for: (i) the silicalite systems as starting point, (ii) the anionic structures with one Si atom replaced by one Al and (iii) the neutral structures with aluminum and a hydrogen atom. In the latter, the hydrogen was positioned so that it interacted, in turn, with three of the four oxygen atoms of the AlO_4 tetrahedral unit. In the following the different acidic sites will be labeled as T*n*O*m*, where *T* is the tetrahedral center corresponding to the silicon atom substituted by aluminum whereas *n* and *m* are couples of numbers pointing out the specific topological site as reported in Fig. 2. Excluding T5O14 and T6O14 sites, where the added hydrogen would not be accessible, 40 cases were obtained out of the 32 topologically distinct acidic sites of the β-zeolite. Some aluminum-hydrogen configurations were considered twice in different model systems, as an internal consistency check. The site-topological label assignment was made by comparison with labels reported in the crystallographic information file of the BEA framework, using the VESTA program [53].

Gaussian16 [54] was used with B3LYP hybrid exchange-correlation functional corrected by the third order Grimme empirical treatment of

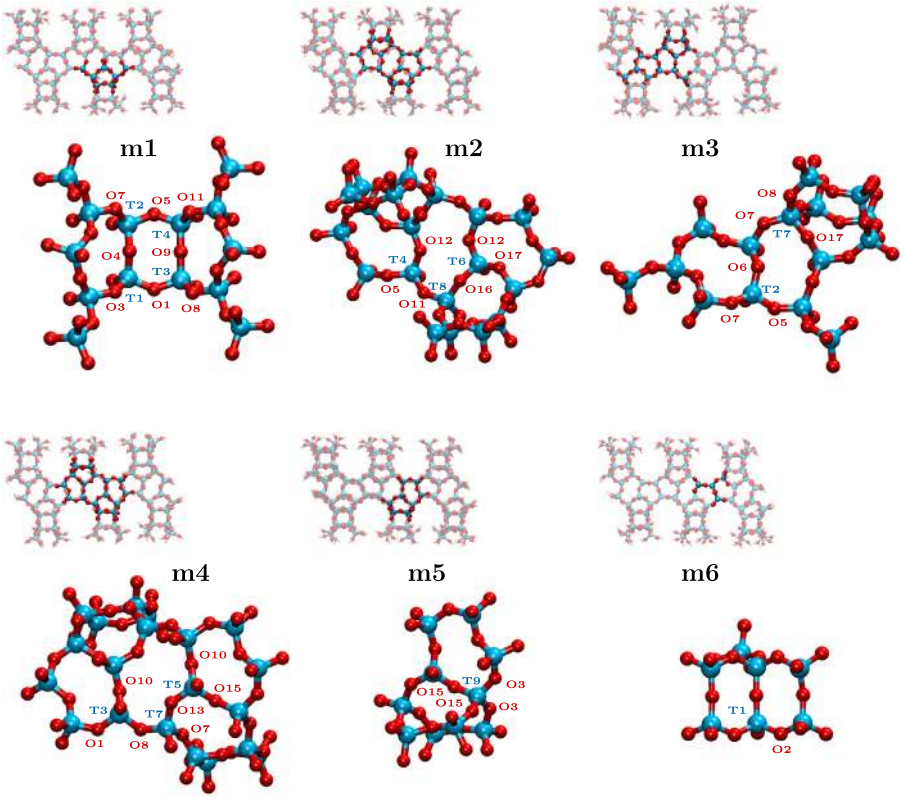

Fig. 2. ONIOM model systems, m1–m6, embedded in the real system and, having chosen a convenient orientation, isolated. The topological labels of the examined tetrahedral and oxygen sites are reported for each model system.

dispersion interactions (B3LYP-D3, [55]); the cc-pVDZ basis set was employed for all atoms. The chosen low level of theory for the application of ONIOM was the Universal Force Field. A singlet multiplicity state was considered for both high and low level. Inspection of the calculated harmonic vibrational normal modes confirmed that the investigated structures correspond to minima on the potential energy surface of their respective systems.

2.2. Periodic DFT calculations

The structural model used for periodic DFT calculations is the BEA unit cell (a = b = 12.631 Å, c = 26.186 Å, $\alpha = \beta = \gamma = 90°$) provided by IZA [52] and illustrated in Fig. 3. Periodic geometry optimization were performed for the 30 structures originated by replacing, one at a time, all the topologically distinct silicon atoms with aluminum and adding one H atom on the corresponding not equivalent oxygen centers.

All periodic calculations were performed by using the SIESTA approach as implemented in the code [56] bearing the same name. The PBE exchange–correlation functional was chosen, along with double-ζ quality numerical basis sets generated with an energy shift of 0.005 Ry. New generation norm-conserving pseudopotentials were employed; they were taken from the database of the PseudoDojo project [57] (labeled as *nc-sr-04_pbe_standard*). The psml format is supported by the dedicated SIESTA-PSML-R1 version of the code [58]. Sampling was performed using a value of 450 Ry for the mesh cutoff and a 2 × 2 × 2 Monkhorst–Pack grid, which was refined at 4 × 4 × 4 after a first relaxation of the system geometry.

2.3. Cluster approach

Starting from optimized structures previously obtained through periodic DFT calculations, a zeolite unit cell reshaping procedure was performed to obtain clusters, then adjusted for the valences of terminal

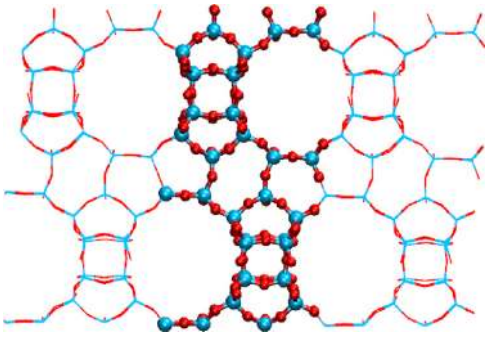

Fig. 3. BEA unit cell of 192 atoms (ball-and-stick), within the periodic framework (wired), viewed along the ac plane. Cell parameters are: a = b = 12.631 Å, c = 26.186 Å, $\alpha = \beta = \gamma = 90°$.

oxygen and silicon atoms. The reshape procedure, aimed at placing the acidic hydrogen atom roughly in the center of the new born fragment, replicates the neighborhood of the hydrogen atom which in the periodic calculation gave that specific arrangement after geometry optimization. Thus, the so obtained clusters are homogeneous, both each other and singly with their starting optimized structures. In detail, in order to build a reshaped cell, the position of the aluminum atom was fixed, both in the anionic and in the corresponding neutral structures, in the center of a new defined cell, having the same a, b and c constants of the original BEA repetition unit. The atoms whose coordinates are inside this new cell do not undergo variations, while those that fall outside of it are translated back inside, by applying to them the a, b, c vectors. It should be noted that the choice of Al as the center of the new cell, being the interest in the definition of the clusters the acidic hydrogen atom, is justified by the proximity of the latter to Al and, on the other hand, its absence in the anionic structures. Fig. 4 shows, taking the site T1O1 as

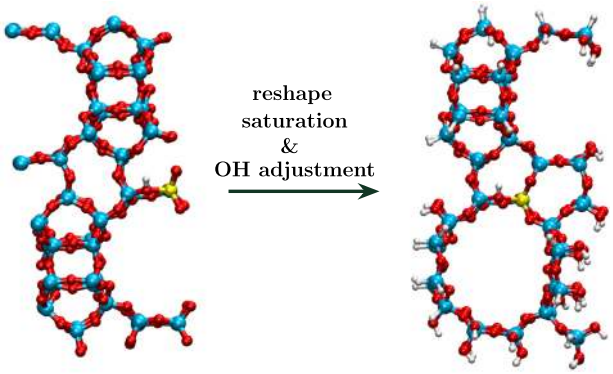

Fig. 4. T1O1 acidic site within the BEA unit cell (left) and the fragment, with terminal hydrogen atoms, chosen to describe the same site (right) in the cluster approach. O=red, Si=cyan, Al=yellow, H=white.

an example, the system at the start and at the end of the described procedure, which was applied for the 30 neutral species and the 9 corresponding anions. After the reshaping stage is completed, we are left with many undersaturated Si and O nuclei at the cell boundaries. An automatic saturation procedure, whose algorithm is described in the following, was then applied to prepare the structure for a cluster calculation. For every undersaturated nuclei in the cell, consider: case (1) it is a Si atom, so from 1 up to 3 neighboring oxygen atoms could be missing: in this case the correct number of hydrogen atoms were placed in an appropriate tetrahedral arrangement around Si, taking into account position and orientation of the already existing Si–O bonds; whenever an Si–H moiety was less than two Si–O bonds apart from the acidic site, it was substituted by Si–OH; case (2) it is a O atom, in which case only a single neighboring Si could be missing, and consequently a single hydrogen was added at 109.5° Si–O–H angle. It is worth to note that: (i) in the authors' opinion, the average Si–O–Si value of 136° typical of zeolites is too wide for a proper Si–O–H angle, an issue that could give rise to energetic artifacts depending on the number of their occurrence, hence the choice for the 109.5° value; (ii) all the terminating -OH groups are oriented in the same spatial direction (and so not in the direction of the next Si in the zeolite framework) in order to avoid the occurrence of having two saturating hydrogens too close each another, which is a possibility since two different oxygen atoms may be bonded to the same silicon atom. Wherever this is not the case and the saturated hydroxyl group is close to the Al region, the orientation was adjusted in order to match the one occurring in the zeolite structure. The final geometry was checked to ascertain that no border H-atom was less than 4.5 Å from the acid hydrogen site, a distance that was considered scarcely influent regarding the dispersion interactions between the real and the fictitious hydrogen atoms.

For the described cluster approach, the same exchange–correlation functional and basis set used for the model systems of the ONIOM calculations were employed. It should be emphasized that the SIESTA and the cluster approaches are intimately related one to the other and the latter, which starts from the optimized structures obtained by the periodic treatment, can be considered as an automatic, non-empirical correction of the former in view of the evaluation of deprotonation energies.

3. Results and discussion

In Table 1, DPE values for the 30 investigated topologically distinct acidic sites of BEA, obtained by using the three chosen computational approaches (ONIOM, SIESTA, cluster) are reported as three different sets. Deprotonation energy was calculated merely as the difference between the SCF energy of the aluminated β-zeolite anionic form and the SCF energy of the corresponding neutral form. Extrapolated energies were used in the case of the ONIOM approach. Actually, the use of ONIOM allows to define systems small enough to make affordable the calculation of vibrational frequencies, hence thermochemical properties. By comparing the calculated DPE values based on the ONIOM energy with those based on the ONIOM enthalpy, it can be estimated that the thermal contributions to the deprotonation energy (leading to a decrease of the DPE) span between 27 and 36 kJ mol^{-1}, depending on the nature of the zeolite site. This range is in agreement with the average value of 29 kJ mol^{-1} estimated in the literature [45] for the contribution due to the difference of vibrational zero-point energies in various zeolites, and can be considered simply as a constant contribution as regards a discussion about the relative results obtained with the three approaches here described.

The three energy sets found with the different methods were normalized in the 0–100 interval following the expression

$$\mathrm{DPE}^{\mathrm{M}}_{\mathrm{n},i} = 100 \cdot \frac{\mathrm{DPE}^{\mathrm{M}}_{i} - \mathrm{DPE}^{\mathrm{M}}_{\mathrm{min}}}{\mathrm{DPE}^{\mathrm{M}}_{\mathrm{max}} - \mathrm{DPE}^{\mathrm{M}}_{\mathrm{min}}} \quad (1)$$

where the normalized deprotonation energy of the ith site according to method M, $\mathrm{DPE}^{\mathrm{M}}_{\mathrm{n},i}$, is defined with respect to the raw $\mathrm{DPE}^{\mathrm{M}}_{i}$ and the minimum and maximum DPE values found within the corresponding set. All the data were then collected in the histogram of Fig. 5, which is divided into three equally spaced bands to qualitatively indicate low, medium and high site acidity, being clear that the x-axis is sorted in ascending order based on the numbering of silicon (and then oxygen) labels only.

A tentative explanation of the ONIOM behavior reported in the histogram is given in the following. As can be noticed from Fig. 2, in β-zeolite the T8 and T9 sites feature only two non equivalent oxygen atoms (O11 and O16 the former, O3 and O15 the latter). The two T9O3 and the two T9O15 sites are well defined in the same m5 model. Further, as revealed by the presence of double ONIOM bars in the histograms reported in Fig. 5, other cases have been examined twice (duplicate sites), using different model systems. This makes it possible to obtain indications on the suitability of the model system choice, thus of the application on this zeolitic system of the ONIOM method itself. Among the 8 duplicate sites there are some cases where the ONIOM results fall inside different acidity groups, depending on the involved model system. The most striking ones are precisely the sites T2O5 and T4O11, and, to a lesser extent, T2O7. As an example, T4O11 is predicted to have a very low acidity by the m1 model while is among the most acidic sites according to the m2 model. On the other hand, similar qualitative results are obtained in the case of T4O5 and T7O7 sites (belonging to the same acidity zone), while small differences are reported for T3O1, T3O8 and T7O8. Notably, in all the three duplicate sites exhibiting more significant differences the model system m1 is involved, always giving the highest value, which would suggest a bias of this model system. For the T4O5 site, instead, m1 and m2 are in excellent agreement, while T3O1 and T3O8 show only subtle differences between m1 and the other model systems in which they are taken into consideration. Without going into details on the many factors that are certainly involved, the phenomenon may find explanation in the basis nature of a model, which for definition cannot capture all facets of the reality. In fact, it is easy to imagine that the same ideal topological site of the periodic zeolite can be described differently by two different model systems. In particular, the neighborhood of the rings to which the site belongs can be different, being this neighborhood necessarily a subset of what defines the topology of the same model site.

It is necessary to highlight that particular attention was given to ensure that the acidic hydrogen was surrounded by atoms treated at DFT level within the ONIOM approach, and that it was positioned at least 3 bonds away from the low-level region. However, in almost all the model systems the silicon atom which is replaced by the aluminum atom features only three of the four Si atoms belonging to the tetrahedrons around it in the high level of calculation. This could limit the relaxation of the structure during geometry optimization, with

Table 1
DPE values[a] calculated with the ONIOM (O), SIESTA (S) and cluster (C) approaches.

Site	O	S	C	Site	O	S	C
T1O1	1344.9 (m1)[b]	1019.8	1220.9	**T4O12**	1355.2 (m2)	1049.3	1237.9
T1O2	1367.4 (m6)	1042.7	1233.3	**T5O10**	1275.3 (m4)	1034.7	1210.2
T1O3	1351.9 (m1)	1025.7	1223.8	**T5O13**	1352.3 (m4)	1022.8	1189.7
T1O4	1354.0 (m1)	1007.9	1197.6	**T5O15**	1336.6 (m4)	1026.4	1192.2
T2O4	1357.0 (m1)	1008.9	1209.0	**T6O12**	1324.0 (m2)	1037.6	1230.3
T2O5	1370.3 (m1) | 1304.0 (m3)	1025.6	1219.5	**T6O16**	1336.3 (m2)	1036.2	1227.4
T2O6	1339.0 (m3)	1014.2	1210.9	**T6O17**	1330.6 (m2)	1021.9	1213.2
T2O7	1368.7 (m1) | 1330.8 (m3)	1013.2	1202.1	**T7O7**	1328.6 (m3) | 1313.6 (m4)	1011.6	1181.8
T3O1	1364.8 (m1) | 1339.1 (m4)	1019.1	1205.9	**T7O8**	1306.1 (m3) | 1313.4 (m4)	1020.1	1195.3
T3O8	1346.8 (m1) | 1218.8 (m4)	1016.6	1211.5	**T7O13**	1319.3 (m4)	1020.2	1189.1
T3O9	1371.0 (m1)	1025.6	1219.0	**T7O17**	1287.6 (m3)	1024.2	1204.4
T3O10	1336.5 (m4)	1031.4	1217.4	**T8O11**	1326.6 (m2)	1027.4	1178.8
T4O5	1370.8 (m1) | 1355.0 (m2)	1015.2	1195.4	**T8O16**	1340.9 (m2)	1043.1	1192.5
T4O9	1382.3 (m1)	1031.4	1216.5	**T9O3**	1331.8 (m5) | 1318.1 (m5)	1028.0	1194.7
T4O11	1371.9 (m1) | 1288.8 (m2)	1020.3	1202.4	**T9O15**	1316.6 (m5) | 1345.8 (m5)	1015.8	1194.9

[a] Expressed in kJ mol^{-1}.

[b] The employed model system is indicated in parentheses.

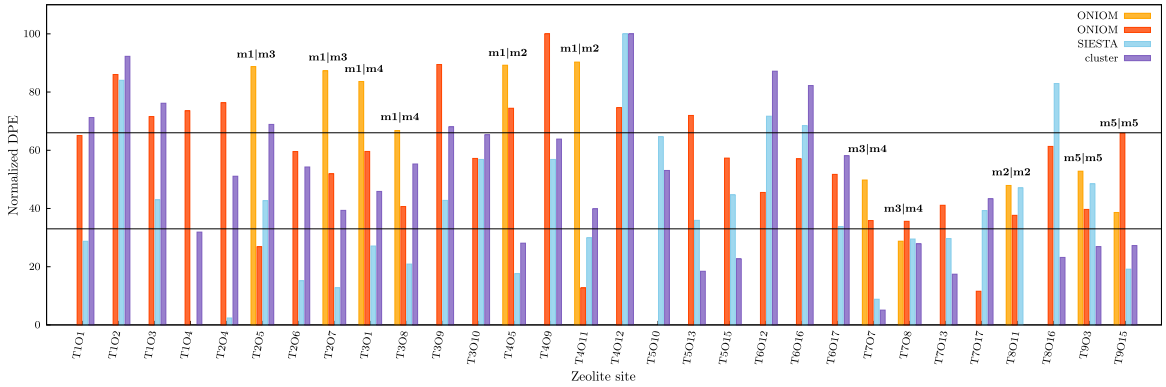

Fig. 5. Sub-histograms of normalized DPE values calculated with ONIOM, SIESTA and cluster approaches characterizing the topologically distinct acidic sites of BEA. Whenever four bars are reported on a site sub-histogram, the first two refer to ONIOM results obtained from two different model systems (indicated by the labels above) or even from different sites of the same model system. A missing bar in a sub-histogram indicates the zero value for the corresponding case. Horizontal lines equally divide the histogram in three acidity zones.

consequences on the deprotonation energies. Since this situation was also found in literature [29], it was tried to solve the problem by including the missing silicon and some other oxygen atoms in the model systems. This attempt anyway proved to be unviable due to the intrinsic characteristics of the β-zeolite structure. In fact the addition of atoms into the model system often makes ONIOM layers definition impossible, as an example showing one atom in the real system bonded to more than one atom of the model system. Even the shaping of smaller 5T systems centered at the topological silicon of interest was not always possible due to the same problems in the ONIOM partitioning. Li et al. in fact, got around the problem by removing some oxygen atoms from the high level, an expedient that created model systems which were not homogeneous with each other and that might cause significant artifacts considering their small size.

All this considered, the ONIOM approach does not seem a satisfactory mean to adequately investigate the acidity of the 9 topologically distinct site of the β-zeolite. In order to avoid the problem of both duplicate sites, differently described by the model systems, and of shaping incomplete silicon tetrahedron around the topological site, we suggest to eliminate the choice of model systems upstream, and carry out periodic calculations followed by a refining treatment using a cluster approach, as illustrated in the following.

Actually, a drawback still exists in using periodic DFT when dealing with charged unit cells, namely in geometry optimizations of zeolite anionic structures: the interaction between charges of all the images leads, in fact, to energy artifacts that must be taken into account and compensated. This is an open problem yet, as highlighted by the work of Iglesia et al. [36]. One of the best proposed procedures to address this issue contemplates an *a posteriori* correction, following the Freysoldt–Neugebauer–Van de Walle (FNV) scheme [43], which applies to the energies, while the respective geometries remain unchanged. Therefore, one can reasonably trust on the optimized geometries found for anions and, as proposed in this work, use them as a starting point for a cluster DFT approach.

In such a method, each acidic site that in periodic calculations is located inside the unit cell, subject to periodic boundary conditions, is now described by a finite fragment of the zeolite framework. For this reason, changes to the starting structures are necessary to reproduce in the new system the chemical local environment that characterizes each site, hence the reshape procedure detailed in the Models and Methods section. The approach here proposed features several advantages: (i) it avoids issues arising in the choice of a model system, (ii) even if the geometry optimization is not performed again, it is based on reliable geometries, properly adapted by placing the acidic hydrogen atom homogeneously in all the sites, (iii) without suffering from charges interaction artifacts, it supplies DPE values more accurate than those obtained by any periodic DFT analysis and (iv) it offers the possibility to choose exchange–correlation functionals and basis sets more appropriate, with respect to those commonly available in softwares for periodic calculations, to discriminate the intrinsic acidity of the zeolitic sites.

Referring to the DPE values obtained with the proposed cluster approach, an acidity strength order of the investigated 30 topologically distinct acidic sites of BEA can be extrapolated. Among them 11 belongs to the middle portion of the range, 11 cases feature the highest intrinsic Brønsted acidity, in particular T7O7 and T8O11, and the remaining 8 sites are less acidic, especially T4O12, T1O2 and T6O12. In order to

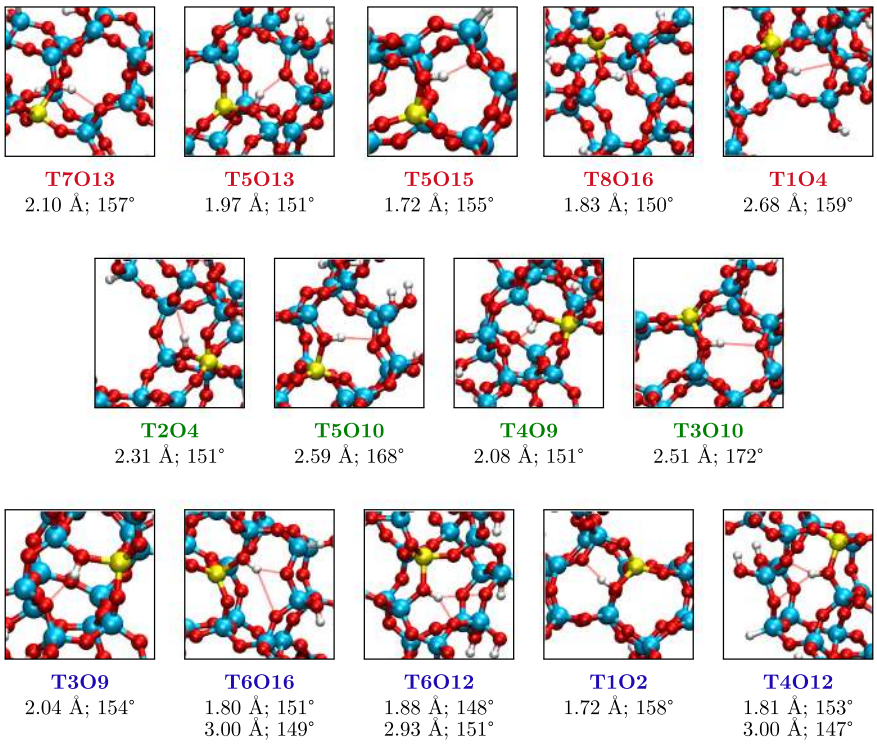

Fig. 6. Structural details of the most significant hydrogen bonds detected in the topological configurations investigated, according to the cluster method. Below each image corresponding values of the O···H distances and O–H···O angles are reported. Different colors are used to label the acidity group to which each site belongs: high, medium and low acidity are associated with red, green and blue, respectively.

get a deeper insight into the cause of the acidity trend, a structural analysis of the 30 sites was performed in terms of the hydrogen bond parameters involving the acidic hydrogen atom. Structures with strong hydrogen bonds, namely those showing H-bond, O···H, distance ranging from 1.5 to 3.0 Å and O–H···O angle in-between 150° and 180° are depicted in Fig. 6, in descending order of acidity. The presence of H-bonds was detected in almost all the sites belonging to the low and medium-low acidity groups and just occasionally in the other groups (high and medium-high acidity). When this last issue occurred, the site is less acid than the one which shares the same T and does not show H-bond formation, like it is the case, e.g., of T8O16 and T8O11. A correlation may be therefore drawn between hydrogen bond formation and the occurrence of a low acidity characterizing the corresponding site. In particular, it has been devised that H-bonds are formed when proton donor and acceptor oxygen atoms belong to the same (5- or 6-membered) ring. At the bottom of the low acidity range, sites T4O12, T6O12 and T6O16 show two hydrogen bonds with the right orientation. The correlation above can be considered as a further evidence which substantiates the findings of Katada et al. [34] about the factors affecting the vibrational frequency of the O–H stretching, taken as an index of site acidity.

It is, at this point, noteworthy to compare the most and the least acidic sites according to the three computational approaches employed. The site showing the highest intrinsic acidity is T8O11 according to the here proposed cluster approach (strictly followed by T7O7, the two sites showing the acidic hydrogen that protrude in the main channel, a fact surely auspicable when β-zeolite is to be used as an acidic catalyst), while T5O10 and T1O4 are indicated by ONIOM and SIESTA methods, respectively. In this respect, the ONIOM approach sensibly fails if compared to the cluster one.

The optimized ONIOM and SIESTA structures both show hydrogen bonds in the corresponding most acidic site (see Fig. 6), being this occurrence the possible cause of their collocation within the medium acidity group when they are treated by the cluster approach. An excellent agreement between SIESTA and cluster is found regarding the least acidic site, as they both predict that this role belongs to the T4O12 site, where the proton is involved in two strong hydrogen bonds. Conversely, ONIOM indicates the near T4O9 site as the least acidic one, being in any case T4O12 in the region of the low acidity.

Deprotonation energies range from 1382 to 1275 kJ mol^{-1} in the case of ONIOM, while they are between 1049–1008 kJ mol^{-1} for periodic calculations and 1238–1179 kJ mol^{-1} employing the cluster approach. It must be noted that only the acidity interval resulting from this latter is in line with the one proposed for zeolites by Jones et al. [36] and Trachta et al. [35], while the one guessed by ONIOM is overestimated, probably due to a destabilization of the anionic form caused by the fact that its negative charge cannot be properly delocalized on the small model systems. As a matter of fact, if the average of the Brønsted acidity of all the Al–O sites —evaluated by the cluster method— is considered, the value of 1207 kJ mol^{-1}, with a root mean square deviation of 15 kJ mol^{-1}, is obtained.

A striking difference between the data of Jones et al. on β-zeolite and those obtained in this work is observed when the comparison between periodic and cluster outcomes is performed. Indeed, the DPE values reported by Jones et al. for BEA, according to their periodic calculations, are comprised between 1561 and 1583 kJ mol^{-1} (neglecting the Al5O14 and Al6O14 sites), and their ensemble averaged $\langle$DPE$\rangle$ decreases around 1200 kJ mol^{-1} only after applying an empirical shift determined by the comparison with previous results based on embedded or cluster models. Conversely, the periodic SIESTA results here reported, with an average DPE of 1025 kJ mol^{-1} (RMSD of 6 kJ mol^{-1}), are well below with respect to those of the cluster values. Still, Jones et al. [36] proved that their overestimated data were not due to simple problems related to the charged cell issue, since the FNV correction [43] just increased the divergence from the seemingly accepted value of 1200 kJ mol^{-1}. In fact, the FNV correction should destabilize the charged species and in any case, for singly negative charged systems and large employed cells, it should not have a utterly significant magnitude [59]. In the work of Trachta et al. [35] raw periodic data are not reported, but they get close to the mean value

Table 2
DPE values according to the Boltzmann average over the different oxygen sites next to a common tetrahedral site. The (e, p) numbers between parenthesis next to the O site are the energy (relative to the most stable case in the same T site) and population at room temperature, respectively.

T site	O sites	⟨DPE⟩[a]
1	O1 (23.0, 0.000); O2 (0.1, 0.487); O3 (17.1, 0.001); O4 (0.0, 0.512)	1215.0
2	O4 (16.7, 0.001); O5 (0.0, 0.982); O6 (11.4, 0.010); O7 (12.4, 0.007)	1219.3
3	O1 (12.3, 0.006); O8 (14.9, 0.002); O9 (5.8, 0.087); O10 (0.0, 0.905)	1217.5
4	O5 (34.1, 0.000); O9 (17.9, 0.001); O11 (29.0, 0.000); O12 (0.0, 0.999)	1237.9
5	O10 (0.0, 0.958); O13 (11.9, 0.008); O15 (8.3, 0.034)	1209.4
6	O12 (0.0, 0.632); O16 (1.3, 0.367); O17 (15.7, 0.001)	1229.2
7	O7 (12.6, 0.004); O8 (4.0, 0.140); O13 (4.0, 0.143); O17 (0.0, 0.712)	1199.6
8	O11 (14.8, 0.003); O16 (0.0, 0.997)	1192.5
9	O3 (0.0, 0.993); O15 (12.1, 0.007)	1194.7

[a] Relative energy values and ⟨DPE⟩ are expressed in kJ mol^{-1}.

of 1245 kJ mol^{-1} after correction. Still, in one of the last works on zeolite acidity, specifically on the very same β-zeolite here investigated, Vorontsov and Smirniotis [60] reported indeed uncorrected data, according to which DPE values should be in the narrow 1592–1603 kJ mol^{-1} range. Since all the authors above used plane waves as basis set for their periodic calculations, it can be hypothesized that the divergence between ours and their data should be searched in the difference between the used computational approaches; in details, being the same the DFT exchange–correlation functional, it seems that a plane-wave type description of the zeolite electron density gives results which substantially differ from those obtained by a SIESTA-based approach using strictly localized numerical basis sets.

In order to better compare our results with those found in the literature and to report Brønsted acidities which depend only on the position of the Al/Si substituted T site, a Boltzmann average of the DPE values corresponding to different oxygen sites attached on the same T site was considered. Barrierless processes were assumed for the proton shifts between the oxygen centers above. The energies used for the determination of Boltzmann populations are those obtained by means of the SIESTA approach for the optimized geometries (the relative energy values should be reliable, since they are those of neutral systems), while the DPE values employed in the average are those obtained with the cluster method (see Table 1). By taking a look at Table 2 it can be noticed that the ⟨DPE⟩ values span a narrower segment (45 kJ mol^{-1}) with respect to the raw values, showing a mean value of 1212.8 kJ mol^{-1}. Further, this acidity interval can be divided into three subranges, with an energy interval of ca. 10 kJ mol^{-1} in-between; in particular, the high acidity sites T7, T8 and 79 are in the 1195–1200 kJ mol^{-1} range, the medium acidity T1, T2, T3 and T5 sites are within 1209–1219 kJ mol^{-1} and the two low acidity sites T4 and T6 fall in the 1229–1238 kJ mol^{-1} range. If DPE differences within each interval are neglected, the following acidity ranking of the β-zeolite T sites can be finally written:

$$T8 \approx T7 \approx T9 > T5 \approx T1 \approx T3 \approx T2 > \approx T6 \approx T4 \quad (2)$$

This ⟨DPE⟩ order is obviously affected by the stability of the protonated form, which in turn depends on the occurring of hydrogen bond interactions. If only the most acidic site of each TnOm set is considered for the ranking, this one would become

$$T8 \approx T7 > T5 > T4 \approx T9 \approx T1 > T2 \approx T3 > T6 \quad (3)$$

with all the DPEs comprised in the 1179–1213 kJ mol^{-1} range. By comparing the two rankings above, the most striking difference is the position of T4, an issue which is not surprising since the most acid T4 site (T4O5) is also the least stable, being the very low acid T4O12 site the only one having an appreciable Boltzmann population at room temperature. Moreover, it is here to emphasize that the Boltzmann-averaged DPE ranking (2) could be somehow different if other computational approaches were employed; this not only for the approximations inherent in the modelistic choices but also for the intrinsic accuracy of energy differences calculated by (periodic) density functional theory, which could be pretty far from the chemical accuracy (4 kJ mol^{-1}) needed to obtain trustworthy Boltzmann populations. In particular, within the present investigated cases, we think that the position of T1 suffer from the largest uncertainty. As a matter of fact, T1 (and to a lesser extent T7) is the only site whose acidity is heavily affected by the Boltzmann averaging procedure (see Table 2); the two sites T1O2 and T1O4 are essentially isoenergetic but their DPEs differ by ca. 35 kJ mol^{-1} according to the cluster approach (and also according to the SIESTA one, see Table 1): if the error on their energy difference was ±4 kJ mol^{-1} (but almost surely it is much larger than this), the error on the ⟨DPE⟩ would be ±12 kJ mol^{-1}, meaning that T1 would be tossed either high or low on the acidity scale.

Finally, the discrepancy between the position of T8 in the acidity order calculated by our cluster approach (guessing T8 as the most acidic site) and the one reported by Vorontsov and Smirniotis [60] (putting T8 as the least acidic) is to be discussed. In fact, the difference between the raw, periodic, DPE values of T8 and of the most acidic site (T2) according to Vorontsov and Smirniotis is only ca. 8 kJ mol^{-1}, and could be affected by accuracy flaws. The T8 site is indeed in the least acidic range if our SIESTA values are considered, but it becomes the one with the lowest DPE after the application of the cluster approach correction.

4. Conclusions

The β-zeolite's Brønsted acidity has been characterized in terms of the deprotonation energy (DPE) values of 30 topologically distinct acidic sites. DPEs were computed through three different approaches within the DFT framework, namely: (i) an ONIOM embedding scheme, (ii) periodic calculations according to the SIESTA formalism and (iii) a novel cluster method specifically designed to avoid the disadvantages related to the other two approaches. By the cluster approach a range of nearly 60 kJ mol^{-1} was found which, divided into three equally spaced portions, gives 11, 11 and 8 sites setting high, medium and low Brønsted acidity, respectively. The formation of hydrogen bonds, actually detected in all the three groups of sites, was identified as a significant factor, if only to determine, within the same T site, to which oxygen atom the proton is preferentially bonded, hence site Boltzmann populations. As a matter of fact, if Boltzmann averaged DPE values are calculated, even considering that the limited accuracy of the computational methods could heavily influence the position of some sites in the acidity scale, it can be concluded that three acidity groups invariably exist, which are separated by about 10 kJ mol^{-1} one from the other. This insight on the acidity of β-zeolite as well as the relative topology can provide fundamental information for the use of this material in catalysis, orienting the active sites optimization through the occurring relationship between the aluminum placement and the activity/selectivity of the catalyst.

A general disagreement is found between the results obtained by the employed approaches, ONIOM, SIESTA and cluster, both in the absolute and relative DPE values. If the cluster method is taken as the most appropriate, this disagreement is to be attributed to the difficulty

in the definition of a generally reliable model system, in the case of ONIOM, and to the intrinsic problems of periodic formalisms related to charged cells, in the SIESTA case. Regarding the latter, it seems that the use of localized atomic orbitals, which defines the SIESTA formalism, leads to underestimate the site deprotonation energies in β-zeolite, oppositely to what happens in calculations based on plane waves, delocalized by definition. The suggested cluster approach, consisting in the evaluation of DPE by means of non-periodic single point DFT calculations starting from reshaped zeolite cell whose geometry was optimized by the SIESTA method, is therefore proposed as a suitable tool to correct in an algorithmic way the DPE values resulting from periodic calculations. This because it avoids the necessity of empirical corrections and constitutes a homogeneous computational model. Indeed, it would allow to treat essentially in the same modelistic way the zeolite acidic sites, possible modifiers of the acidity strength (like, *e.g.* defects or embedded metal particles) and the reactions in which zeolite catalytic activity is eventually involved. In the investigation of processes occurring inside the zeolite cavities, for example, the reacting molecule would conveniently result located at the center of the system, just like the zeolite proton itself. The simple cluster approach proposed in this work can be easily extended to other zeolite architectures without any conceptual modification.

CRediT authorship contribution statement

Laura Gueci: Conceptualization, Methodology, Investigation, Data curation, Writing – original draft. **Francesco Ferrante:** Conceptualization, Methodology, Data curation, Software, Writing – review & editing, Supervision. **Marco Bertini:** Investigation, Data curation, Software, Writing – review & editing. **Chiara Nania:** Investigation, Data curation, Writing – review & editing. **Dario Duca:** Conceptualization, Project administration, Writing – review & editing.

Declaration of competing interest

The authors declare that they have no known competing financial interests or personal relationships that could have appeared to influence the work reported in this paper.

Data availability

Optimized geometries and total energies of all the investigated structures.

Appendix A. Supplementary data

Supplementary material related to this article can be found online at https://doi.org/10.1016/j.commatsci.2023.112687.

References

[1] Y. Li, J. Yu, New stories of zeolite structures: their descriptions, determinations, predictions, and evaluations, Chem. Rev. 114 (2014) 7268–7316, http://dx.doi.org/10.1021/cr500010r.

[2] M. Dusselier, M.E. Davis, Small-pore zeolites: Synthesis and catalysis, Chem. Rev. 118 (2018) 5265–5329, http://dx.doi.org/10.1021/acs.chemrev.7b00738.

[3] P. Tamizhdurai, P.S. Krishnan, A. Ramesh, K. Shanthi, Isomerization of hydrocarbons over Pt supported on micro-mesoporous ZSM-5, Polyhedron 154 (2018) 314–324, http://dx.doi.org/10.1016/j.poly.2018.06.032.

[4] F. Berger, M. Rybicki, J. Sauer, Adsorption and cracking of propane by zeolites of different pore size, J. Catal. 395 (2021) 117–128, http://dx.doi.org/10.1016/j.jcat.2020.12.008.

[5] T. Kaka Khel, P. Maki-Arvela, M. Azkaar, Z. Vajglova, A. Aho, J. Hemming, et al., Hexadecane hydrocracking for production of jet fuels from renewable diesel over proton and metal modified H-beta zeolites, Mol. Catal. 476 (2019) 110515, http://dx.doi.org/10.1016/j.mcat.2019.110515.

[6] Z. Wen, H. Zhu, X. Zhu, Density functional theory study of the zeolite-catalyzed methylation of benzene with methanol, Catal. Lett. 150 (2020) 21–30.

[7] D. Yu Murzin, Acid site density as a kinetic descriptor of catalytic reactions over zeolites, Chemistry 4 (2022) 1609–1623, http://dx.doi.org/10.3390/chemistry4040105.

[8] A.A. Sadovnikov, O.V. Arapova, V. Russo, A.L. Maximov, D. Yu. Murzin, E.R. Naranov, Synergy of acidity and morphology of micro-/mesoporous materials in the solid-acid alkylation of toluene with 1-decene, Ind. Eng. Chem. Res. 61 (2022) 1994–2009, http://dx.doi.org/10.1021/acs.iecr.1c04169.

[9] C. Chizallet, C. bouchy, K. Larmier, G. Pirngruber, Molecular views on mechanisms of Brønsted acid-catalized reactions in zeolites, Chem. Rev. 123 (2023) 6107–6196, http://dx.doi.org/10.1021/acs.chemrev.2c00896.

[10] C. Liu, G. Li, E.J.M. Hensen, E.A. Pidko, Relationship between acidity and catalytic reactivity of faujasite zeolite: A periodic DFT study, J. Catal. 344 (2016) 570–577, http://dx.doi.org/10.1016/j.jcat.2016.10.027.

[11] A. Vjunov, J.L. Fulton, T. Huthwelker, S. Pin, D. Mei, G.K. Schenter, et al., Quantitatively probing the Al distribution in zeolites, J. Am. Chem. Soc. 136 (2014) 8296–8306, http://dx.doi.org/10.1021/ja501361v.

[12] D. Zhai, Y. Liu, H. Zheng, L. Zhao, J. Gao, C. Xu, et al., A first-principles evaluation of the stability, accessibility, and strength of Brønsted acid sites in zeolites, J. Catal. 352 (2017) 627–637, http://dx.doi.org/10.1016/j.jcat.2017.06.035.

[13] R. Zhao, Z. Zhao, S. Li, W. Zhang, Insights into the correlation of aluminum distribution and Brønsted acidity in H-Beta zeolites from solid-state NMR spectroscopy and DFT calculations, J. Phys. Chem. Lett. 8 (2017) 2323–2327, http://dx.doi.org/10.1021/acs.jpclett.7b00711.

[14] F. Arena, F. Ferrante, R. Di Chio, G. Bonura, F. Frusteri, L. Frusteri, et al., DFT and kinetic evidences of the preferential CO oxidation pattern of manganese dioxide catalysts in hydrogen stream (PROX), Appl. Catal. B 300 (2022) 120715, http://dx.doi.org/10.1016/j.apcatb.2021.120715.

[15] F. Ferrante, A. Prestianni, M. Bertini, D. Duca, H_2 transformations on graphene supported palladium cluster: DFT-MD simulations and NEB calculations, Catalysts 10 (2020) http://dx.doi.org/10.3390/catal10111306.

[16] F. Ferrante, C. Nania, D. Duca, Computational investigation of isoeugenol transformations on a platinum cluster – I: Direct deoxygenation to propylcyclohexane, Mol. Catal. 529 (2022) 112541, http://dx.doi.org/10.1016/j.mcat.2022.112541.

[17] F. Ferrante, M. Bertini, C. Ferlito, L. Lisuzzo, G. Lazzara, D. Duca, A computational and experimental investigation of halloysite silicic surface modifications after alkaline treatment, Appl. Clay Sci. 232 (2023) 106813, http://dx.doi.org/10.1016/j.clay.2022.106813.

[18] L. Gueci, F. Ferrante, A. Prestianni, R. Di Chio, A.F. Patti, D. Duca, et al., DFT insights into the oxygen-assisted selective oxidation of benzyl alcohol on manganese dioxide catalysts, Inorg. Chim. Acta. 511 (2020) 119812, http://dx.doi.org/10.1016/j.ica.2020.119812.

[19] L. Gueci, F. Ferrante, A. Prestianni, F. Arena, D. Duca, Benzyl alcohol to benzaldehyde oxidation on MnO_x clusters: Unraveling atomistic features, Mol. Catal. 513 (2021) 111735, http://dx.doi.org/10.1016/j.mcat.2021.111735.

[20] C. Nania, M. Bertini, L. Gueci, F. Ferrante, D. Duca, DFT insights into competing mechanisms of guaiacol hydrodeoxygenation on a platinum cluster, Phys. Chem. Chem. Phys. 25 (2023) 10460–10471, http://dx.doi.org/10.1039/D2CP06077A.

[21] R. Cortese, D. Campisi, A. Prestianni, D. Duca, Alkane dehydrogenation on defective BN quasi-molecular nanoflakes: DFT studies, Mol. Catal. 493 (2020) 110891, http://dx.doi.org/10.1016/j.mcat.2020.110891.

[22] L. Gueci, M. Bertini, C. Nania, F. Ferrante, D. Duca, DFT study of Pt particle growth inside β-zeolite cages, J. Phys. Chem. C 127 (2023) 14765–14775, http://dx.doi.org/10.1021/acs.jpcc.3c02957.

[23] E. Broclawik, P. Kozyra, M. Mitoraj, M. Radon, P. Rejmak, Zeolites at the molecular level: What can be learned from molecular modeling, Molecules 26 (2021) http://dx.doi.org/10.3390/molecules26061511.

[24] F. Ferrante, T. Rubino, D. Duca, Butene isomerization and double-bond migration on the H-ZSM-5 outer surface: A density functional theory study, J. Phys. Chem. C 115 (2011) 14862–14868, http://dx.doi.org/10.1021/jp203284f.

[25] A.V. Vorontsov, H. Valdes, G.S. Smirniotis, Design of active sites in zeolite catalysts using modern semiempirical methods: The case of mordenite, Comput. Theor. Chem. 1166 (2019) 112572, http://dx.doi.org/10.1016/j.comptc.2019.112572.

[26] L.E. Sandoval-Diaz, J.A. Gonzalez-Amaya, C.A. Trujillo, General aspects of zeolite acidity characterization, Microporous Mesop. Mater. 215 (2015) 229–243, http://dx.doi.org/10.1016/j.micromeso.2015.04.038.

[27] P. Sazama, E. Tabor, P. Klein, B. Wichterlova, S. Sklenak, L. Mokrzycki, et al., Al-rich beta zeolites. Distribution of Al atoms in the framework and related protonic and metal-ion species, J. Catal. 333 (2016) 102–114, http://dx.doi.org/10.1016/j.jcat.2015.10.010.

[28] M. Boronat, A. Corma, What is measured when measuring acidity in zeolites with probe molecules? ACS Catal. 9 (2019) 1539–1548, http://dx.doi.org/10.1021/acscatal.8b04317.

[29] S. Li, Z. Zhao, R. Zhao, D. Zhou, W. Zhang, Aluminum location and acid strength in an aluminum-rich beta zeolite catalyst: A combined density functional theory and solid-state NMR study, ChemCatChem 9 (2017) 1494–1502, http://dx.doi.org/10.1002/cctc.201601623.

[30] S. Wang, Y. He, W. Jiao, J. Wang, W. Fan, Recent experimental and theoretical studies on Al siting/acid site distribution in zeolite framework, Curr. Opin. Chem. Eng. 23 (2019) 146–154, http://dx.doi.org/10.1016/j.coche.2019.04.002.

[31] M. Niwa, K. Suzuki, N. Katada, T. Kanougi, T. Atoguchi, Ammonia IRMS-TPD study on the distribution of acid sites in mordenite, J. Phys. Chem. B 109 (2005) 18749–18757, http://dx.doi.org/10.1021/jp051304g.
[32] K. Suzuki, N. Katada, M. Niwa, Detection and quantitative measurements of four kinds of OH in HY zeolite, J. Phys. Chem. C 111 (2007) 894–900, http://dx.doi.org/10.1021/jp065054v.
[33] K. Suzuki, G. Sastre, N. Katada, M. Niwa, Ammonia IRMS-TPD measurements and DFT calculation on acidic hydroxyl groups in CHA-type zeolites, Phys. Chem. Chem. Phys. 9 (2007) 5980–5987, http://dx.doi.org/10.1039/B711961E.
[34] N. Katada, H. Tamagawa, M. Niwa, Quantitative analysis of acidic OH groups in zeolite by ammonia IRMS-TPD and DFT: Application to BEA, Catal. Today 226 (2014) 37–46, http://dx.doi.org/10.1016/j.cattod.2013.08.006.
[35] M. Trachta, O. Bludský, R. Vakulík J. Bulánek, M. Rubeš, Investigation of Brønsted acidity in zeolites through adsorbates with diverse proton affinities, Sci. Rep. 13 (2023) 12380, http://dx.doi.org/10.1038/s41598-023-39667-5.
[36] A.J. Jones, E. Iglesia, The strength of Brønsted acid sites in microporous aluminosilicates, ACS Catal. 5 (2015) 5741–5755, http://dx.doi.org/10.1021/acscatal.5b01133.
[37] M. Brändle, J. Sauer, Acidity differences between inorganic solids induced by their framework structure, a combined quantum mechanics/molecular mechanics ab initio study on zeolites, J. Am. Chem. Soc. 120 (1998) 1556–1570, http://dx.doi.org/10.1021/ja9729037.
[38] U. Eichler, M. Brändle, J. Sauer, Predicting absolute and site specific acidities for zeolite catalysts by a combined quantum mechanics/interatomic potential function approach, J. Phys. Chem. B 101 (1997) 10035–10050, http://dx.doi.org/10.1021/jp971779a.
[39] A.J. Jones, R.T. Carr, S.I. Zones, E. Iglesia, Acid strength and solvation in catalysis by MFI zeolites and effects of the identity, concentration and location of framework heteroatoms, J. Catal. 312 (2014) 58–68, http://dx.doi.org/10.1016/j.jcat.2014.01.007.
[40] P. Deshlahra, E. Iglesia, Reactivity descriptors in acid catalysis: acid strength, proton affinity and host–guest interactions, Chem. Commun. 56 (2020) 7371–7398, http://dx.doi.org/10.1039/D0CC02593C.
[41] J. Sauer, M. Sierka, Combining quantum mechanics and interatomic potential functions in ab initio studies of extended systems, J. Comput. Chem. 21 (2000) 1470–1493, http://dx.doi.org/10.1002/1096-987X(200012)21:16<1470::AID-JCC5>3.0.CO;2-L.
[42] M. Rybicki, J. Sauer, Acid strength of zeolitic Brønsted sites - dependence on dielectric properties, Catal. Today 323 (2019) 86–93, http://dx.doi.org/10.1016/j.cattod.2018.04.031.
[43] C. Freysoldt, J. Neugebauer, C.G. Van de Walle, Fully ab initio finite-size corrections for charged-defect supercell calculations, Phys. Rev. Lett. 102 (2009) 016402, http://dx.doi.org/10.1103/PhysRevLett.102.016402.
[44] F. Bruneval, J.P. Crocombette, X. Gonze, B. Dorado, M. Torrent, F. Jollet, Consistent treatment of charged systems within periodic boundary conditions: The projector augmented-wave and pseudopotential methods revisited, Phys. Rev. B 89 (2014) 045116, http://dx.doi.org/10.1103/PhysRevB.89.045116.
[45] M. Trachta, R. Bulánek, O. Bludský, M. Rubeš, Brønsted acidity in zeolites measured by deprotonation energy, Sci. Rep. 12 (2022) 7301, http://dx.doi.org/10.1038/s41598-022-11354-x.
[46] P. Boron, M. Rutkowska, B. Gil, B. Marszalek, L. Chmielarz, S. Dzwigaj, Experimental evidence of the mechanism of selective catalytic reduction of NO with NH_3 over Fe-containing BEA zeolites, ChemSusChem 12 (2019) 692–705, http://dx.doi.org/10.1002/cssc.201801883.
[47] G.J. Gomes, M.F. Zalazar, C.A. Lindino, F.R. Scremin, P.R.S. Bittencourt, M.B. Costa, et al., Adsorption of acetic acid and methanol on H-beta zeolite: An experimental and theoretical study, Microporous Mesop. Mater. 252 (2017) 17–28, http://dx.doi.org/10.1016/j.micromeso.2017.06.008.
[48] S. Klinyod, B. Boekfa, S. Pornsatitworakul, T. Maihom, N. Jarussophon, P. Treesukol, et al., Theoretical and experimental study on the 7-hydroxy-4-methylcoumarin synthesis with H-beta zeolite, ChemistrySelect 4 (2019) 10660–10667.
[49] Z. Lei, L. Liu, C. Dai, Insight into the reaction mechanism and charge transfer analysis for the alkylation of benzene with propylene over H-beta zeolite, Mol. Catal. 454 (2018) 1–11, http://dx.doi.org/10.1016/j.mcat.2018.05.010.
[50] P.S.F. Mendes, C. Chizallet, J. Perez-Pellitero, P. Raybaud, J.M. Silva, M.F. Ribeiro, et al., Interplay of the adsorption of light and heavy paraffins in hydroisomerization over H-beta zeolite, Catal. Sci. Technol. 9 (2019) 5368–5382, http://dx.doi.org/10.1039/C9CY00788A.
[51] R. Barakov, N. Shcherban, P. Maki-Arvela, P. Yaremov, I. Bezverkhyy, J. Warna, et al., Hierarchical beta zeolites as catalysts in α-pinene oxide isomerization, ACS Sustain. Chem. Eng. 10 (2022) 6642–6656, http://dx.doi.org/10.1021/acssuschemeng.2c00441.
[52] Database of zeolite structures, 2020, @http://www.iza-structure.org/databases/ URL http://www.iza-structure.org/databases/. (Accessed 17 July 2020).
[53] K. Momma, F. Izumi, VESTA 3 for three-dimensional visualization of crystal, volumetric and morphology data, J. Appl. Crystallogr. 44 (2011) 1272, http://dx.doi.org/10.1107/S0021889811038970.
[54] M.J. Frisch, G.W. Trucks, H.B. Schlegel, G.E. Scuseria, M.A. Robb, J.R. Cheeseman, et al., Gaussian16 Revision C.01, Gaussian Inc., Wallingford CT, 2016.
[55] S. Grimme, Supramolecular binding thermodynamics by dispersion-corrected density functional theory, Chem. Eur. J. 18 (2012) 9955, http://dx.doi.org/10.1002/chem.201200497.
[56] J.M. Soler, E. Artacho, J.D. Gale, J. García A. Junquera, P. Ordejón, et al., The SIESTA method for ab initio order-N materials simulation, J. Phys.: Condens. Matter. 14 (2002) 2745–2779, http://dx.doi.org/10.1088/0953-8984/14/11/302.
[57] M.J. van Setten, M. Giantomassi, E. Bousquet, M.J. Verstraete, D.R. Hamann, X. Gonze, et al., The PseudoDojo: Training and grading a 85 element optimized norm-conserving pseudopotential table, Comput. Phys. Commun. 226 (2018) 39–54, http://dx.doi.org/10.1016/j.cpc.2018.01.012.
[58] A. Garcia, M.J. Verstraete, Y. Pouillon, J. Junquera, The PSML format and library for norm-conserving pseudopotential data curation and interoperability, Comput. Phys. Commun. 227 (2018) 51–71, http://dx.doi.org/10.1016/j.cpc.2018.02.011.
[59] C. Freysoldt, J. Neugebauer, C.G. Van de Walle, Electrostatic interactions between charged defects in supercells, Phys. Status Solidi b 248 (2011) 1067–1076, http://dx.doi.org/10.1002/pssb.201046289.
[60] A.V. Vorontsov, P.G. Smirniotis, DFT study on the stability and the acid strength of Brønsted acid sites in zeolite β, J. Phys. Chem. A 126 (2022) 7840–7851, http://dx.doi.org/10.1021/acs.jpca.2c04872.

THE JOURNAL OF PHYSICAL CHEMISTRY C
A JOURNAL OF THE AMERICAN CHEMICAL SOCIETY

pubs.acs.org/JPCC

Article

DFT Study of Pt Particle Growth inside β-Zeolite Cages

Laura Gueci, Marco Bertini, Chiara Nania, Francesco Ferrante,* and Dario Duca

Cite This: J. Phys. Chem. C 2023, 127, 14765−14775

Read Online

ACCESS | Metrics & More | Article Recommendations | Supporting Information

ABSTRACT: The preferred location and the corresponding energetics of zeolite-embedded single metal atoms and small metal particles are hot topics within active site optimization and catalyst tuning, even as part of bifunctional materials design. In this context, periodic density functional theory was used to provide insights on the interactions of a platinum atom with the microporous cages of a purely silicious β-zeolite (BEA) framework. Cluster growth was subsequently addressed, up to Pt_3@BEA systems, following a one-by-one platinum atom addition; platinum migration between cages was taken into account as well. An unbiased approach was employed, which allowed a wide panorama of structures being considered in addition to a thorough analysis in terms of energetics, cluster geometries, and cavity distortions. Calculations revealed that the optimal interaction geometry for a single platinum atom is realized where two strong Pt−O bonds in almost linear arrangement can form, regardless of the cavity involved. This can cause distortions or even breaking of the zeolite structure, a factor which however is not decisive in determining the energetics of systems with two and three platinum atoms. Platinum migration is associated with energy barriers ranging from 100 to 200 kJ mol^{-1}, depending on the cages. Up to the dimensions considered here, preference for clustering is observed, being the embedded Pt_3 systems in almost all cases energetically favored with respect to isolated atoms within the BEA framework.

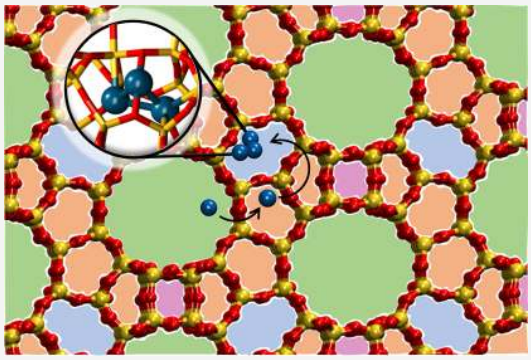

INTRODUCTION

Zeolites are crystalline aluminosilicates successfully used as heterogeneous catalysts in many acid-catalyzed reactions due to their well-determined topology and microporous structure, together with the associated adsorption and shape-selective properties.[1,2] Hydroisomerization and hydrocracking of paraffins, alkylation, alkoxylation, and selective reduction of nitrogen oxides provide some examples of processes exploiting zeolites Brønsted acid strength. This is associated with the silicon−aluminum framework substitution and the addition of a charge compensating H^+ cation.[3−6] A key factor in these applications is the presence of metallic components, thus forming bifunctional catalysts[7] that exploit the hydrogenation/dehydrogenation activity of a noble metal such as platinum or palladium. As an acidic component, β-zeolite (BEA) is one of the most notable and extensively used.[8−12] In the BEA structure, silicon and oxygen atoms are linked together to form 3D intersecting 12-membered rings (diameter of 6−7 Å along the [010] and [100] axes, 5−6 Å along [001]), together with 6-, 5-, and 4-membered rings. These give raise to smaller pores which are still wide enough to host metal atoms.[13−15] However, in general, the metal can be located not only inside the cavities but also on the outer surface of the crystals or even supported on an inorganic binder in composite materials.[16−18] Many experimental efforts have been addressed to study the effects of synthesis variables on the metal location and particle dispersion, which in turn affect the activity and selectivity of the catalyst.[19−23] In this respect, a prominent role is played also by the defective sites (mostly silanol groups located on the mesopore surface) of which BEA is particularly abundant;[24,25] synthetic strategies can be tuned to exploit defective sites in order to enhance the catalytic activities.[26]

The advantages of an atomistic approach on tuning catalyst properties are well established.[27−39] In particular, computational chemistry, mostly based on density functional theory (DFT), had an enormous impact on the development of zeolite catalytic materials and processes.[40−46] As a matter of fact, while Hou et al.[47] have investigated, by means of periodic DFT calculations, the stabilization of platinum atoms and/or clusters inside the cavities of medium-size high-silica zeolites (i.e., LTA, SOD, CHA, FAU), to the best of our knowledge, a step-by-step computational approach on platinum clustering inside large pores of aluminosilicates is still missing. In fact, commonly either singly supported platinum atoms or Pt nanoparticles are considered, without giving any idea about their formation yet.[48−50] In this context, the present work aims at providing atomistic-level insights on (i) the preferential

Received: May 5, 2023
Revised: July 10, 2023
Published: July 20, 2023

location of a platinum atom embedded in β-zeolite cages, (ii) the energetics related to platinum atoms' migration, and (iii) the cluster growth process up to a Pt_3 seed. The investigation employs a one-by-one atom addition approach driven by an unbiased algorithm, described in the next section. Thus, a wide panorama of structures being considered, the analysis is performed on energetics, cluster geometries, and cavity distortions. Migration of a platinum atom between different zeolite cages is also addressed, searching for the related transition state. For the here-reported study, a pristine BEA structure was employed, being this the necessary starting point for every wider investigation aiming at the characterization of the growth energetics of metal particles in β-zeolite models, which include, e.g., aluminum substitution in different ratios and the presence of various kinds of defects.

MODELS AND METHODS

The structural model used for periodic DFT calculations is the β-zeolite unit cell (a = 12.631 Å, b = 12.631 Å, c = 26.186 Å; $\alpha = \beta = \gamma = 90°$) taken from the crystallographic information file provided by the International Zeolite Association (IZA) website.[13] The model structure, see Figure 1, is reported in

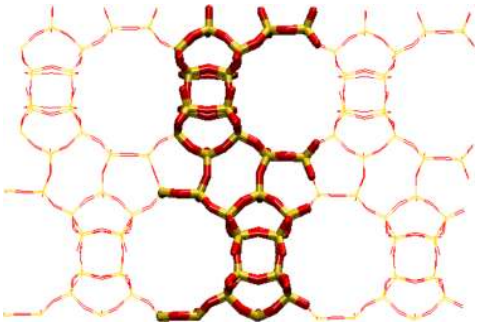

Figure 1. BEA unit cell of 192 atoms (licorice representation; O = red, Si = yellow), within the periodic framework (wired representation), viewed along the ac plane. The used cell parameters are $a = b$ = 12.631 Å, $=c$ = 26.186 Å, and $\alpha = \beta = \gamma = 90°$.

the IZA atlas as a mixture of α and β BEA polymorphs, most properly labeled as *BEA. After geometry optimization of the silicate structure, a comprehensive mapping of the embedding sites was performed, with the systematic approach described below, aimed at locating the preferred position for single platinum atoms. Due to the great variety of topological sites characterizing the β-zeolite, an unbiased approach is desirable to fix the starting coordinates of the platinum atoms within the structure. Only by this leading scenario, after geometry optimization of the embedded platinum fragments, it is conceivable to obtain minima suitable to characterize the potential energy surface originating by the different starting configurations. Therefore, the following procedure was implemented. A 3D grid of points with predefined thickness was created to map the BEA unit cell, resulting in 10 points along a and b crystallographic axes (from the 0.00 to the 12.43 coordinate, in Å) and 20 points along c (from 0.00 to 26.21 Å). Each of the 2000 grid points represents a possible set of xyz coordinates of an embedded platinum atom. Cases in which the added Pt atom resulted too close to the silicon and/or oxygen atoms of the zeolite framework were excluded based on the van der Waals radii. In particular, the minimum Pt−O (or Pt−Si) distance threshold of 1.8 Å was chosen. In order to discard those geometries showing weak platinum−zeolite interactions, it was fixed, as a further constraint, that the distance between Pt and the nearest framework center should not exceed 3.0 Å. This way 683 cases out of thousands were selected. Single-point calculations were performed on the latter, and relative energies were used to sort the structures in order of stability. Noticeably, many of them showed almost the same energy, which was ascertained to correspond to similar, if not identical, structures. A relative energy threshold (first sieve) allowed us to single out the most promising 14 cases among the 683. These were subjected to the ensuing geometry optimization procedure, which let some structures to collapse to the same geometry minimum (second sieve) and left only 8 Pt-zeolite structures. Following this, another energetic filter (third sieve), ruled by visual inspection, allowed us to select new geometries where to add a second platinum atom. Starting from the creation of a grid of points inside the unit cell, the procedure was repeated on each of these selected geometries to find the best arrangments for two platinum atoms inside the zeolite cages and repeated once again for the Pt_3@BEA case. For systems with two or three Pt atoms, minimum and maximum Pt−X (X = Si, O, Pt) distances have also been set. That is, the coordinates of the new atom were accepted if the distance with respect to the platinum atom(s) already present was within the range 2.4−2.8 Å, the thresholds with silicon and oxygen being the same as before. Moreover, the grid step was adjusted to locate a greater number of geometries in the proximity of the already adsorbed Pt center(s). The flowchart of this procedure, aimed at including the largest number of significant structures, is illustrated in Scheme 1. The information related to the different steps of the algorithm for the three Pt_n systems is reported in Table 1. It must be stressed that the criteria adopted for the sieves aimed at reducing the number of possible structures to investigate by isolating the most significant cases. Due to the topological heterogeneity of the analyzed systems, the energetic threshold values were varied, being lower when the number of structures to be selected was greater. In any case, in the course of the analysis, structures were also included, irrespective of their relative energetic stability, which after an accurate visual inspection showed a heuristic potential to evolve into structures of likely interest, when the number of included platinum atoms changed.

The cluster growth was evaluated calculating the ΔE for the following processes:

$$2Pt@BEA \rightarrow Pt_2@BEA + BEA \quad (1)$$

$$3Pt@BEA \rightarrow Pt_3@BEA + 2BEA \quad (2)$$

$$Pt_2@BEA + Pt@BEA \rightarrow Pt_3@BEA + BEA \quad (3)$$

where the reactants are the same zeolite fragments in which either two or three platinum atoms or a single atom with a diatomic cluster was adsorbed but did not interact with each other. The products instead represent a zeolite in which a platinum cluster is formed. A negative value of the concurrent energy differences means that the product cluster formation inside the zeolite is favored.

In order to investigate the distortions of the zeolite cavities produced by the embedding of platinum atoms, a point R, whose coordinates matched those of the first embedded platinum atom, was chosen, and around this, the zeolite nuclei distribution was explored. In these structures, all O−R and Si−

https://doi.org/10.1021/acs.jpcc.3c02957
J. Phys. Chem. C 2023, 127, 14765−14775

Scheme 1. Flowchart of the Algorithm Employed to Locate the Preferential Position of a Single Platinum Atom and to Study the Cluster Formation[a]

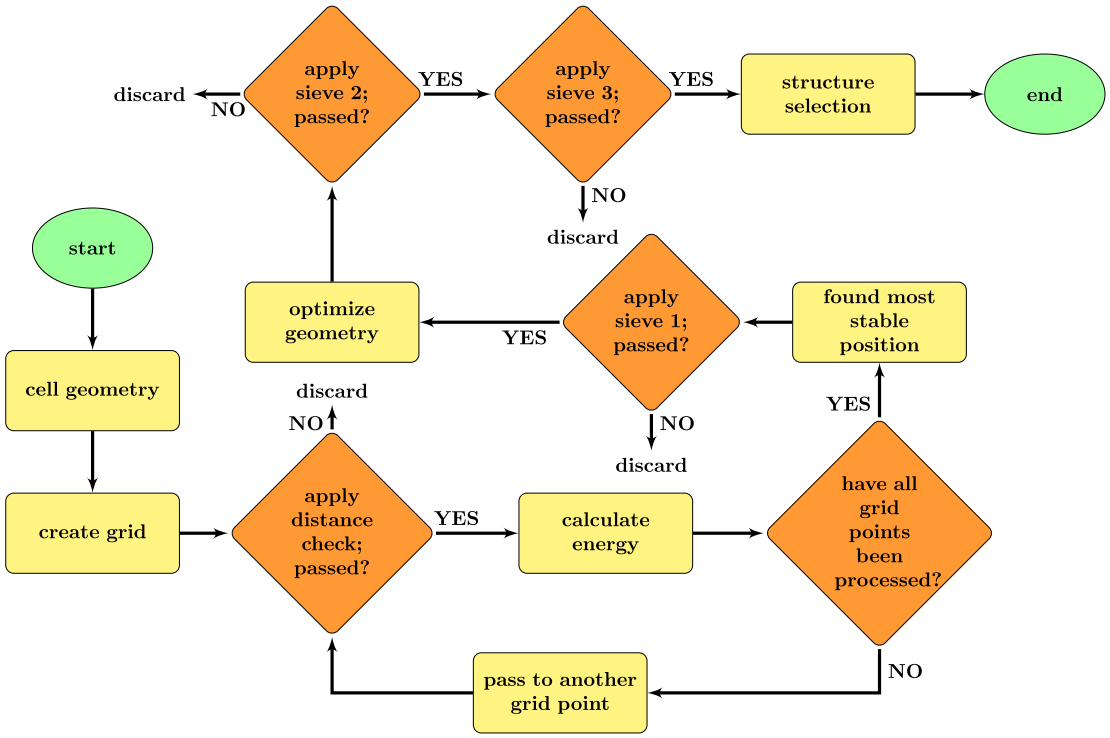

[a]At the beginning of the procedure, the starting geometry is the optimized silicate framework; selected geometries are then used as input for the second and third platinum atom addition.

Table 1. Numbers of Structures Following the Application of the Three Sieves Characterizing the Systems with One, Two, and Three Platinum Atoms

	starting structures	structures after		
		1st sieve[a]	2nd sieve[a]	3rd sieve[a,b]
Pt_1@BEA	683	14	8	4
Pt_2@BEA	10, 19, 61, 58	40	3, 4, 3, 2	5
Pt_3@BEA	17, 18, 17, 17, 29	20	2, 3, 2, 4, 3	

[a]For details on the procedure summarized by the term "sieve", see the text and Scheme 1. [b]The third sieve selects the m most stable structures with n Pt atoms and allows one to pick out m sets of new starting structures containing $n + 1$ Pt atoms. For example, after having applied the third sieve to the Pt_1@BEA case, four geometries are left, which can be labeled a, b, c, and d; a second Pt atom is added to each of these so that 148 starting structures are built for the Pt_2@BEA system, i.e., 10 structures originating from a, 19 structures from b, 61 from c, and 58 from d.

R distances (corresponding to the O−Pt and Si−Pt distances in the Pt-zeolite system) were computed and then sorted in increasing order. After choosing an exploration radius around R, all of the nuclei at a distance greater than this radius were discarded, thus narrowing the analysis focus closer to R. Considering the cell parameters of the employed model, we chose a value of 6.2 Å for the exploration radius, thus avoiding spurious effects caused by periodic boundary conditions, while still encompassing an appropriately large number of zeolite nuclei. For each oxygen and silicon center included in the exploration radius of single couples of pristine and platinum-embedded structures, two displacements are computed. The first is the absolute displacement of nucleus A, $\Delta_a^A \equiv |\mathbf{R}_p^A - \mathbf{R}_e^A|$, attributable to the platinum presence, where $\mathbf{R}_p^A$ are the coordinates of A in the pristine zeolite and $\mathbf{R}_e^A$ are those in the embedded zeolite. The second, conversely, is the radial displacement of A with respect to the central point R, $\Delta_r^A \equiv |\mathbf{R}_e^A - \mathbf{R}| - |\mathbf{R}_p^A - \mathbf{R}|$.

COMPUTATIONAL DETAILS

All calculations were performed within the density functional theory framework (DFT) by using the SIESTA approach as implemented in the code bearing the same name.[51] The PBE exchange−correlation functional in the spin-polarized form was chosen,[52] along with a double-ζ quality numerical basis set. Sampling of reciprocal space was performed using a 2 × 2 × 2 Monkhorst−Pack grid and a value of 450 Ry for the mesh cutoff. Preliminary calculations performed in selected cases allowed us to conclude that a larger Monkhorst−Pack grid affected the energy of the investigated systems in a negligible way.

The search for transition states associated with the Pt atom migration was performed by means of the Empathes code,[53] which implements the nudged elastic band method (NEB) and is interfaced with the SIESTA program. Every NEB calculation used 8 images, generated by the image-dependent pair potential approach and connected each other by dynamic springs. The FIRE algorithm was employed to optimize the elastic band, with a convergence threshold of (5×10^{-3} E_h/Å) on the norm of NEB total forces.

RESULTS AND DISCUSSION

Single Pt Atom Embedded in BEA Cages. As shown by Table 1, 8 different structures have been identified for the

https://doi.org/10.1021/acs.jpcc.3c02957
J. Phys. Chem. C 2023, 127, 14765−14775

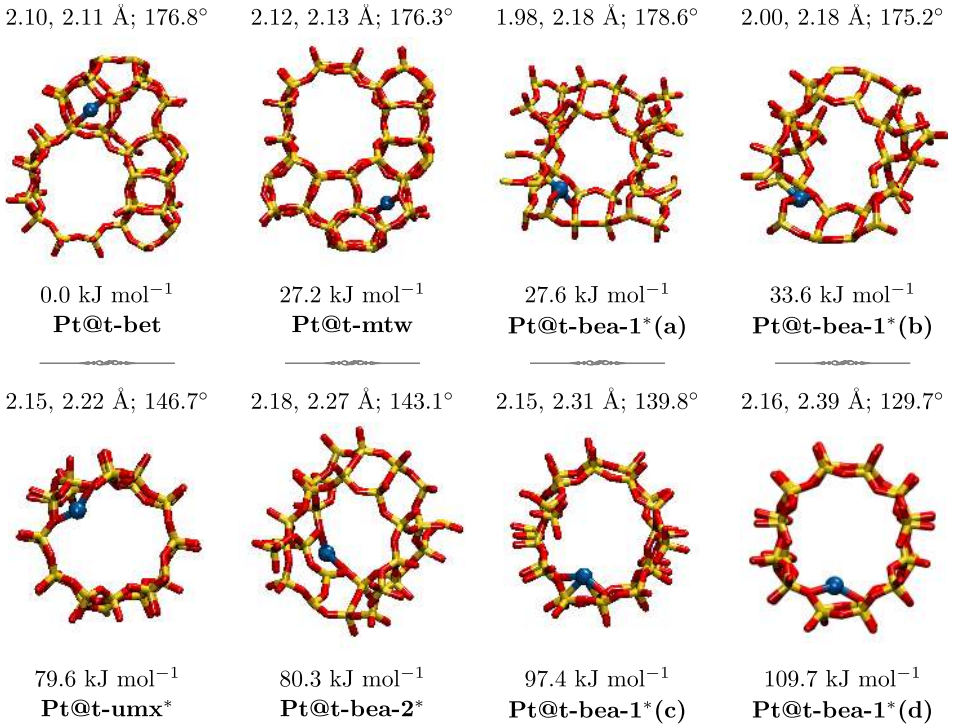

Figure 2. Local views of the eight Pt@BEA-optimized geometries (O = red, Si = yellow, Pt = blue). Relevant Pt−O distances and O−Pt−O angles are reported above each structure; below there are the relative energy values, calculated with respect to the more stable species, along with the tiling arrangement labels used to identify, in accordance with IZA,[13] the cavity in which the platinum atom is located.

adsorption of a single platinum atom within the BEA framework. In these, the metal atom is inside a unique zeolite cavity. The energy differences characterizing the various structures can be attributed to the occurrence of different local topologies. It is noteworthy that, even if spin-polarized calculations were performed, the results obtained for all of the investigated systems always indicate a singlet multiplicity state. As a matter of fact, this is in agreement with other evidences of spin-state lowering that takes place in the supported system when a platinum atom is interacting with the zeolite framework with respect to unsupported ones.[47] Figure 2 shows a local view of the eighth optimized geometries. To emphasize the visualization of the rings and cavities involved, it was decided to not show the whole unit cell. In each case, a portion of the zeolite framework close to the Pt atom was conversely selected for the image representation, obtained by repeating the unit cell in space when needed. In accordance with the tiling arrangement accepted by IZA,[13] the optimized structures can be divided into the following five groups:

- t-bet cavity, in which the Pt atom interacts with 5-membered rings (5T);
- t-mtw cavity, with the Pt atom located in-between two 6-membered rings;
- t-bea-1* cavity, where the Pt atom protrudes toward the main channel and interacts with 5T or 4T rings;
- t-umx* cavity, in which the Pt atom interacts with a 6T ring in a main channel; and
- t-bea-2* cavity, where the Pt atom located in the main channel is near but not inside the t-bet cavity.

Among the final Pt@BEA systems investigated here, four cases can be assigned to the t-bea-1* cavity and these, in order to be distinguished, are labeled with additional letters "a−d". In Figure 2, significant structural parameters are shown above the corresponding structures. In details they are the bond distances between platinum and the two nearest oxygen atoms and the related O−Pt−O bond angle. Finally, relative energies are also indicated. These were calculated as the difference between the energy corresponding to the structure of the involved system and that of the most stable one, taken as reference. Accordingly, an order of stability among the structures could be extrapolated. Those containing the t-bet smallest cavities resulted preferred, followed by those showing 6T ring pores. Systems in which platinum is located within the main channel are up to 80−110 kJ mol^{-1} higher in energy with respect to the most stable Pt@t-bet species.

Analyzing things more in depth, it can be inferred that this trend is not strictly dependent on the channel sizes but rather on local interactions involving different zeolite surface fragments and metal atoms. In detail, in the most stable configurations, platinum is found to form strong bonds with a couple of oxygen atoms (2.09−2.12 Å) and, more importantly, an almost straight O−Pt−O bond angle. In particular, it seems that, regardless of the involved cavity size, optimized structures are more stable when the O−Pt−O angle is close to 180°. In this context, it is possible to frame the energetics of Pt@t-bea-1*(a) and Pt@t-bea-1*(b) species, showing O−Pt−O angles of 178.6 and 175.2°, respectively. In these, the platinum atom embedded in the main channel is in fact stabilized by an energy that is close to that observed for the same metal atom when allocated in a smaller cavity. It can be conversely observed that the four t-bea-1* fragments hosting the platinum atom in the same cavity show energies that vary in a significant way, and stronger interactions invariably occur when the O−Pt−O bond angle is almost linear. Finally, it is important to note that in the case of Pt@t-bea-1*(a) and Pt@t-bea-1*(b) species, the formation of this particular bond angle was driven by the

https://doi.org/10.1021/acs.jpcc.3c02957
J. Phys. Chem. C 2023, 127, 14765−14775

displacement of an oxygen atom from the silicon to which it was bonded, resulting in a visible alteration of the framework regularity, which will be further discussed later on.

Pt Migration. In the hypothesis that a given metal atom approaches the smaller cages of a zeolite from its main channels, platinum migration from the latter to the Pt@t-bet cavity was modeled according to this mechanism. The metal shift between the two smaller cavities was also studied. In the first process, the Pt@t-bea-1*(b) species was chosen as the starting arrangement to represent a system bearing a platinum atom in the main channel. From this, the Pt atom shift took place in two steps, going through an intermediate, which resulted to be 20.5 kJ mol^{-1} more stable than the corresponding system and 13.1 kJ mol^{-1} higher in energy if compared with the final one (see Figure S1). The two energy barriers, namely, those from the reactant to the intermediate and from this one to the Pt@t-bet product resulted 102.6 and 127.6 kJ mol^{-1}, respectively.

In the second process, the platinum atom migrates in a single step (an high energy ephemeral intermediate is actually in the path), crossing the wall that separates the two cavities; the associated energy barrier was equal to 203.4 kJ mol^{-1}. It is interesting to note that, over the minimum energy path found by the NEB calculation (Figure S2), the platinum atom rotates by pivoting on an oxygen bridging the two cavities. As a consequence, a breakage in the zeolite structure is observed, while the O−Si bond distances get back to the usual values in the product. The occurrence of structures that show the breaking of the zeolite framework deserves further discussion. In fact, this has already been discussed in the literature for zeolites with 6-membered rings,[47] where that situation represented the most stable configuration for an embedded platinum atom. In our case, it is interesting to note how geometries were found in which the breaking occurred in the proximity of a 5T ring. This kind of structure, however, features an energy sensibly higher than that of the stablest structures found with the systematic search algorithm employed in the present work (see Scheme 1).

Pt_2 and Pt_3 Clusters inside the BEA Framework. Starting from the four most stable geometries with one adsorbed platinum atom, 12 cases of Pt_2@BEA systems have been identified (see Table 1) and five were selected after having applied the third sieve. All systems, whose optimized geometries are reported in Figure 3, resulted to be in a singlet multiplicity state. In the most stable of them, the second platinum atom (i) is placed at about 2.5 Å from the first, (ii) slightly protrudes into the main zeolite channel, and (iii) attracts one oxygen atom forming an almost straight bond angle. Two pretty similar cases follow. In this, once again, the first platinum atom is located in the t-mtw cavity and the second, positioned in the main t-bea-1* channel, attracts one oxygen atom toward itself to form an almost linear bond angle. In a ca. 50 kJ mol^{-1} less stable arrangement, the first Pt atom is located in the smaller t-bet cavity, while the second, at 2.87 Å from the first, protrudes into the main channel and causes the rupture of the zeolite framework with the formation of a 176.7° O−Pt−O bond angle. Notably, two of these platinum−oxygen interactions, which seemingly rule the energetics of Pt@BEA adducts, are present. Since the analysis performed on the framework (see the "Cavity Distortions" section) showed minor distortions, the lower stability of this system can be interpreted in terms of the Pt−Pt distance. In fact, the interaction between the two metal atoms is rather weak, being

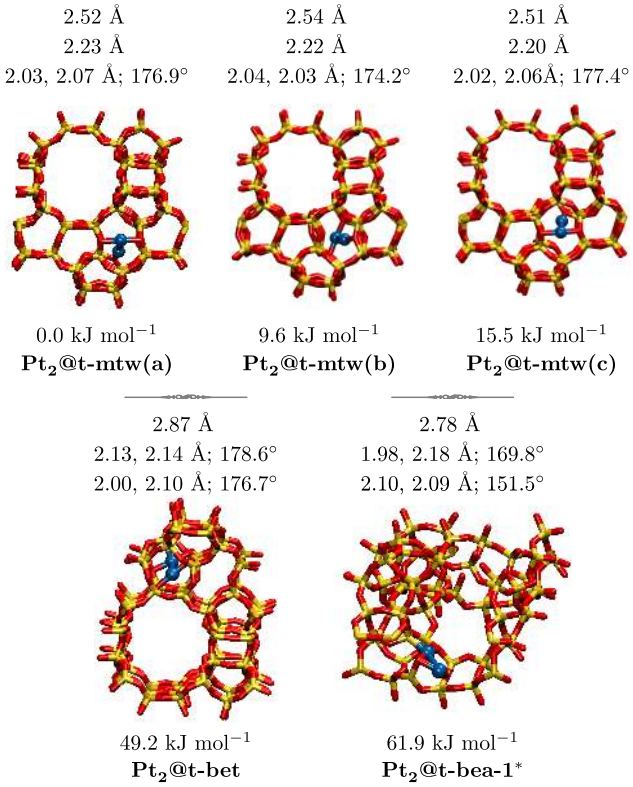

Figure 3. Local views of the five Pt_2@BEA-optimized geometries (O = red, Si = yellow, Pt = blue). Above each structure, the Pt−Pt bond distance is reported, together with relevant Pt−O distances and O−Pt−O angles for the first and the second embedded Pt atoms. Below there are the relative energy values, calculated with respect to the most stable species, along with the label used to identify the systems, underlying the cavity in which the first platinum atom is located.

the bond distance sensibly higher than the optimal value of 2.34 Å, obtained for the isolated Pt_2 dimer in the triplet state, at the same calculation level of theory. Finally, two platinum atoms at 2.78 Å from each other are located in the t-bea-1* channel and share an oxygen atom to form bond angles that strongly deviates from the linearity (151.5 and 169.8°), presumably leading for this reason to the less stable among the considered Pt_2@BEA systems, being its relative energy 61.9 kJ mol^{-1}.

The tendency of platinum to cluster was evaluated for the various cases, and it was found a clustering behavior that allows further justification of the particular stability of the Pt_2@t-mtw structures, where the platinum atoms are more intimately bonded. Thus, the Pt−Pt distance plays a significant role to understand the energetics of Pt_2@BEA systems, together with the O−Pt−O interactions and framework distortions.

An analogous analysis was performed for the addition of the third platinum atom. According to the proposed systematic approach, 14 Pt_3@BEA structures were identified and grouped in 5 sets originating by the Pt_2@BEA system (see Table 1). In the following, however, only minima within 30 kJ mol^{-1} of relative energy are taken into account for each cavity group, for a total of 8 cases. The optimized structures, all in the singlet multiplicity state, are reported in Figure 4, together with significant structural parameters of the three metal atoms. In the most stable case, two platinum atoms are located inside the t-mtw cavity, with the third Pt that protrudes into the main

https://doi.org/10.1021/acs.jpcc.3c02957
J. Phys. Chem. C 2023, 127, 14765−14775

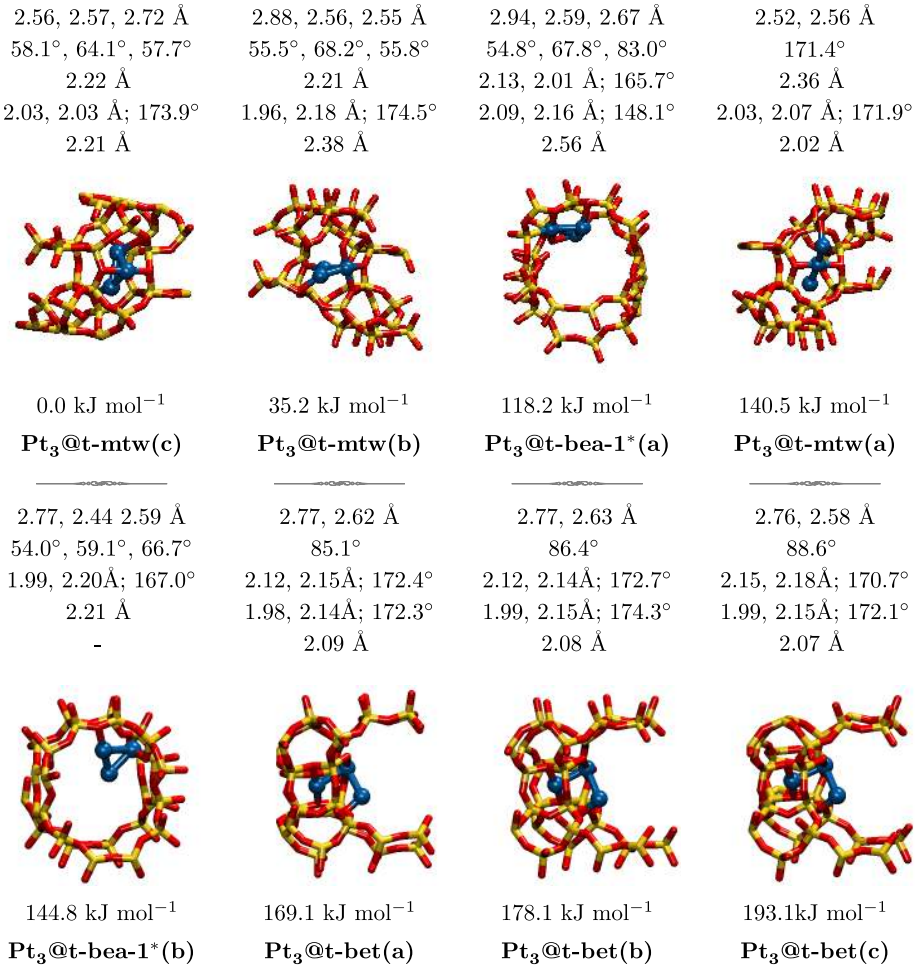

Figure 4. Local views of the eight Pt_3@BEA-optimized geometries. O = red, Si = yellow, Pt = blue. Above each structure, Pt−Pt distances and angles are reported, together with relevant Pt−O distances and O−Pt−O angles for the first, second, and third embedded Pt atoms. The relative energy values, calculated with respect to the most stable species, are shown below each structure, together with the tiling label identifying the cavity where the first platinum is located.

channel, forming an isosceles triangle characterized by Pt−Pt bond distances of 2.56, 2.57, and 2.72 Å. Only one platinum atom, the second in order of addition to the zeolite structure, features the typical O−Pt−O interaction. In a nearly 35 kJ mol^{-1} less stable structure, the Pt_3 cluster assumes the shape of an isosceles triangle, reversed with respect to the previous case, that is with a single Pt inside the t-mtw cavity and the other two in the main channel. The second platinum atom evenly interacts with 3 oxygen atoms, and there is a rupture of the zeolitic framework regularity due to the formation of the linear O−Pt−O configuration, further discussed in the next section. With the third structure, named Pt_3@t-bea-1*(a), the relative energy rises to 118.2 kJ mol^{-1}, and the cluster assumes the shape of a scalene triangle at the intersection between the two main 12T channels of BEA. Two platinum atoms share an oxygen within the favorable O−Pt−O interacting mode, and consequently framework distortions are present as for the Pt_2@ t-bea-1* system. The fourth system, characterized by a relative energy of 140.5 kJ mol^{-1}, features an almost linear arrangement of the three platinum atoms (angle 171.4°) with distances equal to 2.52 and 2.56 Å. Only the second Pt atom interacts with two oxygens in the linear O−Pt−O fragment, being the framework just slightly perturbed. At almost equal energy (144.8 kJ mol^{-1}) a new structure similar to the other Pt_3@t-bea-1* follows in which, however, the scalene triangle formed by the Pt_3 cluster at the intersection between the channels has fewer interactions with the zeolite walls: this is especially true for the third platinum atom, which finds the closest oxygen 3.66 Å apart. Only the first Pt shows the preferential interaction with two oxygens, and due to this, a t-bet cavity is broken, as happened for the same site with one and two platinum atoms. The last three systems, belonging to the t-bet group, are characterized by the fact that the Pt_3 cluster assumes a bent shape with angles of 85.1, 86.4, and 88.6°, going toward the least stable case, which has a relative energy of 193.1 kJ mol^{-1}. In these systems, irrespective of the involved energy, two platinum atoms interact with two oxygen atoms, being the connected cavity broken, while the third Pt only sees a single O atom nearby.

Overall, it is evident the sensible difference in energy among the 8 selected systems, where the first two differ by 35.2 kJ mol^{-1} while the less stable structure is nearly 190 kJ mol^{-1} higher in energy than the Pt_3@t-mtw(c) reference. These findings can be rationalized in terms of the embedded cluster geometry compared to that of the in vacuo Pt_3 structure, investigated at the same computational level. The latter indeed appears to be an equilateral triangle in a singlet multiplicity state, with Pt−Pt bond distances of 2.48 Å. It can be argued, by

https://doi.org/10.1021/acs.jpcc.3c02957
J. Phys. Chem. C 2023, 127, 14765−14775

comparing the more and less stable cases, that the system is more stable as the embedded Pt_3 cluster gets closer to this ideal configuration. The second factor determining the stability of the studied systems is the possibility of interactions with the zeolite walls; in these terms, we can in fact interpret the energetic order found between the two Pt_3@t-bea-1* cases. Interestingly, Pt_3@t-mtw(a), where a linear arrangement occurs, has an energy in-between the two Pt_3@t-bea-1* systems. It evidently represents a peculiar zeolitic fragment suitable to accommodate, without the occurrence of large framework distortions, the three platinum atoms, characterized by Pt−Pt bond distances similar to those of both the more stable Pt_3@BEA system and the in vacuo triangular platinum cluster.

Cavity Distortions. Figures 5−7 display the graphs obtained by performing a framework distortion analysis

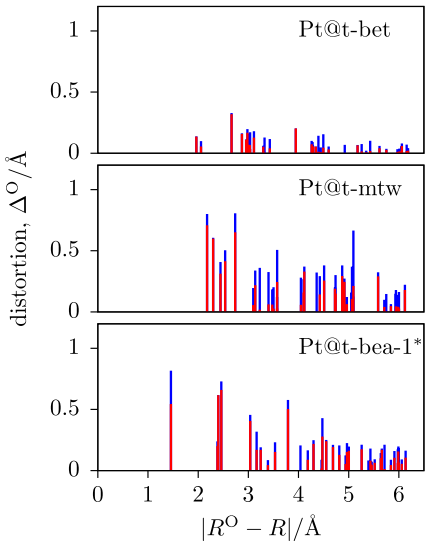

Figure 5. Absolute (Δ_a^O, blue) and radial (Δ_r^O, red) displacements of the framework oxygen atoms in Pt@BEA systems with respect to the pristine zeolite structure, within an exploration radius of 6.2 Å around the coordinates of the reference point R. Panels of the different cavities in which the platinum atom is located are reported in increasing relative energy, from top to bottom.

focused on the oxygen atoms, following the approach outlined in the "Models and Methods" section, for all of the Pt_n@BEA systems. Accordingly, in a given graph, the values in the abscissa represent the distance between the reference point R and the oxygen atoms in the pristine BEA cell, while in the ordinate are reported the modules of both the absolute (Δ_a^O) and radial (Δ_r^O) displacements from that distance. The corresponding graphs that refer to the silicon atoms are reported in Figures S3−S5. Incidentally, for Pt@BEA structures only the cases corresponding to cavities for which the equivalent systems with two and three platinum atoms are present were taken into account; the t-bea-1*(b) species of Figure 2 was, for example, not considered. The graph relating to the t-bet system in Figure 5 shows minimal distortions; in fact, the two most intense peaks consist of displacements by ∼0.3 and 0.2 Å, while all of the silicon positions in the framework remains almost unchanged (see Figure S3). These data allow one to interpret the particular stability of the t-bet cage structure: the O−Pt−O interaction occurs naturally into a frame that is quite already suitable, in terms of volume and zeolite framework topology, to effectively host one platinum atom. Rising in relative energy, the graph of the t-mtw system shows, among all, 5 oxygen peaks between 2.10 and 2.80 Å, mostly of the radial kind, whose absolute displacements range from 0.4 to 0.8 Å. They correspond to five of the t-mtw cavity oxygen atoms closer to the reference point R. Therefore, these oxygen centers undergo sensible modifications when Pt is inserted, while once again, the Si atoms mostly maintain their positions since the oxygen atom rotates around the Si−O−Si axis. The last graph of Figure 5 shows several oxygen peaks with magnitude greater than 0.5 Å: at 1.45, 2.40, and 2.46 Å and then again at 3.79 Å. Also two silicon atoms have undergone displacements of ca. 0.4 Å. The corresponding distortions showed different Δ characters, as proved by the peaks at 2.18 and 2.32 Å in Figure S3. Analyzing the structure in more details, it can be observed that the latter are indeed coupled with the first two oxygen signals discussed above, jointly corresponding to a situation in which the framework is broken. In fact, the silicon atoms move away from each other, each bringing an oxygen atom with itself. As a consequence, there is a Si−O distance of 2.66 Å (whereas in the pristine zeolite framework, it is 1.66 Å).

Moving to systems with two zeolite-embedded platinum atoms, Figure 6 shows the Δ_a^O and Δ_r^O characteristics of the

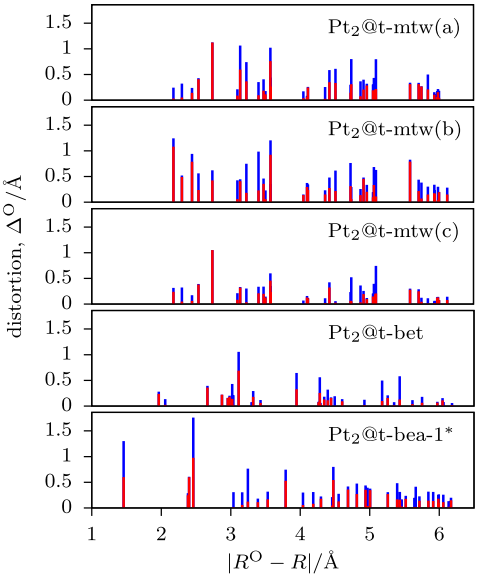

Figure 6. Absolute (Δ_a^O, blue) and radial (Δ_r^O, red) displacements of the framework oxygen atoms in Pt_2@BEA systems with respect to the pristine zeolite structure, within an exploration radius of 6.2 Å around the coordinates of the reference point R. Panels of the different cavities in which the platinum dimer is located are reported in increasing relative energy, from top to bottom.

two platinum atom systems. The first three panels, corresponding to the most stable t-mtw structures, exhibit several intense (up to 1.1 Å of absolute displacement) and closely spaced peaks in the range between 2.17 and 3.57 Å. This finding lets us to infer that for the Pt_2@BEA systems, the zeolite distortions are not predominant in destabilizing the supported structures with respect to the original BEA units. The box relating to the Pt_2@t-bet species is characterized by very slight distortions compared to the others, despite the presence of a peak for oxygen at ca. 3.10 Å, with a distortion value close to 1.0 Å, and two peaks for silicon at distances of

https://doi.org/10.1021/acs.jpcc.3c02957
J. Phys. Chem. C 2023, 127, 14765−14775

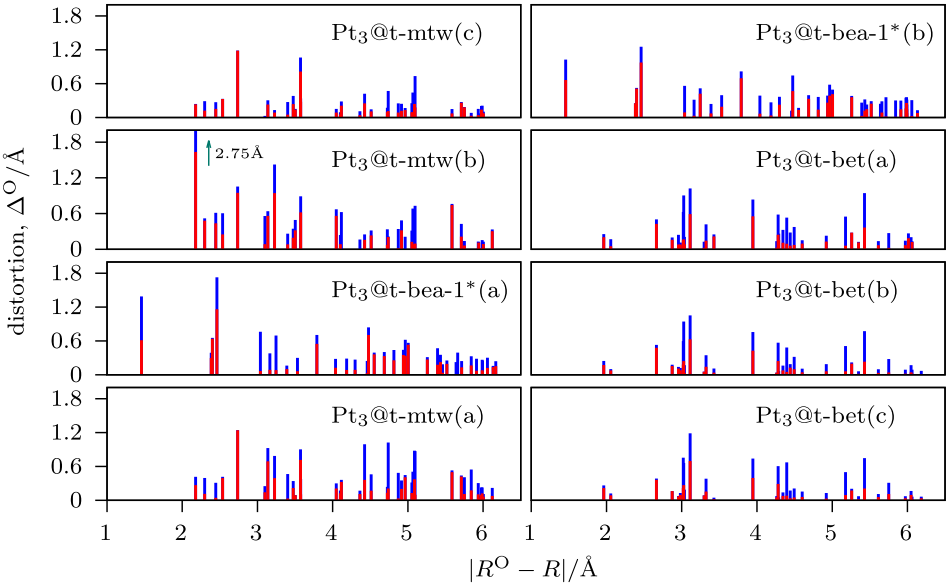

Figure 7. Absolute (Δ_a^O, blue) and radial (Δ_r^O, red) displacements of the framework oxygen atoms in Pt_3@BEA systems with respect to the pristine zeolite structure, within an exploration radius of 6.2 Å around the coordinates of the reference point R. Panels of the different cavities in which the platinum cluster is located are reported in increasing relative energy, from top to bottom and left to right. The arrow in the Pt_3@t-mtw(b) panel indicates an off-scale point at Δ_a^O = 2.75 Å.

2.76 and 3.95 Å, both showing a distortion value equal to 0.4 Å (see Figure S4), that were negligible in the graph of the Pt@t-bet system. They correspond to a break of the zeolite framework in which the Si atom, showing larger radial displacements, moves away, jointly with the oxygen atom, from the other silicon so that the latter is found at a distance of 2.83 Å (against 1.66 Å of the original structure). The driving force of this break can be identified in the oxygen attraction exerted by the platinum atom to form an almost linear arrangement. Finally, for the less stable Pt_2@t-bea-1* structure, the same peaks of Si and O that characterized the cavity with a single embedded platinum atom are present, only subjected both to subtle variations in magnitude and to the already discussed framework modifications. It is interesting to point out that the first oxygen peak, located at 1.45 Å and showing a distortion value equal to 1.3 Å, is now associated with one O−Pt−O interaction mode between the oxygen and both the two metal atoms, as discussed in the previous section. Furthermore, this peak and the one centered at 2.46 Å have radial displacements in the average, but they reach the maximum values of the absolute displacement among all of the systems.

Figure 7 reports the distortion behaviors taking place in the different BEA cavities related to systems with three platinum atoms embedded in the zeolite framework. The most stable Pt_3@t-mtw(c) case unveils the two highest peaks (1.18 and 1.06 Å) at 2.73 and 3.57 Å from the center taken as reference, thus being very similar to the behavior of the corresponding site with two platinum atoms; in fact, only the second peak became slightly more intense. The next panel shows the same peaks in the range 2.17−3.57 Å that were already observed for the Pt_2@t-mtw structures, with little changes in the signal behaviors. The one at 3.22 Å couples with the silicon peak at 2.94 Å of 1.08 Å of absolute displacement (which conversely was negligible in the Si graph of the supported Pt_2 structure) in a break of the zeolitic framework where the two atoms move apart to a final Si−O distance of 3.30 Å. An off-scale oxygen peak is also observed, corresponding to an O atom that moved, significantly, in order to bond with two other silicon atoms different to those present in the initial couple. Its position is now actually occupied by the added third platinum atom. The behavior of t-bea-1*(a) has not undergone substantial changes passing from the system involving two to that involving three embedded platinum atoms, neither for oxygen nor for silicon displacement. The same result is observed in the subsequent panel and the, there represented, Pt_2@t-mtw(a) system. The Pt_3@t-bea-1*(b) species presents a framework break produced by the first Pt atom already added to the zeolite. However, the graph shows less intense peaks with respect to both its parent structures having one and two platinum atoms. Pt_3@t-bea-1*(a) is less stable than the related (b) one due to fewer interactions occurring between the cluster and the zeolite walls. The values reported in the panels regarding the Pt_3@t-bet geometry group are very similar to each other. If compared to the equivalent structures characterized by the presence of two platinum atoms, the O and Si peaks related to the rupture of the framework are once again systematically observed, being those of silicon at slightly higher intensity (0.50−0.60 Å against the previous values of 0.40 Å, see Figures 7 and S5). Furthermore, other peaks of oxygen atoms reaching values of about 1.0 Å are also present, with a characteristic prevalence of an angular component of the displacement, as can be deduced by the large difference between Δ_a^O and Δ_r^O.

Energetics of the Clustering Process. The tendency to clustering was evaluated inside all of the considered cavities by calculating the ΔE values according to processes (eqs 1−3). The results are collected in Table 2. Besides, Figure 8 shows the relative energies concerning sets of systems characterized by the presence of embedded Pt cluster having a different number (1−3) of atoms inside the cavities. As can be noticed from the negative values in the first column, Pt_2 clusters are favored over two isolated Pt atoms, and this is true regardless of the kind of cavity. The greatest tendency toward growth however occurs in the cases where the t-mtw cavity is involved. This is the second in order of stability as regards the location

https://doi.org/10.1021/acs.jpcc.3c02957
J. Phys. Chem. C 2023, 127, 14765−14775

Table 2. ΔE Values Related to the Processes Represented by eqs 1−3, Calculated for Every BEA Cavity Investigated

	process ΔE (kJ mol^{-1})		
structure	step 1	step 2	step 3
t-bet(a)	−16.2	+8.6	+24.8
t-bet(b)	−16.2	+18.1	+34.3
t-bet(c)	−16.2	+32.6	+48.8
t-bea-1*(a)	−70.8	−143.3	−72.5
t-bea-1*(b)	−70.8	−116.7	−45.9
t-mtw(a)	−119.8	−101.7	+18.1
t-mtw(b)	−110.3	−207.0	−96.7
t-mtw(c)	−104.3	−242.2	−137.9

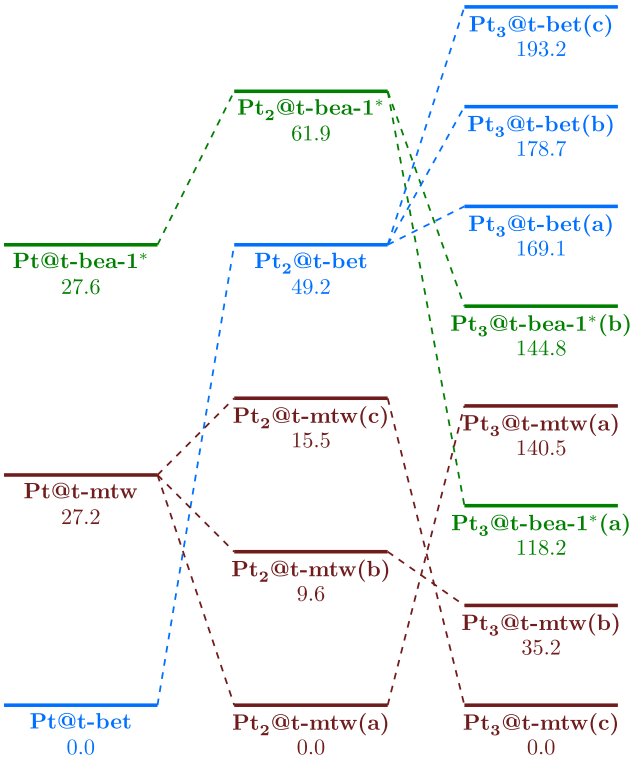

Figure 8. Energetics of and relations between the Pt_n@BEA systems considered for evaluating the clustering tendency. Vertically, cases with 1, 2, and 3 platinum atoms inside the different cavities are reported (left to right). The relative energy within the group is given below the cavity label. Horizontally, cases with the metal atoms in a certain cavity (t-bet, t-mtw, and t-bea-1*, represented by different colors) are connected to their parent Pt_{n-1} system by dashed lines.

of a single platinum atom but is actually energetically preferred over the others for the Pt_2@BEA systems. The structures involved in the different systems easily explain these findings. In fact, as previously highlighted, the t-bet cavity is already suitable for hosting one platinum atom, while the t-mtw cavity undergoes distortions of the framework. However, in the latter, two metal atoms exhibit a smaller bond distance hence higher cluster-like features.

The values reported in the second column shows that Pt_3@BEA systems are favored over three isolated atoms, except for the t-bet sites. Growth in this cavity is indeed thermodynamically unfavorable. This is not surprising, given that in this case, a comparison is performed between the worst condition for clustering within the Pt_3 group (see Figure 8) with the best energetic condition that is possible to find for a single Pt embedded in the zeolite. From the structural point of view, the t-bet cavity is too small to accommodate the three platinum atoms; in fact, already the second Pt added in this cavity protrudes toward the main channel so that the cluster is characterized by little interactions with the zeolite walls. In the case of the other two types of cavities, on the other hand, the presence of a Pt_3 particle is strongly favored, with ΔE values ranging from about 115 to 240 kJ mol^{-1}.

The third column of Table 2 shows the difference between the energy of an embedded Pt_3 cluster in a given cavity and the energy of both one metal dimer and one metal atom placed in two distinct cavities of the same type. The positive value of +18.1 kJ mol^{-1} characterizing the t-mtw(a) cavity, see Table 2, stands out, as an example, from this kind of data adjustment, which leads to an internal comparison of the three possible structures in the t-mtw group. If the preferred system for two platinum atoms is the first, the addition of a further Pt atom leads to a not particularly stable situation due to the lack of significant interactions between the metal triangle-shaped cluster and the zeolite framework. Thus, the growth process to Pt_3 most likely follows the c-type structure formation.

Needless to say, clustering could be further investigated, even until complete saturation of the main zeolite channel is reached. However, this is clearly outside the scope of the present work, since the studied systems are intended to be used as catalysts. Thus, on the contrary, a minimum size is desirable, provided that the corresponding minimum size cluster is effective to have catalytic activity and hence, as a prerequisite, is available to interact with substrates in the main zeolite channel.

CONCLUSIONS

An approach within the DFT framework was employed to identify preferential location of platinum atoms inside a β-zeolite model and to study the growth of a minimal cluster. Pt atom migration through cages was also addressed, by means of a transition state search following the NEB approach.

A comparative structural analysis involving different cavities and platinum atom numbers showed that the optimal geometry involving a single platinum atom takes place when the formation of a O−Pt−O unit in an almost linear arrangement occurs. This seems to be the driving force that mainly determine the local structure properties of the metal-functionalized BEA and may cause breaking of the zeolite structure even when only one platinum atom is included in a cage. Energetic preference for clustering was observed against the occurring of multiple distinct interactions between zeolite sites and metal centers, leading to slightly different cluster geometries. With respect to this, the Pt−Pt distance is actually a sensible factor in orienting the energetics of the Pt_2@BEA species while the cluster geometry become very significant in the case of the Pt_3@BEA species, where the closer the shape of the cluster is to that of an equilateral triangle, the more stable the corresponding fragment results.

Platinum migration characterized by the crossing of the wall of different cavities may occur with relatively low energy barriers, although occasionally, due to the local topology, the same process could be hindered by prohibitive energy values.

Since zeolite systems with metal atoms protruding toward the main zeolite channel, where reactions are likely to occur, have potential catalytic activity, future developments will be addressed to simulate, on Pt-embedded zeolites, catalytic

https://doi.org/10.1021/acs.jpcc.3c02957
J. Phys. Chem. C 2023, 127, 14765−14775

reactions of interest in the fuel industry, such as paraffin hydrogenation/dehydrogenation, as part of hydroisomerization or cracking processes.

■ ASSOCIATED CONTENT

Supporting Information

The Supporting Information is available free of charge at https://pubs.acs.org/doi/10.1021/acs.jpcc.3c02957.

Diagrams representing minimum energy paths for Pt migration between the zeolite cages; graphs for silicon atom displacement analysis; and optimized geometries of the most stable Pt_n@BEA systems (PDF)

■ AUTHOR INFORMATION

Corresponding Author

Francesco Ferrante − *Dipartimento di Fisica e Chimica "Emilio Segrè", Università degli Studi di Palermo, 90128 Palermo, Italy;* orcid.org/0000-0002-2989-4365; Phone: +39 091 23897979; Email: francesco.ferrante@unipa.it; Fax: +39 091 590015

Authors

Laura Gueci − *Dipartimento di Fisica e Chimica "Emilio Segrè", Università degli Studi di Palermo, 90128 Palermo, Italy;* orcid.org/0000-0002-7837-2037

Marco Bertini − *Dipartimento di Fisica e Chimica "Emilio Segrè", Università degli Studi di Palermo, 90128 Palermo, Italy*

Chiara Nania − *Dipartimento di Fisica e Chimica "Emilio Segrè", Università degli Studi di Palermo, 90128 Palermo, Italy*

Dario Duca − *Dipartimento di Fisica e Chimica "Emilio Segrè", Università degli Studi di Palermo, 90128 Palermo, Italy;* orcid.org/0000-0003-0281-8634

Complete contact information is available at: https://pubs.acs.org/10.1021/acs.jpcc.3c02957

Notes

The authors declare no competing financial interest.

■ REFERENCES

(1) Ennaert, T.; Van Aelst, J.; Dijkmans, J.; De Clercq, R.; Schutyser, W.; Dusselier, M.; Verboekend, D.; Sels, B. F. Potential and Challenges of Zeolite Chemistry in the Catalytic Conversion of Biomass. *Chem. Soc. Rev.* **2016**, *45*, 584−611.

(2) Mäki-Arvela, P.; Khel, T. A.; Azkaar, M.; Engblom, S.; Murzin, D. Y. Catalytic Hydroisomerization of Long-Chain Hydrocarbons for the Production of Fuels. *Catalysts* **2018**, *8*, 534.

(3) Sun, Y.; Han, S. Mechanistic Investigation of Methanol to Propene Conversion Catalyzed by H-Beta Zeolite: A Two-Layer ONIOM Study. *J. Mol. Model.* **2013**, *19*, 5407−5422.

(4) Boroń, P.; Rutkowska, M.; Gil, B.; Marszalek, B.; Chmielarz, L.; Dzwigaj, S. Experimental Evidence of the Mechanism of Selective Catalytic Reduction of NO with NH_3 over Fe-Containing BEA Zeolites. *ChemSusChem* **2019**, *12*, 692−705.

(5) Gramigni, F.; Selleri, T.; Nova, I.; Tronconi, E. Catalyst Systems for Selective Catalytic Reduction + NO_x Trapping: from Fundamental Understanding of the Standard SCR Reaction to Practical Applications for Lean Exhaust After-Treatment. *React. Chem. Eng.* **2019**, *4*, 1165−1178.

(6) Berger, F.; Rybicki, M.; Sauer, J. Adsorption and Cracking of Propane by Zeolites of Different Pore Size. *J. Catal.* **2021**, *395*, 117−128.

(7) Wang, H.; Wang, L.; Xiao, F.-S. Metal@Zeolite Hybrid Materials for Catalysis. *ACS Cent. Sci.* **2020**, *6*, 1685−1697.

(8) Nie, X.; Janik, M. J.; Guo, X.; Liu, X.; Song, C. Reaction Mechanism of tert-Butylation of Phenol with tert-Butyl Alcohol over H-β Zeolite: An ONIOM Study. *Catal. Today* **2011**, *165*, 120−128.

(9) Gomes, L. C.; de Oliveira Rosas, D.; Chistone, R. C.; Zotin, F. M. Z.; de Araujo, L. R. R.; Zotin, J. L. Hydroisomerization of n-Hexadecane using Pt/Alumina-Beta Zeolite Catalysts for Producing Renewable Diesel with Low Pour Point. *Fuel* **2017**, *209*, 521−528.

(10) Khel, T. K.; Päivi, M. A.; Azkaar, M.; Vajglová, Z.; Aho, A.; Hemming, J.; Peurla, M.; Eränen, K.; Kumar, N.; Murzin, D. Yu. Hexadecane Hydrocracking for Production of Jet Fuels from Renewable Diesel over Proton and Metal Modified H-Beta Zeolites. *Mol. Catal.* **2019**, *476*, No. 110515.

(11) Guo, Y.; Du, X.; Liu, L.; Dong, Y.; Lei, Z. Reaction Mechanism of Benzene Alkylation with Propylene Catalyzed by HZSM-5 Zeolite and H-Beta Zeolite. *Mater. Today Commun.* **2021**, *26*, No. 101757.

(12) Laluc, M.; Barakov, R.; Mäki-Arvela, P.; Shcherban, N.; Murzin, D. Yu. Catalytic Activity of Hierarchical Beta Zeolites in the Prins Cyclization of (−)-Isopulegol with Acetone. *Appl. Catal., A* **2021**, *618*, No. 118131.

(13) Database of Zeolite Structures. http://www.iza-structure.org/databases/ (accessed July 17, 2020).

(14) Vjunov, A.; Fulton, J. L.; Huthwelker, T.; Pin, S.; Mei, D.; Schenter, G. K.; Govind, N.; Camaioni, D. M.; Hu, J. Z.; Lercher, J. A. Quantitatively Probing the Al Distribution in Zeolites. *J. Am. Chem. Soc.* **2014**, *136*, 8296−8306.

(15) Li, S.; Zhao, Z.; Zhao, R.; Zhou, D.; Zhang, W. Aluminum Location and Acid Strength in an Aluminum-Rich Beta Zeolite Catalyst: A Combined Density Functional Theory and Solid-State NMR Study. *ChemCatChem* **2017**, *9*, 1494−1502.

(16) Batalha, N.; Pinard, L.; Pouilloux, Y.; Guisnet, M. Bifunctional Hydrogenating/Acid Catalysis: Quantification of the Intimacy Criterion. *Catal. Lett.* **2013**, *143*, 587−591.

(17) Gutierrez-Acebo, E.; Leroux, C.; Chizallet, C.; Schuurman, Y.; Bouchy, C. Metal/Acid Bifunctional Catalysis and Intimacy Criterion for Ethylcyclohexane Hydroconversion: When Proximity Does Not Matter. *ACS Catal.* **2018**, *8*, 6035−6046.

(18) Mendes, P. S. F.; Silva, J. M.; Ribeiro, M. F.; Daudin, A.; Bouchy, C. From Powder to Extrudate Zeolite-Based Bifunctional Hydroisomerization Catalysts: on Preserving Zeolite Integrity and Optimizing Pt Location. *J. Ind. Eng. Chem.* **2018**, *62*, 72−83.

(19) Wang, Y.; Tao, Z.; Wu, B.; Xu, J.; Huo, C.; Li, K.; Chen, H.; Yang, Y.; Li, Y. Effect of Metal Precursors on the Performance of Pt/ZSM-22 Catalysts for n-Hexadecane Hydroisomerization. *J. Catal.* **2015**, *322*, 1−13.

(20) Liu, L.; Lopez-Haro, M.; Lopes, C. W.; Li, C.; Concepcion, P.; Simonelli, L.; Calvino, J. J.; Corma, A. Regioselective Generation and Reactivity Control of Subnanometric Platinum Clusters in Zeolites for High-Temperature Catalysis. *Nat. Mater.* **2019**, *18*, 866−873.

(21) Liu, Y.; Li, Z.; Yu, Q.; Chen, Y.; Chai, Z.; Zhao, G.; Liu, S.; Cheong, W.; Pan, Y.; Zhang, Q.; et al. A General Strategy for Fabricating Isolated Single Metal Atomic Site Catalysts in Y Zeolite. *J. Am. Chem. Soc.* **2019**, *141*, 9305−9311.

(22) Tian, Y.; Duan, H.; Zhang, B.; Gong, S.; Lu, Z.; Dai, L.; Qiao, C.; Liu, G.; Zhao, Y. Template Guiding for the Encapsulation of Uniformly Subnanometric Platinum Clusters in Beta-Zeolites Enabling High Catalytic Activity and Stability. *Angew. Chem., Int. Ed.* **2021**, *60*, 21713−21717.

(23) Vajglová, Z.; Kumar, N.; Peurla, M.; Hupa, L.; Semikin, K.; Sladkovskiy, D. A.; Murzin, D. Y. Effect of the Preparation of Pt-Modified Zeolite Beta-Bentonite Extrudates on Their Catalytic Behavior in n-Hexane Hydroisomerization. *Ind. Eng. Chem. Res.* **2019**, *58*, 10875−10885.

(24) Wright, P. A.; Zhou, W.; Pérez-Pariente, J.; Arranz, M. Direct Observation of Growth Defects in Zeolite Beta. *J. Am. Chem. Soc.* **2005**, *127*, 494−495.

(25) Medeiros-Costa, I. C.; Dib, E.; Nesterenko, N.; Dath, J.-P.; Gilson, J.-P.; Mintova, S. Silanol Defect Engineering and Healing in

Zeolites: Opportunities to Fine-Tune their Properties and Performances. *Chem. Soc. Rev.* **2021**, *50*, 11156−11179.
(26) Kokuryo, S.; Miyake, K.; Uchida, Y.; Mizusawa, A.; Kubo, T.; Nishiyama, N. Defect Engineering to Boost Catalytic Activity of Beta Zeolite on Low-Density Polyethylene Cracking. *Mater. Today Sustainability* **2022**, *17*, No. 100098.
(27) Gambo, Y.; Adamu, S.; Abdulrasheed, A. A.; Lucky, R. A.; Ba-Shammakh, M. S.; Hossain, M. M. Catalyst Design and Tuning for Oxidative Dehydrogenation of Propane - A Review. *Appl. Catal., A* **2021**, *609*, No. 117914.
(28) Vorontsov, A. V.; Valdés, H.; Smirniotis, P. G. Design of Active Sites in Zeolite Catalysts Using Modern Semiempirical Methods: The Case of Mordenite. *Comput. Theor. Chem.* **2019**, *1166*, No. 112572.
(29) Prestianni, A.; Ferrante, F.; Sulman, E. M.; Duca, D. Density Functional Theory Investigation on the Nucleation and Growth of Small Palladium Clusters on a Hyper-Cross-Linked Polystyrene Matrix. *J. Phys. Chem. C* **2014**, *118*, 21006−21013.
(30) Ferrante, F.; Prestianni, A.; Duca, D. Computational Investigation of Alkynols and Alkyndiols Hydrogenation on a Palladium Cluster. *J. Phys. Chem. C* **2014**, *118*, 551−558.
(31) Ferrante, F.; Prestianni, A.; Cortese, R.; Schimmenti, R.; Duca, D. Density Functional Theory Investigation on the Nucleation of Homo- and Heteronuclear Metal Clusters on Defective Graphene. *J. Phys. Chem. C* **2016**, *120*, 12022−12031.
(32) Cortese, R.; Schimmenti, R.; Ferrante, F.; Prestianni, A.; Decarolis, D.; Duca, D. Graph-Based Analysis of Ethylene Glycol Decomposition on a Palladium Cluster. *J. Phys. Chem. C* **2017**, *121*, 13606−13616.
(33) Guo, X.; Huang, S. Tuning Nitrogen Reduction Reaction Activity via Controllable Fe Magnetic Moment: A Computational Study of Single Fe Atom Supported on Defective Graphene. *Electrochim. Acta* **2018**, *284*, 392−399.
(34) Cortese, R.; Schimmenti, R.; Prestianni, A.; Duca, D. DFT Calculations on Subnanometric Metal Catalysts: A Short Review on New Supported Materials. *Theor. Chem. Acc.* **2018**, *137*, 59.
(35) Cortese, R.; Campisi, D.; Prestianni, A.; Duca, D. Alkane Dehydrogenation on Defective BN Quasi-Molecular Nanoflakes: DFT Studies. *Mol. Catal.* **2020**, *493*, No. 110891.
(36) Ferrante, F.; Prestianni, A.; Bertini, M.; Duca, D. H_2 Transformations on Graphene Supported Palladium Cluster: DFT-MD Simulations and NEB Calculations. *Catalysts* **2020**, *10*, 1306.
(37) Gueci, L.; Ferrante, F.; Prestianni, A.; Di Chio, R.; Patti, A. F.; Duca, D.; Arena, F. DFT Insights into the Oxygen-Assisted Selective Oxidation of Benzyl Alcohol on Manganese Dioxide Catalysts. *Inorg. Chim. Acta* **2020**, *511*, No. 119812.
(38) Gueci, L.; Ferrante, F.; Prestianni, A.; Arena, F.; Duca, D. Benzyl Alcohol to Benzaldehyde Oxidation on MnO_x Clusters: Unraveling Atomistic Features. *Mol. Catal.* **2021**, *513*, No. 111735.
(39) Arena, F.; Ferrante, F.; Di Chio, R.; Bonura, G.; Frusteri, F.; Frusteri, L.; Prestianni, A.; Morandi, S.; Martra, G.; Duca, D. DFT and Kinetic Evidences of the Preferential CO Oxidation Pattern of Manganese Dioxide Catalysts in Hydrogen Stream (PROX). *Appl. Catal., B* **2022**, *300*, No. 120715.
(40) Broclawik, E.; Kozyra, P.; Mitoraj, M.; Radoń, M.; Rejmak, P. Zeolites at the Molecular Level: What Can Be Learned from Molecular Modeling. *Molecules* **2021**, *26*, 1511.
(41) Barone, G.; Li Manni, G.; Prestianni, A.; Duca, D.; Bernas, H.; Murzin, D. Yu. Hydrogenolysis of Hydroxymatairesinol on Y Derived Catalysts: A Computational Study. *J. Mol. Catal. A* **2010**, *333*, 136−144.
(42) Ferrante, F.; Rubino, T.; Duca, D. Butene Isomerization and Double-Bond Migration on the H-ZSM-5 Outer Surface: A Density Functional Theory Study. *J. Phys. Chem. C* **2011**, *115*, 14862−14868.
(43) Prestianni, A.; Cortese, R.; Duca, D. Propan-2-ol Dehydration on H-ZSM-5 and H-Y Zeolite: A DFT Study. *React. Kinet. Mech. Catal.* **2013**, *108*, 565−582.
(44) Jones, A. J.; Iglesia, E. The Strength of Brønsted Acid Sites in Microporous Aluminosilicates. *ACS Catal.* **2015**, *5*, 5741−5755.
(45) Klinyod, S.; Boekfa, B.; Pornsatitworakul, S.; Maihom, T.; Jarussophon, N.; Treesukol, P.; Wattanakit, C.; Limtrakul, J. Theoretical and Experimental Study on the 7-Hydroxy-4-Methylcoumarin Synthesis with H-Beta Zeolite. *ChemistrySelect* **2019**, *4*, 10660−10667.
(46) Ren, Q.; Rybicki, M.; Sauer, J. Interaction of C3-C5 Alkenes with Zeolitic Brønsted Sites: π-Complexes, Alkoxides, and Carbenium Ions in H-FER. *J. Phys. Chem. C* **2020**, *124*, 10067−10078.
(47) Hou, D.; Grajciar, L.; Nachtigall, P.; Heard, C. J. Origin of the Unusual Stability of Zeolite-Encapsulated Sub-Nanometer Platinum. *ACS Catal.* **2020**, *10*, 11057−11068.
(48) Xu, D.; Wang, S.; Wu, B.; Huo, C.; Qin, Y.; Zhang, B.; Yin, J.; Huang, L.; Wen, X.; Yang, Y.; Li, Y. Tailoring Pt Locations in KL Zeolite by Improved Atomic Layer Deposition for Excellent Performance in n-Heptane Aromatization. *J. Catal.* **2018**, *365*, 163−173.
(49) Injongkol, Y.; Khemthong, P.; Yodsin, N.; Wongnongwa, Y.; Sosa, N.; Youngjan, S.; Butburee, T.; Rungtaweevoranit, B.; Kiatphuengporn, S.; Wittayakun, J.; et al. Combined in Situ XAS and DFT Studies on the Role of Pt in Zeolite-Supported Metal Catalysts for Selective n-Hexane Isomerization. *Fuel* **2022**, *314*, No. 123099.
(50) Schweitzer, J.-M.; Rey, J.; Bignaud, C.; Bučko, T.; Raybaud, P.; Moscovici-Mirande, M.; Portejoie, F.; James, C.; Bouchy, C.; Chizallet, C. Multiscale Modeling as a Tool for the Prediction of Catalytic Performances: The Case of n-Heptane Hydroconversion in a Large-Pore Zeolite. *ACS Catal.* **2022**, *12*, 1068−1081.
(51) Soler, J. M.; Artacho, E.; Gale, J. D.; García, A.; Junquera, J.; Ordejón, P.; Sánchez-Portal, D. SIESTA Method for Ab Initio Order-N Materials Simulation. *J. Phys.: Condens. Matter* **2002**, *14*, 2745−2779.
(52) Perdew, J. P.; Burke, K.; Wang, Y. Generalized Gradient Approximation for the Exchange-Correlation Hole of a Many-Electron System. *Phys. Rev. B* **1996**, *54*, 16533−16539.
(53) Bertini, M.; Ferrante, F.; Duca, D. Empathes: A General Code for Nudged Elastic Band Transition States Search. *Comput. Phys. Commun.* **2022**, *271*, No. 108224.

https://doi.org/10.1021/acs.jpcc.3c02957
J. Phys. Chem. C 2023, 127, 14765−14775

Bibliography

[1] G. Kalghatgi, H. Levinsky, and M. Colket, "Future transportation fuels," *Prog. Energy Combust. Sci.*, vol. 69, p. 103, 2018.

[2] G. J. Suppes and T. S. Storvick, "Chapter 2 - sources of energy," in *Sustainable Power Technologies and Infrastructure* (G. J. Suppes and T. S. Storvick, eds.), p. 29, Boston: Academic Press, 2016.

[3] J. G. Speight, *GASOLINE*, ch. 6, p. 104. John Wiley & Sons Ltd, 2014.

[4] A. Demirbas, "Present and future transportation fuels," *Energ. Source Part A*, vol. 30, p. 1473, 2008.

[5] M. J. Ramos, A. de Lucas, V. Jiménez, P. Sánchez, and V. J. L., "Hydroisomerization of different refinery naphtha streams by using a beta zeolite catalyst," *Fuel Process. Technol.*, vol. 89, p. 721, 2008.

[6] I. G. Crow and K. Shippen, "22 - electricity generation," in *Plant Engineer's Reference Book (Second Edition)* (D. A. Snow, ed.), p. 22, Oxford: Butterworth-Heinemann, second edition ed., 2002.

[7] A. P. P. Pires, Y. Han, J. Kramlich, and M. Garcia-Perez, "Chemical composition and fuel properties of alternative jet fuels," *Bioresour.*, vol. 13, p. 2632, 2018.

[8] L. C. Gomes, D. de Oliveira Rosas, R. C. Chistone, F. M. Z. Zotin, L. R. R. de Araujo, and J. L. Zotin, "Hydroisomerization of n-hexadecane using Pt/alumina-Beta zeolite catalysts for producing renewable diesel with low pour point," *Fuel*, vol. 209, p. 521, 2017.

[9] J. Watson, B. Si, Z. Wang, T. Wang, A. Valentine, and Y. Zhang, "Towards transportation fuel production from food waste: Potential of biocrude oil distillates for gasoline, diesel, and jet fuel," *Fuel*, vol. 301, p. 121028, 2021.

[10] K.-C. Park and S.-K. Ihm, "Comparison of Pt/zeolite catalysts for n-hexadecane hydroisomerization," *Appl. Catal. A: Gen.*, vol. 203, p. 201, 2000.

[11] Bouchy, C., Hastoy, G., Guillon, E., and Martens, J. A., "Fischer-tropsch waxes upgrading via hydrocracking and selective hydroisomerization," *Oil Gas Sci. Technol.*, vol. 64, p. 91, 2009.

[12] S. K. Tanneru and P. H. Steele, "Direct hydrocracking of oxidized bio-oil to hydrocarbons," *Fuel*, vol. 154, p. 268, 2015.

[13] R. Saab, K. Polychronopoulou, L. Zheng, S. Kumar, and A. Schiffer, "Synthesis and performance evaluation of hydrocracking catalysts: A review," *J. Ind. Eng. Chem.*, vol. 89, p. 83, 2020.

[14] J. E. Rorrer, A. M. Ebrahim, Y. Questell-Santiago, J. Zhu, C. Troyano-Valls, A. S. Asundi, A. E. Brenner, S. R. Bare, C. J. Tassone, G. T. Beckham, and Y. Román-Leshkov,

"Role of bifunctional Ru/acid catalysts in the selective hydrocracking of polyethylene and polypropylene waste to liquid hydrocarbons," *ACS Catal.*, vol. 12, p. 13969, 2022.

[15] K. Murata, Y. Liu, M. M. Watanabe, M. Inaba, and I. Takahara, "Hydrocracking of algae oil into aviation fuel-range hydrocarbons using a Pt-Re catalyst," *Energy Fuels*, vol. 28, p. 6999, 2014.

[16] P. Mäki-Arvela, T. A. Kaka Khel, M. Azkaar, S. Engblom, and D. Yu. Murzin, "Catalytic hydroisomerization of long-chain hydrocarbons for the production of fuels," *Catalysts*, vol. 8, p. 534, 2018.

[17] J. Walendziewski, M. Stolarski, R. Łużny, and B. Klimek, "Hydroprocesssing of light gas oil-rape oil mixtures," *Fuel Process. Technol.*, vol. 90, p. 686, 2009.

[18] M. Herskowitz, M. V. Landau, Y. Reizner, and D. Berger, "A commercially-viable, one-step process for production of green diesel from soybean oil on Pt/SAPO-11," *Fuel*, vol. 111, p. 157, 2013.

[19] J. Weitkamp, "Catalytic hydrocracking–mechanisms and versatility of the process," *ChemCatChem*, vol. 4, p. 292, 2012.

[20] G. J. Gomes, M. F. Zalazar, C. A. Lindino, F. R. Scremin, P. R. S. Bittencourt, M. B. Costa, and N. M. Peruchena, "Adsorption of acetic acid and methanol on H-beta zeolite: An experimental and theoretical study," *Microporous Mesoporous Mater.*, vol. 252, p. 17, 2017.

[21] N. Batalha, L. Pinard, Y. Pouilloux, and M. Guisnet, "Bifunctional hydrogenating/acid catalysis: Quantification of the intimacy criterion," *Catal. Lett.*, vol. 143, p. 587, 2013.

[22] H. Deldari, "Suitable catalysts for hydroisomerization of long-chain normal paraffins," *Appl. Catal. A: Gen.*, vol. 293, p. 1, 2005.

[23] M. Guisnet, ""Ideal" bifunctional catalysis over Pt-acid zeolites," *Catal. Today*, vol. 218-219, p. 123, 2013.

[24] R. Yadav and A. Sakthivel, "Silicoaluminophosphate molecular sieves as potential catalysts for hydroisomerization of alkanes and alkenes," *Appl. Catal. A: Gen.*, vol. 481, p. 143, 2014.

[25] T. Hengsawad, C. Srimingkwanchai, S. Butnark, D. E. Resasco, and S. Jongpatiwut, "Effect of metal-acid balance on hydroprocessed renewable jet fuel synthesis from hydrocracking and hydroisomerization of biohydrogenated diesel over Pt-supported catalysts," *Ind. Eng. Chem. Res.*, vol. 57, p. 1429, 2018.

[26] T. Chang and S. Liu, "Role of the mesoporous diameters of hierarchical ZSM-22/MCM-41 zeolite for n-alkane isomerization," *Mol. Catal.*, vol. 503, p. 111420, 2021.

[27] Q. Zhang, X. Liu, S. Hu, G. Ye, X. Zhou, and W. Yuan, "Optimal design of hierarchically structured ZSM-5 zeolites for n-hexane isomerization," *AICHE J.*, vol. 67, p. e17355, 2021.

[28] G. Xing, S. Liu, Q. Guan, and W. Li, "Investigation on hydroisomerization and hydrocracking of C15–C18 n-alkanes utilizing a hollow tubular Ni-Mo/SAPO-11 catalyst with high selectivity of jet fuel," *Catal. Today*, vol. 330, p. 109, 2019.

[29] Y. Du, B. Feng, Y. Jiang, L. Yuan, K. Huang, and J. Li, "Solvent-free synthesis and n-hexadecane hydroisomerization performance of SAPO-11 catalyst," *Eur. J. Inorg. Chem.*, vol. 2018, p. 2599, 2018.

[30] E. R. Zanatta, T. O. Reinehr, J. L. M. Barros, E. A. da Silva, and P. A. Arroyo, "Hydroisomerization of n-hexadecane under mesoporous molecular sieve Pt/Al-SBA-15," *Mol. Catal.*, vol. 512, p. 111737, 2021.

[31] X. Wei, O. V. Kikhtyanin, V. N. Parmon, W. Wu, X. Bai, J. Zhang, L. Xiao, X. Su, and Y. Zhang, "Synergetic effect between the metal and acid sites of Pd/SAPO-41 bifunctional catalysts in n-hexadecane hydroisomerization," *J. Porous Mater.*, vol. 25, p. 235, 2018.

[32] Z. Chen, S. Liu, H. Wang, Q. Ning, H. Zhang, Y. Yun, J. Ren, and Y.-W. Li, "Synthesis and characterization of bundle-shaped ZSM-22 zeolite via the oriented fusion of nanorods and its enhanced isomerization performance," *J. Catal.*, vol. 361, p. 177, 2018.

[33] Z. Feng, W. Wang, Y. Wang, X. Bai, X. Su, L. Yang, and W. Wu, "Hydroisomerization of n-decane over the Pd/ZSM-22 bifunctional catalysts: The effects of dynamic and static crystallization to the zeolite," *Microporous Mesoporous Mat.*, vol. 274, p. 1, 2019.

[34] Z. Vajglova, N. Kumar, M. Peurla, L. Hupa, K. Semikin, D. A. Sladkovskiy, and D. Yu. Murzin, "Effect of the preparation of Pt-modified zeolite Beta-bentonite extrudates on their catalytic behavior in n-hexane hydroisomerization," *Ind. Eng. Chem. Res.*, vol. 58, p. 10875, 2019.

[35] L. C. Loc, N. Gaidai, N. Tri, D. T. K. Thoa, V. Kogan, H. T. Cuong, and Y. Agafonov, "Kinetics of n-hexane hydroisomerization over HZSM-5 supported platinum catalysts. Features of the process mechanism and the Ni-promoting effect," *Mol. Catal.*, vol. 515, p. 111880, 2021.

[36] Y. Zhang, D. Liu, B. Lou, R. Yu, Z. Men, M. Li, and Z. Li, "Hydroisomerization of n-decane over micro/mesoporous Pt-containing bifunctional catalysts: Effects of the MCM-41 incorporation with Y zeolite," *Fuel*, vol. 226, p. 204, 2018.

[37] T. Kaka Khel, P. Maki-Arvela, M. Azkaar, Z. Vajglova, A. Aho, J. Hemming, M. Peurla, K. Eränen, N. Kumar, and D. Yu. Murzin, "Hexadecane hydrocracking for production of jet fuels from renewable diesel over proton and metal modified H-Beta zeolites," *Mol. Catal.*, vol. 476, p. 110515, 2019.

[38] P. B. Weisz, "Polyfunctional heterogeneous catalysis," in *Advances in Catalysis* (D. Eley, P. Selwood, P. B. Weisz, A. Balandin, J. De Boer, P. Debye, P. Emmett, J. Horiuti, W. Jost, G. Natta, E. Rideal, and H. Taylor, eds.), vol. 13, p. 137, Academic Press, 1962.

[39] J. Zecevic, G. Vanbutsele, K. P. de Jong, and J. A. Martens, "Nanoscale intimacy in bifunctional catalysts for selective conversion of hydrocarbons," *Nature*, vol. 528, p. 245, 2015.

[40] T. Demuth, X. Rozanska, L. Benco, J. Hafner, R. van Santen, and H. Toulhoat, "Catalytic isomerization of 2-pentene in H-ZSM-22–A DFT investigation," *J. Catal.*, vol. 214, p. 68, 2003.

[41] R. A. van Santen *et al.*, *Chemical kinetics and catalysis*. Springer Science & Business Media, 2013.

[42] R. W. Taft, *Progress in physical organic chemistry*. John Wiley & Sons, 2009.

[43] G. Cheng, X.-X. Wang, S.-H. Zhang, K.-K. Zhu, Z.-J. Sui, X.-G. Zhou, D. Chen, and Y.-A. Zhu, "On the product and transition-state shape selectivities in 2-heptene isomerization," *Chem. Phys. Lett.*, vol. 812, p. 140263, 2023.

[44] J. Rey, A. Gomez, P. Raybaud, C. Chizallet, and T. Bučko, "On the origin of the difference between type a and type b skeletal isomerization of alkenes catalyzed by zeolites: The crucial input of ab initio molecular dynamics," *J. Catal.*, vol. 373, p. 361, 2019.

[45] C. Wattanakit, S. Nokbin, B. Boekfa, P. Pantu, and J. Limtrakul, "Skeletal isomerization of 1-butene over ferrierite zeolite: A quantum chemical analysis of structures and reaction mechanisms," *J. Phys. Chem. C*, vol. 116, p. 5654, 2012.

[46] B. Huang, P. Bai, M. Neurock, and R. J. Davis, "Conversion of n-hexane and n-dodecane over H-ZSM-5, H-Y and Al-MCM-41 at supercritical conditions," *Appl. Catal. A: Gen.*, vol. 546, p. 149, 2017.

[47] J. Hajek, J. Van der Mynsbrugge, K. De Wispelaere, P. Cnudde, L. Vanduyfhuys, M. Waroquier, and V. Van Speybroeck, "On the stability and nature of adsorbed pentene in Brønsted acid zeolite H-ZSM-5 at 323 K," *J. Catal.*, vol. 340, p. 227, 2016.

[48] P. Cnudde, K. De Wispelaere, J. Van der Mynsbrugge, M. Waroquier, and V. Van Speybroeck, "Effect of temperature and branching on the nature and stability of alkene cracking intermediates in H-ZSM-5," *J. Catal.*, vol. 345, p. 53, 2017.

[49] M. Król, "Natural vs. Synthetic zeolites," *Cryst.*, vol. 10, p. 622, 2020.

[50] E. Cataldo, L. Salvi, F. Paoli, M. Fucile, G. Masciandaro, D. Manzi, C. M. Masini, and G. B. Mattii, "Application of zeolites in agriculture and other potential uses: A review," *Agronomy*, vol. 11, p. 1547, 2021.

[51] "Database of Zeolite Structures @ http://www.iza-structure.org/databases/." (accessed July 17, 2020).

[52] K. Margeta and A. Farkaš, "Introductory chapter: Zeolites - from discovery to new applications on the global market," in *Zeolites* (K. Margeta and A. Farkaš, eds.), ch. 1, IntechOpen, 2020.

[53] T. Pan, Z. Wu, and A. C. Yip, "Advances in the green synthesis of microporous and hierarchical zeolites: a short review," *Catal.*, vol. 9, p. 274, 2019.

[54] M. Moshoeshoe, M. S. Nadiye-Tabbiruka, and V. Obuseng, "A review of the chemistry, structure, properties and applications of zeolites," *Am. J. Mater. Sci*, vol. 7, p. 196, 2017.

[55] A. Ruíz-Baltazar, R. Esparza, M. Gonzalez, G. Rosas, and R. Pérez, "Preparation and characterization of natural zeolite modified with iron nanoparticles," *J. Nanomater.*, vol. 16, p. 274, 2015.

[56] T. Derbe, S. Temesgen, and M. Bitew, "A short review on synthesis, characterization, and applications of zeolites," *Adv. Mater. Sci. Eng.*, vol. 2021, p. 1, 2021.

[57] B. Kozera-Sucharda, B. Gworek, and I. Kondzielski, "The simultaneous removal of zinc and cadmium from multicomponent aqueous solutions by their sorption onto selected natural and synthetic zeolites," *Minerals*, vol. 10, p. 343, 2020.

[58] G. Barone, N. Armata, A. Prestianni, T. Rubino, D. Duca, and D. Yu. Murzin, "Confined but-2-ene catalytic isomerization inside H-ZSM-5 models: A DFT study," *J. Chem. Theory Comput.*, vol. 5, p. 1274, 2009.

[59] P. Maki-Arvela, I. Simakova, Z. Vajglova, N. Kumar, and D. Yu. Murzin, "Relating extrusion as a method of bifunctional catalysts synthesis and their catalytic performance," *Cat. Today*, vol. 423, p. 113933, 2022.

[60] E. Pérez-Botella, S. Valencia, and F. Rey, "Zeolites in adsorption processes: State of the art and future prospects," *Chem. Rev.*, vol. 122, p. 17647, 2022.

[61] A. Campanile, B. Liguori, C. Ferone, D. Caputo, and P. Aprea, "Zeolite-based monoliths for water softening by ion exchange/precipitation process," *Sci. Rep.*, vol. 12, p. 3686, 2022.

[62] A. M. Beale, F. Gao, I. Lezcano-Gonzalez, C. H. F. Peden, and J. Szanyi, "Recent advances in automotive catalysis for nox emission control by small-pore microporous materials," *Chem. Soc. Rev.*, vol. 44, p. 7371, 2015.

[63] T. Ennaert, J. Van Aelst, J. Dijkmans, R. De Clercq, W. Schutyser, M. Dusselier, D. Verboekend, and B. F. Sels, "Potential and challenges of zeolite chemistry in the catalytic conversion of biomass," *Chem. Soc. Rev.*, vol. 45, p. 584, 2016.

[64] U. Olsbye, S. Svelle, M. Bjørgen, P. Beato, T. V. W. Janssens, F. Joensen, S. Bordiga, and K. P. Lillerud, "Conversion of methanol to hydrocarbons: How zeolite cavity and pore size controls product selectivity," *Angew. Chem. Int. Ed. Eng.*, vol. 51, p. 5810, 2012.

[65] A. Olivos-Suarez, A. Szecsenyi, E. Hensen, J. Ruiz-Martinez, E. Pidko, and J. Gascon, "Strategies for the direct catalytic valorization of methane using heterogeneous catalysis: Challenges and opportunities," *ACS Catal.*, vol. 6, p. 2965, 2016.

[66] V. Blay, B. Louis, R. Miravalles, T. Yokoi, K. A. Peccatiello, M. Clough, and B. Yilmaz, "Engineering zeolites for catalytic cracking to light olefins," *ACS Catal.*, vol. 7, p. 6542, 2017.

[67] G. Barone, G. Casella, S. Giuffrida, and D. Duca, "H-ZSM-5 Modified Zeolite: Quantum Chemical Models of Acidic Sites," *J. Phys. Chem. C*, vol. 111, p. 13033, 2007.

[68] G. Barone, D. Duca, F. Ferrante, and G. La Manna, "CASSCF/CASPT2 analysis of the fragmentation of H_2 on a Pd_4 cluster," *Int. J. Quantum Chem.*, vol. 110, p. 558, 2010.

[69] N. Armata, G. Baldissin, G. Barone, R. Cortese, V. D'Anna, F. Ferrante, S. Giuffrida, G. Li Manni, A. Prestianni, T. Rubino, Z. Varga, and D. Duca, "Molecular-level characterization of heterogeneous catalytic systems by algorithmic time dependent monte carlo," *Top. Catal.*, vol. 52, p. 431, 2009.

[70] N. Armata, G. Baldissin, G. Barone, R. Cortese, V. D'Anna, F. Ferrante, S. Giuffrida, G. Li Manni, A. Prestianni, T. Rubino, and D. Duca, "Structural and kinetic DFT characterization of materials to rationalize catalytic performance," *Top. Catal.*, vol. 52, p. 444, 2009.

[71] F. Ferrante, T. Rubino, and D. Duca, "Butene isomerization and double-bond migration on the H-ZSM-5 outer surface: A density functional theory study," *J. Phys. Chem. C*, vol. 115, p. 14862, 2011.

[72] A. Prestianni, R. Cortese, and D. Duca, "Propan-2-ol dehydration on H-ZSM-5 and H-Y zeolite: A DFT study," *React. Kinet. Mech Catal.*, vol. 108, p. 565, 2013.

[73] Y. Li and J. Yu, "New stories of zeolite structures: their descriptions, determinations, predictions, and evaluations," *Chem. Rev.*, vol. 114, p. 7268, 2014.

[74] G. Sastre and A. Corma, "Topological descriptor for oxygens in zeolites. Analysis of ring counting in tetracoordinated nets," *J. Phys. Chem. C*, vol. 113, p. 6398, 2009.

[75] V. A. Blatov, O. Delgado-Friedrichs, M. O'Keeffe, and D. M. Proserpio, "Three-periodic nets and tilings: natural tilings for nets," *Acta Crystallogr. A*, vol. 63, p. 418, 2007.

[76] C.-Y. Chen and S. I. Zones, *Post-Synthetic Treatment and Modification of Zeolites*, ch. 6, p. 155. John Wiley & Sons, Ltd, 2010.

[77] N. Kosinov, C. Liu, E. J. M. Hensen, and E. A. Pidko, "Engineering of transition metal catalysts confined in zeolites," *Chem. Mater.*, vol. 30, p. 3177, 2018.

[78] P. Sánchez-López, Y. Kotolevich, R. I. Yocupicio-Gaxiola, J. Antúnez-García, R. K. Chowdari, V. Petranovskii, and S. Fuentes-Moyado, "Recent advances in catalysis based on transition metals supported on zeolites," *Front. Chem.*, vol. 9, 2021.

[79] L. Liu, M. Lopez-Haro, C. W. Lopes, C. Li, P. Concepcion, L. Simonelli, J. J. Calvino, and A. Corma, "Regioselective generation and reactivity control of subnanometric platinum clusters in zeolites for high-temperature catalysis," *Nat. Mater.*, vol. 18, p. 866, 2019.

[80] Y. Liu, Z. Li, Q. Yu, Y. Chen, Z. Chai, G. Zhao, S. Liu, W.-C. Cheong, Y. Pan, Q. Zhang, L. Gu, L. Zheng, Y. Wang, Y. Lu, D. Wang, C. Chen, Q. Peng, Y. Liu, L. Liu, J. Chen, and Y. Li, "A general strategy for fabricating isolated single metal atomic site catalysts in Y zeolite," *J. Am. Chem. Soc.*, vol. 141, p. 9305, 2019.

[81] J. Li, M. Gao, W. Yan, and J. Yu, "Regulation of the Si/Al ratios and Al distributions of zeolites and its impact on properties," *Chem. Sci.*, vol. 14, p. 1935, 2022.

[82] J. Regalbuto, *Catalyst preparation: science and engineering*. CRC press, 2016.

[83] P. Munnik, P. E. de Jongh, and K. P. de Jong, "Recent developments in the synthesis of supported catalysts," *Chem. Rev.*, vol. 115, p. 6687, 2015.

[84] B. A. Mehrabadi, S. Eskandari, U. Khan, R. D. White, and J. R. Regalbuto, "A review of preparation methods for supported metal catalysts," *Adv. Catal.*, vol. 61, p. 1, 2017.

[85] M. Campanati, G. Fornasari, and A. Vaccari, "Fundamentals in the preparation of heterogeneous catalysts," *Cat. Today*, vol. 77, p. 299, 2003.

[86] C. Liu, G. Li, E. J. M. Hensen, and E. A. Pidko, "Relationship between acidity and catalytic reactivity of faujasite zeolite: A periodic DFT study," *J. Catal.*, vol. 344, p. 570, 2016.

[87] A. Vjunov, J. L. Fulton, T. Huthwelker, S. Pin, D. Mei, G. K. Schenter, N. Govind, D. M. Camaioni, J. Z. Hu, and J. A. Lercher, "Quantitatively probing the Al distribution in zeolites," *J. Am. Chem. Soc.*, vol. 136, p. 8296, 2014.

[88] D. Zhai, Y. Liu, H. Zheng, L. Zhao, J. Gao, C. Xu, and B. Shen, "A first-principles evaluation of the stability, accessibility, and strength of Brønsted acid sites in zeolites," *J. Catal.*, vol. 352, p. 627, 2017.

[89] R. Zhao, Z. Zhao, S. Li, and W. Zhang, "Insights into the correlation of aluminum distribution and Brønsted acidity in H-Beta zeolites from solid-state NMR spectroscopy and DFT calculations," *J. Phys. Chem. Lett.*, vol. 8, p. 2323, 2017.

[90] Y. Wang, Z. Tao, B. Wu, J. Xu, C. Huo, K. Li, H. Chen, Y. Yang, and Y. Li, "Effect of metal precursors on the performance of Pt/ZSM-22 catalysts for n-hexadecane hydroisomerization," *J. Catal.*, vol. 322, p. 1, 2015.

[91] Y. Tian, H. Duan, B. Zhang, S. Gong, Z. Lu, L. Dai, C. Qiao, G. Liu, and Y. Zhao, "Template guiding for the encapsulation of uniformly subnanometric platinum clusters in Beta-zeolites enabling high catalytic activity and stability," *Angew. Chem. Int. Ed. Eng.*, vol. 60, p. 21713, 2021.

[92] R. Cortese, D. Campisi, A. Prestianni, and D. Duca, "Alkane dehydrogenation on defective BN quasi-molecular nanoflakes: DFT studies," *Mol. Catal.*, vol. 493, p. 110891, 2020.

[93] L. Gueci, F. Ferrante, A. Prestianni, R. Di Chio, A. F. Patti, D. Duca, and F. Arena, "DFT insights into the oxygen-assisted selective oxidation of benzyl alcohol on manganese dioxide catalysts," *Inorg. Chim. Acta*, vol. 511, p. 119812, 2020.

[94] F. Ferrante, A. Prestianni, M. Bertini, and D. Duca, "H_2 transformations on graphene supported palladium cluster: DFT-MD simulations and NEB calculations," *Catalysts*, vol. 10, p. 1306, 2020.

[95] L. Gueci, F. Ferrante, A. Prestianni, F. Arena, and D. Duca, "Benzyl alcohol to benzaldehyde oxidation on MnO_x clusters: Unraveling atomistic features," *Mol. Catal.*, vol. 513, p. 111735, 2021.

[96] F. Arena, F. Ferrante, R. Di Chio, G. Bonura, F. Frusteri, L. Frusteri, A. Prestianni, S. Morandi, G. Martra, and D. Duca, "DFT and kinetic evidences of the preferential CO oxidation pattern of manganese dioxide catalysts in hydrogen stream (PROX)," *Appl. Catal. B: Env.*, vol. 300, p. 120715, 2022.

[97] F. Ferrante, C. Nania, and D. Duca, "Computational investigation of isoeugenol transformations on a platinum cluster – I: Direct deoxygenation to propylcyclohexane," *Mol. Catal.*, vol. 529, p. 112541, 2022.

[98] F. Ferrante, M. Bertini, C. Ferlito, L. Lisuzzo, G. Lazzara, and D. Duca, "A computational and experimental investigation of halloysite silicic surface modifications after alkaline treatment," *Appl. Clay Sci.*, vol. 232, p. 106813, 2023.

[99] C. Nania, M. Bertini, L. Gueci, F. Ferrante, and D. Duca, "DFT insights into competing mechanisms of guaiacol hydrodeoxygenation on a platinum cluster," *Phys. Chem. Chem. Phys.*, vol. 25, p. 10460, 2023.

[100] F. Ferrante, M. Bertini, L. Gueci, and D. Duca, "Butene isomerization on palladium surfaces: Time-dependent monte carlo studies," *Ind. Eng. Chem. Res.*, vol. 62, p. 20608, 2023.

[101] D. Xu, S. Wang, B. Wu, C. Huo, Y. Qin, B. Zhang, J. Yin, L. Huang, X. Wen, Y. Yang, and Y. Li, "Tailoring Pt locations in KL zeolite by improved atomic layer deposition for excellent performance in n-heptane aromatization," *J. Catal.*, vol. 365, p. 163, 2018.

[102] Y. Injongkol, P. Khemthong, N. Yodsin, Y. Wongnongwa, N. Sosa, S. Youngjan, T. Butburee, B. Rungtaweevoranit, S. Kiatphuengporn, J. Wittayakun, F. Roessner, and S. Jungsuttiwong, "Combined in situ XAS and DFT studies on the role of Pt in zeolite-supported metal catalysts for selective n-hexane isomerization," *Fuel*, vol. 314, p. 123099, 2022.

[103] J.-M. Schweitzer, J. Rey, C. Bignaud, T. Bučko, P. Raybaud, M. Moscovici-Mirande, F. Portejoie, C. James, C. Bouchy, and C. Chizallet, "Multiscale modeling as a tool for the prediction of catalytic performances: The case of n-heptane hydroconversion in a large-pore zeolite," *ACS Catal.*, vol. 12, p. 1068, 2022.

[104] D. Hou, L. Grajciar, P. Nachtigall, and C. J. Heard, "Origin of the unusual stability of zeolite-encapsulated sub-nanometer platinum," *ACS Catal.*, vol. 10, p. 11057, 2020.

[105] L. E. Sandoval-Diaz, J. A. Gonzalez-Amaya, and C. A. Trujillo, "General aspects of zeolite acidity characterization," *Microporous Mesoporous Mater.*, vol. 215, p. 229, 2015.

[106] P. Sazama, E. Tabor, P. Klein, B. Wichterlova, S. Sklenak, L. Mokrzycki, V. Pashkkova, M. Ogura, and J. Dedecek, "Al-rich beta zeolites. Distribution of Al atoms in the framework and related protonic and metal-ion species," *J. Catal.*, vol. 333, p. 102, 2016.

[107] M. Boronat and A. Corma, "What is measured when measuring acidity in zeolites with probe molecules?," *ACS Catal.*, vol. 9, p. 1539, 2019.

[108] S. Li, Z. Zhao, R. Zhao, D. Zhou, and W. Zhang, "Aluminum location and acid strength in an aluminum-rich beta zeolite catalyst: A combined density functional theory and solid-state NMR study," *ChemCatChem*, vol. 9, p. 1494, 2017.

[109] S. Wang, Y. He, W. Jiao, J. Wang, and W. Fan, "Recent experimental and theoretical studies on Al siting/acid site distribution in zeolite framework," *Curr. Opin. Chem. Eng.*, vol. 23, p. 146, 2019.

[110] M. Niwa, K. Suzuki, N. Katada, T. Kanougi, and T. Atoguchi, "Ammonia IRMS-TPD study on the distribution of acid sites in mordenite," *J. Phys. Chem. B*, vol. 109, p. 18749, 2005.

[111] K. Suzuki, N. Katada, and M. Niwa, "Detection and quantitative measurements of four kinds of OH in HY zeolite," *J. Phys. Chem. C*, vol. 111, p. 894, 2007.

[112] K. Suzuki, G. Sastre, N. Katada, and M. Niwa, "Ammonia IRMS-TPD measurements and DFT calculation on acidic hydroxyl groups in CHA-type zeolites," *Phys. Chem. Chem. Phys.*, vol. 9, p. 5980, 2007.

[113] N. Katada, H. Tamagawa, and M. Niwa, "Quantitative analysis of acidic OH groups in zeolite by ammonia IRMS-TPD and DFT: Application to BEA," *Catal. Today*, vol. 226, p. 37, 2014.

[114] Z. Vajglova, N. Kumar, M. Peurla, J. Peltonen, I. Heinmaa, and D. Yu. Murzin, "Synthesis and physicochemical characterization of beta zeolite-bentonite composite materials for shaped catalysts," *Catal. Sci. Technol.*, vol. 8, p. 6150, 2018.

[115] M. E. Martinez-Klimov, P. Maki-Arvela, Z. Vajglova, C. Schmidt, O. Yevdokimova, M. Peurla, N. Kumar, K. Eranen, and D. Yu. Murzin, "Bifunctional Pt catalysts supported on a zeolite-binder matrix for the hydrodeoxygenation of isoeugenol for renewable jet fuel production," *Top. Catal.*, vol. 66, p. 1296, 2023.

[116] M. Martinez-Klimov, O. Yevdokimova, P. Mäki-Arvela, J. Cueto, N. Shcherban, Z. Vajglova, K. Eränen, and D. Yu. Murzin, "Hydrodeoxygenation of isoeugenol in continuous mode using bifunctional Pt-Beta 25-binder catalysts for renewable jet fuel production," *Sustain. Energy Fuels*, vol. 8, p. 90, 2023.

[117] M. Trachta, O. Bludský, J. Vakulík, R. Bulánek, and M. Rubeš, "Investigation of Brønsted acidity in zeolites through adsorbates with diverse proton affinities," *Sci. Rep.*, vol. 13, p. 12380, 2023.

[118] A. J. Jones and E. Iglesia, "The strength of Brønsted acid sites in microporous aluminosilicates," *ACS Catal.*, vol. 5, p. 5741, 2015.

[119] M. Brändle and J. Sauer, "Acidity differences between inorganic solids induced by their framework structure. a combined quantum mechanics/molecular mechanics ab initio study on zeolites," *J. Am. Chem, Soc,*, vol. 120, p. 1556, 1998.

[120] U. Eichler, M. Brändle, and J. Sauer, "Predicting absolute and site specific acidities for zeolite catalysts by a combined quantum mechanics/interatomic potential function approach," *J. Phys. Chem. B*, vol. 101, p. 10035, 1997.

[121] A. J. Jones, R. T. Carr, S. I. Zones, and E. Iglesia, "Acid strength and solvation in catalysis by MFI zeolites and effects of the identity, concentration and location of framework heteroatoms," *J. Catal.*, vol. 312, p. 58, 2014.

[122] P. Deshlahra and E. Iglesia, "Reactivity descriptors in acid catalysis: acid strength, proton affinity and host-guest interactions," *Chem. Commun.*, vol. 56, p. 7371, 2020.

[123] J. Sauer and M. Sierka, "Combining quantum mechanics and interatomic potential functions in ab initio studies of extended systems," *J. Comput. Chem.*, vol. 21, p. 1470, 2000.

[124] M. Rybicki and J. Sauer, "Acid strength of zeolitic Brønsted sites - dependence on dielectric properties," *Catal. Today*, vol. 323, p. 86, 2019.

[125] C. Freysoldt, J. Neugebauer, and C. G. Van de Walle, "Fully ab initio finite-size corrections for charged-defect supercell calculations," *Phys. Rev. Lett.*, vol. 102, p. 016402, 2009.

[126] F. Bruneval, J.-P. Crocombette, X. Gonze, B. Dorado, M. Torrent, and F. Jollet, "Consistent treatment of charged systems within periodic boundary conditions: The projector augmented-wave and pseudopotential methods revisited," *Phys. Rev. B*, vol. 89, p. 045116, 2014.

[127] M. Trachta, R. Bulánek, O. Bludský, and M. Rubeš, "Brønsted acidity in zeolites measured by deprotonation energy," *Sci. Rep.*, vol. 12, p. 7301, 2022.

[128] E. Gutierrez-Acebo, C. Leroux, C. Chizallet, Y. Schuurman, and C. Bouchy, "Metal/acid bifunctional catalysis and intimacy criterion for ethylcyclohexane hydroconversion: When proximity does not matter," *ACS Catal.*, vol. 8, p. 6035, 2018.

[129] P. S. F. Mendes, J. M. Silva, M. F. Ribeiro, A. Daudin, and C. Bouchy, "From powder to extrudate zeolite-based bifunctional hydroisomerization catalysts: on preserving zeolite integrity and optimizing Pt location," *J. Ind. Eng. Chem.*, vol. 62, p. 72, 2018.

[130] K. Cheng, L. I. van der Wal, H. Yoshida, J. Oenema, J. Harmel, Z. Zhang, G. Sunley, J. Zevcevic, and K. P. de Jong, "Impact of the spatial organization of bifunctional metal–zeolite catalysts on the hydroisomerization of light alkanes," *Angew. Chem.*, vol. 132, p. 3620, 2020.

[131] G. Noh, Z. Shi, S. I. Zones, and E. Iglesia, "Isomerization and β-scission reactions of alkanes on bifunctional metal-acid catalysts: Consequences of confinement and diffusional constraints on reactivity and selectivity," *J. Catal.*, vol. 368, p. 389, 2018.

[132] "Zeolyst products @https://www.zeolyst.com/our-products/standard-zeolite-powders/zeolite-beta.html." (accessed Dicember 12, 2023).

[133] P. S. Mendes, G. Lapisardi, C. Bouchy, M. Rivallan, J. M. Silva, and M. F. Ribeiro, "Hydrogenating activity of Pt/zeolite catalysts focusing acid support and metal dispersion influence," *Appl. Catal. A: Gen.*, vol. 504, p. 17, 2015.

[134] F. Alvarez, F. Ribeiro, G. Perot, C. Thomazeau, and M. Guisnet, "Hydroisomerization and hydrocracking of alkanes: 7. Influence of the balance between acid and hydrogenating functions on the transformation of n-decane on PtHY catalysts," *J. Catal.*, vol. 162, p. 179, 1996.

[135] N. Batalha, L. Pinard, Y. Pouilloux, and M. Guisnet, "Bifunctional hydrogenating/acid catalysis: Quantification of the intimacy criterion," *Catal. Lett.*, vol. 143, p. 587, 2013.

[136] J. Morávková, R. Pilař, O. Bortnovsky, D. Kaucký, A. Vondrová, J. Rathousky, G. Sádovská, and P. Sazama, "The effect of the nanoscale intimacy of platinum and acid centres on the hydroisomerization of short-chain alkanes," *Appl. Catal. A: Gen.*, vol. 634, p. 118535, 2022.

[137] Z. Vajglova, N. Kumar, M. Peurla, L. Hupa, K. Semikin, D. A. Sladkovskiy, and D. Yu. Murzin, "Deactivation and regeneration of Pt-modified zeolite Beta-Bindzil extrudates in n-hexane hydroisomerization," *J. Chem.Technol. Biotechnol.*, vol. 96, p. 1645, 2021.

[138] J. Oenema, J. Harmel, R. P. Vélez, M. J. Meijerink, W. Eijsvogel, A. Poursaeidesfahani, T. J. Vlugt, J. Zečević, and K. P. de Jong, "Influence of nanoscale intimacy and zeolite micropore size on the performance of bifunctional catalysts for n-heptane hydroisomerization," *ACS Catal.*, vol. 10, p. 14245, 2020.

[139] K. Momma and F. Izumi, "VESTA 3 for three-dimensional visualization of crystal, volumetric and morphology data," *J. Appl. Crystallogr.*, vol. 44, p. 1272, 2011.

[140] M. J. Frisch, G. W. Trucks, H. B. Schlegel, G. E. Scuseria, M. A. Robb, J. R. Cheeseman, G. Scalmani, V. Barone, G. A. Petersson, H. Nakatsuji, X. Li, M. Caricato, A. V. Marenich, J. Bloino, B. G. Janesko, R. Gomperts, B. Mennucci, H. P. Hratchian, J. V. Ortiz, A. F. Izmaylov, J. L. Sonnenberg, D. Williams-Young, F. Ding, F. Lipparini, F. Egidi, J. Goings, B. Peng, A. Petrone, T. Henderson, D. Ranasinghe, V. G. Zakrzewski, J. Gao, N. Rega, G. Zheng, W. Liang, M. Hada, M. Ehara, K. Toyota, R. Fukuda, J. Hasegawa, M. Ishida, T. Nakajima, Y. Honda, O. Kitao, H. Nakai, T. Vreven, K. Throssell, J. A. Montgomery, Jr., J. E. Peralta, F. Ogliaro, M. J. Bearpark, J. J. Heyd, E. N. Brothers, K. N. Kudin, V. N. Staroverov, T. A. Keith, R. Kobayashi, J. Normand, K. Raghavachari, A. P. Rendell, J. C. Burant, S. S. Iyengar, J. Tomasi, M. Cossi, J. M. Millam, M. Klene, C. Adamo, R. Cammi, J. W. Ochterski, R. L. Martin, K. Morokuma, O. Farkas, J. B. Foresman, and D. J. Fox, "Gaussian16 Revision C.01," 2016. Gaussian Inc. Wallingford CT.

[141] S. Grimme, "Supramolecular binding thermodynamics by dispersion-corrected density functional theory," *Chem. Eur. J.*, vol. 18, p. 9955, 2012.

[142] J. M. Soler, E. Artacho, J. D. Gale, A. García, J. Junquera, P. Ordejón, and D. Sánchez-Portal, "The SIESTA method for ab initio order-N materials simulation," *J. Phys. Conden. Matter*, vol. 14, p. 2745, 2002.

[143] M. J. van Setten, M. Giantomassi, E. Bousquet, M. J. Verstraete, D. R. Hamann, X. Gonze, and G.-M. Rignanese, "The PseudoDojo: Training and grading a 85 element optimized norm-conserving pseudopotential table," *Comp. Phys. Commun.*, vol. 226, p. 39, 2018.

[144] A. Garcia, M. J. Verstraete, Y. Pouillon, and J. Junquera, "The PSML format and library for norm-conserving pseudopotential data curation and interoperability," *Comp. Phys. Commun.*, vol. 227, p. 51, 2018.

[145] C. Freysoldt, J. Neugebauer, and C. G. Van de Walle, "Electrostatic interactions between charged defects in supercells," *Phys. Status Solidi B*, vol. 248, p. 1067, 2011.

[146] A. V. Vorontsov and P. G. Smirniotis, "DFT study on the stability and the acid strength of Brønsted acid sites in zeolite β," *J. Phys. Chem. A*, vol. 126, p. 7840, 2022.

[147] J. P. Perdew, K. Burke, and Y. Wang, "Generalized gradient approximation for the exchange-correlation hole of a many-electron system," *Phys. Rev. B*, vol. 54, p. 16533, 1996.

[148] M. Bertini, F. Ferrante, and D. Duca, "Empathes: A general code for nudged elastic band transition states search," *Comput. Phys. Commun.*, vol. 271, p. 108224, 2022.

[149] C. A. Schneider, W. S. Rasband, and K. W. Eliceiri, " NIH Image to ImageJ: 25 years of image analysis," *Nat. Methods*, vol. 9, p. 671, 2012.

[150] C. Emeis, "Determination of Integrated Molar Extinction Coefficients for Infrared Absorption Bands of Pyridine Adsorbed on Solid Acid Catalysts," *J. Catal.*, vol. 141, p. 347, 1993.

[151] E. Vrbkova, L. Sekerova, E. Vyskovcilova, M. Zapletal, and L. vCerveny, "Iron-modified zeolite BETA: efficient catalyst in methyllaurate, 2-hexyl-1,3-dioxolane, 4-methyl-2-propyltetrahydro-2H-pyran-4-ol and 4-methyl-2-phenyl-tetrahydro-2H-pyran-4-ol synthesis," *Res. Chem. Intermed.*, vol. 48, p. 1403, 2022.

[152] I. Simakova, P. Mäki-Arvela, M. Martinez-Klimov, J. Muller, Z. Vajglova, M. Peurla, K. Eränen, and D. Yu. Murzin, "Continuous synthesis of menthol from citronellal and citral over Ni-beta-zeolite-sepiolite composite catalyst," *Appl. Catal. A: Gen.*, vol. 636, p. 118586, 2022.

[153] D. Kubicka, N. Kumar, T. Venalainen, H. Karhu, I. Kubickova, H. Osterholm, and D. Yu. Murzin, "Metal-support interactions in zeolite-supported noble metals: Influence of metal crystallites on the support acidity," *J. Phys. Chem. B*, vol. 110, p. 4937, 2006.

[154] H. Chen, Y. J. Zhang, P. Y. He, and L. C. Liu, "DFT studies on Al distribution and Brønsted acid sites in zeolite ECR-1," *Integr. Ferroelectr.*, vol. 207, p. 118, 2020.

[155] M. S. Hamdy, F. A. Alqahtani, M. Shkir, K. F. Fawy, M. Benaissa, M. B. B. Hamida, and N. Elboughdiri, "Effect of different zeolite supports on the catalytic behavior of platinum nanoparticles in cyclohexene hydrogenation reaction," *Catalysts*, vol. 12, p. 1106, 2022.